Cover Page

The handle http://hdl.handle.net/1887/37607 holds various files of this Leiden University dissertation

Author: Siero, Eric
Title: A recipe for desert : analysis of an extended Klausmeier model
Issue Date: 2016-02-09

A recipe for desert
Analysis of an extended Klausmeier model

Contents

1 Introduction

Ingredients of a recipe for disaster

Drylands are regions with little precipitation[1] that cover about 41% of earth's land surface, with a human population of over 2 billion [10] (Figure 1.1). Climate change and population growth impose increased amounts of stress on vegetation in drylands. Human population in drylands grew by 18.5% between 1990 and 2000 [10] and is continuing to increase. Together with increased aspirations for raised standards of living this results in, e.g., the proliferation of livestock [10].

The United Nations Convention to Combat Desertification (UNCCD, established in 1994) defines desertification as land degradation in arid, semi-arid and dry sub-humid areas resulting from various factors, including climatic variation and human activities. In the absence of vegetation, nutrients in the soil are swept away in the event of rain: the disappearance of vegetation triggers soil erosion processes, leaving behind an inhospitable environment unable to offer the services to build a livelihood.

Desertification can be expressed as the ineffective use of the scarce water resource [84], which is lost through evaporation and runoff instead of being used by plants (through transpiration) [142]. In case vegetation has disappeared, all of the water is lost (none is used by plants) and the desertification process is complete.

Clearly, the disappearance of vegetation is something to be avoided. Much is at stake to predict and prevent the formation and expansion of bare deserts. For this, the dynamics of the vegetation need to be understood, at least on a qualitative level.

---

[1]A measure of aridity is defined by dividing the Precipitation by the Potential Evaporation and Transpiration (P/PET). Drylands can be defined by an aridity index less than 0.65, with a subdivision ranging from hyper-arid (< 0.05) to arid ($0.05 - 0.2$) to semi-arid ($0.2 - 0.5$) to dry subhumid ($0.5 - 0.65$).
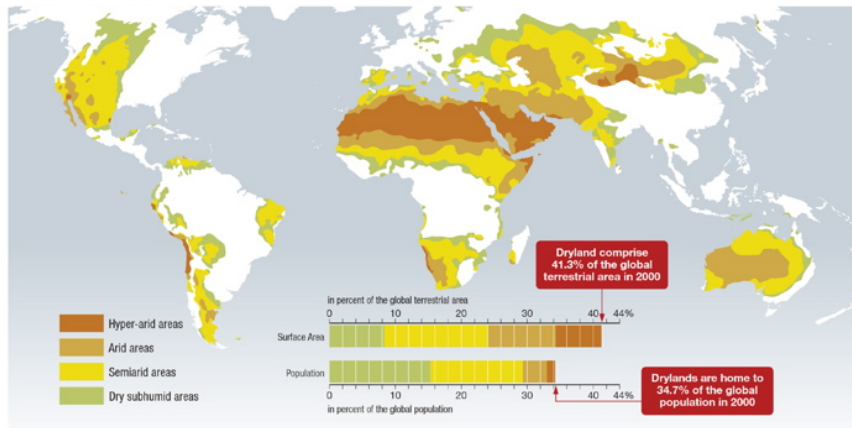
Figure 1.1: Map of the distribution of the four types of dryland over the world [10].

Desertification and climate

In drylands, water is a crucial ingredient for sustenance of vegetation and soil quality. The 2013 report by the Intergovernmental Panel on Climate Change (IPCC) states a *"high confidence* that the contrast of annual mean precipitation between dry and wet regions (...) will increase over most of the globe as temperatures increase" [87], meaning that wet areas become wetter and dry areas become dryer. Under the scenario with a radiative forcing of $7.6\,\mathrm{Wm^{-2}}$, which is an imposed net change in the energy balance of the Earth system, in the year 2100 "many mid-latitude and subtropical arid and semi-arid regions will *likely* experience less precipitation" [87]. A drop in the annual precipitation increases environmental stress and is an important driver of desertification. As a side note, increased levels of CO_2 do lead to a higher water use efficiency by plants through decreased transpiration [32].

Rather than only acting as input, desertification also feeds back to the climate, which is another reason for it having attracted global attention. Desertification changes the albedo (reflectance coefficient of sunlight), both local through changes in plant cover [23] and nonlocal through deposition of desert dust [13]. Additionally, desertification implies reduced carbon sequestration within vegetation and soil [73].
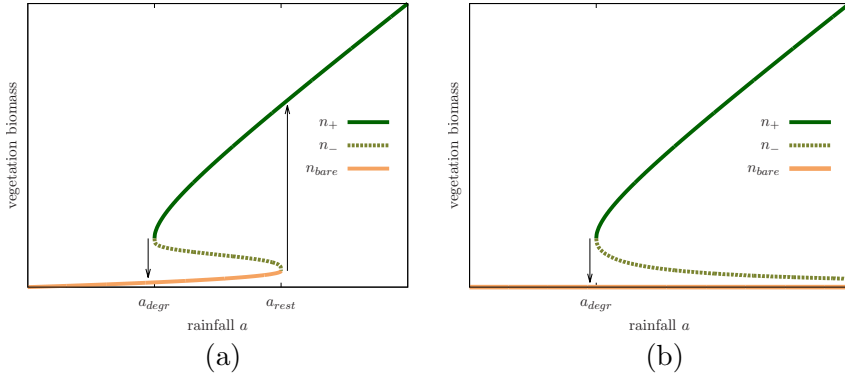
Figure 1.2: Catastrophic transition from a vegetated state n_+ to a degraded bare state n_{bare}, as rainfall reaches the tipping point a_{degr}. The intermediate vegetated state n_- is unstable. (a) The system suffers from hysteresis since the rainfall level required for restoration $a_{rest} > a_{degr}$. (b) In this system the degradation is not reversible by a rainfall increase.

Vegetation on the verge of collapse

Vegetation improves the infiltration characteristics of the soil [150], which increases the water supply to the vegetation itself. So the presence of vegetation reasserts itself. If environmental conditions deteriorate, the amount of vegetation may become critical. Beyond the tipping point, too little vegetation may lead to a smaller water supply: a positive feedback loop that initiates the total collapse of the vegetation (Figure 1.2). Restoration of the ecosystem is difficult because of soil erosion and the infiltration feedback loop, leading to hysteresis or irreversibility.

Brief overview of arid ecosystem models

Various low-dimensional models have been proposed to help explain desertification and vegetation patterns. Early on, in 1997 a scalar (1-component) model for the vegetation was set up [108], with kernel functions with varying ranges built to represent long range inhibition, medium range reproduction and short range toxic interactions. The modeling gained momentum with the publication of the 2-component Klausmeier model [97] in 1999, where a surface water component interacts with the vegetation component. In [202] (2001) the second component is utilized for soil water. Multiple 3-component

models have been studied, where both surface and soil water take part, as in [79] (2001) or [148] (2002) and [70] (2004). In [70] (2004) long range inhibition is present due to extended root systems and soil water diffusion.

These models can of course be further expanded, e.g. by explicitly incorporating herbivores [196] or distinguishing functional groups of vegetation with different traits [69]. Incorporation of additional mechanisms makes the analysis more challenging, which often necessitates subsequent simplifying assumptions. In this thesis, attention is mostly restricted to extensions of the Klausmeier model that maintain the 2-component structure of this model. A more complete overview of arid ecosystem models is presented in [19].

Desertification scenarios with increasing complexity

Disregarding differences between plant species and temporarily disregarding spatial heterogeneity, vegetation can be represented by a single scalar. In this case, desertification may be understood as the tipping of a vegetated state. In regions where water is scarce, vegetation growth is limited by water supply and is basically modeled by

$$\text{water change} = \text{rainfall} - \text{evaporation} - \text{uptake},$$
$$\text{plant change} = \qquad\qquad -\text{plant death} + \text{uptake}.$$

The rainfall can change seasonally and tends to be intermittent in time [98, 179], but here we view rainfall as a climatic parameter that may slowly change over time and is constant in the absence of climate change. The water evaporation is modeled by a linear term. Water is regarded as surface water, and the process of infiltration and subsequent uptake of soil water are combined in the surface water uptake terms. Since both the infiltration and the soil water uptake are assumed to be linear in the vegetation, the surface water uptake terms are quadratic in the vegetation [97]. Plant death is, for simplicity, modeled by a linear term.

After rescaling [180], representing water by w and vegetation by n and their change in time by the derivatives w_t and n_t, the model is given by

$$\begin{aligned}
w_t &= a - w - wn^2, \\
n_t &= -mn + wn^2,
\end{aligned} \tag{1.1}$$

the *nonspatial* Klausmeier model [97]. For $a \geq 2m$ (and $m < 2$) it has a stable vegetated state (w_+, n_+) that disappears in a fold bifurcation at
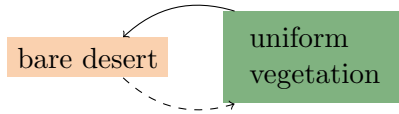
Figure 1.3: Desertification diagram for nonspatial models. The transition from the desert to the vegetated state is represented by a dashed arrow to signify irreversibility.

$a_{degr} = 2m$, as in Figure 1.2(b). If rainfall drops below a_{degr}, the system falls down to the degraded bare desert state and recovery to (w_+, n_+) is troublesome. This is graphically represented by the transition diagram in Figure 1.3.

We will now see that allowing for spatially heterogeneous solutions adds complexity to the desertification scenario. The aforementioned infiltration feedback loop has a short range, since only nearby vegetation benefits from the improved infiltration characteristics of the soil. Overall, vegetation is in competition for water, which may flow relatively long distances over bare soil before infiltrating at a vegetation patch. The short range facilitation and long range competition together drive the formation of periodic vegetation patterns [150].

The widespread appearance of these vegetation patterns in all tropical and subtropical arid areas has been evidenced. They are ubiquitous at the interface between arid and semi-arid regions [36]. These patterns include gapped, labyrinthine, banded and spot patterns (Figure 1.4). The patterns are found on flat or constant-slope terrain without spatial heterogeneities other than those that can be attributed to the vegetation itself [156]. Field observations of vegetation patterns necessitate the development of spatially extended models.

To spatially extend (1.1), we need to take into account processes that displace the surface water and vegetation. We start out in one space dimension x. We allow for the possibility of the terrain having a constant slope, in the Klausmeier model [97] the downslope advection is assumed to be dominant and displacement is modeled by $2cw_x$. We extend the Klausmeier model by adding a (possibly nonlinear) diffusion $d_1 w^\gamma{}_{xx}$ [199]. This form with $\gamma = 2$ can be derived from the shallow water equations [70]. The dispersal of plants is modeled by diffusion $d_2 n_{xx}$, with $d_2 \ll d_1$. This gives

$$
\begin{aligned}
w_t &= d_1 w^\gamma{}_{xx} + 2cw_x + a - w - wn^2, \\
n_t &= d_2 n_{xx} \qquad\qquad - mn + wn^2.
\end{aligned}
\tag{1.2}
$$
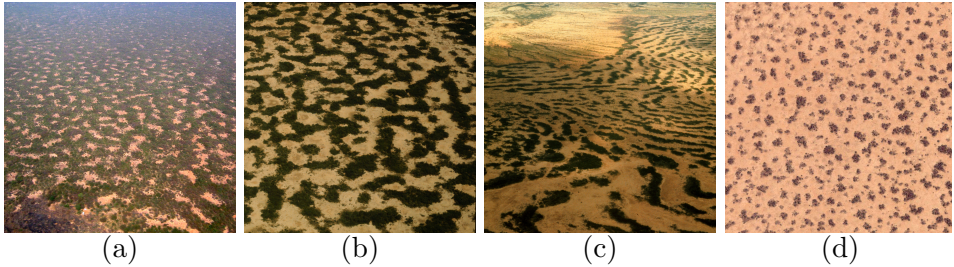
Figure 1.4: Periodic vegetation patterns. Aerial photograph of (a) pattern of gaps, (b) labyrinth, (c) banded pattern [149]. (d) Satellite image of a spot pattern over Sudan.

Figure 1.5: Desertification diagram for the extended Klausmeier model in one space dimension.

Because vegetation patterns extend over large areas, the model domain is taken to be unbounded, so without boundary conditions. Since the modeling equations are strikingly similar to the Gray-Scott model [74], this puts vegetation patterns in the same framework as patterns in chemical reactions.

In the spatially extended model, for decreasing rainfall the fold bifurcation of the spatially homogeneous solution (w_+, n_+) is preceded by a Turing bifurcation [190]. At the Turing bifurcation periodic patterns form. In Chapter 2 we show that a further decrease of the rainfall parameter leads to a coarsening cascade of patterns with larger and larger wavelength (or equivalently smaller and smaller wavenumber ($= 2\pi/$wavelength)). Eventually, for sufficiently small rainfall, the bare desert state is reached (Figure 1.5).

The occurrence of vegetation patterns can thus be regarded as a rough early warning signal for the final transition to the bare desert state, with larger wavelengths signalling a more imminent danger of complete collapse. This is in accordance with one of Ni's conjectures [133], which states that the last patterns to destabilize have large wavelengths.

We now add a second space dimension by replacing the second derivatives to x by second derivatives to both x and y, denoted by the Laplace operator $\Delta = \partial_x^2 + \partial_y^2$. Restricting to the case with linear water diffusion, the extended
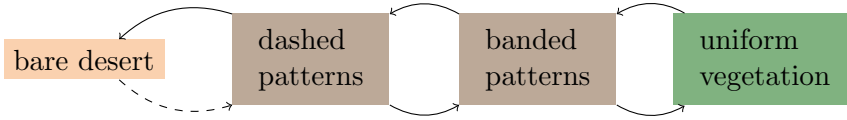
Figure 1.6: Desertification diagram for the extended Klausmeier model in two space dimensions.

Klausmeier model becomes

$$
\begin{aligned}
w_t &= d_1 \Delta w + 2cw_x + a - w - wn^2, \\
n_t &= d_2 \Delta n \qquad\qquad - mn + wn^2.
\end{aligned}
\tag{1.3}
$$

The slope is assumed to be in the x-direction, so that the advection term remains the same.

The restriction to one space dimension overestimates stability of the vegetation patterns, which correspond to vegetation bands (Figure 1.4(c)) when viewed as solutions of the two-dimensional extended Klausmeier model. Stability of vegetation bands in two space dimensions implies stability of the patterns in one space dimension but not the other way around: stable 1D patterns may be unstable against perturbations with a nontrivial transverse component.

In Chapter 3 we show that vegetation patterns indeed can be transversely unstable. The extent in which this occurs depends strongly on the slope of the terrain, which was modeled by the advective term. The smaller the slope, the more the banded patterns tend to be transversally unstable. Banded vegetation patterns on steeper slopes remain stable for a wider range of values of the rainfall parameter, thus are ecologically more resilient. In this case the desertification process only diverges from the one-dimensional case after the coarsening cascade of banded patterns with longer and longer wavelengths has progressed.

As a result of the breakup of banded vegetation patterns at low rainfall values, dashed patterns are formed. This way we have identified a possible natural next step in the desertification process, as depicted in Figure 1.6. The appearance of dashed patterns could be a warning signal that the transition to the bare desert state is imminent.

7

Dramatic sudden loss of productivity or gradual decline?

The current consensus is that in the final step of the desertification process, like in Figure 1.2(b), the ecosystem occupies a vegetated state with a reasonable amount of biomass but then undergoes a critical transition where all biomass is lost [149, 163]. This is what happens in the nonspatial Klausmeier model (1.1). How does this relate to the desertification scenarios for the spatially extended Klausmeier model we described?

As mentioned previously, the spatially extended Klausmeier model is in accordance with Ni's conjecture: the last patterns to destabilize have large wavelengths. These patterns form out of patterns with a smaller wavelength through a coarsening cascade. Large wavelength patterns have vegetation patches that are few and far between, summing up to a small amount of biomass. This means that the final transition to the bare desert state comprises only a minor loss of biomass. Thus, adhering to Ni's conjecture opposes the popular view that desertification entails a sudden large final jump in biomass.

In Chapter 4 we present a model refinement for capturing grazing, as an addition to the linear local vegetation death term already present in most arid ecosystem models. For this we employ nonlocal terms, so that the grazing pressure at one location depends on the presence of vegetation elsewhere. Because the grazing pressure on isolated vegetation patches may increase since there are no alternative foraging sites, the large wavelength patterns may become inadmissible in the presence of grazers.

We make a distinction between sustained and natural grazing. In sustained grazing systems, we assume that the number of herbivores is constant. In this case we indeed see dramatic transitions from vegetated states to the bare desert state, since none of the states with low biomass are admissible. Thus the situation is conceptually like Figure 1.2(b). In natural grazing systems, herbivore numbers drop if biomass decreases. If the number of herbivores drops fast enough, a transition from a high productivity (with a large herbivore number) to a low productivity (with a small herbivore number) system state occurs. Since in principle recovery to high productivity states is possible, the situation is similar to Figure 1.2(a).

The spatially extended Klausmeier model without nonlocal grazing adheres to Ni's conjecture and generally doesn't show a dramatic sudden loss of productivity. Only after introducing nonlocal grazing terms, do these dramatic regime shifts occur. In sustained grazing systems, Ni's conjecture does

not hold. In systems with natural grazing, a dramatic loss of productivity may lead to a low productivity state, after which Ni's conjecture may still hold.

Outline

In Chapter 2, which is based on [180], we numerically study the extended Klausmeier model in one space dimension (1.2). We show model dynamics with a slowly decreasing rainfall parameter that leads the system from a homogeneously vegetated quasi steady equilibrium state through a Turing instability to a periodic pattern. A further decrease of the rainfall parameter leads to a coarsening cascade of patterns with larger and larger wavelength (or equivalently smaller and smaller wavenumber ($= 2\pi/$wavelength)). Eventually, for sufficiently small rainfall, the bare desert state is reached (Figure 1.4).

An important conceptual tool is the Busse balloon, first used in fluid mechanics [21], which represents all stable periodic vegetation patterns of the autonomous system (where the parameters are time independent). These patterns are represented by (rainfall, wavenumber)-pairs. By performing simulations with a slowly changing rainfall parameter, the system traces out a trajectory in (parameter, wavenumber)-space when it resides in a periodic system state. For small rates of change the length of the trajectory outside the Busse balloon is small, so destabilization can be predicted accurately. For large rates of change the discrepancy can become considerable, to the point that the system directly transitions from a state with the Turing wavenumber to the bare desert state, omitting the coarsening cascade.

The trajectories also depend on the application of noise. A higher noise level introduces heterogeneity in the population of vegetation patches, so that a larger share of the patches survive destabilization, leading to a coarsening cascade with smaller (and thus more) jumps in wavenumber and smaller trajectories outside the Busse balloon. Period doubling (wavenumber halving) occurs often, except in the regime with high wavenumbers/high rainfall, high noise levels and small rates of change.

Chapter 3 is based on [176]. We begin by presenting a general linear stability analysis of homogeneous steady states of inhibitor-activator type in
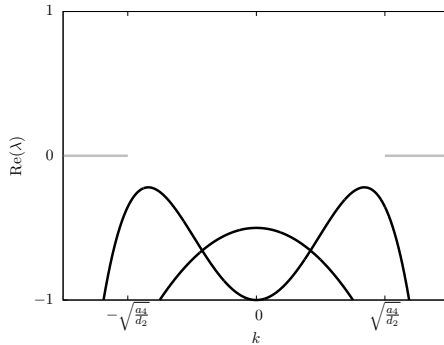
Figure 1.7: Sketch of real parts of curves of spectrum $\mathrm{Re}(\lambda)$ of the linearization about the homogeneous steady state (u_*, v_*), as a function of the linear wavenumber k. The spectrum can only cross the imaginary axis $\mathrm{Re}(\lambda) = 0$ in between the grey line segments.

a reaction-advection-diffusion system. These systems are of the form

$$u_t = d_1 \Delta u + c_1 u_x + f(u, v),$$
$$v_t = d_2 \Delta v + c_2 v_x + g(u, v).$$

A homogeneous steady state (u_*, v_*) is of inhibitor-activator type if both $\frac{\partial f}{\partial u}(u_*, v_*) < 0$ and $a_4 := \frac{\partial g}{\partial v}(u_*, v_*) > 0$. This setup allows for the simultaneous treatment of both a diffusion driven Turing instability and a differential flow driven instability, and mixtures of both, with differential flow being the difference between the advection coefficients $|c_1 - c_2|$. We unravel the role of the differential flow in the selection of striped patterns at pattern formation in two space dimensions.

The analysis starts out in one space dimension. Here a pivotal upper estimate on destabilizing wavenumbers (Figure 1.7) allows for the removal of the wavenumber in the analysis. Thus all requirements can be set on the linearization of the kinetics and the spatiality of the problem is put to the background. This paves the way to results on the:

- monotonicity of the destabilization locus;
- direction of motion of emerging patterns.

Subsequently we employ a Squire transformation, which extends applicability of the previous results to two space dimensions and shows that destabilization of the homogeneous steady state occurs through perturbations perpendicular to the advection. The Squire transformation was, like the Busse balloon, first used in fluid mechanics [183].

All results are shown to apply to the extended Klausmeier model. This means that the Turing instability monotonically moves to larger rainfall values for increasing slope (advection), destabilization occurs by perturbations perpendicular to the slope and the emerging vegetation patterns move uphill.

Numerical analysis for the arid ecosystem model in two space dimensions shows that vegetation bands are (ecologically) more resilient in a regime with a steeper slope (advection). Under increasing environmental stress, banded vegetation eventually breaks up in a dashed vegetation pattern, which identifies dashed vegetation patterns as a next step in the desertification process. Observational studies back up that vegetation bands are rarely found at low precipitation, at low wavenumber, and in the absence of a slope. In accordance with this last finding, we prove, in an asymptotic scaling regime, that long wavelength striped patterns are transversely unstable on flat terrain.

In Chapter 4, which contains unpublished material, we extend the Klausmeier model with nonlocal grazing terms. For this we use well-established theory concerning herbivore distribution and responses to available biomass distributions. We make a distinction between sustained grazing - where the number of herbivores is assumed to be kept constant, and natural grazing - where herbivores are themselves responsible for acquiring a sufficient forage intake.

Through a linear analysis we investigate how the destabilization of the homogeneously vegetated state is affected by the introduction of grazing terms. The formation of vegetation patterns may be suppressed if the effective foraging potential is a superlinear function of the vegetation, meaning that herbivores are strongly attracted to locations with much vegetation.

As already discussed, we show how sustained grazing systems do not adhere to Ni's conjecture, since in this case long wavelength patterns are not the last patterns to destabilize. Whereas natural grazing has the potential to make a divide between high productivity and low productivity system states.

In Chapter 5, based on [127], we change gears and study the question of well-posedness in the context of quasilinear systems of partial differential equations (PDEs). Quasilinear PDEs are a class of PDEs that are 'less linear' than semi-linear but 'more linear' than fully nonlinear PDEs. A PDE is semi-linear if its highest order derivative terms have coefficients that are independent of the dependent variable, it is quasilinear if its highest

order derivative terms have coefficients that may depend on the dependent variable but not on its derivatives.

In arid ecosystem modeling, the quasilinearity stems from a water-dependent diffusion coefficient of the water component, that results from the modeling of surface water flow through the shallow water equations [70]. This corresponds to $\gamma = 2$ in (1.2), where $w^2{}_{xx} = ww_{xx} + 2w_x{}^2$, so that the coefficient of the highest order derivative w_{xx} indeed depends on w. These types of differential equations also arise in the modeling of flow through porous media and are therefore often referred to as porous medium equations [200].

For illustration, let's consider a real life example. Since everyone has (had) a mother, it makes sense to ask "What's the name of your mother?" to anyone. But since not everyone has a child, it may be ill-posed to ask "What's the name of your child?". Depending on the context, the question "What's the name of your child?" can be well-posed or ill-posed. For instance, when posed to a man pushing a stroller this question should work well, but not when posed to the child inside. Only after affirming that the person in question has a child, it makes sense to ask for properties of the child.

Likewise, when analyzing a model, the most fundamental question to ask is whether the model makes *any* sense: under what conditions does a solution exist? Thus we look for functional analytic settings where the existence of a solution can be established. Only then it makes sense to wonder if the model makes the *right* sense in relation to the (natural) system that is being modeled: does the model solution behave in accordance with observations or experiments?

For systems of quasilinear PDEs on unbounded domains the issue of well-posedness and stability of nonlinear waves was not straightforward to reconcile based on the existing quite abstract literature. We settle well-posedness by presenting various suitable function spaces in which (unique) solutions to systems of PDEs exist, using various results from the theory of maximal regularity. To assess stability of a nonlinear wave, it is necessary to choose a function space of perturbations in which the evolution problem of the perturbations is well-posed. In addition we prove an orbital instability result for spectrum invading the half plane with positive real part, without assuming a spectral gap or the existence of an unstable eigenvalue.

We apply the results to the GKGS model [199], which is a slight variation of the extended Klausmeier model where $a - w$ is replaced by $a(1 - w)$. In this context the vegetation bands are the nonlinear waves.

Chapter 6 contains a brief outlook on future research possibilities.

Project collaborators

This thesis has been written at the Mathematical Institute, Leiden University, under supervision of Arjen Doelman and Jens Rademacher (University of Bremen). The research has been done in close collaboration with ecologists Max Rietkerk, Maarten Eppinga en Koen Siteur at the Copernicus Institute of Sustainable Development, Utrecht University.

Funding

2 Beyond Turing: the response of patterned ecosystems to environmental change.

Spatially periodic patterns can be observed in a variety of ecosystems. Model studies revealed that patterned ecosystems may respond in a nonlinear way to environmental change, meaning that gradual changes result in rapid degradation. We analyze this response through stability analysis of patterned states of an arid ecosystem model. This analysis goes one step further than the frequently applied Turing analysis, which only considers stability of uniform states. We found that patterned arid ecosystems systematically respond in two ways to changes in rainfall: 1) by changing vegetation patch biomass or 2) by adapting pattern wavelength. Minor adaptations of pattern wavelength are constrained to conditions of slow change within a high rainfall regime, and high levels of stochastic variation in biomass (noise). Major changes in pattern wavelength occur under conditions of either low rainfall, rapid change or low levels of noise. Such conditions facilitate strong interactions between vegetation patches, which can trigger a sudden loss of half the patches or a transition to a degraded bare state. These results highlight that ecosystem responses may critically depend on rates, rather than magnitudes, of environmental change. Our study shows how models can increase our understanding of these dynamics, provided that analyses go beyond the conventional Turing analysis.

2.1 Introduction

Spatially periodic patterning of sessile biota can be observed in a variety of ecosystems including arid ecosystems [116], mussel beds [195], boreal peatlands [118] and tropical peatlands [11]. Such spatially periodic patterns can typically not be explained by underlying heterogeneity in the environment, which suggests that they are self-organized. Self-organization into periodic patterns is the result of positive feedbacks that act locally (short range activation) in combination with distal negative feedbacks (long range inhibition; [68]). This combination of feedbacks is also referred to as scale-dependent feedbacks [151]. In arid ecosystems, the combination of locally reduced evaporation through shading and water uptake by laterally extended roots is known to induce such scale-dependent feedbacks [70, 124]. Scale-dependent feedbacks can also result from the fact that in arid ecosystems plants tend to improve soil structure which allows more water to infiltrate during rain events [150, 186]. This results in increased water availability and increased plant growth, meaning that locally a positive feedback loop is active. However, water availability farther away is negatively affected by this facilitative effect: surface water accumulates on bare soils during intense rain events and moves towards vegetated areas due to a gentle slope or due to infiltration differences on flat terrain [97, 148]. In arid ecosystems, local positive feedbacks are therefore linked to a flux of resource that results in long range inhibition and consequently in pattern formation. This type of scale-dependent feedback is referred to as the resource-concentration mechanism [149]. The positive feedbacks that are often involved in pattern formation [151] are associated with nonlinear ecosystem response to environmental change [34, 149]. This means that gradual changes in environmental conditions may result in sudden significant losses in productivity and in degradation of patterned ecosystems.

Reaction-(advection-)diffusion models have been developed to understand the mechanisms responsible for pattern formation, to study the conditions under which scale-dependent feedbacks are strong enough for patterning to occur and to get more insight in the possible nonlinear behavior of patterned ecosystems, e.g. [70, 97, 148, 202]. In these models, patterns typically arise from a uniform system state that becomes unstable to heterogeneous perturbations. This type of instability is referred to as Turing instability (after A.M. Turing, 1912-1954; [190]) and is thought to be involved in for example the formation of patterns on animal coats [120], on sea shells [121] and

in chemical systems [74, 139]. Using linear stability analysis, it is possible to find the parameter ranges for which a uniform system state is Turing unstable.

At present, Turing analysis is used as a relatively simple way to study the environmental conditions under which one would expect periodic patterns to be observed, e.g. [61, 70, 79, 95, 97, 125]. However, since Turing analysis only considers the stability of uniform system states, it provides very little information about the behavior of ecosystems that are in a patterned state. Therefore, previous studies have been exploring this behavior using numerical approaches. These studies revealed a number of interesting properties of patterned ecosystems. Various model studies suggest that patterns can be expected under conditions where uniform system states are still stable and under conditions too harsh for uniform cover to be sustained, e.g. [148, 202]. These findings imply that stable uniform and stable patterned states can coexist for a range of environmental conditions [149]. The coexistence of alternative stable ecosystem states can result in so-called critical transitions [162] if environmental conditions change, which are associated with sudden losses of productivity and ecosystem degradation [164]. Numerical studies that looked in more detail to the dynamics of patterned ecosystem states suggest that multiple stable patterned states, with different wavelength or spatial configurations, can coexist and that this can result in hysteresis and more gradual ecosystem adaptation if environmental conditions change [16, 174].

Although studies with numerical approaches uncovered some interesting characteristics of patterned ecosystems, recent studies have been exploring whether the use of analytically based methods provides more detailed insights [172, 199]. These approaches go one step further than Turing analysis as they consider the stability of patterned rather than uniform ecosystem states. By combining stability analysis on patterned states with model runs, [172] demonstrated that hysteresis can be explained by the coexistence of multiple stable states. His study also suggests that the rate at which environmental conditions change may affect system response. This is of particular importance as current human activities induce anomalous rates of environmental change, e.g. [89]. Although these results suggest that information about the stability of patterned states is essential in understanding ecosystem response to changing environmental conditions, the application of stability analysis on patterned states in the field of ecology has been limited so far and various ecologically relevant questions remain to be answered [198, pp. 95-100].

One of the processes that are not well understood is the process of pattern wavelength adaptation. Patterned ecosystems can respond to environmental change by adapting pattern wavelength and the study by [172] showed that this process is affected by the rate of environmental change. It is, however, unknown why and how patterned ecosystems adapt and why this depends on the rate of change. In this study we therefore aim to provide a mechanistic understanding of how patterned ecosystems respond to environmental change, considering both the magnitude of change as well as the rate of change. By applying stability analysis on patterned system states, we first show that the use of Turing analysis can yield false negatives and false positives with regard to predicting the existence of observable (i.e. stable) patterns. Based on the mechanisms that are involved in pattern destabilization, we then discuss possible types of pattern adaptation. Using model runs, we demonstrate that knowledge about the stability of patterned states is crucial in understanding the response of ecosystems subject to environmental change and show how the rate of change in environmental conditions and the level of imposed spatio-temporal noise affect system response. Finally, we propose that competition for resources between patches of vegetation provides a possible ecological explanation for the obtained results. In this study we use an extended version of an arid ecosystem model by [97] as introduced by [199], which we will discuss in the next section.

2.2 Model description and analyses

2.2.1 Model description

The extended version of the Klausmeier model is a reaction-advection-diffusion model in which the formation of spatial vegetation patterns is the result of competition for surface water. The model has two state variables that are functions of both time t and space x ($x \in \mathbb{R}$): plant biomass n and surface water w. Notice that we will consider only one spatial dimension (x), following [199] and [172]. The model is given by equation (2.1) and (2.2). We use a non-dimensional version the model in order to reduce the number of parameters. For a dimensional version of the model and the physical

meaning of the parameters, see appendix 2.A.

$$\frac{\partial w}{\partial t} = a - w - wn^2 + v\frac{\partial w}{\partial x} + e\frac{\partial^2 w^\gamma}{\partial x^2} \tag{2.1}$$

$$\frac{\partial n}{\partial t} = wn^2 - mn + \frac{\partial^2 n}{\partial x^2} \tag{2.2}$$

The change in surface water w (equation (2.1)) is controlled by rainfall a, surface water losses (second term) and uptake by plants through infiltration and transpiration (third term). As in the original model by [97], the movement of surface water due to gradients in the terrain is captured with an advection term (fourth term). We extended the model by adding diffusion of surface water (fifth term). We did this for three reasons. First, the diffusion term has a physical basis as it can be derived from the shallow water equations [70]. Second, it allows us to capture the movement of surface water induced by spatial differences in infiltration rate [148]. Third, it enables us to demonstrate that the type stability analysis we use to study the system's response to change can be applied to both reaction-advection-diffusion and reaction-diffusion model ($v \neq 0$ and $v = 0$ respectively).

The dynamics in plant biomass n (equation (2.2)) are determined by plant growth which is linearly related to water uptake (first term) and by plant mortality (second term). As in the original model, plant dispersion is modeled with a diffusion term (third term).

The non-dimensional version of the model has five parameters. We chose parameter values that are valid for grass as reported by [97]. Plant mortality was set to $m = 0.45$ and for flat and sloped terrain $v = 0$ and $v = 182.5$ respectively. As we are interested in the response of the system to changes in rainfall, we use rainfall a as bifurcation parameter and let it vary between $a = 0$ to $a = 3.5$. For simplicity we chose $\gamma = 1$. [199] showed that the value of γ does not qualitatively affect the structure of stability regions. Therefore the results presented in the following sections are not expected to differ qualitatively for other values of γ. Finally, e was calibrated to obtain patterns in a realistic rainfall range according to studies listed by [37], which appeared to be for $e = 500$. For conversion of these dimensionless parameters to dimensional parameters, see appendix 2.A.

The extended Klausmeier model falls in the broader class of reaction-advection-diffusion models referred to as activator-depleted substrate systems [59] with vegetation being the activator and surface water being the substrate. In addition, it shows strong similarities with other well studied

models, depending on parameter choice. Naturally, if $e = 0$ we return to the original (one dimensional) Klausmeier model [97]. With $v = 0$ and $\gamma = 1$ the model is equal to the model studied by [94] and the well studied chemical model by [74]. Finally, the model has been studied by [199] for constant rainfall a.

It should be mentioned that apart from the model by [97] and derivations thereof [94, 199] a large body of model studies have been published that dedicate pattern formation in arid ecosystems to a variety of mechanisms, including competition for surface water [57,79,148], competition through soil water uptake by roots [125, 202], a combination of these mechanisms [70] or plant-plant interactions only [108–111]. These models may be suitable depending on system characteristics such as climate, soil and plant properties and can be used to answer specific research questions. However, here we limit our study to the analysis of the more generic extended Klausmeier model as it captures pattern formation in a relatively parsimonious way.

2.2.2 Analyses

In order to study the response of the system to changes in rainfall a, knowledge is required about the rainfall ranges for which stable spatially uniform and patterned states of equations (2.1) and (2.2) exist. We derived the existence of system states and assessed their stability by performing linear stability analysis. This type of analysis, together with the obtained stability regions in parameter space, will be discussed in detail in the next section. The boundaries of the stability regions were obtained by tracking the marginally stable patterned system states [51, 171] using AUTO continuation software [41, AUTO-07p].

As the rainfall a changes stable states may lose their stability. The stability regions, as obtained using stability analysis, provide insight in when a system state destabilizes. However, the behavior of the system after destabilization (e.g. re-stabilization) is a priori unknown. To study this, we performed runs of the model with linearly increasing and decreasing rainfall a. The model runs were performed in MATLAB (version 2012a - 7.14.0.739; The MathWorks, Inc.) using a vector of 1024 elements that represent a domain with a size of 1000 (500 meters). Periodic boundary conditions were used to diminish boundary effects and to mimic an infinite domain. We studied the response of the system under different rates of change in a ($\frac{da}{dt} = -10^{-7}$, -10^{-4} and -10^{-2}). We added spatially and temporally

uncorrelated multiplicative uniformly distributed noise to both components of the model every $\frac{1}{4}$ year (noise amplitude $= 0$, $5 \cdot 10^{-5}\%$ and 0.05%). The noise was added to diminish numerical artifacts, such as the system residing in unstable system states, and represents potential sources of noise that are not captured by the deterministic equations.

The state of the system can be expressed in terms of pattern wavenumber κ ($= \frac{2\pi}{\text{wavelength}}$). To enable comparison between the model runs and the stability regions, we assessed the wavenumber of the patterns as generated by the model by applying discrete Fourier transformations. This is explained in detail in appendix 2.B.

2.3 Stability of uniform and patterned states: from Turing instability to the Busse balloon

In this section we discuss the stability of uniform and patterned states of the extended Klausmeier model. In subsection 2.3.1 we briefly review well-known linear stability analysis (Turing analysis) as applied to uniform system states. We then continue by discussing the mathematically more challenging stability analysis of patterned states in subsection 2.3.2. Finally we compare the stability regions obtained in both subsections and discuss the ecologically relevant results in subsection 2.3.3.

2.3.1 Existence and stability of uniform system states

Determining the stability of uniform steady states to uniform perturbations is a fairly easy task: first one derives the steady states of the system, and then one perturbs the steady states. The stability of the system state is then defined by the sign of the exponential growth rate of the perturbation: the maximum real part of eigenvalues λ. Solely negative real parts of eigenvalues imply a (asymptotically) stable state, whereas a positive real part means that the system state is unstable. A bifurcation occurs when due to a parameter change the growth rate of a perturbation $\max(\text{Re}(\lambda))$ becomes positive (here $\max()$ refers to the maximum of a set values and $\text{Re}()$ takes the real part of a complex number). The system is marginally stable at such an onset of instability. Marginal stability marks the boundaries of stability regions in parameter space.

Uniform system states can be derived by setting equations (2.1) and (2.2)

to zero while neglecting advection and diffusion fluxes. The extended Klausmeier model presented in the previous section has three uniform steady states for $a > 2m$ (see appendix 2.D.1 for a derivation). Two of the steady states are vegetated (so $\bar{n} > 0$), of which one is stable to uniform perturbations for ecologically relevant parameter values ($m < 2$) and one is unstable (see appendix 2.D.2 for stability analysis). A stable bare desert state ($\bar{n} = 0$) exists for all values of a. At $a = a_{SN} := 2m$ a saddle-node bifurcation occurs. Here the vegetated states cease to exist, meaning that for $a < a_{SN}$ only a stable bare state exists.

Perturbations in natural systems are generally heterogeneous. To account for this in the stability analysis, spatially heterogeneous perturbations can be added to the uniform states [59, 190]. Heterogeneous perturbations can be represented as sinusoids with wavenumber κ ($= \frac{2\pi}{\text{wavelength}}$) of which the amplitude grows (or decays) with a rate of $\max(\text{Re}(\lambda(\kappa)))$.

When perturbing the stable uniformly vegetated state of the extended Klausmeier model with such sinusoids (appendix 2.D.3), a range of values for a can be found for which the state is Turing unstable. Here the amplitude of a perturbing sinusoid grows over time ($\max(\text{Re}(\lambda(\kappa, a))) > 0$). Whether this occurs does not only depend on intrinsic model parameters, such as a, but also on the wavenumber of the sinusoid κ. The solid red line in figure 2.1a,b borders the region in (a, κ)-space for which the uniformly vegetated state is Turing unstable. Assuming that the amplitude of the imposed perturbations grow while their wavenumber is preserved, one would expect patterns to exist in this region. Therefore this can be seen as a *Turing prediction region*. If rainfall decreases over time, patterns will form directly after the Turing bifurcation T [199, or Turing-Hopf bifurcation TH if $v \neq 0$] as here the uniform state becomes unstable. These patterns will have a wavenumber close to κ_T (or κ_{TH}): the wavenumber of the perturbation that initializes the Turing bifurcation. Model runs show that when randomly perturbing uniform states that are Turing unstable, the system tends to evolve to a state with a pattern wavenumber close to the wavenumber of the perturbation with the largest growth rate, also referred to as most unstable mode (dashed red line in figure 2.1a,b; [174]). As we will show in section 2.4 however, pattern wavenumber can strongly deviate from the this wavenumber if environmental conditions change.

2.3.2 Existence and stability of patterned system states

So far we have discussed the stability of uniform system states. The patterned states that arise from a Turing unstable uniform state are, however, not necessarily stable themselves. Unlike uniform steady states, it is generally not possible to find explicit expressions for patterned states by hand. For this and subsequent determination of stability we rely on numerics.

Patterns may exist in the form of so-called *wavetrains*: vegetation bands that slowly migrate in uphill direction. In fact for $v = 182.5$ this is the case for all patterns. To deal with this a comoving frame $\xi = x - st$ is introduced. Here s is equal to the migration speed: a pattern dependent property that is assumed to be constant in space and time. This results in additional advection terms in both equations. A pattern (w_p, n_p) with wavenumber κ exists for rainfall a if and only if it is a solution to the system

$$0 = a - w_p - w_p n_p^2 + (v + s)\frac{dw_p}{d\xi} + e\frac{d^2 w_p^\gamma}{d\xi^2} \tag{2.3}$$

$$0 = w_p n_p^2 - m n_p + s\frac{dn_p}{d\xi} + \frac{d^2 n_p}{d\xi^2} \tag{2.4}$$

on the domain $[0, \frac{2\pi}{\kappa}]$ with periodic boundary conditions. See appendix 2.E.1 for a derivation of these equations. Notice that, besides the parameters of the extended Klausmeier model (equations (2.1) and (2.2)), migration speed s and wavenumber κ now appear as additional parameters. Parameters s and κ can be used to express the state of the system.

Since the existence of unstable patterned states is not of immediate interest we also require stability. To determine this we need to linearize about (w_p, n_p) leading to ordinary differential equations with a dependency on w_p and n_p (appendix 2.E.2). The perturbations are no longer represented by sinusoidals. Instead they are given by products of two functions: a sinusoidal $e^{i\nu}$ (with wavenumber ν) and an a priori unknown periodic function with the same wavenumber κ as the pattern. The eigenvalues of the corresponding perturbations are complex and depend on ν.

Stable patterns exist in what is referred to as the *Busse balloon* (after F.H. Busse; [21]): the region in (parameter,κ)-space for which at least one stable periodic solution exists [199]. If a patterned state is stable, it is said to be in the Busse balloon. Busse balloons for the extended Klausmeier model are depicted in figure 2.1a,b (bordered by the black solid line). Apart from the

patterned states, a stable uniform bare state ($\kappa = 0$) exists for all rainfall values.

Stability regions are bordered by marginally stable solutions. Therefore a Busse balloon can be constructed by finding marginally stable solutions. If one marginally stable solution is known it is possible to track marginal stability while changing a parameter (with the use of continuation software AUTO; [41]). A precise description of this procedure can be found in the article by [147]. The Busse balloon is obtained by plotting the wavenumbers κ of the marginally stable solutions against the changing parameter. In order to track marginal stability we also need to know exactly how the eigenvalues obtain a positive real part: what is the destabilization mechanism?

In [199] it is rigorously proven through the derivation of amplitude equations (Ginzburg-Landau analysis) that stable patterns exist close to the Turing(-Hopf) bifurcation: it is derived that the bifurcation is supercritical (for the scalings considered). Close to the Turing(-Hopf) bifurcation the region in (a, κ)-space where stable patterns exist is bounded by a parabola of marginally stable patterns [199]. Also, the destabilization mechanism is identified as being a *sideband instability* or *Eckhaus instability*.

The sideband instability is characterized by a change in sign of the curvature of the eigenvalues attached to the origin ($\nu = 0$), as depicted in figure 2.1c. For marginally stable patterns, which separate stable from unstable patterns, there is no curvature at $\nu = 0$. This corresponds to a second derivative at $\nu = 0$ that equals zero. If, due to changing rainfall, patterns lose their stability, perturbations with ν close (but unequal) to zero become able to destabilize patterned states.

With the current parameter combination the sideband is the dominant destabilization mechanism for the extended Klausmeier model [199]. Only for very small wavenumbers κ it is superseded by intertwining Hopf instabilities [51]. In this case, onset of instability occurs away from $\nu = 0$, but continuation with AUTO is still possible [51, 147].

The perturbations, which consist of products of $e^{i\nu}$ and functions with the same wavenumber as the pattern κ, need not be periodic, but can be for particular values of ν. For example, perturbations with $\nu = 0$ are periodic with pattern wavenumber κ, since $e^0 = 1$. As shown in figure 2.1c, perturbations with wavenumber κ ($\nu = 0$) are not able to destabilize a patterned state: due to translation symmetry the growth rates of these perturbations remain zero. Perturbations with $\nu = \pi$ are periodic with wavenumber $\kappa/2$

since $e^{\pi i} = -1$. If perturbations with wavenumber $\kappa/2$ ($\nu = \pi$) become able to destabilize a patterned state, a so-called spatial *period doubling bifurcation* occurs. Growth of these perturbations results in a halving of the pattern wavenumber. Recall that the wavelength is inversely proportional to the wavenumber, so the wavelength (spatial period) doubles. According to figure 2.1c, perturbations of this kind are the last to destabilize a patterned state as rainfall a decreases, however they do attain the largest growth rate soon after. The black dashed line in figure 2.1a,b depicts the period doubling instability.

In summary, we discussed that the stability of patterned states can be assessed by tracking marginal stability. To do this, knowledge about the destabilization mechanisms is required. For the extended Klausmeier model the sideband instability is the dominant destabilization mechanism, meaning the curvature (second derivative) of the curve of eigenvalues (figure 2.1c) can be used to trace the boundary of the stable pattern region.

2.3.3 Ecological implications

We determined the stability of patterned ecosystem states and discussed some important destabilization mechanisms, but what ecologically relevant information can we extract from figure 2.1?

First, we observe that the Turing prediction region and the Busse balloon only partly overlap. A large part of the patterns in the Turing prediction region turn out to be unstable, and are therefore unlikely to observed. Furthermore, stable patterns exist outside the Turing prediction region for $a < a_{SN}$ and if $v \neq 0$, also for $a > a_{SN}$. These patterns cannot form directly from a Turing unstable uniform state. Although stable patterns do no appear at rainfall values above the Turing(-Hopf) bifurcation for the extended Klausmeier model, this may be different for other models, e.g. [148]. The differences between the Turing prediction region and the Busse balloon suggest that a relatively simple Turing analysis gives very limited information about the parameter regimes for which one can expect patterns to be observed.

Second, figure 2.1 shows that for a given rainfall value a range of stable patterned states exists. Since the system has many stable states, it can be considered *multistable*. The current state, in terms of wavenumber κ, consequently depends on history, meaning that hysteresis can be expected.

Third, a pattern with a given wavenumber κ is stable for a range of a. This means that the same pattern wavenumber can in theory be observed for
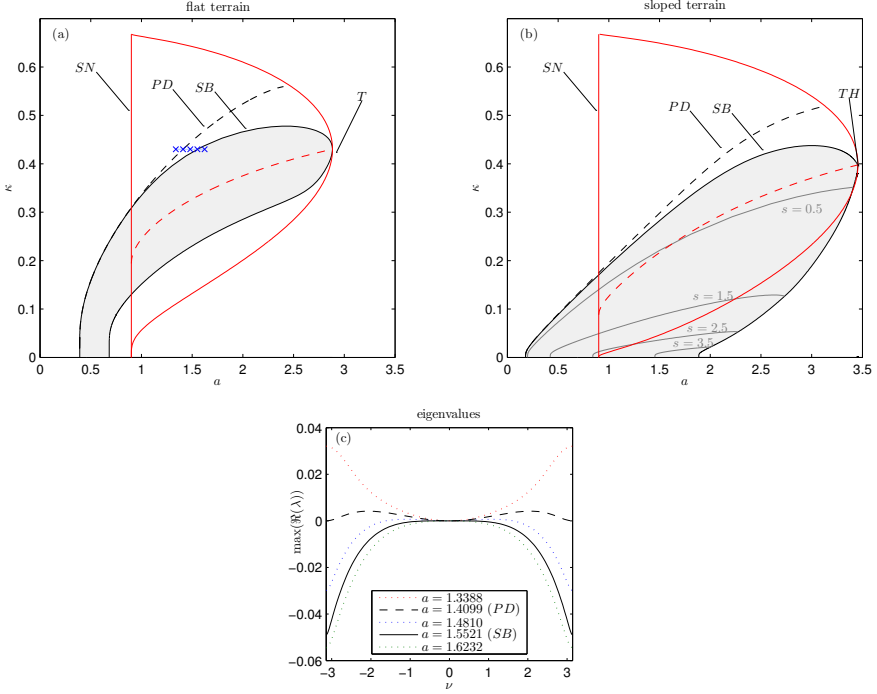
Figure 2.1: Stability regions of the non-dimensional extended Klausmeier model (equations (2.1) and (2.2)) in (a, κ)-space for flat (a; $v = 0$) and sloped terrain (b; $v = 182.5$). In (a) and (b) a represents rainfall and κ is the wavenumber of the patterned state. The black solid curve indicates the location of the sideband instability and borders the stable pattern region or Busse balloon (shaded area). A period doubling bifurcation occurs on the black dashed line. The grey curves in (b) show the contours of constant uphill pattern migration speed s. The red solid line borders the Turing prediction region where perturbations of the uniformly vegetated state grow in amplitude. On the right hand border of the Turing prediction region uniform states are marginally stable to spatial perturbations. On the left hand border of this region the Turing unstable uniform state ceases to exist (saddle-node bifurcation SN; $a = a_{SN} := 2m$). The wavenumber of the perturbation with the largest growth rate is indicated by the red dashed line. The highest rainfall value at which the uniformly vegetated state is Turing unstable is marked as the Turing bifurcation point T (or Turing-Hopf bifurcation point TH if $v \neq 0$). (c) The maximum real part of eigenvalues for perturbations of patterned states plotted against Floquet wavenumber ν. The perturbed patterned states have a wavenumber of $\kappa = 0.43009$ ($\approx \kappa_T$). Notice that the perturbed states are marked with crosses in (a). At $a \approx 1.5521$ a sideband bifurcation (SB) occurs. Here the curvature at $\nu = 0$ changes sign. At $a \approx 1.4099$ a period doubling bifurcation (PD) occurs. Here $\max(\mathrm{Re}(\lambda(\nu)))$ at $\nu = \pi \approx 3.14$ becomes positive.

a range of external conditions. Furthermore, if external conditions change, one would expect the wavenumber of a pattern to remain constant as long as it is stable, i.e. as long as the external conditions remain within the range for which the pattern is stable.

Fourth, the shape of the Busse balloon allows high wavenumbers to be stable only at high values of a. The opposite is true for low wavenumbers. The presence of a slope affects the shape of the Busse balloon. Pattern formation occurs at higher rainfall rates and patterned states can sustain under more arid conditions on sloped terrains. The absence of a slope allows high wavenumber patterns to be stable, while the rainfall range for which stable low wavenumber patterns exist is narrow. On sloped terrains in contrast low wavenumber patterns can be expected to be observed for a wide rainfall range.

Finally, we observe that the period doubling instability approaches the boundary of the Busse balloon as rainfall a decreases. Meaning that at low rainfall values, period doubling takes place almost simultaneously with the destabilization of a pattern. In addition, the boundary of the Busse balloon is steeper at low rainfall values. This means that at low rainfall values an incremental decline in rainfall could result in desertification if the system is close to the boundary of the Busse balloon.

2.4 System response to changing environmental conditions

The obtained information about the stability and destabilization of patterned states is not enough to fully understand the behavior of patterned ecosystems when subject to changing environmental conditions. This is because the linearization we implicitly apply only enables us to describe the behavior of the system close to the steady state. Consequently, if the system is pushed away from a steady state (during pattern destabilization) it is a priori unknown to which state it will evolve (restabilization). In this section we study the behavior of the system while gradually changing the rainfall parameter and relate this behavior to the findings presented in the previous section. First we describe history dependence within the system resulting from multistability in subsection 2.4.1. In subsection 2.4.2 we then study in more detail the restabilization of the system and its dependence on the rate with which rainfall changes and on the level of noise imposed on the system.

Finally, in subsection 2.4.3 we propose an ecological mechanism that controls system restabilization.

2.4.1 Bouncing through the Busse balloon

The non-dimensional extended Klausmeier model (equations (2.1) and (2.2)) was run with the rainfall a changing over time with a rate of $\frac{da}{dt} = \pm 10^{-4}$. This rate of change corresponds to a change in annual rainfall of about 0.1 mm year^{-1}.

Figure 2.2 shows how the system responds to changing rainfall on flat terrain ($v = 0$). When rainfall decreases, patterns in plant biomass emerge shortly after the uniformly vegetated state becomes Turing unstable (figure 2.2a). The mean plant biomass of the patterned state does not differ much from that of the Turing unstable uniform system state (figure 2.2d). The wavenumber of the pattern does not change as long as the pattern is stable. The pattern amplitude in contrast increases during pattern formation after which it slowly decreases with declining a. At some point, the decreasing rainfall forces the system outside the Busse balloon and the pattern destabilizes (figure 2.2c). This results in a pattern with a lower wavenumber and a larger amplitude. These transitions are not distinguishable in mean biomass (figure 2.2d). The adaptation of the wavenumber is accompanied by the extinction of what can be considered as vegetation patches. When a reaches a value for which no stable patterned state exists, desertification occurs and all remaining patches go extinct simultaneously.

If rainfall increases over time similar behavior can be observed (figure 2.2b), however now patterns destabilize at the lower border of the Busse balloon and the wavenumber increases until eventually a uniformly vegetated state is reached (figure 2.2c). During wavenumber adaptation vegetation patches split up. Since the trajectories for decreasing and increasing rainfall differ, hysteresis occurs [172].

On sloped terrain (figure 2.3), patterns emerge in the form of vegetation bands that migrate in uphill direction (traveling waves). As the Busse balloon is wider in terms of wavenumber κ the hysteresis effect is more pronounced when compared to flat terrain. As shown by figure 2.3, the migration speed of the vegetation bands gets lower as rainfall decreases. However, during wavenumber adaptation vegetation bands accelerate leading to slightly elevated migration speeds directly after transition.

Although wavenumber adaptation occurs some time after patterned states

destabilize, as discussed earlier by [172], figures 2.2 and 2.3 indicate that the Busse balloon helps in understanding how patterned ecosystems respond to changes: 1) as long as the system is in the Busse balloon it responds by changing the amplitude (and migration speed) of the patterns, 2) if, due to changing rainfall a, the system is forced outside the Busse balloon it responds by changing its pattern wavenumber.

At first sight, the Busse balloon does not seem to provide insight in what determines the selection of a new wavenumber after pattern destabilization. In the next section we show how wavenumber selection is affected by the rate at which the rainfall changes and by the amount of spatio-temporal noise to which the system is exposed.

2.4.2 Wavenumber selection: the role of rate of change and noise

The model was run for $v = 0$ with different rates of change in rainfall $\left| \frac{da}{dt} \right|$ (with $\frac{da}{dt} < 0$) and different noise levels. As shown in figure 2.4, wavenumber adaptation occurs with increasing step size (in terms of wavenumber κ) for increasing rates of change. At high rates of change, desertification can take place at rainfall levels for which stable patterned states still exist. For the level of noise imposed on the system, the opposite is true: higher noise levels result in smaller step size. At sufficiently high noise levels, patches go extinct one-by-one and the system tends to closely follow the boundary of the Busse balloon.

We observe that during some wavenumber adaptations period doubling occurs, meaning that half of the vegetation patches go extinct simultaneously [207]. The occurrence of period doubling is related to the position of the system in (a, κ)-space at which the wavenumber adaptation is initiated, which is in turn determined by rate of change and noise level. If wavenumber adaptation takes place close to the boundary of the Busse balloon, which is the case for low rates of change or high noise levels, period doubling does not occur. If wavenumber adaptation is initiated farther away from the boundary of the Busse balloon, period doubling occurs, provided that the system surpassed the period doubling instability PD and that period doubling results in a stable patterned solution.

At low rainfall values we find that period doubling occurs more frequently (even at high noise levels). Here the period doubling instability PD approaches the sideband instability SB (boundary of the Busse balloon). As a result the period doubling instability PD is surpassed even at low rates of
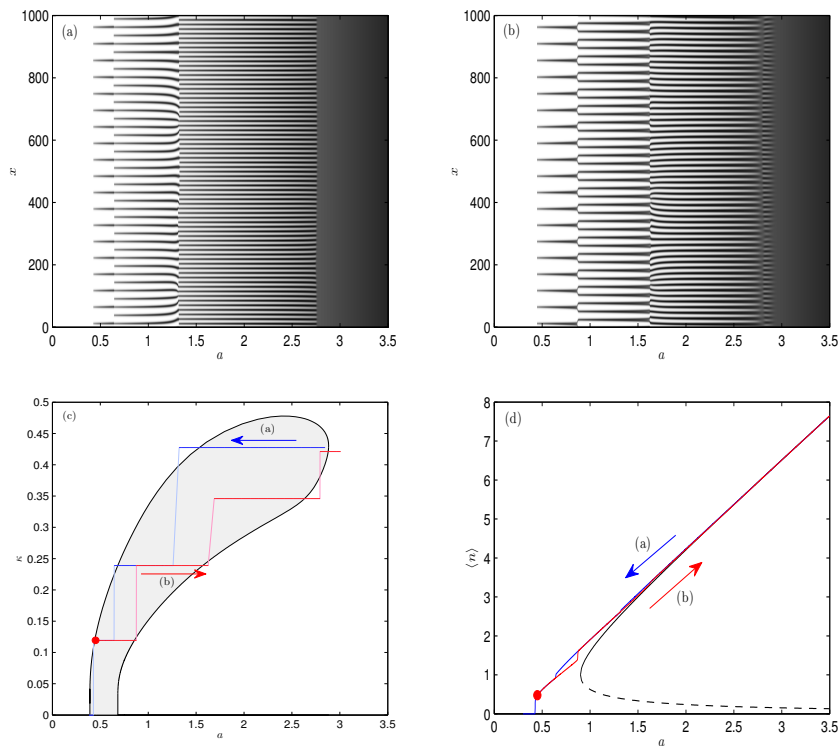
Figure 2.2: Plant density n in space for runs of the non-dimensional extended Klausmeier model with $v = 0$ (flat terrain), for $\frac{da}{dt} = -10^{-4}$ (a) and $\frac{da}{dt} = 10^{-4}$ (b). The former run starts from the homogeneously vegetated steady state. The latter is initiated with the patterned solution of the first at $a = 0.45$. Spatially and temporally uncorrelated multiplicative uniformly distributed noise with an amplitude of $5 \cdot 10^{-5}\%$ is added to the plant density every $\frac{1}{4}$ year. The trajectories through the Busse balloon in (c) were obtained by applying a discrete Fourier transformation with respect to x (see appendix 2.B). In (d), the mean biomass is plotted for both runs. The solid and dashed black lines are the uniform steady states.
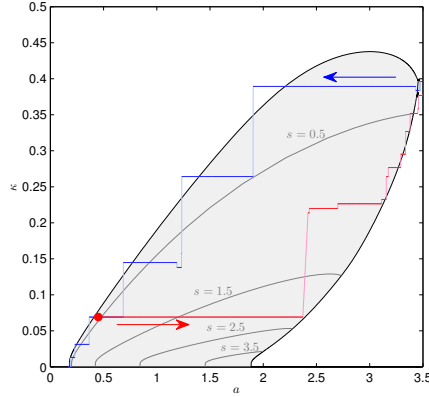
Figure 2.3: See the caption of figure 2.2, but now $v = 182.5$ (sloped terrain). The grey curves show the contours of constant uphill pattern migration speed.

change.

2.4.3 Competition between and rearrangement of patches

In the previous subsections we showed that wavenumber adaptation driven by changing environmental conditions can be a discontinuous process: many patches can go extinct simultaneously if a pattern destabilizes. In addition, we found that rainfall, the rate of change in rainfall and the level of noise on the system affect the number of patches that go extinct. Here we provide an interpretation of the observed system responses by taking a closer look to what happens during wavenumber adaptation.

Figure 2.5 shows plant biomass and surface water for part of the modeled domain during one of the wavenumber adaptations in a model run with declining rainfall. The figure shows that the extinction of one vegetation patch results in growth of its neighboring patches, which in turn negatively affects their neighbors. This triggers a cascade, eventually resulting in extinction of half of the patches.

The interaction between neighboring patches in the extended Klausmeier model can be explained by the competition for water. Vegetation patches harvest water from an area bordered by water divides where $\frac{dw}{dx} = 0$. The uptake of water by patches that share a water divide, which is controlled by patch biomass, determines the position of the water divide. An increase
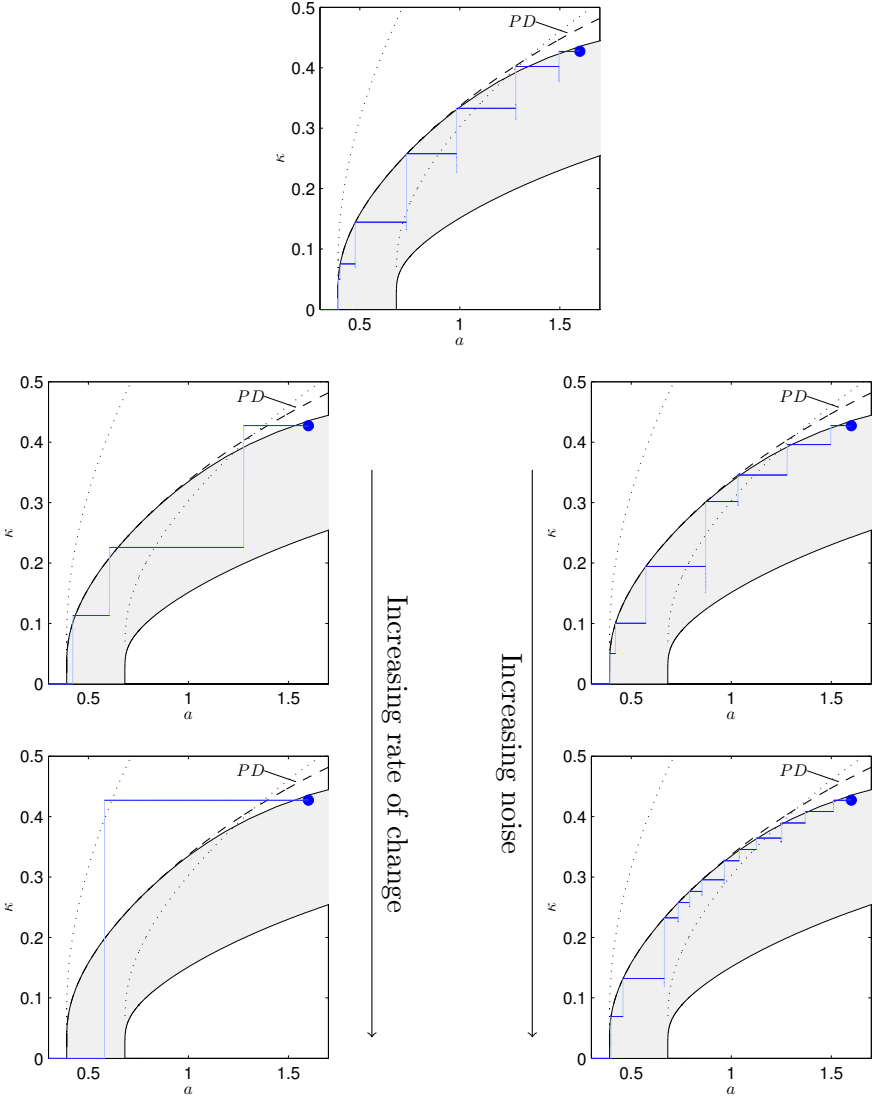
Figure 2.4: Trajectories through the Busse balloon for runs with decreasing rainfall and with different rates of change in a and different noise levels. The trajectories were obtained by applying a discrete Fourier transformation with respect to x (see appendix 2.B). The runs were initiated with a stable pattern solution at $\kappa \approx \kappa_T$ and $a = 1.6$ and end in the desert state $\kappa = 0$. The solid line depicts the sideband instability SB, the dashed line is the period doubling instability PD. The area bordered by the dotted curves was extrapolated from the Busse balloon and depicts the area in which period doubling would result in a stable patterned solution. The top panel plus the two panels on the left have no noise, the rate of change in rainfall $\left|\frac{da}{dt}\right|$ changes respectively from 10^{-7} to 10^{-4} to 10^{-2}. The two panels on the right have noise amplitude $5 \cdot 10^{-5}\%$ (upper) and 0.05% (lower) while the rate of change of a is equal to that of the top panel (10^{-7}).

in patch biomass with respect to neighboring patches will widen the water harvesting area of a patch. The opposite occurs if a patch is weaker than its neighbors. Since the water harvesting area affects water availability, it feeds back to patch biomass eventually resulting in growth or extinction of a patch.

We observe (figure 2.6) that wavenumber adaptations during which less than half of the vegetation patches goes extinct are accompanied by rapid spatial rearrangement of patches, while no movement of patches can be observed if half (period doubling) or all patches go extinct (desertification). The movement of neighboring patches during rearrangement seems to weaken the feedbacks described above: if one patch goes extinct its neighboring patches fill up the created space, thereby diminishing the stress on remaining patches.

Patch rearrangement generally occurs if wavenumber adaptation is initiated between the sideband instability and the period doubling instability. At low rainfall values, the period doubling instability approaches the sideband instability. At these rainfall values rearrangement of patches becomes less likely, as pattern destabilization almost coincides with the period doubling instability PD. High rates of change in rainfall also do not allow for patch rearrangement. High noise levels in contrast can trigger wavenumber adaptation before the system crosses the period doubling instability PD, resulting in patch rearrangement and one-by-one extinction of vegetation patches.

2.5 Discussion and conclusions

In this study we showed that patterned ecosystems systematically respond in two ways to changing environmental conditions: 1) by adjusting patch biomass (pattern amplitude) or 2) by changing pattern wavelength (wavenumber). In the latter case patches go extinct or split up and may rearrange. In arid ecosystems, gradual wavelength adaptation is constrained to conditions of high rainfall, slow changes in rainfall and high levels of stochastic spatial variation in biomass (noise). The adaptation process is less gradual under conditions of either low rainfall, rapid change or low levels of noise. Such conditions do not allow vegetation patches to rearrange, and facilitate the simultaneous extinction of half the patches or even a transition to a degraded state without any patches.
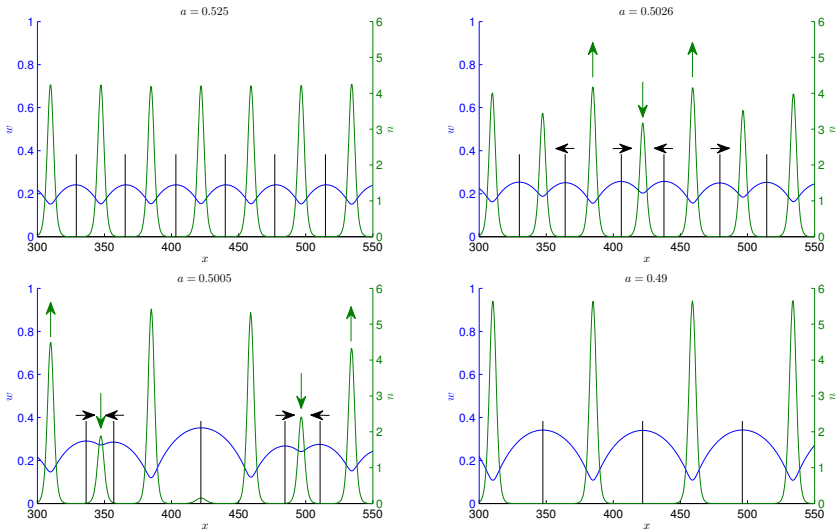
Figure 2.5: Plant biomass n and water w against space x, for $v = 0$ and $\frac{da}{dt} = -10^{-4}$. The black lines mark the position of water divides. The black arrows indicate the direction of the movement of the water divides. The green arrows indicate the growth or decay in n.
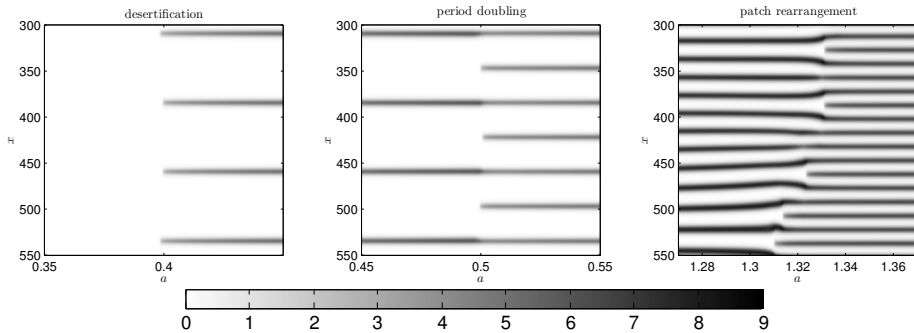
Figure 2.6: Plant density n in space x against rainfall a during different wavenumber adaptations in a model run with declining rainfall. Rearrangement of patches during a transition only occurs at high rainfall values. At low rainfall patches do not rearrange promptly and period doubling or desertification occurs.

We found that an overview of stable patterned states, the Busse balloon, is a powerful tool in understanding the response of patterned ecosystems to changing environmental conditions. If a system is in a stable patterned state (i.e. in the Busse balloon), a pattern tends to solely adapt its amplitude, while if the system leaves the Busse balloon, a pattern adapts its wavenumber. The ability of patches to rearrange is determined by the period doubling instability. Once the system surpasses this instability, patches do not rearrange, leading to extinction of half or all the patches.

Our findings suggest that the response of patterned ecosystems to environmental change does not only depend on the magnitude of change, but also on the rate with which conditions change: patterned ecosystems may not be able to respond in a gradual way to rapid environmental change. Similar behavior can be observed in a number of non-spatial models, e.g. [113, 165]. Nonlinear response to rapid environmental change may as well occur in more comprehensive models that are used for policy making. This may imply that merely setting targets for tolerable change may not be sufficient to prevent ecosystem degradation and that to ensure gradual ecosystem adaptation, identification of critical rates of change is required as well.

Besides the rate of change in environmental conditions, the level of noise to which the system is exposed seems to play an essential role in ecosystem response. Our study shows that relatively small amplitude noise brings heterogeneity in the population of patches which leads to more gradual ecosystem adaptation to environmental change. Larger amplitude noise, on the other hand, is known to be a cause of critical transitions [83].

Our findings are in agreement with a recent study by [39] based on areal images of patterned vegetation in Sudan. Like [39] we found that pattern wavenumber declines with increasing aridity and that, when compared to flat terrain, a wider range of pattern wavenumbers can be found on sloped terrain. Although our stability analysis suggest that low wavenumber patterns are stable (and thus can be observed in theory), [39] did not find such patterns. This might be explained by the fact that, at least for flat terrain, low wavenumber patterns are stable only for a relatively small rainfall range (figure 2.1a). A second explanation can be found in the steepness of the boundary of the Busse balloon. Wavenumber adaptation forced by environmental changes generally results in increased ecosystem resilience as it increases the distance to critical thresholds (the boundary of the Busse balloon). However, if the boundary of the Busse balloon is steep, as is the case for low wavenumber patterns at low rainfall values (figure 2.1a), the

system remains close to the boundary of the Busse balloon meaning that the increase in ecosystem resilience is relatively small. As a result patterned arid ecosystems are relatively fragile in this parameter region. Variations in seasonal and annual precipitation, to which all arid ecosystems are exposed, can easily trigger desertification. Consequently, low wavenumber patterns are less likely to be observed.

By assessing the existence and stability of patterned system states we went one step further than Turing analysis, frequently applied in previous studies, e.g. [61, 70, 79, 95, 97, 125]. In a wide range of ecosystems, scale-dependent feedbacks are thought to involve local positive feedbacks [151]. Such local positive feedbacks allow stable patterned states to exist under conditions where uniform cover can no longer be sustained. Analysis of patterns in these parameter regions is of importance because of proximity to critical thresholds. Using conventional Turing analysis, however, it is fundamentally impossible to do so. The novel approach we presented in this paper is a promising way forward in understanding the behavior of spatially explicit ecosystem models under these conditions.

The findings presented in this paper are in accordance with previous model studies. Analysis of the original Klausmeier model by [174] and [172] already suggested the existence of patterned states in parameter regions where Turing unstable states are absent, see also [148], and that hysteresis can occur in pattern wavenumber and migration speed. In contrast to the study by [172] we used wavenumber as state variable instead of migration speed. In practice, wavenumber is a property that is easier to assess than migration speed [30, 38]. In addition, migration speed cannot be used as state variable if all patterns are stationary. This is the case on flat terrain in the extended Klausmeier model, but on sloped terrain patterns can be fixed as well [58, 185]. The existence of a multitude of stable patterned states has been demonstrated in other models as well [16, 124, 172, 208]. In this paper we showed that transitions between stable patterned states can be forced by changing environmental conditions. Previous studies show that such transitions can also be triggered by disturbances in the form of the uniform biomass removal [124] or patch removal [208].

Although our findings seem to be in line with observations [39], most findings remain to be tested using areal images and field data. Empirical proof for a Busse balloon requires a constant pattern wavelength to be observed for a range of environmental conditions or, alternatively, a range of pattern wavelengths to be observed for a fixed set of environmental conditions. It

would also be interesting to see if competition between neighboring patches indeed occurs and how the competition strength depends on environmental stress. If time series of areal images are available, it may also be possible to observe hysteresis in pattern wavelength.

To get more insight in the behavior of real ecosystems we propose that future studies apply stability analysis on patterned system states of other (more realistic) models. Constructing Busse balloons for other models will allow to relate findings to measurable parameters. Stability analysis of models in which multiple pattern forming mechanisms are captured, such as the model by [70], would allow studying how the relative strength of these mechanisms affects the global behavior of patterned ecosystems [96]. In addition, future studies could consider two spatial dimensions as this may qualitatively affect the model behavior described in this paper. Accounting for more than one spatial dimension in stability analysis is mathematically challenging, since more complex spatial patterns can evolve (gaps, labyrinths and spots; [139, 148]) and more destabilization mechanisms may potentially destabilize a patterned system state [85]. Finally, as soon as bare ground forms between patches, the movement and stability of patches can be described by pulse interaction, see [48, 184] and references therein. This may provide insight in the ecologically relevant process of wavenumber adaptation forced by environmental change.

The changes in climate projected for the coming decades [86] are likely to affect the functioning of patterned ecosystems worldwide. We showed that in order to understand the behavior of patterned ecosystems that are subject to change, mathematical techniques are required that go beyond conventional Turing analysis. By assessing the stability of patterned ecosystem states and by studying the relevant destabilization mechanisms we were able to explain when and how arid ecosystems may adapt their pattern wavelength. Identification of the Busse balloon, together with the period doubling instability, provides a theoretical framework for future theoretical and empirical studies. These studies may provide enhanced insights in the response of other ecological models to change, the response of real ecosystems to change, and the ecological mechanisms responsible for this response.

Acknowledgments

2.A A non-dimensional extended Klausmeier model.

The extended Klausmeier model is given by equation (2.A.1) and (2.A.2). In table 2.1, the values of the parameters are listed for both grass and trees, as estimated by [97]. The diffusion term was calibrated to obtain patterns in a realistic parameter range. A non-dimensional version of the model (equation (2.A.3) and (2.A.4)) is used throughout the paper. Table 2.2 shows how the dimensionless parameters can be obtained.

$$
\frac{\partial W}{\partial T} = A - LW - RWN^2 + V\frac{\partial W}{\partial X} + E\frac{\partial^2 W^\Gamma}{\partial X^2} \qquad (2.A.1)
$$

$$
\frac{\partial N}{\partial T} = RJWN^2 - MN + D\frac{\partial^2 N}{\partial X^2} \qquad (2.A.2)
$$

$$
\frac{\partial w}{\partial t} = a - w - wn^2 + v\frac{\partial w}{\partial x} + e\frac{\partial^2 w^\gamma}{\partial x^2} \qquad (2.A.3)
$$

$$
\frac{\partial n}{\partial t} = wn^2 - mn + \frac{\partial^2 n}{\partial x^2} \qquad (2.A.4)
$$

2.B Wavenumber plotting by fast Fourier transform

In this appendix we explain how we compute the trajectories through (parameter,κ)-space, as depicted in the main text, by using the discrete or *fast Fourier transform*.

In the model runs the plant biomass $n(x)$ is represented by a vector $n(j)$, $j = 1, 2, ..., N$, of $N = 1024$ elements and the spatial domain size is $L = 1000$. The vector can be expressed as a linear combination of vectors $v_l(j) = e^{\frac{2\pi i l}{N}j}$, where $l = 0, 1, 2, ..., N - 1$. The v_l represent sinusoidals with wavenumber

Table 2.1: Values and units for the variables and parameters of the extended Klausmeier model (equation (2.A.1) and (2.A.2)). Values adopted from [97]. E was calibrated to obtain patterns in a realistic parameter range, according to [37].

Parameter/Variable	Value (grass)	Value (tree)	Unit
W			kg m^{-2}(=mm)
N			kg m^{-2}
X			m
T			year
A	0 - 950	0 - 950	kg m^{-2} year^{-1} (= mm year^{-1})
L	4	4	year^{-1}
R	100	1.5	kg m^{-2} year^{-1} kg^{-2} (=mm year^{-1} kg^{-2})
V	0 or 365	0 or 365	m year^{-1}
E	500	500	m^2 year^{-1} mm$^{1-\Gamma}$
Γ	1	1	-
J	0.003	0.002	kg kg^{-1} (=kg L^{-1})
M	1.8	0.18	year^{-1}
D	1	1	m^2 year^{-1}

Table 2.2: Physical meaning and values for the variables and parameters of the non-dimensional extended Klausmeier model (equation (2.A.3) and (2.A.4))

Parameter/Variable	Physical meaning	Value (grass)	Value (tree)
w	$WR^{1/2}L^{-1/2}J$	$0.015W$	$0.0012W$
n	$NR^{1/2}L^{-1/2}$	$5N$	$0.61N$
x	$XL^{1/2}D^{-1/2}$	$2X$	$2X$
t	TL	$4T$	$4T$
a	$AR^{1/2}L^{-3/2}J$	$0.00375A$	$0.0003062A$
m	ML^{-1}	$0.25M$	$0.25M$
v	$VL^{-1/2}D^{-1/2}$	$0.5V$	$0.5V$
e	ED^{-1}	E	E
γ	Γ	Γ	Γ
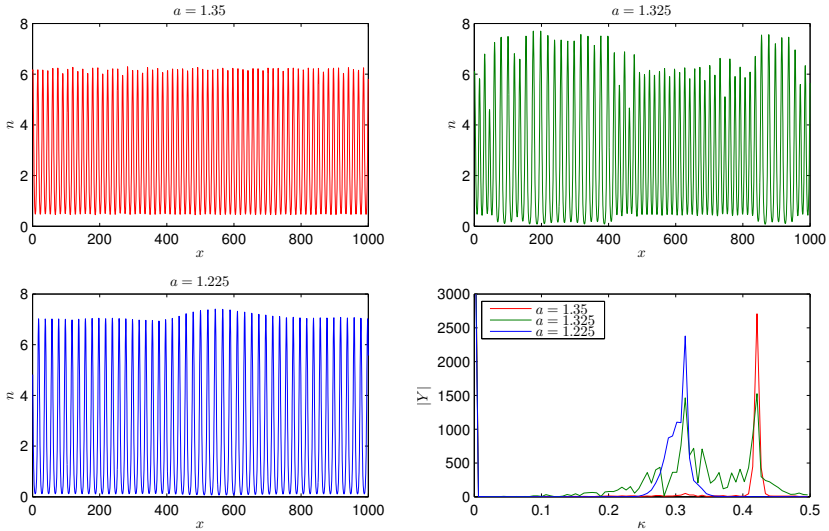
Figure 2.7: Plant biomass n against space x before, during and after wavenumber adaptation in the model run with declining rainfall of figure 2.2 and the Fourier transform of the corresponding vectors.

$\kappa = \frac{2\pi l}{L}$. The weight of v_l in n can be computed by the discrete Fourier transform

$$Y(\kappa) = \sum_{j=1}^{N} n(j)v_l(-j). \tag{2.B.1}$$

The absolute value of $Y(\kappa)$ is a measure of how much n resembles a sinusoidal with wavenumber κ. If a single $Y(\kappa)$ has a large absolute value compared to all other $Y\ (\kappa \neq 0)$, then the state is (nearly) periodic with wavenumber κ.

The trajectories through (parameter,κ)-space, as depicted in the main text, were obtained by picking the wavenumber where $|Y|$ attained its maximum, $\kappa = 0$ excluded. The wavenumber is only plotted when the maximum is relatively large, which suppresses plotting during transient dynamics.

Figure 2.7 shows that during wavenumber adaptation the spread in κ increases. After wavenumber adaptation the spread decreases slowly. As the pattern settles, the maximum wavenumber can still change. As l is an integer, κ can only attain certain values. Therefore the settling of the pattern can result in small jumps in pattern wavenumber.

2.C General equations for perturbations.

We derive equations for perturbations of a general system state in the extended Klausmeier model. These equations will be of use in appendix 2.D.2, 2.D.3 and 2.E.2. For ease of the computations we restrict to the linear diffusion case $\gamma = 1$. Let (w, n) be a system state that is perturbed by (w', n'). We obtain an expression for the governing equations of the perturbation by the following calculations:

$$
\begin{aligned}
\frac{\partial w'}{\partial t} &= \frac{\partial(w + w')}{\partial t} - \frac{\partial w}{\partial t} \\
&= e\frac{\partial^2(w + w')}{\partial x^2} + v\frac{\partial(w + w')}{\partial x} + a - (w + w') - (w + w')(n + n')^2 \\
&\quad - \left(e\frac{\partial^2 w}{\partial x^2} + v\frac{\partial w}{\partial x} + a - w - wn^2 \right) \\
&= e\frac{\partial^2 w'}{\partial x^2} + v\frac{\partial w'}{\partial x} - w'(1 + n^2) - 2n'wn - 2w'n'n - n'^2 w - w'n'^2 \\
&\approx e\frac{\partial^2 w'}{\partial x^2} + v\frac{\partial w'}{\partial x} - w'(1 + n^2) - 2n'wn \quad\quad (2.\text{C.}1)
\end{aligned}
$$

$$
\begin{aligned}
\frac{\partial n'}{\partial t} &= \frac{\partial(n + n')}{\partial t} - \frac{\partial n}{\partial t} \\
&= \frac{\partial^2(n + n')}{\partial x^2} + (w + w')(n + n')^2 - m(n + n') \\
&\quad - \left(\frac{\partial^2 n}{\partial x^2} + wn^2 - mn \right) \\
&= \frac{\partial^2 n'}{\partial x^2} + w'n^2 + n'(2wn - m) + 2w'n'n + n'^2 w + w'n'^2 \\
&\approx \frac{\partial^2 n'}{\partial x^2} + w'n^2 + n'(2wn - m) \quad\quad (2.\text{C.}2)
\end{aligned}
$$

The final approximate equalities are equalities in a linear approximation: for small perturbations (w', n') the products $w'n'$ and n'^2 are negligible.

In an abstract formulation equations (2.C.1) and (2.C.2) can be rewritten as:

$$
\frac{\partial}{\partial t}\begin{pmatrix} w' \\ n' \end{pmatrix} = A\begin{pmatrix} w' \\ n' \end{pmatrix} \quad\quad (2.\text{C.}3)
$$

where the so-called spectrum, a generalization of the concept of eigenvalues,

of the differential operator

$$A = \begin{pmatrix} e\frac{\partial^2}{\partial x^2} + v\frac{\partial}{\partial x} - 1 - n^2 & -2wn \\ n^2 & \frac{\partial^2}{\partial x^2} + 2wn - m \end{pmatrix} \qquad (2.C.4)$$

determines the stability of (w, n).

2.D Analysis of the homogeneous steady states.

For completeness we will give a thorough analysis of the homogeneous steady states of the extended Klausmeier model. This also serves the purpose of showing how easily results can be obtained by hand in this case, compared to the restricted possibilities for the analysis of patterns in appendix 2.E. The results of section 2.D.1 and 2.D.2 also hold for $\gamma = 2$.

2.D.1 Existence of spatially homogeneous steady states

If w and n are spatially homogeneous, gradients in w and n are absent, and the advection-diffusion terms of (2.1) and (2.2) vanish. Since only a single type of derivative remains, the partial differential equations become ordinary differential equations. The steady uniform states can then be found by solving (2.D.1) and (2.D.2).

$$\frac{dw}{dt} = a - w - wn^2 = 0 \qquad (2.D.1)$$

$$\frac{dn}{dt} = wn^2 - mn = (wn - m)n = 0 \qquad (2.D.2)$$

Clearly $\bar{n}_B = 0$ solves (2.D.2) and consequently $\bar{w}_B = a$. This is a bare desert state, as plant biomass equals zero. Alternatively (2.D.2) is solved if $n = \frac{m}{w}$. Substituting this in (2.D.1) and multiplying with $-w$ we obtain the quadratic equation $w^2 - aw + m^2 = 0$. This quadratic equation can be solved to obtain two solutions for w and from $n = \frac{m}{w}$ the corresponding solution
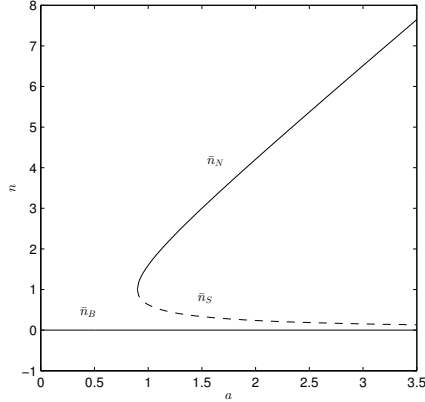
Figure 2.8: Homogeneous steady states of the (extended) Klausmeier model expressed in plant biomass n as function of rainfall a for $m = 0.45$.

for n can be computed. The outcome is given by:

$$\bar{w}_S = \frac{2m^2}{a - \sqrt{a^2 - 4m^2}} \tag{2.D.3}$$

$$\bar{n}_S = \frac{a - \sqrt{a^2 - 4m^2}}{2m} \tag{2.D.4}$$

$$\bar{w}_N = \frac{2m^2}{a + \sqrt{a^2 - 4m^2}} \tag{2.D.5}$$

$$\bar{n}_N = \frac{a + \sqrt{a^2 - 4m^2}}{2m} \tag{2.D.6}$$

Here the argument of the square root needs to be positive, so these states only exist for $a \geq 2m$. Note that the two states coincide at $a = 2m$, in fact here a so-called saddle-node bifurcation takes place. In the following subsection we will show that $(\bar{w}_S, \bar{n}_S)$ has a stable and an unstable direction (saddle, unstable) and $(\bar{w}_N, \bar{n}_N)$ either has two stable or unstable directions (node). Note that we have covered all possible cases of (2.D.2) and thus no other homogeneous steady states can exist. Moreover, all the steady states are non-negative. We will continue by studying their stability.

2.D.2 Stability of the homogeneous steady states against homogeneous perturbations

By perturbing the steady states obtained in appendix 2.D, their stability can be determined. If a perturbation grows over time, the steady state is unstable. The steady state is stable, if all perturbations decay. In this appendix, we show how linear stability analysis can be used to assess the stability of uniform system states to homogeneous perturbations. We will do this by using the equations derived for perturbations in appendix 2.C.

Since perturbations are assumed to be homogeneous (2.C.1) and (2.C.2) simplify to:

$$\frac{\partial w'}{\partial t} = -w'(1 + \bar{n}^2) - 2\bar{n}'w\bar{n} \tag{2.D.7}$$

$$\frac{\partial n'}{\partial t} = w'\bar{n}^2 + n'(2\bar{w}\bar{n} - m) \tag{2.D.8}$$

This can be compactly written as:

$$\begin{pmatrix} \frac{dw'}{dt} \\ \frac{dn'}{dt} \end{pmatrix} = \begin{pmatrix} -1 - \bar{n}^2 & -2\bar{w}\bar{n} \\ \bar{n}^2 & 2\bar{w}\bar{n} - m \end{pmatrix} \begin{pmatrix} w' \\ n' \end{pmatrix} \tag{2.D.9}$$

where the matrix is readily identified as the Jacobian matrix J of the reaction terms. As is well-known, the stability can be determined by looking at the real parts of the eigenvalues of the Jacobian.

For the bare state plugging in $\bar{n}_B = 0$ in the Jacobian matrix yields

$$J = \begin{pmatrix} -1 & 0 \\ 0 & -m \end{pmatrix}. \tag{2.D.10}$$

The eigenvalues can now be read of from the diagonal ($\lambda_1 = -1$, $\lambda_2 = -m$) so the bare state is always stable (for $m > 0$).

In case of the saddle-node states we recall that $nw = m$ (appendix 2.D.1). So the Jacobian matrix becomes

$$J = \begin{pmatrix} -1 - \bar{n}_{S,N}^2 & -2m \\ \bar{n}_{S,N}^2 & m \end{pmatrix}. \tag{2.D.11}$$

The eigenvalues can be computed directly by solving the characteristic equation involving the determinant det:

$$\det(J - \lambda I) = \det \begin{pmatrix} -1 - \bar{n}^2 - \lambda & -2m \\ \bar{n}^2 & m - \lambda \end{pmatrix}$$

$$= \lambda^2 + \lambda(1 + \bar{n}^2 - m) - m + m\bar{n}^2 = 0 \tag{2.D.12}$$

Solving this we obtain:

$$\lambda_\pm = -\frac{1}{2}\left(1 + \bar{n}^2 - m\right) \pm \sqrt{m\left(1 - \bar{n}^2\right) + \frac{1}{4}\left(1 + \bar{n}^2 - m\right)^2} \qquad (2.D.13)$$

Which has the form:

$$\lambda_\pm = \alpha \pm \sqrt{\beta + \alpha^2} \qquad (2.D.14)$$

For this general form it holds:

	$\beta > 0$	$\beta < 0$
$\alpha > 0$	$\mathrm{Re}(\lambda_+) > 0$	$\mathrm{Re}(\lambda_+) > 0$
	$\mathrm{Re}(\lambda_-) < 0$	$\mathrm{Re}(\lambda_-) > 0$
$\alpha < 0$	$\mathrm{Re}(\lambda_+) > 0$	$\mathrm{Re}(\lambda_+) < 0$
	$\mathrm{Re}(\lambda_-) < 0$	$\mathrm{Re}(\lambda_-) < 0$

$$(2.D.15)$$

We first show that $(\bar{w}_S, \bar{n}_S)$ has both a stable and an unstable direction (saddle, unstable), as was claimed in appendix 2.D.1. For this it suffices to show that $\beta = m(1 - \bar{n}_S^2) > 0$. Since $a > 2m$ (appendix 2.D.1)

$$\bar{w}_S = \frac{2m^2}{a - \sqrt{a^2 - 4m^2}} = \frac{2m^2\left(a + \sqrt{a^2 - 4m^2}\right)}{a^2 - a^2 + 4m^2} = \frac{a}{2} + \frac{1}{2}\sqrt{a^2 - 4m^2} > m$$

$$(2.D.16)$$

Now $\bar{n}_S = \frac{m}{\bar{w}_S} < 1$ so $\beta > 0$.

Second we show that $(\bar{w}_N, \bar{n}_N)$ is a node (i.e. is either stable or unstable in both directions), as was claimed in appendix 2.D.1, but we will not directly determine the stability. This is equivalent to $\beta = m(1 - \bar{n}_N^2) < 0$. Since $a > 2m$ we have

$$\bar{n}_N = \frac{a + \sqrt{a^2 - 4m^2}}{2m} = \frac{a}{2m} + \frac{1}{2m}\sqrt{a^2 - 4m^2} > 1 \qquad (2.D.17)$$

So indeed $\beta < 0$.

Finally the eigenvalues belonging to the node can have positive (unstable) or negative (stable) real parts. Both eigenvalues are negative if and only if $\alpha = -\frac{1}{2}(1 + \bar{n}_N^2 - m) < 0$, this is automatically satisfied if $m < 1$, so in particular if $m = 0.45$. For general m it can be calculated that the stability boundary is given by pairs (m, a) that satisfy:

$$a = \frac{m^2}{\sqrt{m - 1}} \text{ and } m \geq 2 \qquad (2.D.18)$$

This boundary is plotted in figure 2.9.
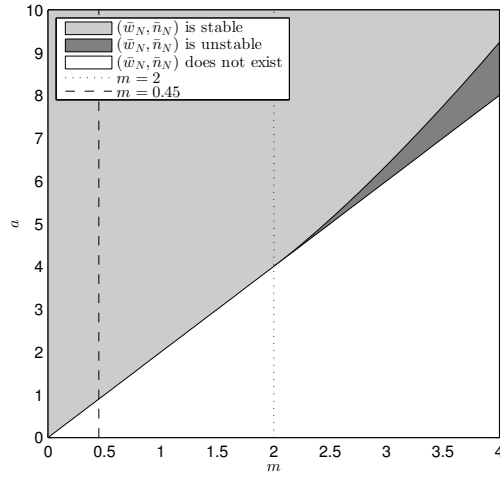
Figure 2.9: Region in parameter space where $(\bar{w}_N, \bar{n}_N)$ is stable, unstable or does not exist.
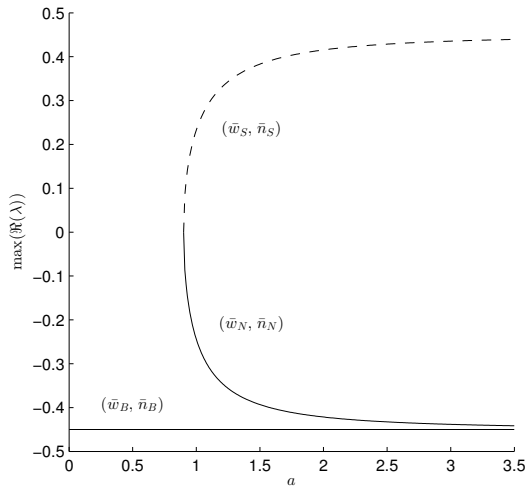
Figure 2.10: The maximum real part of λ for the spatially uniform steady states plotted against a. Perturbations are assumed to be spatially homogeneous and $m = 0.45$.

2.D.3 Turing analysis of the steady states

In the full model the steady states are also subject to heterogeneous perturbations. States that were thought of as being stable against homogeneous perturbation may be unstable against a wider class of perturbations. For simplicity we restrict to $\gamma = 1$.

The usual approach is to assume that the spatial dependence of the perturbation has the form of a sinusoid: we represent it by a complex exponential $e^{i\kappa x}$.[1] This is convenient because $\frac{d}{dx}e^{i\kappa x} = i\kappa e^{i\kappa x}$ and $\frac{d^2}{dx^2}e^{i\kappa x} = -\kappa^2 e^{i\kappa x}$. Substituting

$$\begin{pmatrix} w'(t,x) \\ n'(t,x) \end{pmatrix} = e^{i\kappa x} \begin{pmatrix} \tilde{w}(t) \\ \tilde{n}(t) \end{pmatrix} \tag{2.D.19}$$

in (2.C.1) and (2.C.2) and dividing by $e^{i\kappa x}$ yields:

$$\frac{\partial \tilde{w}}{\partial t} = -\kappa^2 e\tilde{w} + i\kappa v\tilde{w} - \tilde{w}(1 + n^2) - 2\tilde{n}wn \tag{2.D.20}$$

$$\frac{\partial \tilde{n}}{\partial t} = -\kappa^2 \tilde{n} + \tilde{w}n^2 + \tilde{n}(2wn - m) \tag{2.D.21}$$

This can be written in a single matrix equation:

$$\begin{pmatrix} \frac{d\tilde{w}}{dt} \\ \frac{d\tilde{n}}{dt} \end{pmatrix} = \begin{pmatrix} -\kappa^2 e + i\kappa v - 1 - \bar{n}^2 & -2\bar{w}\bar{n} \\ \bar{n}^2 & -\kappa^2 + 2\bar{w}\bar{n} - m \end{pmatrix} \begin{pmatrix} \tilde{w} \\ \tilde{n} \end{pmatrix} \tag{2.D.22}$$

The justification of the assumption that the perturbation is sinusoidal is given by the Fourier transform, which links the spectrum of the operator A in the abstract formulation (2.C.3) to the eigenvalues of the above matrix.

For the bare state $\bar{n}_B = 0$, so the matrix simplifies to

$$\begin{pmatrix} -\kappa^2 e + i\kappa v - 1 & 0 \\ 0 & -\kappa^2 - m \end{pmatrix} \tag{2.D.23}$$

so $\lambda_1 = -\kappa^2 e + i\kappa v - 1$ and $\lambda_2 = -\kappa^2 - m$. Since the real parts $\text{Re}(\lambda_1) = -\kappa^2 e - 1$ and $\text{Re}(\lambda_2) = -\kappa^2 - m$ both remain negative for any κ, the bare state is also stable against heterogeneous perturbations. Because the saddle is already unstable against homogeneous perturbations we focus our attention on the node. Since $\bar{w}_N\bar{n}_N = m$ the matrix becomes

$$\begin{pmatrix} -\kappa^2 e + i\kappa v - 1 - \bar{n}_N^2 & -2m \\ \bar{n}_N^2 & -\kappa^2 + mi \end{pmatrix}, \tag{2.D.24}$$

---

[1] If there are only second order spatial derivatives present, assuming the form $\cos(\kappa x)$ or $\sin(\kappa x)$ is equivalent.
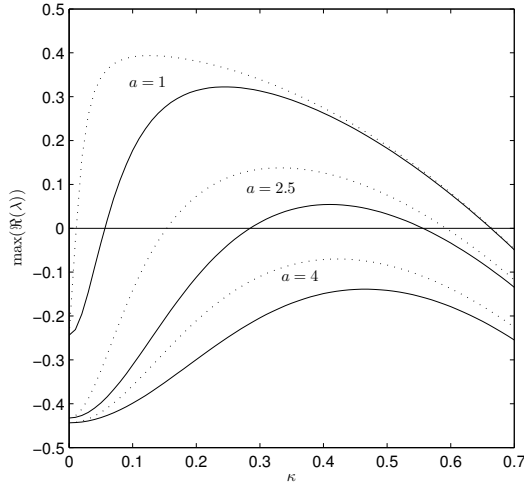
Figure 2.11: The maximum real part of λ for heterogeneous perturbations of $(\bar{w}_N, \bar{s}_N)$, plotted as function of κ, for different values of a and for $v = 0$ (solid lines) and $v = 182.5$ (dotted lines), $m = 0.45$. The boundary of the Turing prediction region depicted in figure 2.1 is located at the intersection points of the curves with the x-axis. The maxima of the curves correspond to the most unstable wavenumber.

from which we can obtain the eigenvalues by solving the dispersion relation:

$$\det \begin{pmatrix} -\kappa^2 e + i\kappa v - 1 - \bar{n}_N^2 - \lambda & -2m \\ \bar{n}_N^2 & -\kappa^2 + m - \lambda \end{pmatrix} = 0 \qquad (2.D.25)$$

This again yields a quadratic equation in λ, which can be solved for λ. The eigenvalues λ are now not only a function of model parameters, but also a function of wavenumber κ. Figure 2.11 shows solutions of (2.D.25) (which depends on a through $\bar{n}_N$) for several values of a for $m = 0.45$. The curves pass through the real axis between $a = 4$ and $a = 2.5$ in both the case $v = 0$ and $v = 182.5$, the node becomes Turing unstable somewhere in between (precise values are given in the caption of figure 2.1).

2.E Analysis of patterns

In the previous appendix all of the analysis could be done by hand. This is very much in contrast to the analysis of patterns. Here we give some results that can be obtained analytically for the extended Klausmeier model.

2.E.1 Existence of patterns

Here we derive that patterns are solutions of the equations (2.3) and (2.4). These equations are solved numerically.

In general, patterned states may migrate uphill (if $v \neq 0$). We will denote the migration speed (in the direction of increasing x) of these so-called wavetrains by s. Allowing for $s = 0$, any pattern can be written in the form $(w(t, x), n(t, x)) = (w_p(x - st), n_p(x - st)) = (w_p(\xi), n_p(\xi))$, where w_p and n_p are periodic functions describing the wave profile and $\xi = x - st$ is a comoving frame coordinate. By using the chain rule, e.g.

$$\frac{\partial w(x, t)}{\partial t} = \frac{dw_p(\xi)}{d\xi} \frac{\partial \xi}{\partial t} = -s \frac{dw_p}{d\xi} \tag{2.E.1}$$

after substituting the forms in (2.1) and (2.2) we obtain

$$0 = a - w_p - w_p n_p^2 + (v + s) \frac{dw_p}{d\xi} + e \frac{d^2 w_p^\gamma}{d\xi^2} \tag{2.E.2}$$

$$0 = w_p n_p^2 - m n_p + s \frac{dn_p}{d\xi} + \frac{d^2 n_p}{d\xi^2} \tag{2.E.3}$$

which are the equations we set out to find.

2.E.2 Stability of patterns

We will study the stability of a pattern $(w(t, x), n(t, x))$ in the case $\gamma = 1$, so the equations for the perturbation (2.C.1) and (2.C.2) hold. We show these equations again, now with explicit dependence on the coordinates:

$$\frac{\partial w'(t, x)}{\partial t} = e \frac{\partial^2 w'(t, x)}{\partial x^2} + v \frac{\partial w'(t, x)}{\partial x} - w'(t, x) \left(1 + n(t, x)^2\right)$$
$$- 2n'(t, x) w(t, x) n(t, x) \tag{2.E.4}$$

$$\frac{\partial n'(t, x)}{\partial t} = \frac{\partial^2 n'(t, x)}{\partial x^2} + w'(t, x) n(t, x)^2$$
$$+ n'(t, x) \left(2w(t, x) n(t, x) - m\right) \tag{2.E.5}$$

Here w and n are not constant, which prevents us from applying a sinusoidal substitution as in Turing analysis (appendix 2.D.3). As in appendix 2.E.1 we write $(w(t, x), n(t, x)) = (w_p(\xi), n_p(\xi))$ with $\xi = x - st$. To make optimal use of this form we apply a change of coordinates $(t, x) \mapsto (t, \xi)$. Simultaneously we substitute $(w', n') = e^{\lambda t} (\tilde{w}(\xi), \tilde{n}(\xi))$ and after division by $e^{\lambda t}$ we obtain:

$$\lambda \tilde{w} = e\frac{d^2 \tilde{w}}{d\xi^2} + (v+s)\frac{d\tilde{w}}{d\xi} - \tilde{w}(1+n_p^2) - 2\tilde{n}w_p n_p \qquad (2.\text{E}.6)$$

$$\lambda \tilde{n} = \frac{d^2 \tilde{n}}{d\xi^2} + s\frac{d\tilde{n}}{d\xi} + \tilde{w}n_p^2 + \tilde{n}(2w_p n_p - m) \qquad (2.\text{E}.7)$$

This is a system of two second order ordinary differential equations. After defining $\tilde{q} = \dfrac{d\tilde{w}}{d\xi}$ and $\tilde{r} = \dfrac{d\tilde{n}}{d\xi}$ it can be rewritten as a first order system of four ordinary differential equations:

$$\frac{d}{d\xi}\begin{pmatrix} \tilde{w} \\ \tilde{q} \\ \tilde{n} \\ \tilde{r} \end{pmatrix} = \begin{pmatrix} 0 & 1 & 0 & 0 \\ \frac{\lambda+1+n_p^2}{e} & \frac{-v-s}{e} & \frac{2w_p n_p}{e} & 0 \\ 0 & 0 & 0 & 1 \\ -n_p^2 & 0 & m - w_p n_p & -s \end{pmatrix}\begin{pmatrix} \tilde{w} \\ \tilde{q} \\ \tilde{n} \\ \tilde{r} \end{pmatrix} \qquad (2.\text{E}.8)$$

Since the matrix of coefficients is periodic, we are ready to use Floquet theory. Through Floquet theory it is possible to express the spectrum as the union of curves of eigenvalues of a related problem. The spatial part of the perturbations that act as eigenfunctions satisfy:

$$\tilde{w}\left(\xi + \frac{2\pi}{\kappa}; \nu\right) = e^{i\nu}\tilde{w}(\xi; \nu) \qquad (2.\text{E}.9)$$

$$\tilde{n}\left(\xi + \frac{2\pi}{\kappa}; \nu\right) = e^{i\nu}\tilde{n}(\xi; \nu) \qquad (2.\text{E}.10)$$

where κ is now the pattern wavenumber and $\nu \in (-\pi, \pi]$. Note that $\frac{2\pi}{\kappa}$ is the wavelength of the pattern. A corresponding curve of eigenvalues was exhibited as a function of ν in figure 2.1c, for different values of a. Regarding the stability we will not go into more details but note that the procedure for assessing stability is explained further in [147].

A special case is when $\nu = \pi$. Then $e^{i\nu} = -1$. It follows that $\tilde{w}(\xi+\frac{4\pi}{\kappa}; \pi) = -\tilde{w}(\xi + \frac{2\pi}{\kappa}; \pi) = \tilde{w}(\xi; \pi)$, and similarly for $\tilde{n}$, so the perturbation has twice the wavelength of the pattern. When the real part of the corresponding eigenvalue becomes positive, the pattern can be destabilized by such a perturbation and the period will be doubled (period doubling instability).

3 Striped pattern selection by advective reaction-diffusion systems: Resilience of banded vegetation on slopes

For water-limited arid ecosystems, where water distribution and infiltration play a vital role, various models have been set up to explain vegetation patterning. On sloped terrains, vegetation aligned in bands has been observed ubiquitously. In this paper, we consider the appearance, stability, and bifurcations of 2D striped or banded patterns in an arid ecosystem model. We numerically show that the resilience of the vegetation bands is larger on steeper slopes by computing the stability regions (Busse balloons) of striped patterns with respect to 1D and transverse 2D perturbations. This is corroborated by numerical simulations with a slowly decreasing water input parameter. Here, long wavelength striped patterns are unstable against transverse perturbations, which we also rigorously prove on flat ground through an Evans function approach. In addition, we prove a Squire theorem for a class of two-component reaction-advection-diffusion systems that includes our model, showing that the onset of pattern formation in 2D is due to 1D instabilities in the direction of advection, which naturally leads to striped patterns.

   This paper has been motivated by studies in one space dimension of a scaled phenomenological model for vegetation on possibly sloped planes in arid ecosystems [180, 199].[1] One-dimensional patterns ideally represent striped patterns in two space dimensions by trivially extending them into a transversal direction. Such patterns are referred to as banded vegetation and have received considerable attention after reports of widespread observations [38, 193]. Understanding the appearance and disappearance of vegetation bands may ultimately help prevent land degradation. The restriction to one space dimension may overestimate stability: patterns that are stable against 1D perturbations are not necessarily stable against all 2D perturbations. Natural questions to pose are:

- Which of the 1D stable patterns extend to 2D stable striped patterns?
- In case of destabilization by 2D perturbations, which mechanisms are responsible?

In this paper we answer these questions for the arid ecosystem model and determine the impact of slope induced advection of water. The influence of advection on striped pattern formation is studied in a more general setting. This approach provides a clear argumentation that is unobscured by model-specific details. Equally important, the results will be applicable to a wide range of models. Applicability to the arid ecosystem model is carefully checked though, assuring that the abstract requirements can in fact be met in practice.

3.1 Introduction

The original Klausmeier model [97] is an ecohydrological model for modeling vegetation patterns on sloped terrain in arid ecosystems, with a (surface) water component w and a plant biomass or vegetation component n. The flow of water is modeled by downhill advection only. By adding a water diffusion term to the model we arrive at the *extended Klausmeier model* [180]

---

[1]With [180] corresponding to Chapter 2.

studied in this article. In dimensionless form it is given by

$$w_t = d\Delta w + 2cw_x + a - w - wn^2$$
$$n_t = \Delta n - mn + wn^2$$

(3.1)

where $\Delta = \frac{\partial^2}{\partial x^2} + \frac{\partial^2}{\partial y^2}$, posed on the plane. Generally the diffusion coefficient $d \gg 1$, since water diffuses much faster than vegetation. The parameter c measures the advection of water down a hillslope, $a \geq 0$ models precipitation and $m > 0$ an effective death rate. The terms $\pm wn^2$ model water uptake by the vegetation and $-w$ evaporation.

The model (3.1) with $c = 0$ and $a - w$ replaced by the term $a(1-w)$ is called the Gray-Scott model, introduced in [74]. The generalized form of (3.1) with the term $a(1 - w)$ has been referred to as the generalized Klausmeier-Gray-Scott model, in $[127,199]^2$ also the impact of nonlinear diffusion of the water component has been studied.

Both the Klausmeier model and the Gray-Scott model exhibit patterns [97,139]. We will study the influence of the advection parameter c on striped patterns. For fixed c we view the rainfall parameter a as the primary parameter to vary, as done in previous studies [180,199].

The choice of parameter values in (3.1) will correspond to choices in [180] which are themselves based on [97]. Since we are considering a scaled model, some of the parameters are a mix of parameters from the original Klausmeier model [97]. For instance, what we refer to as slope driven advection c in (3.1) is influenced by the evaporation rate from the original model, which has been scaled to 1 in (3.1), see [180]. So determining which values of c are realistic is non-trivial. This is resolved by choosing c over a wide range, giving an overview of the different possibilities. Unless stated otherwise, $m = 0.45$ and $d = 500$.

The *Busse balloon* [21] is a representation of spatially periodic stable patterns that exist in a system, each pattern is represented by its wavenumber $\kappa := 2\pi/\text{wavelength}$. Uniting the stable patterns for a range of parameter values creates a planar region. For (3.1) on flat ground (no advection, $c = 0$), the Busse balloon of 1D stable patterns is illustrated by the union of the two colored regions in Figure 3.1, as already presented in [180]. The extensions of these 1D patterns to 2D striped patterns, which are represented by the same single wavenumber, are only 2D stable in the dark-green (teal) region near the Turing bifurcation T. In Section 3.3.3 the nature and construction

---

[2]With [127] corresponding to Chapter 5.
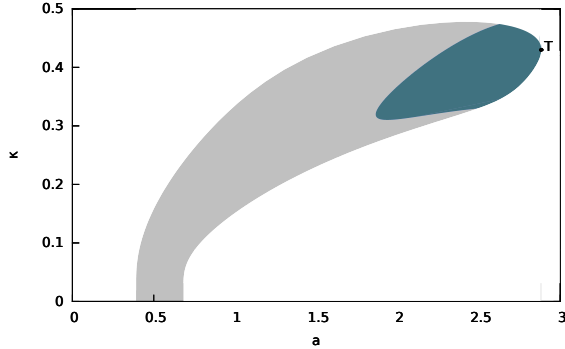
Figure 3.1: Busse balloon representation of striped patterns on flat ground ($c = 0$) for the extended Klausmeier model (3.1) (with $d = 500$, $m = 0.45$). Here each pattern is represented by a point in (a, κ)-space, where $\kappa = 2\pi$/wavelength is the wavenumber. A Turing bifurcation occurs at T. The union of the two colored regions consists of one-dimensional (spatially periodic) patterns that are 1D stable [180]. The dark-green (teal) colored region consists of those patterns that extend to 2D stable striped patterns, patterns in grey extend to 2D unstable patterns.

of these two types of Busse balloons will be considered. Moreover, we will study the influence of slope induced advection of water c and compare the stability results with simulations with a slowly decreasing rainfall parameter a.

In 1D, in simulations with decreasing rainfall a, the dynamics (after pattern formation) is essentially restricted to transitions from one pattern to another, before reaching the bare desert state [180]. In 2D these transitions correspond to stripe-to-stripe pattern transitions. Regarding striped patterns in 2D, the additional instabilities we find always induce an amplitude modulation in the transverse direction along the stripes so that the bifurcating solutions decompose into spots, in analogy to findings focussing on a single (homoclinic) stripe [53, 100, 103]. We find that destabilizing modes relate neighboring stripes either synchronously, leading to a stripe-to-rectangle pattern transition, or phase shifted by half a period, leading to a stripe-to-rhomb pattern transition. For this reason, and as a convenient terminology, we refer to these as (transverse) *stripe-rectangle* and *stripe-rhomb* breakup, respectively. Details are given in Section 3.3.1, where we will moreover trace the 2D patterns that bifurcate from the striped patterns numerically, using software from [54, 192].

The main numerical result for (3.1), framed in the terminology that is appropriate in this context, concerns the influence of the slope (advection, c) on

banded (or striped) vegetation resilience. Ecological resilience is measured by the magnitude of disturbance that can be absorbed before the system redefines its structure [76, 81]. For (3.1) it holds that

1. Increased resilience: the ecological resilience of banded vegetation is larger on steep slopes than on gentle slopes (Section 3.3.3).

Figure 3.1 shows numerically that for $c = 0$ and small wavenumbers κ, none of the 1D patterns extend to 2D stable striped patterns. In accordance we prove through the use of geometric singular perturbation theory and an Evans function approach, that

2. Transverse instability: in absence of advection (no slope, $c = 0$) long wavelength striped patterns of (3.1) are unstable w.r.t. transverse instabilities (Corollary 3.2, Section 3.3.2).

Next to striped pattern (in)stability it is also relevant to study the onset of striped pattern formation, and the influence of the advection c. The analytical results of Section 3.2.1 and 3.2.2 are obtained in the setting of general two-component reaction-advection-diffusion systems. Specifically, we study systems posed on the plane,

$$
\begin{aligned}
u_t &= d_1 \Delta u + c_1 u_x + f(p, u, v) \\
v_t &= d_2 \Delta v + c_2 v_x + g(p, u, v),
\end{aligned}
\tag{3.2}
$$

where p is an abstract parameter and $u(t, x, y), v(t, x, y) \in \mathbb{R}$. The advection coefficients $c_1, c_2 \in \mathbb{R}$ are arbitrary, and we assume that $d_1 \geq 0$ and $d_2 > 0$; compare Lemma 3.4 (Appendix 3.A). We refer to the difference between the coefficients of the advection terms, $|c_1 - c_2|$, as *differential flow* [154].

We consider the linear stability of a homogeneous steady state (u_*, v_*) of inhibitor-activator type that is stable against homogeneous perturbations. We define

$$
a_1 := \frac{\partial f}{\partial u}(u_*, v_*), \ a_2 := \frac{\partial f}{\partial v}(u_*, v_*), \ a_3 := \frac{\partial g}{\partial u}(u_*, v_*), \ a_4 = \frac{\partial g}{\partial v}(u_*, v_*)
\tag{3.3}
$$

and $A := \left(\begin{smallmatrix} a_1 & a_2 \\ a_3 & a_4 \end{smallmatrix} \right)$, then these assumptions are abbreviated by

$$
\begin{aligned}
A1: \ &\mathrm{tr}(A) < 0 \text{ and } \det(A) > 0 \\
A2: \ &a_1 < 0 \text{ and } a_4 > 0,
\end{aligned}
\tag{3.4}
$$

the latter meaning that u acts as *inhibitor* (or depleted substrate) and v acts as *activator*.

In Section 3.2 we perform a thorough linear stability analysis near criticality. In case of no differential flow, $c_1 = c_2$, destabilization of the homogeneous steady state occurs through a Turing instability leading to the emergence of stationary periodic patterns. In case of nonzero differential flow, $c_1 \neq c_2$, the instability is referred to as Turing-Hopf (or oscillatory Turing) since the patterns that emerge are moving. The initial steps are as in [141], which starts out from the same setting. We derive the following novel results:

3. Direction of motion: if $c_1 > c_2$ and $c_2 \leq 0$, then patterns emerging from the Turing-Hopf bifurcation move in the positive x-direction (Section 3.2.1).

4. Locus monotonicity: the parameter location of the instability monotonically changes if the differential flow increases, assuming sign conditions on $\partial A / \partial p$ (Theorem 3.1, Section 3.2.1).

5. Range monotonicity: the range of destabilizing perturbations of the homogeneous steady state monotonically increases as the differential flow increases (Lemma 3.3, Section 3.2.2).

6. Stripe formation dominance: for nonzero differential flow, perturbations independent of y are responsible for the primary destabilization: at the Turing-Hopf bifurcation striped patterns perpendicular to the direction of the advection appear (Section 3.2.2).

These general results are applicable to the arid ecosystem model (3.1), where the parameter a takes on the role of the abstract parameter p. Interpreting the results in this context we conclude that (within the model) small amplitude vegetation patterns move uphill. Secondly, under decreasing rainfall a pattern formation first occurs on steeper slopes (Corollary 3.1, Section 3.2.3). As soon as the homogeneously vegetated state has become unstable against a specific perturbation, this will remain the case if the rainfall a decreases more. And finally, banded vegetation perpendicular to the slope naturally forms on slopes. The paper ends with a discussion on ecological implications of the results regarding (3.1), links to observations and comparison with other model studies in Section 3.4.

Remark 3.1. *In [19] a listing of ecohydrological models with and without differential flow is given. The general results can be applied to various other disciplines, in particular to differential flow models where the reactants have different advection coefficients. In chemical reactions between differently charged particle species, differential flow can be created by applying an exterior electric field [22, 122, 187, 201]. Similarly, a differential flow induced*

chemical instability ('DIFICI') may be produced within a differential flow reactor with one particle species immobilized, see [123, 154, 155, 161]. Finally, also mussels that feed on algae where (only) the algae flow with tidal currents [203], fit the abstract framework (3.2).

Remark 3.2. *The present insights induce (novel) connections with fluid mechanics. The representation of stable patterns by Busse balloons originates from this field [21]. Although fundamentally different, similar patterns exist e.g. in this context striped patterns are commonly called roll-waves and the transverse instabilities of striped patterns we find correspond to certain 'oblique-roll' instabilities [85]. In both fields the onset of pattern formation can be studied by weakly nonlinear stability theory, for instance on preimposed lattices [71, 72]. The transformation presented in the proof of Lemma 3.3 that lifts the 1D results from Section 3.2.1 to 2D, has a counterpart in fluid mechanics: the 'Squire's transformation'. It leads to the 'Squire's theorem' [56, 183] which is still an active topic of research [88]. Originally it refers to the fact that for shear flow instability of the Orr-Sommerfeld equation the critical Rayleigh number for a three-dimensional parallel flow is determined by two-dimensional perturbations, which links to the restriction to y-independent perturbations in our striped pattern formation dominance result in Section 3.2.2.*

3.2 Striped pattern formation

We choose to first avoid model specific considerations and study pattern formation in the setting of the general system (3.2). We present a comprehensive linear analysis about a homogeneous steady state of inhibitor-activator type near onset of pattern formation. We start our analysis in one spatial dimension in Section 3.2.1 but lift the results to two spatial dimensions in Section 3.2.2.

In Section 3.2.1 we establish the direction of motion of emerging patterns of (3.2) depending on the advection coefficients c_1, c_2. In Section 3.2.1 we prove a result on the monotonic change of the parameter locus of the Turing-Hopf instability as the differential flow $2c = |c_1 - c_2|$ increases, Theorem 3.1. One of the results leading up to this monotonicity result, Lemma 3.1 on the destabilizing impact of increasing c, plays an important role in carrying over the results from 1D to 2D.

In Section 3.2.2 we show that for $c > 0$ destabilization in 2D can be

reduced to destabilization in 1D in the advection direction. We prove that the destabilization locus in 2D coincides with the locus in 1D and we show that the set of destabilizing perturbations is strictly monotonically increasing with the advection c. It is shown that striped patterns naturally arise from a Turing-Hopf instability in 2D.

We subsequently apply the general insights to the extended Klausmeier model (3.1) in Section 3.2.3. The abstract results in this context imply that on slopes vegetation bands form that migrate uphill.

3.2.1 Linear analysis of pattern formation for the general system in 1D

The reduction of (3.2) to one dimension in the direction of the advection is

$$\begin{aligned} u_t &= d_1 u_{xx} + c_1 u_x + f(p, u, v) \\ v_t &= d_2 v_{xx} + c_2 v_x + g(p, u, v). \end{aligned} \tag{3.5}$$

The linear stability of a homogeneous steady state of (3.5) can be determined by computing the linearization. Subsequently applying a Fourier transform yields the matrix

$$M = \begin{pmatrix} -d_1 k^2 + \mathrm{i} c_1 k + a_1 & a_2 \\ a_3 & -d_2 k^2 + \mathrm{i} c_2 k + a_4 \end{pmatrix}$$

where k is the wavenumber of the perturbation and the a_j are the derivatives relevant for determining stability against homogeneous perturbations (see (3.3)). The linear *dispersion relation* is given by

$$d(\lambda, k, p, c) := \det(M - \lambda I) = \lambda^2 + \alpha_1 \lambda_1 + \alpha_0 = 0, \tag{3.6}$$

where $\alpha_1 = -\mathrm{tr}(M)$ and $\alpha_0 = \det(M)$. The eigenvalues λ of M, which are solutions to (3.6), determine (in)stability.

We are free to choose a suitable frame of reference, as the (in)stability of the homogeneous steady state does not depend on it. By changing the reference frame we can manipulate the coefficients α_1 and α_0 in the dispersion relation. When changing to a moving reference frame with speed $\tilde{c}$, i.e. by the substitution $x \mapsto x - \tilde{c}t$, only the time derivative in (3.5) transforms, e.g. $u_t \mapsto u_t - \tilde{c}u_x$. When reflecting space $x \mapsto -x$, only the single derivatives to space are affected, e.g. $u_x \mapsto -u_x$. So the equations can be transformed

into the equivalent

$$
\begin{aligned}
u_t &= d_1 u_{xx} \pm (c_1 + \tilde{c}) u_x + f(p, u, v) \\
v_t &= d_2 v_{xx} \pm (c_2 + \tilde{c}) v_x + g(p, u, v)
\end{aligned}
\tag{3.7}
$$

where the negative sign applies in case of reflection.

A reference frame that will show to be suitable for stability analysis is obtained by choosing $\tilde{c} = -(c_1 + c_2)/2$, so that both advection coefficients have equal absolute value $c = |c_1 - c_2|/2$ but opposite sign. By means of spatial reflection, we can arrange that the first component (inhibitor) advection coefficient has positive sign. So we arrive at the form

$$
\begin{aligned}
u_t &= d_1 \Delta u + c u_x + f(p, u, v) \\
v_t &= d_2 \Delta v - c v_x + g(p, u, v)
\end{aligned}
\tag{3.8}
$$

with a larger c meaning a larger differential flow.

In this reference frame α_1 and α_0 are given by

$$
\begin{aligned}
\alpha_1 &= (d_1 + d_2) k^2 - a_1 - a_4 \\
\alpha_0 &= \left(-d_1 k^2 + ick + a_1\right)\left(-d_2 k^2 - ick + a_4\right) - a_2 a_3.
\end{aligned}
\tag{3.9}
$$

Under assumption $A1$, $\operatorname{tr}(A) < 0$ which implies $\alpha_1 > 0$. The real and imaginary part of α_0 are given by:

$$
\begin{aligned}
\operatorname{Re}(\alpha_0) &= \left(-d_1 k^2 + a_1\right)\left(-d_2 k^2 + a_4\right) + c^2 k^2 - a_2 a_3 \\
&= d_1 d_2 k^4 - \Gamma k^2 + c^2 k^2 + \det(A) \\
\operatorname{Im}(\alpha_0) &= ck\left((d_1 - d_2) k^2 + a_4 - a_1\right)
\end{aligned}
\tag{3.10}
$$

where we introduced $\Gamma := d_1 a_4 + d_2 a_1$.

For the purpose of self-containment we briefly treat the well-known Turing instability ($c = 0$) first. In this case the dispersion relation (3.6) reduces to

$$
\lambda^2 + \left((d_1 + d_2)k^2 - \operatorname{tr}(A)\right)\lambda + d_1 d_2 k^4 - \Gamma k^2 + \det(A) = 0
$$

and implicit differentiation with respect to k yields

$$
2\lambda\left(\frac{\partial \lambda}{\partial k} + (d_1 + d_2)k\right) + \left((d_1 + d_2)k^2 - \operatorname{tr}(A)\right)\frac{\partial \lambda}{\partial k} + 4 d_1 d_2 k^3 - 2\Gamma k = 0.
$$

Imposing stationary criticality ($\lambda = 0$) and that the spectrum is tangential ($\frac{\partial \lambda}{\partial k} = 0$) gives

$$d_1 d_2 k^4 - \Gamma k^2 + \det(A) = 0$$
$$4 d_1 d_2 k^3 - 2\Gamma k = 0.$$

It follows from the last equation that $\Gamma = 2 d_1 d_2 k^2 > 0$ and insertion into the former equation gives $\Gamma^2 = 4 d_1 d_2 \det(A)$, thus a Turing instability occurs if and only if

$$\Gamma = 2\sqrt{d_1 d_2 \det(A)}. \tag{3.11}$$

Concerning general c, we now develop some useful reference material for critical cases where $\mathrm{Re}(\lambda) = 0$. Here the dispersion relation (3.6) reduces to an expression that will prove to be insightful.

Isolating the imaginary part of (3.6) and imposing $\mathrm{Re}(\lambda) = 0$ yields

$$\mathrm{Re}(\alpha_1)\,\mathrm{Im}(\lambda) + \mathrm{Im}(\alpha_0) = 0. \tag{3.12}$$

In the reference frame of (3.8) it holds that $\mathrm{Im}(\alpha_1) = 0$ so that $\mathrm{Im}(\lambda) = -\frac{\mathrm{Im}(\alpha_0)}{\alpha_1}$. If we now combine this with the real part of (3.6) we obtain:

$$\alpha_1^2 \,\mathrm{Re}(\alpha_0) - \mathrm{Im}(\alpha_0)^2 = 0. \tag{3.13}$$

Upon substituting equalities from (3.9), (3.10) into (3.13) and some rewriting, we obtain the following polynomial equation in k^2:

$$\begin{aligned}
\left((d_1 + d_2)k^2 - \mathrm{tr}(A)\right)^2 \left(\left(d_1 d_2 k^2 - \Gamma\right) k^2 + \det(A)\right) & \\
+ 4c^2 \left(\left(d_1 d_2 k^2 - \Gamma\right) k^2 + a_1 a_4\right) k^2 &= 0
\end{aligned} \tag{3.14}$$

First note that all terms in (3.14) are positive except $a_1 a_4 < 0$ and possibly $d_1 d_2 k^2 - \Gamma$ which appears twice. For $c = 0$ this confirms the well-known fact that $\Gamma > 0$ is a necessary condition for a Turing instability, see (3.11). On the other hand this shows that the instability can also be purely driven by ramping up the advection c since the only c-dependent term $4c^2 \left(\left(d_1 d_2 k^2 - \Gamma\right) k^2 + a_1 a_4\right)$ is negative for k^2 small, relating to differential flow instabilities mentioned in the introduction.

We continue with some useful estimates that can be derived from (3.14). We first note an upper bound for the wavenumbers that can become critical given by

$$k^2 < \frac{a_4}{d_2}. \tag{3.15}$$

Suppose on the contrary that $k^2 \geq \frac{a_4}{d_2}$, then $d_1 d_2 k^2 - \Gamma \geq -d_2 a_1 > 0$. Thus also

$$\left(d_1 d_2 k^2 - \Gamma\right) k^2 + a_1 a_4 \geq -d_2 a_1 k^2 + a_1 a_4 \geq 0.$$

Now all terms of (3.14) are positive for $k^2 \in [\frac{a_4}{d_2}, \infty)$, so these wavenumbers cannot be critical.

Hence there exists an upper bound on the wavenumber of destabilizing perturbations, independent of c [141], determined by the activator only. For future reference we note that as a consequence of (3.15) it holds that

$$
\begin{aligned}
\frac{\operatorname{Im}(\alpha_0)}{ck} \pm \alpha_1 \geq \;& \frac{\operatorname{Im}(\alpha_0)}{ck} - \alpha_1 \\
=\;& (d_1 - d_2)k^2 + a_4 - a_1 - \left((d_1 + d_2)k^2 - a_1 - a_4\right) \\
=\;& 2(a_4 - d_2 k^2) > 0.
\end{aligned}
\tag{3.16}
$$

Motion of emerging patterns

Here we determine the direction of motion of patterns emerging from a destabilized homogeneous state, for advection coefficients $c_1 > c_2$ and $c_2 \leq 0$, by applying the reference frame independent result (3.15). We first do this for the limiting case $c_2 = 0 < c_1$, as in (3.1). In this reference frame the coefficients of the dispersion relation (3.6) are

$$
\begin{aligned}
\alpha_1' &= (d_1 + d_2)\, k^2 - a_1 - a_4 - i c_1 k \\
\alpha_0' &= \left(-d_1 k^2 + i c_1 k + a_1\right)\left(-d_2 k^2 + a_4\right) - a_2 a_3.
\end{aligned}
$$

The real part of α_1' and the imaginary part of α_0' are given by

$$
\begin{aligned}
\operatorname{Re}\left(\alpha_1'\right) &= \alpha_1 > 0 \\
\operatorname{Im}\left(\alpha_0'\right) &= c_1 k \left(-d_2 k^2 + a_4\right).
\end{aligned}
$$

Now the speed s' at onset is given by

$$
s' = \frac{\operatorname{Im}(\lambda)}{k} = \frac{\operatorname{Im}(\alpha_0')}{k \operatorname{Re}(\alpha_1')} = \frac{c_1(-d_2 k^2 + a_4)}{\alpha_1} > 0
$$

by (3.12), (3.15) and since $c_1 > 0$. The positive speed means that the direction of movement at criticality is in the positive x-direction, we further note that the speed increases linearly with c_1.

Let s denote the speed of emerging patterns in a system with $c_2 < 0$ but still $c_2 < c_1$. This system can be brought into the form of the limiting case $c_2 = 0$ by substituting $x \mapsto x + c_2 t$, so that $s = s' - c_2 > 0$, since $s' > 0$ and $c_2 < 0$. So movement is again in the positive x-direction. By reflection symmetry it is clear that if $c_1 < c_2$ and $c_2 \geq 0$, then emerging patterns move in the negative x-direction.

Additionally, if we fix c and p we can determine the influence of an incremental change of the wavenumber k on the speed at criticality. This influence is independent of the reference frame, we compute

$$\frac{\partial s'}{\partial k^2} = \frac{-2c \left(d_2 \alpha_1 + (-d_2 k^2 + a_4)(d_1 + d_2) \right)}{\alpha_1^2} < 0 \qquad (3.17)$$

(see (3.9)) so that at criticality an increase of k leads to a decrease of the speed.

Both the positivity of the speed s' and the influence of the wavenumber k are in accordance with what was found previously in the context of (3.1), where water advection is downslope but vegetation bands move uphill [180].

Destabilization by c and monotonicity of the destabilization locus

The following lemma shows that for critical eigenvalues an increase of differential flow, c, will make the corresponding perturbation destabilizing. We recall the assumption (3.4) on stability against homogeneous perturbations $A1$ of a homogeneous steady state of inhibitor-activator type $A2$.

Lemma 3.1. *Suppose that we have a solution to the dispersion relation (3.6) with* $\mathrm{Re}(\lambda) = 0$, $c > 0$, $k \neq 0$, *A1 and A2 hold, then* $\mathrm{sgn}\,\mathrm{Re}\left(\frac{\partial \lambda}{\partial c}\right) > 0$.

Proof. We implicitly differentiate (3.6) to c while keeping k and p fixed:

$$2\lambda \frac{\partial \lambda}{\partial c} + \frac{\partial \alpha_1}{\partial c}\lambda + \alpha_1 \frac{\partial \lambda}{\partial c} + \frac{\partial \alpha_0}{\partial c} = 0 \qquad (3.18)$$

which leads to

$$\frac{\partial \lambda}{\partial c} = -\frac{\frac{\partial \alpha_1}{\partial c}\lambda + \frac{\partial \alpha_0}{\partial c}}{2\lambda + \alpha_1} = -\frac{\overline{2\lambda + \alpha_1}}{|2\lambda + \alpha_1|^2} \frac{\partial \alpha_0}{\partial c} \qquad (3.19)$$

since by (3.9) α_1 is independent of c (the bar denotes complex conjugation). Now by (3.12)

$$|2\lambda + \alpha_1|^2 \operatorname{Re}\left(\frac{\partial \lambda}{\partial c}\right) = -\alpha_1 \operatorname{Re}\left(\frac{\partial \alpha_0}{\partial c}\right) + 2\frac{\operatorname{Im}(\alpha_0)}{\alpha_1} \operatorname{Im}\left(\frac{\partial \alpha_0}{\partial c}\right)$$

$$= -2\alpha_1 c k^2 + 2\frac{\operatorname{Im}(\alpha_0)^2}{\alpha_1 c}.$$

Thus it follows that

$$\frac{\alpha_1}{2ck^2}|2\lambda + \alpha_1|^2 \operatorname{Re}\left(\frac{\partial \lambda}{\partial c}\right) = \frac{\operatorname{Im}(\alpha_0)^2}{c^2 k^2} - \alpha_1^2$$

$$= \left(\frac{\operatorname{Im}(\alpha_0)}{ck} + \alpha_1\right)\left(\frac{\operatorname{Im}(\alpha_0)}{ck} - \alpha_1\right) > 0$$

by (3.16). Since $\alpha_1, c > 0$ it holds that $\operatorname{Re}\left(\frac{\partial \lambda}{\partial c}\right) > 0$. $\qquad\square$

We now include the parameter dependence of (3.8) in our treatment and assume that the homogeneous steady state persists as a function of the parameter p. Thus the linearization $A = \left(\begin{smallmatrix} a_1 & a_2 \\ a_3 & a_4 \end{smallmatrix}\right)$ also becomes a function of p. We will now show that given sign conditions on $\partial A/\partial p$, an increase of p will be either stabilizing or destabilizing.

Lemma 3.2. *Suppose that we have a solution to the dispersion relation* (3.6) *with* $\operatorname{Re}(\lambda) = 0$, *A1 and A2 hold and*

$$\operatorname{sgn}\frac{\partial a_1}{\partial p} = \operatorname{sgn}\frac{\partial a_4}{\partial p} = \operatorname{sgn}\frac{\partial \Gamma}{\partial p} = \operatorname{sgn}\left(-\frac{\partial \det(A)}{\partial p}\right) \qquad (3.20)$$

then $\operatorname{Re}\left(\frac{\partial \lambda}{\partial p}\right)$ *carries the same sign.*[3]

Proof. Now implicit differentiation of (3.6) to p while keeping k and c fixed gives

$$2\lambda\frac{\partial \lambda}{\partial p} + \frac{\partial \alpha_1}{\partial p}\lambda + \alpha_1\frac{\partial \lambda}{\partial p} + \frac{\partial \alpha_0}{\partial p} = 0 \qquad (3.21)$$

which leads to

$$\frac{\partial \lambda}{\partial p} = -\frac{\frac{\partial \alpha_1}{\partial p}\lambda + \frac{\partial \alpha_0}{\partial p}}{2\lambda + \alpha_1} = -\frac{\left(\frac{\partial \alpha_1}{\partial p}\lambda + \frac{\partial \alpha_0}{\partial p}\right)\overline{2\lambda + \alpha_1}}{|2\lambda + \alpha_1|^2}. \qquad (3.22)$$

---

[3]Actually, if $\operatorname{sgn}\frac{\partial a_1}{\partial p} = \operatorname{sgn}\frac{\partial a_4}{\partial p}$ then $\frac{\partial \Gamma}{\partial p}$ carries the same sign automatically.

Since $0 < \alpha_1 \in \mathbb{R}$ it holds that

$$
\begin{aligned}
|2\lambda + \alpha_1|^2 \operatorname{Re}\left(\frac{\partial\lambda}{\partial p}\right) &= -2\lambda^2 \operatorname{Re}\left(\frac{\partial\alpha_1}{\partial p}\right) - \operatorname{Re}\left(\frac{\partial\alpha_0}{\partial p}\right)\alpha_1 - 2\lambda \operatorname{Im}\left(\frac{\partial\alpha_0}{\partial p}\right) \\
&= 2\left(\frac{\operatorname{Im}(\alpha_0)}{\alpha_1}\right)^2 \left(\frac{\partial a_1}{\partial p} + \frac{\partial a_4}{\partial p}\right) - \left(-\frac{\partial\Gamma}{\partial p}k^2 + \frac{\partial\det(A)}{\partial p}\right)\alpha_1 \\
&\quad - 2\frac{\operatorname{Im}(\alpha_0)}{\alpha_1}ck\left(\frac{\partial a_4}{\partial p} - \frac{\partial a_1}{\partial p}\right).
\end{aligned}
$$

Thus $\alpha_1^2\,|2\lambda + \alpha_1|^2 \operatorname{Re}\left(\frac{\partial\lambda}{\partial p}\right)$ equals

$$
\begin{aligned}
&2\operatorname{Im}(\alpha_0)^2\left(\frac{\partial a_1}{\partial p} + \frac{\partial a_4}{\partial p}\right) - \left(-\frac{\partial\Gamma}{\partial p}k^2 + \frac{\partial\det(A)}{\partial p}\right)\alpha_1^3 \\
&\quad + 2ck\alpha_1\operatorname{Im}(\alpha_0)\left(\frac{\partial a_1}{\partial p} - \frac{\partial a_4}{\partial p}\right) \\
&= c^2 k^2\left(\frac{\operatorname{Im}(\alpha_0)}{ck} + \alpha_1 + \frac{\operatorname{Im}(\alpha_0)}{ck} - \alpha_1\right) \\
&\quad \times \left(\left(\frac{\operatorname{Im}(\alpha_0)}{ck} + \alpha_1\right)\frac{\partial a_1}{\partial p} + \left(\frac{\operatorname{Im}(\alpha_0)}{ck} - \alpha_1\right)\frac{\partial a_4}{\partial p}\right) \\
&\quad + \left(\frac{\partial\Gamma}{\partial p}k^2 - \frac{\partial\det(A)}{\partial p}\right)\alpha_1^3.
\end{aligned}
$$

The factors in front of $\frac{\partial a_1}{\partial p}$ and $\frac{\partial a_4}{\partial p}$ are all positive by (3.16). Therefore the signs of the terms in the final expression are determined by the signs in (3.20). $\qquad\square$

We now combine the results at criticality of Lemma 3.1 and 3.2 together with some insights on the global influence of both the advection c and the parameter p on the stability of the homogeneous steady state. In the result below 'const' denotes a positive constant that may be different at any instance.

Theorem 3.1. *We make a distinction between two cases.*

Case 1. Let $I = [p_1, \infty)$ and assume that for $p \in I$ assumptions A1, A2 hold and equation (3.20) holds with sign -1. Assume that at $p = p_1$ the homogeneous steady state is linearly stable for some value of c. Then on I the location of the instability p_T is a strictly monotonically increasing

function of c. If moreover there exists a $q \in I$ such that $p \geq q$ implies both $\Gamma(p) \leq 0$ and

$$-2\frac{\partial a_1}{\partial p}\left(\det(A)(d_1 + d_2) - 2c^2a_4\right) \geq \text{const}, \tag{3.23}$$

then $\lim_{c \to \infty} p_T = \infty$.

   Case 2.   Let $I = (0, p_2]$ and assume that for $p \in I$ assumptions A1, A2 hold and equation (3.20) holds with sign $+1$. Assume that at $p = p_2$ the homogeneous steady state is linearly stable for some value of c. Then on I the location of the instability p_T is a strictly monotonically decreasing function of c. If moreover there exists a $q \in I$ such that $p \leq q$ implies both $\Gamma(p) \leq 0$ and

$$-2\frac{\partial a_1}{\partial p}\left(\det(A)(d_1 + d_2) - 2c^2a_4\right) \leq \frac{-\text{const}}{p}, \tag{3.24}$$

then $\lim_{c \to \infty} p_T = 0$.

Proof. Before making a case distinction, we do some preparatory work. As noted before, from the expression (3.14) it can be seen that the stability of the homogeneous steady state can be manipulated by increasing c. Namely, there is only one term that depends on c and for k^2 small this term is approximated by $4c^2a_1a_4 < 0$. By choosing the right value of c it can be inferred that $\text{Re}(\lambda) = 0$ for some k^2 but nowhere $\text{Re}(\lambda) > 0$. Starting at this criticality the following approximation can be made:

$$\Delta \text{Re}(\lambda) \approx \frac{\partial \text{Re}(\lambda)}{\partial c}\Delta c + \frac{\partial \text{Re}(\lambda)}{\partial p}\Delta p \tag{3.25}$$

where Δ indicates an incremental change in the succeeding quantity. Thus if we locally wish to trace criticality, then we should prescribe that

$$\frac{\partial p}{\partial c} = -\frac{\frac{\partial \text{Re}(\lambda)}{\partial c}}{\frac{\partial \text{Re}(\lambda)}{\partial p}} \tag{3.26}$$

How fast p_T moves is now determined by the maximum/minimum of (3.26) over all critical λ, a maximum/minimum that certainly exists since the dispersion relation is continuous and the evaluation is on a compact set ($k^2 < \frac{a_4}{d_2}$ by (3.15)).

On the other hand we want to incorporate that a sufficient change in the parameter value may stabilize the homogeneous steady state. We pick the term $-2\mathrm{tr}(A)\det(A)(d_1 + d_2)k^2$ from (3.14) to counteract the negative term $4c^2 a_1 a_4 k^2$, thus we are interested in the sign of:

$$4c^2 a_1 a_4 - 2\mathrm{tr}(A)\det(A)(d_1 + d_2) \tag{3.27}$$

As a final preparatory step we compute its derivative:

$$\frac{\partial}{\partial p}\left(4c^2 a_1 a_4 - 2\mathrm{tr}(A)\det(A)(d_1 + d_2)\right)$$

$$= -2\frac{\partial a_1}{\partial p}\left(\det(A)(d_1 + d_2) - 2c^2 a_4\right) + 4c^2 a_1 \frac{\partial a_4}{\partial p} - 2\frac{\partial a_4}{\partial p}\det(A)(d_1 + d_2)$$

$$- 2\mathrm{tr}(A)\frac{\partial \det(A)}{\partial p}(d_1 + d_2) \tag{3.28}$$

We start making a distinction between the two cases.

Case 1. From Lemmas 3.1 and 3.2 and equation (3.26) it follows that p_T is a monotonically increasing function. The only thing left to prove is that $\lim_{c \to \infty} p_T$ is unbounded. For this it is sufficient to show that for any fixed c, the homogeneous steady state can always be stabilized by a sufficient increase of p. By choosing $p \geq q$, the only negative coefficient in (3.14) is $c^2 a_1 a_4 k^2$. In this case the last three terms of (3.28) are positive so:

$$\frac{\partial}{\partial p}\left(4c^2 a_1 a_4 - 2\mathrm{tr}(A)\det(A)(d_1 + d_2)\right)$$

$$\geq -2\frac{\partial a_1}{\partial p}\left(\det(A)(d_1 + d_2) - 2c^2 a_4\right) \geq \mathrm{const}$$

for $p \geq q$ by assumption. So for p large enough the sign of (3.27) will be positive and (3.14) will have no solutions. Together with Lemma 3.4 (Appendix 3.A) this implies stability of the homogeneous steady state.

Case 2. From Lemmas 3.1 and 3.2 and equation (3.26) it follows that p_T is a monotonically decreasing function. The only thing left to prove is that $\lim_{c \to \infty} p_T = 0$. For this it is sufficient to show that for any fixed c, the homogeneous steady state can always be stabilized by a sufficient decrease of p. By choosing $p \leq q$, the only negative coefficient in (3.14) is $c^2 a_1 a_4 k^2$. In this case the last three terms of (3.28) are negative so:

$$\frac{\partial}{\partial p}\left(4c^2 a_1 a_4 - 2\mathrm{tr}(A)\det(A)(d_1 + d_2)\right)$$

$$\leq -2\frac{\partial a_1}{\partial p}\left(\det(A)(d_1 + d_2) - 2c^2 a_4\right) \leq \frac{-\mathrm{const}}{p}$$

for $p \leq q$ by assumption. Because $\int_0^{p'} \frac{1}{p} dp$ diverges, for p small enough the sign of (3.27) will again be positive and equation (3.14) has no solutions, again implying stability by Lemma 3.4 (Appendix 3.A). $\qquad\square$

Uniqueness of the destabilization locus on I for fixed p or fixed c is an immediate consequence of the strict monotonicity. We further note that in the previous theorem case 2 can be reduced to case 1 by taking the parameter $1/p$, so a more concise version without case distinction is possible. We refrain from implementing this because the present treatise fits better with the application to (3.1) that comes next.

3.2.2 Linear analysis of pattern formation for the general system in 2D

In this section we study the destabilization of a homogeneous steady state of the general system (3.2) in two space dimensions, under assumption $A1$ that the homogeneous steady state is stable against homogeneous perturbations and $A2$ that the steady state is of the type inhibitor-activator (3.4).

We use the same reference frame (3.8) with advection coefficients $c_1 = c$ and $c_2 = -c$ as employed in deriving Theorem 3.1 in Section 3.2.1, where c is a measure of differential flow, but we recall that (in)stability does not depend on the reference frame and results hold for general c_1, c_2. The dispersion relation (3.6) introduced in Section 3.2.1, whose solutions determine (in)stability, in 2D depends on two wavenumbers. The wavenumber in the direction of advection x is again denoted k, the additional wavenumber for the y-direction is denoted ℓ. Here the dispersion relation is given by

$$d(\lambda, k, \ell, c) := \det(M - \lambda I) = 0 \qquad (3.29)$$

with M given by

$$M = \begin{pmatrix} -d_1(k^2 + \ell^2) + ick + a_1 & a_2 \\ a_3 & -d_2(k^2 + \ell^2) - ick + a_4 \end{pmatrix}. \qquad (3.30)$$

We can conveniently connect the results developed in Section 3.2.1 to the stability in 2D through the following lemma.

Lemma 3.3. *In the presence of differential flow, $c > 0$, the primary destabilization of a homogeneous steady state of (3.2) satisfying $A1$ and $A2$ at criticality occurs through perturbations with $\ell = 0$. The range of wavenumber*

pairs (k, ℓ) corresponding to destabilizing perturbations is strictly monotonically increasing with c, but bounded above by

$$k^2 + \ell^2 < \frac{a_4}{d_2}. \qquad (3.31)$$

Proof. We start with the important equivalence

$$(\lambda, k, \ell, c) \text{ solves } (3.29) \Leftrightarrow \left(\lambda, \sqrt{k^2 + \ell^2}, 0, \frac{kc}{\sqrt{k^2 + \ell^2}}\right) \text{ solves } (3.29), \qquad (3.32)$$

which follows directly from the equality of the matrices M, see (3.30). Now suppose that the homogeneous steady state is marginally stable for some value of c. By the identity (3.32), the instability with respect to a perturbation with $\ell \neq 0$ is the same as the instability with respect to a perturbation with $\ell = 0$ and smaller c since $k/\sqrt{k^2 + \ell^2} < 1$. Due to the destabilizing impact of c at criticality (see Lemma 3.1), 1D perturbations with smaller c have $\mathrm{Re}(\lambda) < 0$. Hence, the primary destabilization occurs through perturbations with $\ell = 0$.

Strict monotonicity for pairs $(k, 0)$ is already due to Lemma 3.1. Because (in)stability against (k, ℓ) is linked to (in)stability against $(\sqrt{k^2 + \ell^2}, 0)$ through (3.32), this automatically extends to monotonicity for all (k, ℓ). The bound (3.15) extends likewise to (3.31). $\qquad \square$

Note that for $c = 0$, symmetry implies that instability in any direction occurs simultaneously. As mentioned in the introduction, the transformation in (3.32) is known in fluid mechanics as 'Squire's transformation'. For a *supercritical* Turing(-Hopf) bifurcation (stable) small amplitude patterns emerge for parameter values just beyond the bifurcation. In the *subcritical* case the small amplitude patterns exist for parameter values just before the bifurcation. The previous lemma immediately leads to the following result.

Theorem 3.2. *The 2D destabilization locus coincides with the 1D destabilization locus, so the monotonicity result Theorem 3.1 also holds in 2D. In case of a supercritical Turing-Hopf bifurcation, the primary patterns to form are striped patterns perpendicular to the advection.*

3.2.3 Application to the extended Klausmeier model

In this section we check applicability of the general results to the extended Klausmeier model (3.1). The spatially homogeneous steady states of (3.1)

are given by $w_{\text{bare}} = a$, $n_{\text{bare}} = 0$ and

$$
\begin{aligned}
w_\pm &= \frac{2m^2}{a \pm \sqrt{a^2 - 4m^2}} \\
n_\pm &= \frac{a \pm \sqrt{a^2 - 4m^2}}{2m}
\end{aligned}
\tag{3.33}
$$

for $a \geq 2m$ [180]. Since (w_-, n_-) is unstable against spatially homogeneous perturbations [180], we focus on the other vegetated state (w_+, n_+).

We provide some more elementary facts about (3.1), details can be found in [180]. The linearization about (w_+, n_+) is given by the Jacobian matrix $A = \left(\begin{smallmatrix} a_1 & a_2 \\ a_3 & a_4 \end{smallmatrix} \right) = \left(\begin{smallmatrix} -1-n_+^2 & -2m \\ n_+^2 & m \end{smallmatrix} \right)$. Thus clearly $a_1 < 0$ and $a_4 > 0$, so (w_+, n_+) is of inhibitor-activator type (assumption $A2$, see (3.4)). It holds that $\det(A) = m(n_+^2 - 1) > 0$ for $a > 2m$, but $\text{tr}(A) < 0$ if and only if

$$
m \leq 2 \qquad \text{or} \qquad a > \frac{m^2}{\sqrt{m-1}}. \tag{3.34}
$$

For these choices of parameters (w_+, n_+) is stable against homogeneous perturbations (assumption $A1$, see (3.4)). So for a nonzero slope $c > 0$, the uphill motion of patterns considered in Section 3.2.1 indeed applies. Moreover Lemma 3.3 holds, so destabilization occurs through perturbations that are constant in the y-direction perpendicular to the direction of advection. After destabilization the set of destabilizing perturbations becomes larger and larger.

For (3.1) the bound (3.31) on destabilizing perturbations is reduced to $k^2 + \ell^2 < m$. In this paper we work with the estimate $m = 0.45$ for grass, for trees $m = 0.045$ holds (see [97]) and the bound is more restrictive. If $k = 0$ then c does not play a role and destabilization in the y-direction thus occurs independent of c, at $a \approx 2.883$. We will refer to this point as the *anchor point* T_y. The results from Lemma 3.3 are illustrated in Figure 3.2.

Checking the supercriticality condition of Theorem 3.2 analytically, requires the computation of Landau coefficients, which is beyond the scope of this paper. Supercriticality has been proven in an asymptotic scaling of (3.1) in one space dimension in [199] and numerically it is found that this holds in a broad range of parameter space. Through Theorem 3.2, for advection $c > 0$ the Turing-Hopf bifurcation is a natural mechanism for the formation of striped or banded vegetation patterns. We will see this formation of banded vegetation in simulations in Section 3.3.3.

(a) (b)
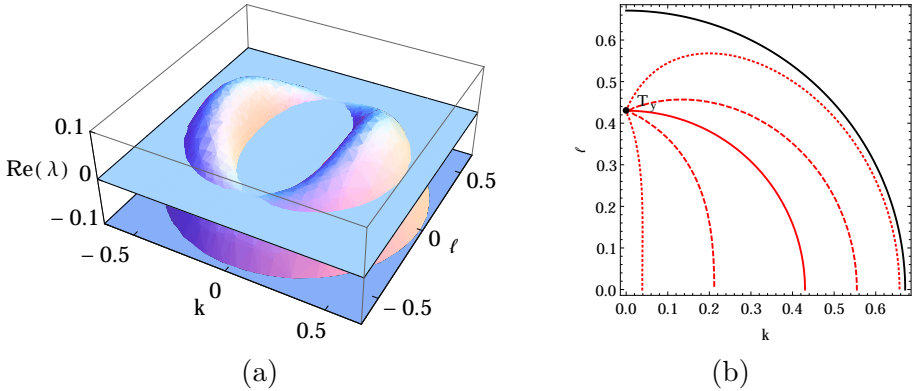
Figure 3.2: The extended Klausmeier model (3.1) for $m = 0.45$ ($d = 500$) at $a \approx 2.883$ (onset of the Turing instability for $c = 0$). (a) Real part of $\lambda(k, \ell, c)$ solving the homogeneous steady state dispersion relation (3.29) for $2c = 182.5$. Notably, $\mathrm{Re}(\lambda)$ is maximal for $\ell = 0$. (b) Contour plots of $\mathrm{Re}(\lambda(k, \ell, c)) = 0$ for $c = 0$ (red, continuous), $2c = 182.5$ (red, dashed) and $2c = 1000$ (red, dotted). For $c = 0$ destabilization occurs in any direction simultaneously. For $c > 0$ the range between the curves corresponding to destabilizing perturbations is increasing, but not beyond the black curve $k^2 + \ell^2 < m$. The anchor point T_y appears at $k = 0$, $\ell \approx 0.430$.

To apply the monotonicity result Theorem 3.1 we need to check some more conditions. In the corollary below it will be shown that, when the parameter a assumes the role of the abstract parameter p, the parameter locus of its destabilization a_T is a strictly monotonically increasing function of c and $\lim_{c \to \infty} a_T = \infty$. Although within the scope of this paper the parameters c and a are most important, the theory developed here is also utilized to show that (when m assumes the role of p) m_T is a monotonically decreasing function of c and $\lim_{c \to \infty} m_T = 0$.

In preparation we make note of some rough estimates for n_+:

$$n_+ \leq \frac{a}{m}, \qquad \frac{\partial n_+}{\partial m} \leq \frac{\partial}{\partial m} \frac{a}{2m} = -\frac{a}{m^2},$$
$$\frac{\partial n_+^2}{\partial a} \geq \frac{\partial}{\partial a} \frac{a^2}{4m^2} = \frac{a}{2m^2}, \qquad \frac{\partial n_+^2}{\partial m} \leq \frac{\partial}{\partial m} \frac{a^2}{4m^2} = \frac{-a^2}{2m^3}. \tag{3.35}$$

We recall that (3.1) is not precisely of the form (3.8) but can be brought into this form by changing the frame of reference, as detailed at the start of Section 3.2.1, and we apply Theorem 3.1 as if we have done so.

Corollary 3.1. *Assume that (3.34) holds for $a = p_1$ and $m = p_2$ and that here the homogeneous steady state (w_+, n_+) is linearly stable for some value of c.*

Then for a on $[p_1, \infty)$ *(with $m = p_2$) the location of the instability a_T is a strictly monotonically increasing function of c. Moreover $\lim_{c \to \infty} a_T = \infty$.*

For m on $(0, p_2]$ (with $a = p_1$) the location of the instability m_T is a strictly monotonically decreasing function of c. Moreover $\lim_{c \to \infty} m_T = 0$.

Proof. The assumptions (3.4) of stability against homogeneous perturbations $A1$ and being of inhibitor-activator type $A2$ must now be checked for an interval of parameter values. The shape of the set of points (a, m) satisfying $A1$ given by (3.34) implies that if we pick $a = p_1$ and $m = p_2$ for which (w_+, n_+) is stable against homogeneous perturbations then this remains true if a is increased or m is decreased, see Figure 3.4. The inhibitor-activator assumption was already found to hold everywhere. So assumptions $A1$ and $A2$ hold for all $a \in [p_1, \infty)$ and $m \in (0, p_2]$.

For the parameter a we apply (3.35) and readily compute that $\frac{\partial a_1}{\partial a} = -\frac{\partial n_+^2}{\partial a} \leq \frac{-a}{2m^2} \leq \frac{-p_1}{2m^2}$, $\frac{\partial a_4}{\partial a} = 0$, $\frac{\partial \Gamma}{\partial a} = \frac{\partial a_1}{\partial a}$ and $\frac{\partial \det(A)}{\partial a} = \frac{\partial a_1}{\partial a} m + 2m \frac{\partial a_3}{\partial a} = m \frac{\partial n_+^2}{\partial a} \geq \frac{a}{2m} \geq \frac{p_1}{2m}$. This shows that (3.20) holds with sign -1, except that $\frac{\partial a_4}{\partial a} = 0$ which is no problem as can be seen from the proof of Lemma 3.2. Since $\frac{\partial \Gamma}{\partial a} \leq \frac{-p_1}{2m^2}$, Γ is negative for a large enough. With the help of the previous computations we can make the following estimate to check (3.23):

$$-2 \frac{\partial a_1}{\partial a} \left(\det(A)(d_1 + d_2) - 2c^2 a_4 \right)$$
$$\geq \frac{p_1}{m^2} \left(\left(\det(A(p_1)) + (a - p_1) \frac{p_1}{2m} \right) (d_1 + d_2) - 2c^2 m \right)$$

and the term on the right will become bigger then any constant if a is taken large enough. So case 1 of Theorem 3.1 applies to the parameter a.

For the parameter m, using (3.35), we compute that $\frac{\partial a_1}{\partial m} = -\frac{\partial n_+^2}{\partial m} \geq \frac{a^2}{2m^3}$, $\frac{\partial a_4}{\partial m} = 1$, $\frac{\partial \Gamma}{\partial m} = d + \frac{\partial a_1}{\partial m}$ and

$$
\begin{aligned}
\frac{\partial \det(A)}{\partial m} &= \frac{\partial a_1}{\partial m} m + a_1 + 2a_3 + 2m \frac{\partial a_3}{\partial m} = m \frac{\partial n_+^2}{\partial m} - 1 + n_+^2 \\
&\leq \left(2m \frac{\partial n_+}{\partial m} + n_+ \right) n_+ \leq \left(2m \frac{-a}{m^2} + \frac{a}{m} \right) \frac{a}{m} = \frac{-a}{m^2},
\end{aligned}
\tag{3.36}
$$

so (3.20) holds with sign $+1$. Clearly, $\Gamma = dm - 1 - n^2$ is negative for
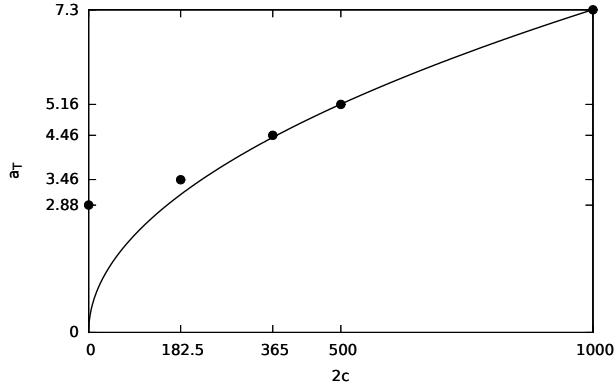
Figure 3.3: The dots represent the location of the instability a_T of (3.1) (with $d = 500$, $m = 0.45$) for several values of $2c$. The result from [199] is illustrated by the graph of $0.231\sqrt{2c}$, with the factor chosen to fit the value at $2c = 1000$.

sufficiently small m. By solving (3.36) we obtain:

$$-2\frac{\partial a_1}{\partial m}\left(\det(A)(d_1 + d_2) - 2c^2 a_4\right)$$
$$\leq -\frac{a^2}{m^3}\left(\left(\det(A(p_2)) - \frac{a}{2p_2} + \frac{a}{2m}\right)(d_1 + d_2) - 2c^2\right)$$

The sign of the term on the right will become negative for m small enough, also $\frac{1}{m^3} > \frac{1}{m}$ for $m < 1$. Hence, case 2 of Theorem 3.1 applies to the parameter m. □

Within the model (3.1), *any* choice of parameters that allows for a stable uniform vegetated state, will behave as described by the previous corollary. Thus the locus of destabilization a_T of the homogeneous steady state moves to higher a as c increases. This is consistent with what we find numerically. In Figure 3.3 we plot the values of a_T for $2c = 0$, 182.5, 365, 500 and 1000, together with a square root function since a_T grows as $\sqrt{c}$ for large c, in a certain scaling regime [199].

Now that we understand the influence of both parameters a and m, we can also fix c and infer the dependence $a_T = a_T(m)$ for free. The following approximation complementary to (3.25) can be made:

$$\Delta \operatorname{Re}(\lambda) \approx \frac{\partial \operatorname{Re}(\lambda)}{\partial a}\Delta a + \frac{\partial \operatorname{Re}(\lambda)}{\partial m}\Delta m$$
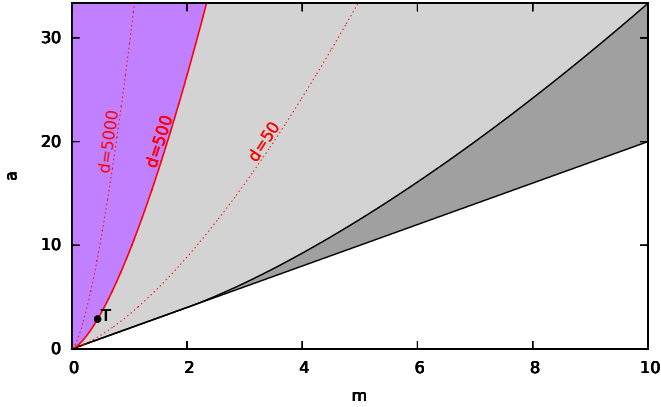
Figure 3.4: Regions of stability of (w_+, n_+) for the extended Klausmeier model (3.1) for $c = 0$. In the white region $a < 2m$ and (w_+, n_+) does not exist. In the dark grey region where $2m < a < \frac{m^2}{\sqrt{m-1}}$, $\operatorname{tr}(A) > 0$. Elsewhere, (w_+, n_+) is stable against homogeneous perturbations. The red curves depict the solution set of $\Gamma = 2\sqrt{d\det(A)}$ for $d = 50, 500, 5000$, see (3.11). At each of these curves (w_+, n_+) undergoes a Turing instability for the corresponding value of d. The relative placement of the curves as a function of d is a consequence of $\Gamma/\sqrt{d}$ being an increasing function of d. By (3.37), $a_T = a_T(m)$ is a strictly monotonically increasing function of m, for every value of d. For $d = 500$, in the light grey area the homogeneous steady state is Turing unstable and in the purple area it is Turing stable. For $m = 0.45$ the Turing instability occurs at $a \approx 2.883$, this point is labeled T in the figure.

with Δ again indicating an incremental change. Now if we locally wish to trace criticality, we should prescribe that

$$\frac{\partial a}{\partial m} = -\frac{\frac{\partial \operatorname{Re}(\lambda)}{\partial m}}{\frac{\partial \operatorname{Re}(\lambda)}{\partial a}} > 0 \qquad (3.37)$$

since we have already seen that $\frac{\partial \operatorname{Re}(\lambda)}{\partial m} > 0$ and $\frac{\partial \operatorname{Re}(\lambda)}{\partial a} < 0$ at criticality. To trace criticality a and m should be simultaneously increased or simultaneously decreased.

Figure 3.4 illustrates the different (in)stability regions of (w_+, n_+) for $c = 0$. From Corollary 3.1 we know that, by increasing the advection c, a homogeneous steady state in the purple region ($d = 500$) can be made unstable. But for any finite c, (w_+, n_+) is stable for a large or m small enough.

3.3 Striped pattern stability in 2D

In this section we restrict our attention to the extended Klausmeier model (3.1), where the differential flow equals the water advection.

Perturbations of the homogeneous state in 2D were represented by two wavenumbers $k, \ell \in \mathbb{R}$ for the x, y-directions respectively in Section 3.2.2. In Section 3.3.1 we will first explain that perturbations of a pattern of stripes perpendicular to the direction of advection x can be represented by $\ell \in \mathbb{R}$ and γ on the unit circle $S^1 \subset \mathbb{C}$, so that $\log(\gamma) \in (-\pi\mathrm{i}, \pi\mathrm{i}]$. The restriction to perturbations with $\ell = 0$ corresponds to perturbations that were already considered in 1D in [180]. Perturbations with $\ell \neq 0$ are not constant in the transverse y-direction along the stripes and may cause them to break up.

In Section 3.3.2 we analytically derive an instability result for localized striped patterns on flat ground ($c = 0$, no advection) through an Evans function approach, proving that in this case a range of 1D stable patterns extends to 2D *unstable* striped patterns. These patterns will be unstable against perturbations for a range of values $\ell > 0$, independent of γ.

We continue by numerically determining the collection of striped patterns that withstand the additional transverse destabilization mechanisms in Section 3.3.3. Here perturbations with $\gamma = \pm 1$ play a special role, as stability against transverse perturbations for $\gamma = \pm 1$ seems to imply stability against all transverse perturbations. We show that the fraction of 2D stable striped patterns within the enveloping 1D Busse balloon increases as the advection c increases, which is relevant for determining ecological resilience.

These results are complemented by simulations of (3.1) with the rainfall a as a slowly decreasing parameter. Similar to [180], we trace the wavenumber of the solution if it is in a striped pattern state. The simulations show that the continuation method employed to determine striped pattern stability successfully predicts the occurrence of stripe breakup; depending on the advection c, the initial stages in the pattern selection process are determined by 1D effects ($\ell = 0$).

3.3.1 Transverse instabilities: breakup of stripes into rectangles or rhombs

In Section 3.2, we computed the linearization about a constant homogeneous state by representing perturbations by complex exponentials using the Fourier transform. Analogously, linearization about a periodic state

with wavelength $2\pi/\kappa$ is possible through a so-called Floquet-Bloch transform (see Appendix 3.B). Now perturbations are represented by functions $\tilde{n}_\gamma$ satisfying a 'γ-twisted' (terminology from [20]) periodicity property

$$\tilde{n}_\gamma\left(x + \frac{2\pi}{\kappa}\right) = \gamma\tilde{n}_\gamma(x) \qquad (3.38)$$

where γ is on the unit circle (and similarly for the water component w). Note that $\gamma = 1$ implies that the perturbation has exactly the same wavelength as the underlying pattern. The striped patterns we study are periodic in the x-direction and constant in the y-direction. Perturbations are thus represented by the combination $\tilde{n}(x,y) = n_\gamma(x)e^{i\ell y}$.

As already noted transverse perturbations with $\gamma = \pm 1$ turn out to be primary destabilization mechanisms, in Section 3.3.3. In this section we will use numerical continuation in two spatial dimensions, introduced in [54,192], to visualize the destabilizing perturbations and the bifurcating 2D patterns for the cases $\gamma = \pm 1$, for the extended Klausmeier model (3.1). With these techniques it becomes possible to map existence and stability of patterns periodic in 2D, as we will illustrate, but an extensive search is outside the scope of this paper.

At the Turing-Hopf point where $a = a_T$, the homogeneous steady state is marginally stable against a perturbation with a distinct wavenumber k_T. Beyond the instability a set of stable striped patterns exists (in the supercritical case), whose wavenumbers form an interval including $\kappa = k_T$. In Table 3.1 we show at which value of a_{rect}, a_{rhomb} this striped pattern becomes unstable against transverse breakup for $\gamma = 1$ respectively $\gamma = -1$ and at what distinct value of ℓ_{rect}, ℓ_{rhomb} of the transverse wavenumber, for several values of $2c$ (with $d = 500$, $m = 0.45$). The table is obtained by continuation methods for one spatial dimension, as will be used in Section 3.3.3

Table 3.1 can be used as input to study striped pattern breakup, e.g. for $c = 0$ in Figure 3.5. In order to find the 2D pattern that bifurcates from the striped pattern with $\kappa = k_T$ for $\gamma = 1$, we start out from the homogeneous steady state (w_+, n_+) and choose $[0, 4\pi/k_T] \times [0, 2\pi/\ell_{\text{rect}}]$ as a domain. At the Turing(-Hopf) point, a two-stripe pattern (Figure 3.5 (b)) bifurcates from (w_+, n_+) as the domain size in x was prepared like this. If by continuation a is decreased to a_{rect}, the two-stripe pattern becomes unstable against a transverse perturbation (Figure 3.5 (c)) and a pattern periodic in both dimensions (Figure 3.5 (d)) bifurcates. By (3.38), for $\gamma = 1$

$2c$	a_T	k_T	a_{rect}	ℓ_{rect}	a_{rhomb}	ℓ_{rhomb}
0	2.883	0.430	2.232	0.433	2.297	0.410
182.5	3.456	0.398	2.107	0.417	2.197	0.394
365	4.460	0.384	2.011	0.418	2.197	0.365
500	5.161	0.385	2.037	0.422	2.349	0.348
1000	7.301	0.398	2.206	0.443	3.074	0.343

Table 3.1: Table of Turing-Hopf loci (a_T) of (3.1) (for $d = 500$, $m = 0.45$), the critical wavenumber at its onset (k_T) and for the striped patterns with $\kappa = k_T$ the critical a-values and wavenumbers ℓ of perturbation along the striped pattern at breakup for $\gamma = 1$ (a_{rect} and ℓ_{rect}) and $\gamma = -1$ (a_{rhomb} and ℓ_{rhomb}).

perturbations are in phase at neighboring stripes (at distance $2\pi/\kappa$) since $\tilde{n}\left(x + \frac{2\pi}{\kappa}, y\right) \equiv \tilde{n}_1\left(x + \frac{2\pi}{\kappa}\right) e^{i\ell y} = \tilde{n}_1(x)e^{i\ell y} = \tilde{n}(x, y)$. Periodically extending the pattern in Figure 3.5 (d) in both dimensions gives a rectangular pattern on the plane.

Likewise for $\gamma = -1$, if we choose $[0, 4\pi/k_T] \times [0, 2\pi/\ell_{\text{rhomb}}]$ the two-stripe pattern emerging at a_T becomes unstable against a different transverse perturbation (Figure 3.6 (c), where $2c = 182.5$) when a is decreased to a_{rhomb} and again a pattern periodic in both dimensions (Figure 3.6 (d)) bifurcates. For $\gamma = -1$, perturbations are in opposite phase at neighboring stripes ($2\pi/\kappa$ apart) since by (3.38) it holds that $\tilde{n}\left(x + \frac{2\pi}{\kappa}, y\right) \equiv \tilde{n}_{-1}\left(x + \frac{2\pi}{\kappa}\right) e^{i\ell y} = -\tilde{n}_{-1}(x)e^{i\ell y} \equiv -\tilde{n}(x, y)$. Periodic extension of the pattern in Figure 3.6 (d) yields a rhombic pattern. In this case the bifurcating rhombic pattern deviates only little from a regular hexagonal pattern.

We note that the inset of Figure 3.5(a) shows that the branch of striped patterns becomes unstable before the stripe-rectangle bifurcation point is reached. This is because the stripe-rhomb bifurcation precedes the stripe-rectangle bifurcation, indeed $a_{\text{rhomb}} > a_{\text{rect}}$ and $\ell_{\text{rhomb}} \approx \ell_{\text{rect}}$ for $c = 0$, so the stripe-rhomb bifurcation is only slightly delayed because it does not immediately satisfy the boundary conditions. In Figure 3.6 the striped pattern does remain stable up to the bifurcation shown.

The stripe-rectangle and stripe-rhomb bifurcations are found to be always subcritical, but relatively quickly the branch folds back, so that it appears supercritical on the larger parameter scale. The methods are not restricted to $\kappa = k_T$, the computations presented in Figure 3.7 show a rhombic pattern with both acute and obtuse angles for long x-wavelengths, which occur for larger c-values.
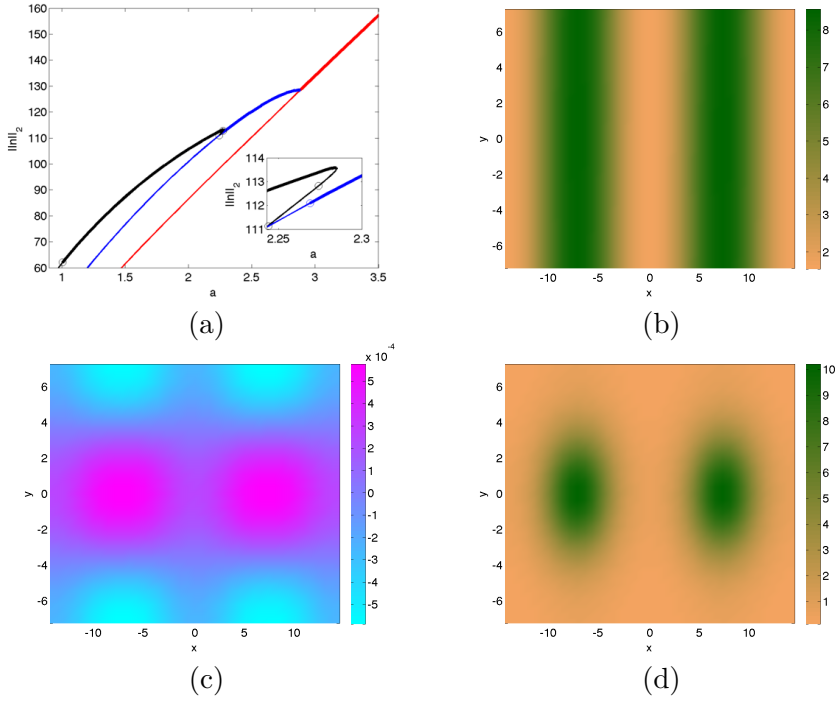
Figure 3.5: (a) Stripe-rectangle bifurcation diagram of (3.1) for $c = 0$ ($d = 500$, $m = 0.45$) with branch of homogeneous equilibrium (red), bifurcating striped patterns with wavenumber $\kappa = k_T$ (blue), subcritically bifurcating rectangular pattern with $\ell = \ell_{\text{rect}}$ (black) and inset magnifying this subcritical bifurcation. For efficiency, the computations where done under zero flux Neumann boundary conditions, and thick lines indicate stability with respect to perturbations that fit the domain. Other panels show striped pattern (b) and destabilizing perturbation (c) at stripe-rectangle bifurcation point, rectangular pattern (d) at $a \approx 1$. Note that the solution plots extend periodically in both space directions.

(a)

(b)

(c)

(d)
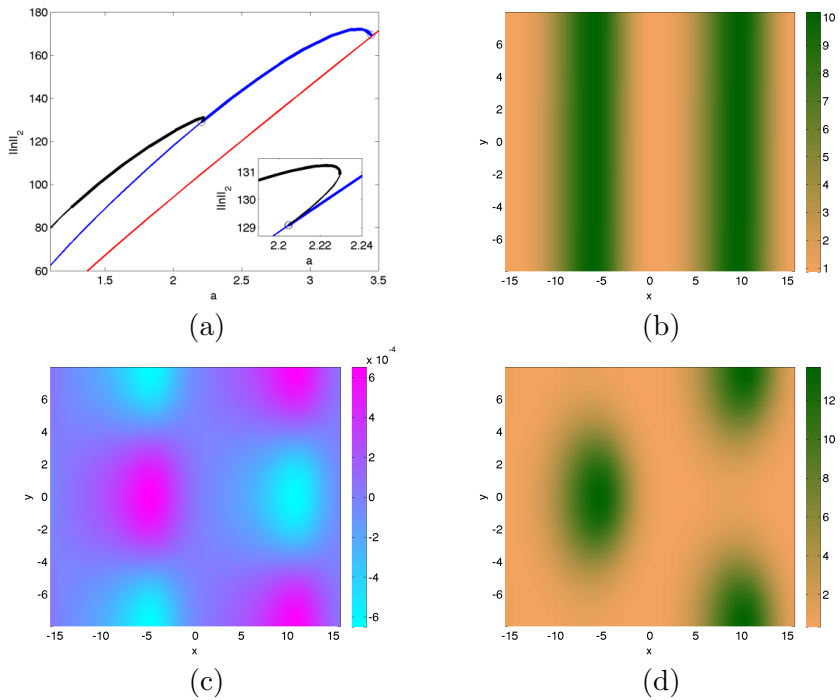
Figure 3.6: Analogue of Figure 3.5 for stripe-rhomb bifurcation for $2c = 182.5$ under cylinder geometry. Periodic extension in both dimensions of (c)-(d) yields a rhombic pattern. Here (d) is the solution on the black branch in (a) at the instability $a \approx 1.2$.
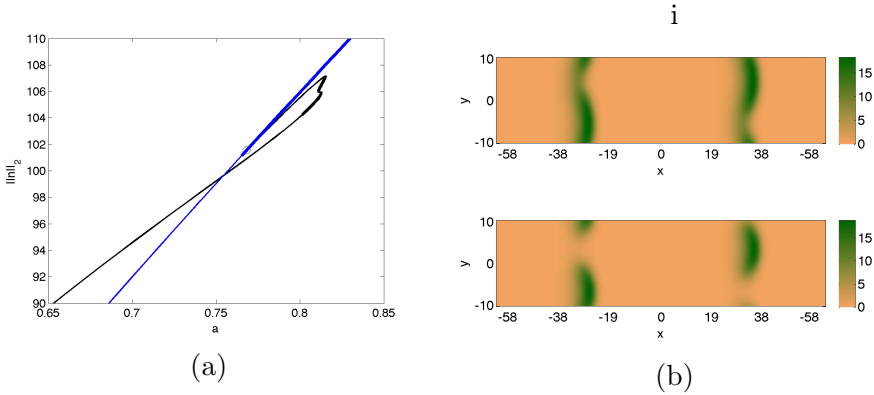
Figure 3.7: (a) Stripe-rhomb bifurcation diagram of (3.1) for $2c = 365$ ($d = 500$, $m = 0.45$) on a domain with periodic boundary conditions: striped patterns with wavenumber $\kappa = 0.1$ (blue), stripe-rhomb patterns (black). Note that most of the solutions on the rhomb branch are unstable (even on this small domain), as their locus is plotted with a thin line. (b) Rhomb patterns (when periodically extended in both directions); upper panel: at the stability change for $a \approx 0.8$ on the lower part of the black branch, lower panel: in the unstable regime for $a \approx 0.65$.

3.3.2 No advection: transverse instability of long wavelength striped patterns

In this mathematically more technical section we consider long wavelength striped patterns of the extended Klausmeier model (3.1) in absence of advection ($c = 0$) and establish instability with respect to perturbations along the stripes ($\ell > 0$) in the spirit of results on solitary homoclinic stripes [53, 100, 103].

By scaling (3.1) into the form of the Gray-Scott model we may use results that have already been derived for this model. Without advection and in a single space dimension, (3.1) is given by

$$w_t = dw_{xx} + a - w - wn^2$$
$$n_t = n_{xx} - mn + wn^2$$

and can be scaled into the standard form of the Gray-Scott equation,

$$u_T = u_{XX} + A(1 - u) - uv^2$$
$$n_T = Dv_{XX} - Bv + uv^2, \qquad (3.39)$$

by setting

$$u(X, T) = \frac{1}{a} w(x, t), \ v(X, T) = \frac{1}{a} n(x, t),$$

with

$$T = a^2 t, \ X = \frac{a}{\sqrt{d}} x,$$

so that

$$A = \frac{1}{a^2}, \ B = \frac{m}{a^2}, \ D = \frac{1}{d}. \tag{3.40}$$

The dynamics of the Gray-Scott model are largely determined by the interplay between two small parameters [43, 44, 101, 102]. Following [43, 44], we therefore introduce,

$$U(\xi, \tau) = \frac{\sqrt{A}}{B\sqrt{BD}} u(X, T), \ V(\xi, \tau) = \frac{\sqrt{BD}}{\sqrt{A}} v(X, T) \tag{3.41}$$

with

$$\tau = BT, \ \xi = \frac{\sqrt{B}}{\sqrt{D}} X, \tag{3.42}$$

which transforms (3.39) into

$$\begin{aligned} DU_\tau &= U_{\xi\xi} - \epsilon^2 [UV^2 - \epsilon\delta(1 - \frac{\delta}{\epsilon}U)] \\ V_\tau &= V_{\xi\xi} + UV^2 - V, \end{aligned} \tag{3.43}$$

with

$$\epsilon = \frac{\sqrt{A}}{B}, \ \delta = \sqrt{BD}. \tag{3.44}$$

An existence result on patterns $(U_\mu(\xi), V_\mu(\xi))$ with a long wavelength $\mathcal{T}(\mu)$, with $\mu > 1$ an amplitude parameter chosen for the parametrization, based on literature on the Gray-Scott model, is presented in Appendix 3.C (Theorem 3.4). Here geometric singular perturbation theory is used, the small parameter exploited is given by $\epsilon = a/m$. Note that in the long wavelength limit considered here, the $V_\mu(\xi)$-component associated to plant biomass is strongly localized, while $W_\mu(\xi)$ varies on a larger scale. The existence of 1D patterns is equivalent to the existence of striped patterns in 2D. Below, η is a scaled version of the second spatial dimension y the same way as ξ relates to x, see (3.42).

To investigate the spectral stability of the striped pattern $(U_\mu(\xi), V_\mu(\xi))$ on the full plane, so $(\xi, \eta) \in \mathbb{R}^2$, we set

$$(U(\xi, \eta, \tau), V(\xi, \eta, \tau)) = (U_\mu(\xi) + u(\xi)e^{i\ell\eta + \lambda\tau}, V_\mu(\xi) + v(\xi)e^{i\ell\eta + \lambda\tau}),$$

with $\ell \in \mathbb{R}$ and $\lambda = \lambda(\mu, \ell) \in \mathbb{C}$. The linearized stability problem for (3.43) reads

$$
\begin{array}{rcrcrcrcr}
D\lambda u & = & u_{\xi\xi} & - & \ell^2 u & - & \varepsilon^2[V_\mu^2 u & + & 2U_\mu V_\mu v & - & \delta^2 u] \\
\lambda v & = & v_{\xi\xi} & - & \ell^2 v & + & V_\mu^2 u & + & 2U_\mu V_\mu v & - & v.
\end{array}
\tag{3.45}
$$

We introduce $\hat{\ell}$ by

$$
\ell = \sqrt{D}\hat{\ell}
\tag{3.46}
$$

and write (3.45) as a coupled system of Sturm-Liouville-type equations

$$
\begin{array}{rclcl}
u_{\xi\xi} & - & D[\hat{\ell}^2 + \lambda - \frac{\varepsilon^2\delta^2}{D}]u & = & \varepsilon^2[V_\mu^2 u + 2U_\mu V_\mu v] \\
v_{\xi\xi} & + & [2U_\mu V_\mu - (1 + \lambda + D\hat{\ell}^2)]v & = & -V_\mu^2 u.
\end{array}
\tag{3.47}
$$

This system can equivalently be written as a 4-dimensional linear system for $\phi(\xi) = (u(\xi), p(\xi), v(\xi), q(\xi))$ with $p = \frac{1}{\varepsilon}\dot{u}$ and $q = \dot{v}$,

$$
\dot{\phi} = \mathcal{A}_\mu(\xi; \lambda, \hat{\ell})\phi,
\tag{3.48}
$$

where the dot denotes differentiation with respect to ξ and $\mathcal{A}_\mu(\xi; \lambda, \hat{\ell})$ is a ξ-periodic matrix,

$$
\mathcal{A}_\mu(\xi; \lambda, \hat{\ell}) = \begin{pmatrix}
0 & \varepsilon & 0 & 0 \\
\varepsilon[V_\mu^2(\xi) + \frac{D}{\varepsilon^2}(\hat{\ell}^2 + \lambda) - \delta^2] & 0 & 2\varepsilon U_\mu(\xi)V_\mu(\xi) & 0 \\
0 & 0 & 0 & 1 \\
-V_\mu^2(\xi) & 0 & -2U_\mu(\xi)V_\mu(\xi) + (1 + \lambda + D\hat{\ell}^2) & 0
\end{pmatrix}
\tag{3.49}
$$

with period $\mathcal{T}(\mu)$ (see Theorem 3.4, Appendix 3.C). For any $\mu > 1$ and $\hat{\ell} \in \mathbb{R}$, system (3.48) determines a spectral problem for $\lambda = \lambda_\mu(\hat{\ell}) \in \mathbb{C}$ (e.g. in the space of complex-valued bounded uniformly continuous functions $BUC(\mathbb{R}^2, \mathbb{C}^4)$).

Following [67], and in the approach of [197], similar to (3.38) the eigenvalue problem (3.48) is considered on the fundamental interval $[-\frac{1}{2}\mathcal{T}(\mu), \frac{1}{2}\mathcal{T}(\mu)]$ with γ-twisted periodic boundary condition,

$$
\phi\left(\frac{1}{2}\mathcal{T}(\mu)\right) = \gamma\phi\left(-\frac{1}{2}\mathcal{T}(\mu)\right)
\tag{3.50}
$$

for $\gamma \in S^1 \subset \mathbb{C}$ on the unit circle.

The stability problem (3.47) that is equivalent to (3.48) has a structure that is very similar to that of the existence problem. In fact, it can be

shown by directly applying the approach of [46, 197] that the v-component of ϕ is strongly localized and exponentially small outside a fast interval $\mathcal{I}_f$, completely similar to $V_\mu(\xi)$ (Theorem 3.4). As a consequence, the slow reduced limit problem for the u component of ϕ – that is defined in the regions $[-\frac{1}{2}\mathcal{T}(\mu), \frac{1}{2}\mathcal{T}(\mu)]\backslash\mathcal{I}_f$ – is given by

$$u_{\xi\xi} - D\left[\hat{\ell}^2 + \lambda - \frac{\epsilon^2\delta^2}{D}\right]u = 0 \tag{3.51}$$

up to exponentially small corrections. Hence, outside $\mathcal{I}_f$, $u(\xi)$ is given by a combination of exponential functions in the spatial variable $\sqrt{D}\xi$ – under the assumption that $\frac{\varepsilon^2\delta^2}{D}$ is small enough, or more formally, that $\varepsilon\delta \ll \sqrt{D}$. However, the length of the fundamental interval $[-\frac{1}{2}\mathcal{T}(\mu), \frac{1}{2}\mathcal{T}(\mu)]$ is of order $\frac{1}{\varepsilon\delta}$ (see (3.C.1)): if $\varepsilon\delta \ll \sqrt{D}$, then an asymptotically bounded solution of (3.51) will be exponentially small at the boundaries of $[-\frac{1}{2}\mathcal{T}(\mu), \frac{1}{2}\mathcal{T}(\mu)]$. As a consequence, the entire family $\lambda(\gamma)$, $\gamma \in S^1$ of γ-eigenvalues will be asymptotically close to the positive eigenvalue λ that one can obtain (at leading order) by just considering solutions of (3.51) that decay exponentially as $\xi \gg \frac{1}{\sqrt{D}}$. Since the rigorous validation of this statement requires an extensive analysis along the lines of [197], we refrain from going further into the details here.

Theorem 3.3. *Assume that the assumptions formulated in Theorem 3.4 hold and consider a spatially periodic striped pattern $(U_\mu(\xi), V_\mu(\xi))$ as given by Theorem 3.4. There are constants $D_{0,1}, D_{0,2} > 0$ and $0 < \hat{\ell}_1 < \hat{\ell}_2$ such that for all $0 < D < D_{0,1}$, $0 < \varepsilon\delta < D_{0,2}\sqrt{D}$, and $\mu \geq 1$, eigenvalue problem (3.48) has a family of γ-eigenvalues, $\gamma \in S^1$, exponentially close to a critical eigenvalue $\lambda_{\mathrm{pole}}(\mu, \hat{\ell})$ that is at leading order given by,*

$$\lambda_{\mathrm{pole}}(\mu, \hat{\ell}) = \frac{5}{4} \text{ for all } \hat{\ell} \in (\hat{\ell}_1, \hat{\ell}_2).$$

The lengthy proof of Theorem 3.3 is given in Appendix 3.D. Note that the extension of $(U_\mu(\xi), V_\mu(\xi))$ in the η-direction is crucial for this instability result: for certain parameter combinations, one-dimensional spatially periodic patterns $(U_\mu(\xi), V_\mu(\xi))$ can certainly be stable [45]. In these cases, $\lambda_{\mathrm{pole}}(\mu, \hat{\ell})$ typically merges with another eigenvalue as $\hat{\ell} > 0$ decreases and forms a pair of complex conjugate eigenvalues that cross through the imaginary axis as $\hat{\ell}$ decreases further – see [103] for a much more detailed analysis of the spectral curves $\lambda(1, \ell)$ associated to the stability of a homoclinic stripe – i.e. the limit $\mu \downarrow 1$.

The instability result Theorem 3.3 establishes that all spatially periodic striped patterns in a certain region of the 1D Busse balloon near $\kappa = 0$ are unstable with respect to transverse perturbations that are spatially periodic in the y-direction (and provides an asymptotic approximation of the destabilizing wavenumbers). This is presented in the following corollary.

Corollary 3.2. *There are constants $D_{0,1}, D_{0,2} > 0$ such that for all $0 < D < D_{0,1}$, $0 < \epsilon\delta < \mathcal{D}_{0,2}\sqrt{D}$ striped patterns $(U_\mu(\xi), V_\mu(\xi))$ as established by Theorem 3.4 – either as solutions of (3.39) or (3.1) – are spectrally unstable.*

This result holds for $c = 0$, but by continuity of the spectrum the same holds for c close to 0. In the case $c \neq 0$ without reflection symmetry, the existence of spatially periodic stripes does not directly follow from the literature and requires a new approach. Both this issue and the associated stability question is considered in [167]. The instability result Theorem 3.3 will be influenced by the advection term c: we will see in Section 3.3.3 that for large c, 2D stable long wavelength striped patterns for (3.1) are found numerically.

3.3.3 Stability of striped patterns

We first briefly explain how numerical continuation is implemented to trace marginal stability of striped patterns of the extended Klausmeier model (3.1) against the various destabilization mechanisms. We recall that in 1D perturbations about a periodic solution are represented by functions with a γ-twisted periodicity property, where $\gamma \in S^1 \subset \mathbb{C}$ is on the unit circle.

By translation invariance of (3.1), for $\gamma = 1$ there is always a neutrally stable eigenvalue $\lambda(1) = 0$. Since $\mathrm{Re}(\lambda(\gamma))$ is invariant with respect to complex conjugation of γ, this leads to genericity of an instability where the curve of $\mathrm{Re}(\lambda)$ at $\lambda = 0$ changes from concave to convex. This destabilization mechanism is known as the Eckhaus or *sideband* instability, which is known to be the primary destabilization mechanism near supercritical Turing(-Hopf) bifurcations.

The sideband instability can be traced numerically using numerical continuation [42] by implementing the constraint $\frac{\partial^2}{\partial\gamma^2}\mathrm{Re}(\lambda(\gamma)) = 0$ at $\gamma = 1$ [147,199]. It has been found that the sideband instability forms the stability boundary far beyond onset of the Turing(-Hopf) instability [180,199].

The continuation of breakup instabilities of striped patterns against perturbations with $\gamma \in S^1$ and $\ell \in \mathbb{R}$ can be similarly implemented by imposing

constraints on $\lambda(\gamma, \ell)$. That is, $\mathrm{Re}(\lambda(\gamma, \ell)) = 0$ and $\frac{\partial}{\partial \ell} \mathrm{Re}(\lambda(\gamma, \ell)) = 0$ where ℓ is variable and $\gamma = 1$ (stripe-rectangle breakup) or $\gamma = -1$ (stripe-rhomb breakup). Here this is done for $2c = 0, 182.5, 365, 500, 1000$ (with $d = 500$, $m = 0.45$) to study the dependence of striped pattern stability on the advection c.

In addition, simulations with a slowly decreasing a are done for $2c = 0, 182.5, 365, 500$ (again with $d = 500$, $m = 0.45$) and a comparison is made. The small growth rates associated with the sideband instability can cause a significant delay in its onset [180]. Unpredictability in the outcome of the sideband instability stems from the fact that the growth rate of the perturbations that are among the first to destabilize remain small after destabilization compared to perturbations that destabilize later. In [180] it has been shown via simulations that for (3.1) in 1D with a slowly changing parameter, pattern adaptation depends on the rate of change and the application of noise. In this article we fix the rate of change to $da/dt = -10^{-5}$ and apply no noise. The simulations are done on a 250×250 square domain with periodic boundary conditions.

In Figure 3.8 the Busse balloon of stable striped patterns of (3.1) is plotted together with the sideband and transverse (breakup) instability curves, for $c = 0$ and $2c = 182.5$. Frame (a) is a more detailed version of Figure 3.1. The representation of a pattern by a wavenumber is not guaranteed to be 1:1. On the contrary, for $2c = 182.5$ a brown fold curve emerges from the lower red small amplitude curve, so that between this red curve and the fold curve a wavenumber corresponds to two patterns. But the solutions beyond the fold are all unstable, so that on the level of the Busse balloon of stable patterns the representation is 1:1. As soon as a curve crosses the fold the plotting style in the Figures 3.8, 3.12 and 3.13 changes to dashed to indicate that it has become less relevant.

For the case $2c = 182.5$ the primary destabilization mode for breakup changes from stripe-rhomb ($\gamma = -1$) to stripe-rectangle ($\gamma = 1$) at $a \approx 1.96$ (and back again near $a = 2.9$). A detailed study at $a \approx 1.96$ shows that $\gamma \neq \pm 1$ do not become the primary destabilization mechanism, see Figure 3.8(d). Checks elsewhere led to the same conclusion, which is the basis for tracing breakup only for $\gamma = \pm 1$.

For $c = 0$ striped patterns are seen in the simulation, but a single orientation is not always attained. In Figure 3.9 we show a simulation where this eventually is the case, because only then the breakup curves give a prediction for destabilization. In this case the stripes are expected to break up
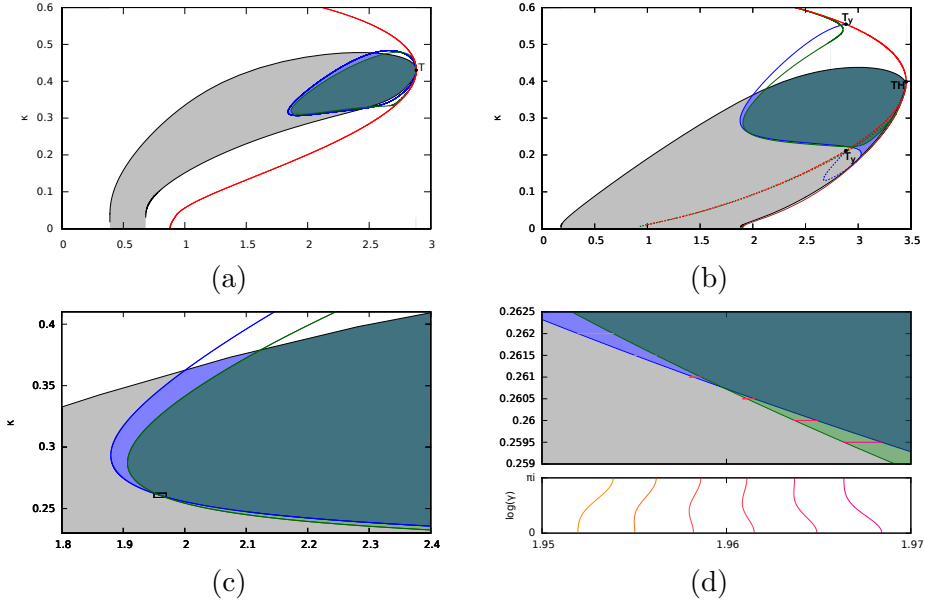
Figure 3.8: Stability of striped patterns of (3.1) with transverse destabilization mechanisms for $d = 500$, $m = 0.45$ and (a) $c = 0$ and (b) $2c = 182.5$, with Turing(-Hopf) bifurcation indicated by $T(H)$. The union of all colored regions bounded by the black sideband curve represents striped patterns that are 1D stable. The blue and green curve indicate marginal stability against stripe-rectangle and stripe-rhomb breakup respectively. Points that represent 1D stable patterns that are stable w.r.t. stripe-rectangle or stripe-rhomb breakup are colored blue resp. green. Full 2D stability is indicated by the dark-green (teal) combination of these colorings. Both ends of the blue curve connect to the anchor point T_y ($T = T_y$ for $c = 0$), see Section 3.2.2. (c) Part of the Busse balloon for $2c = 182.5$ showing that at $a \approx 1.96$ the stripe-rectangle and the stripe-rhomb instabilities interchange roles as primary destabilization mechanism. (d) Upper panel: magnification of region in (c) marked by the black rectangle. For selected values of κ, line segments show range of values of a at marginal stability for $\log(\gamma) \in [0, \pi\text{i}]$. Lower panel: γ-dependence of the line segments in the upper panel; values of γ other then $\gamma = \pm 1$ do not act as primary destabilization mechanism.

(a) $a = 2.9$ (b) $a = 2.8$ (c) $a = 2.75$ (d) $a = 2.74$ (e) $a = 2.69$
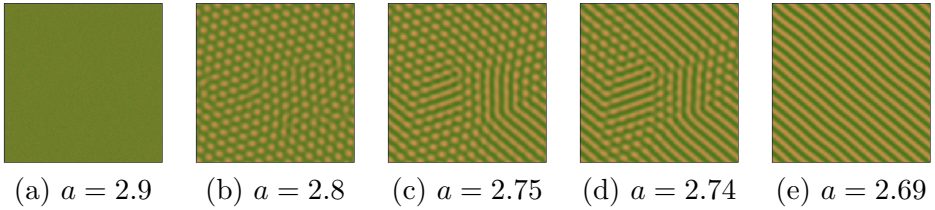
Figure 3.9: Frames from the simulation of (3.1) with slowly decreasing parameter a, $da/dt = -10^{-5}$, for $c = 0$ (with $d = 500$ and $m = 0.45$), gradient ranging from $n = 0$ (sandy-brown) to $n = 9.4$ (dark-green). (a) Initial condition, before Turing. (b) Pattern of gaps. (c)-(d) Gaps connect to form bare stripes, but orientation is space dependent. (e) Globally oriented striped pattern.

(a) $a = 2.15$ (b) $a = 2.14$ (c) $a = 2.1$ (d) $a = 2.09$ (e) $a = 2.06$
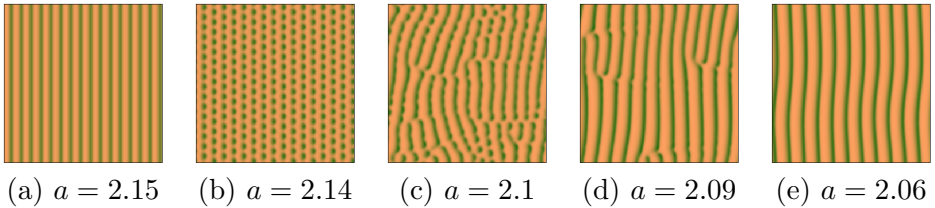
Figure 3.10: Frames from the simulation of (3.1) with slowly decreasing parameter a, $da/dt = -10^{-5}$, for $2c = 182.5$ (with $d = 500$ and $m = 0.45$), gradient ranging from $n = 0$ (sandy-brown) to $n = 17.8$ (dark-green). Striped pattern (a) breaks up into rhombs (b), but the spots reconnect (c) and form a striped pattern with defects (d) that disappear (e).

before hitting the sideband curve, see Figure 3.8(a).

When sideband and breakup curves get close, as is the case for the transition shown in Figure 3.10, interaction between the destabilization mechanisms is possible. As mentioned above the transition from one striped pattern to another through the sideband mechanism may suffer a significant delay. The modulations that arise from the sideband instability may trigger breakup before the stripe-to-stripe pattern transition has occurred [140]. On the other hand, even after the breakup of a striped pattern the system may still return to striped patterns later on, as illustrated by Figure 3.10. We note that the apparent instability of the rhombic pattern of spots in Figure 3.10(b) does not contradict the stability that was indicated in Figure 3.6, since there only perturbations that fit the small domain are included.

For $2c > 0$, striped patterns aligning perpendicular to the advection start to form just below the Turing-Hopf instability. During the decrease of a the system may encounter a sideband a few times first, before transverse instabilities take hold (Figure 3.11).
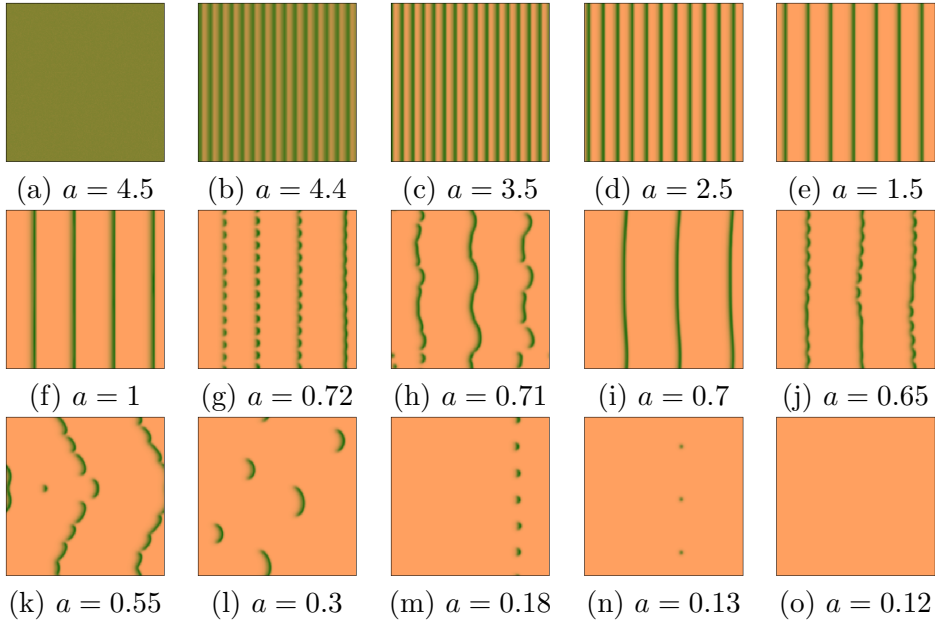
Figure 3.11: Frames from the simulation of (3.1) with slowly decreasing parameter a, $da/dt = -10^{-5}$, for $2c = 365$ (with $d = 500$ and $m = 0.45$), gradient ranging from $n = 0$ (sandy-brown) to $n = 21.45$ (dark-green). Initial condition just before the Turing-Hopf bifurcation (a) and striped pattern right after (b). (c)-(f) Consecutive striped patterns after destabilization by sideband. (g)-(i) Breakup, transient dynamics and return to striped pattern. (j)-(m) Breakup, dynamics in 2D, return to dashed stripe. (n) Transverse spatial period doubling. (o) Bare desert state.

(a) $c = 0$

(b) $2c = 182.5$

(c) $2c = 365$

(d) $2c = 500$
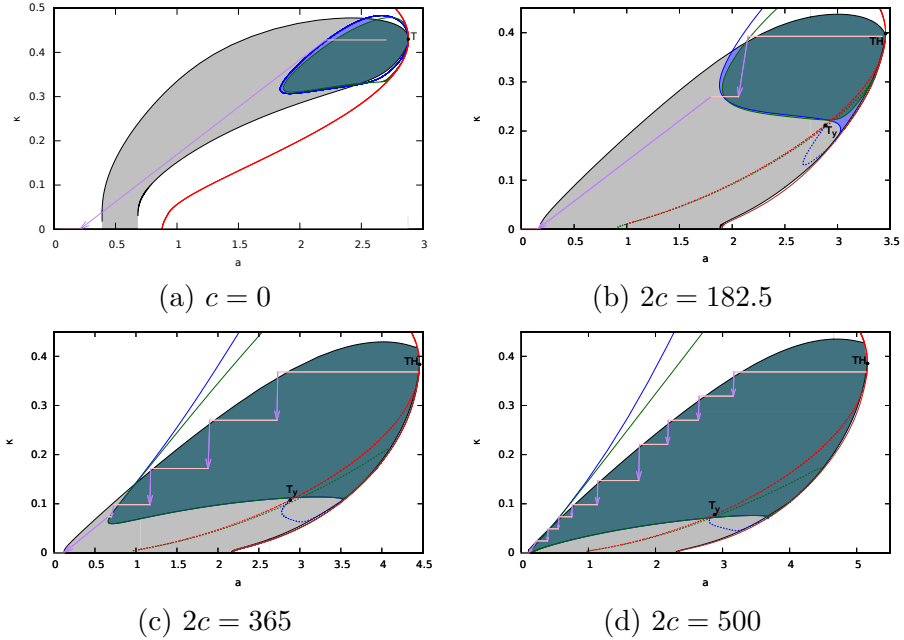
Figure 3.12: Stability of striped patterns of (3.1), see Figure 3.8 (a)-(b) for the meaning of the various colored curves and regions. Connection of the blue breakup curve to the upper anchor point T_y occurs outside the plotting range of κ. Simulations with slowly decreasing parameter a included, $da/dt = -10^{-5}$, the initial condition is a perturbation of the homogeneous state (w_+, n_+) at values of a just before the Turing(-Hopf) bifurcation. During the simulation the wavenumber is indicated with pink if the system resides in a striped pattern state, purple arrows in between indicate transient dynamics or residence in 2D states before returning to a striped pattern (or the bare desert state $\kappa = 0$).

When during a simulation the system resides in a striped pattern it can be represented by a single wavenumber. The plots of the wavenumbers are compared with knowledge of striped pattern stability for each of the values $2c = 0, 182.5, 365$ and 500 in Figure 3.12. The striped pattern destabilizations as observed in the simulations are in good agreement with the continuation results.

We see that in 2D, Hopf-type destabilization mechanisms that become primary destabilization mechanism in 1D for $\kappa \to 0$ (see [51]) are not relevant as long as c becomes not too large. Figure 3.12(d) shows that around $2c = 500$ the first long wavelength (small κ) striped patterns become 2D stable. By increasing c more and more, the transverse instabilities can be suppressed and the stability of striped patterns seems to reduce to the 1D stability of
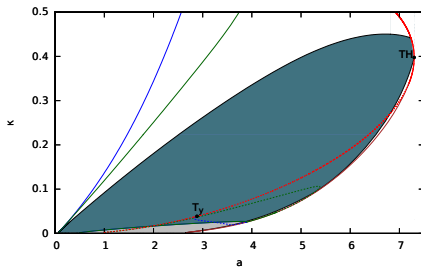
Figure 3.13: Analogue of Figure 3.8 (a)-(b) for $2c = 1000$.

patterns, see Figure 3.13 for the case $2c = 1000$. Simulations for such large values of c seem to require more sophisticated numerical techniques such as an operator splitting approach [209].

The above results show that by increasing the advection c, a larger portion of the 1D Busse balloon becomes 2D stable. We thus observe that for fixed κ, as c increases, the range in a where striped patterns are stable generally increases. So the magnitude of disturbance – measured in the amount of variance in a – that is allowed before a striped pattern wavenumber becomes unstable, increases as c increases. This confirms the result mentioned in the introduction that the ecological resilience of banded vegetation is larger on steeper slopes.

Within the choices of c made in this paper the case studied in Figure 3.8 (c)-(d) is the only instance where, within the 1D Busse balloon, stripe-rectangle destabilization occurs before stripe-rhomb destabilization. For larger values of c, represented by Figure 3.12 (c)-(d) and 3.13, the distance between the stripe-rectangle breakup and stripe-rhomb breakup curves becomes so small that they can (almost) no longer be distinguished. This can be formally understood by the observation that for large c, the destabilization occurs for relatively small values of the wavenumber κ. This implies that the spatially periodic patterns can be interpreted as being built from interacting localized patterns, which we expect to be of semi-strong type [48] by the singularly perturbed nature of the governing equations: here the interaction is to leading order restricted to the fastly diffusive water component. By arguments similar to those in Section 3.3.2 it can be expected that each family of γ-eigenvalues contracts to an asymptotically small region, so that indeed the $\gamma = 1$ stripe-rectangle destabilization and the $\gamma = -1$ stripe-rhomb destabilization curves become almost indistinguishable. Nevertheless, since pulses and spots in semi-strong interaction typically are repuls-

89

ing [25, 48, 184] one also expects the rhombic patterns to be eventually the most favorable, which suggests that stripe-rhomb breakup should precede stripe-rectangle breakup, even if both curves are very close to each other.

3.4 Ecological implications

The extended Klausmeier model (3.1) studied in this paper is a relatively simple scaled phenomenological model, we now turn abstract results into qualitative predictions for arid ecosystems that could be tested empirically. The results may also help in the understanding of more complex models. In this section we refer to striped patterns as banded vegetation. We refer to spots aligned in stripes, such as the rectangular and rhombic patterns, as dashed vegetation patterns [193, 202].

We recall from the introduction (result (1)) and the previous section the main numerical result: the ecological resilience of banded vegetation is larger on steep slopes, with large advection rates, than on gentle slopes. We supplement this by discussing some other implications for arid ecosystem dynamics.

Positive feedback in water-limited systems, as generated by the uptake mechanism of (3.1), is a key ingredient for self-organized vegetation pattern formation [97, 148, 202]. Here the state with uniform vegetation cover becomes unstable, because competition for water and a positive feedback between vegetation density and water harvesting capacity will create densely vegetated and more sparsely vegetated patches. Under influence of the slope the resulting patterns are vegetation bands aligned to contours [38, 193] as the Turing-Hopf instability is a natural mechanism for the formation of banded vegetation perpendicular to the slope (Theorem 3.2).

The competition for water and the uptake mechanism continue to play an important role in pattern adaptation as environmental stress due to decreasing rainfall a increases further. Competition for water between vegetation bands leads to stripe-to-stripe pattern transitions where some vegetation bands disappear and the wavenumber decreases, due to the sideband instability [180].

Competition for water within each vegetation band leads to breakup by transverse instabilities. Thus in some sense the same mechanisms that give rise to banded vegetation patterns are eventually responsible for their breakup. The selection of a rectangular or rhombic structure at breakup depends on the interaction between vegetation bands, as sketched at the end

of Section 3.3.3.

In Section 3.2.1 it was shown for models like (3.1) that vegetation bands move in uphill direction at onset. This movement is hard to establish or refute from observations, due to the small speeds that are involved. In [38], at three sites unequivocal photographical evidence of upslope migration has been presented, but in other cases it remains unclear. Soil characteristics not contained in (3.1), may be pivotal for the migration capability of vegetation patterns [58, 156].

In (3.1) we do not take into account possible mechanical action of (fast) flowing water on the strength and structure of the soil either. Particularly in case of dashed vegetation patterns – when downslope flowpaths become long – this could be an important factor, by creating erosion (e.g. gully formation) but also possibly deposition of soil. The validity of (3.1) may decrease if the slope parameter c increases, because these processes undermine the sheet flow of water that underpins (3.1). The problem of finding the correct value of c can be rather complicated, as mentioned in the introduction.

From Corollary 3.1 we know that the Turing-Hopf bifurcation locus moves to higher rainfall a as the slope c increases. Since at the Turing-Hopf bifurcation banded vegetation patterns form, it would be interesting to see if observations of banded vegetation under high rainfall regimes are linked to topographies that consist of relatively steep slopes. Observations reported in [12, 193] suggest that this may be the case.

We now turn to the numerics done in Section 3.3.3. In the simulations in the case of no slope ($c = 0$), vegetation bands still form although the orientation may (initially) be space-dependent, as in labyrinths. For gentle slopes labyrinths are observed instead of banded vegetation [12, 39]. For still relatively gentle slopes c, i.e. $2c \leq 182.5$ (original estimate by [97] for (3.1)), only a small portion of the 1D Busse balloon is 2D stable. In this case no banded vegetation is expected for either small wavenumber κ or small rainfall a, see Figure 3.8. This is in accordance with what is reported in [39]. Here at low rainfall, vegetation is mostly found not to be organized in a periodic pattern, or organized in a periodic pattern of spots. The kernel density that links to how frequent a banded vegetation pattern is observed as a function of the wavenumber κ, converges to zero well before $\kappa = 0$.

In the extended Klausmeier model (3.1) for $d > 0$, when decreasing the rainfall a, banded vegetation eventually breaks up into dashed patterns. This was suggested by [193] and was also found in [202]. The numerics we

performed show that only on very steep slopes the breakup of vegetation bands is avoided. The original Klausmeier model, where $d = 0$, has been extensively studied in [173] and the references therein. Here breakup does not occur [170]. This is due to the fact that competition is now restricted within upslope segments of constant y, as no water is flowing in the direction of the contour. Observations of dashed patterns support incorporating a more realistic mechanism for water flow, as is done in (3.1). Banded vegetation breakup was not reported in [207] either.

We showed that the shape of the Busse balloon strongly depends on landscape topography. Hence, linking real vegetation patterns to desertification thresholds requires inclusion of the particular landscape setting (i.e. the slope) in which the patterns are observed.

In this paper we refer to vegetation stripes as banded vegetation and separately identify dashed patterns. Dashed patterns are currently not treated as a separate class of patterns in observational studies and may be classified as banded vegetation instead [12, 35, 193]. We have shown that dashed vegetation patterns naturally arise from the breakup of vegetation stripes and signify a next step in the desertification process. Therefore a distinction between vegetation stripes and dashed patterns in the classification of vegetation patterns in observations could be considered valuable. Through observations it may be possible to see if dashed vegetation patterns are generally found at smaller rainfall a than banded vegetation. If this is the case, a restoration strategy based on dashed patterns instead of banded vegetation could in some cases be more successful, or equally successful but more economic [119]. These prediction could be tested empirically.

3.5 Acknowledgments

3.A Stability against large wavenumber perturbations

Lemma 3.4. *For large k, solutions to the dispersion relation (3.6) of (3.8) have $\mathrm{Re}(\lambda) < 0$.*

Proof. In the introduction, we prescribed after (3.2) that $d_1 \geq 0$ and $d_2 > 0$. If $d_1, d_2 > 0$ then the system (3.8) is characterized as being parabolic, which is well-known to imply stability against perturbations with large wavenumbers. Thus we only need to check for the case $d_1 = 0$. We first only use that either $d_1 = 0$ or $d_2 = 0$, so that $d_1 d_2 = 0$.

The dispersion relation (3.6) reads $d(\lambda, k, p, c) = \lambda^2 + \alpha_1 \lambda + \alpha_0 = 0$ where still $\alpha_1 = (d_1 + d_2)k^2 + O(1)$ but $\alpha_0 = \mathrm{i} c(d_1 - d_2)k^3 + (c^2 - d_1 a_4 - d_2 a_1)k^2 + O(k)$ since $d_1 d_2 = 0$, see (3.9). In order to find the solution branches for large k, we substitute an expansion $\lambda = k^2 \lambda_2 + k\lambda_1 + \lambda_0 + O(1/k)$ with $\lambda_j = O(1)$.

In case $\lambda_2 \neq 0$ we find, by comparing terms of order k^4, that $\lambda_2 = -(d_1 + d_2) < 0$, which yields a parabolic asymptotically stable branch.

In case $\lambda_2 = 0$ we find the second branch (hence all solution branches of the quadratic equation). By comparing terms of order k^3, we obtain

$$\lambda_1 = c \frac{d_2 - d_1}{d_1 + d_2} \mathrm{i}$$

which is purely imaginary. Stability is thus determined by λ_0, and comparing terms of order k^2 gives

$$\lambda_0 = \frac{(d_1 a_4 + d_2 a_1) - c^2 - \lambda_1^2}{d_1 + d_2}.$$

Now we use that $d_1 = 0$ so that $\lambda_1^2 = -c^2$ and $\lambda_0 = a_1 < 0$ by the inhibitor assumption from $A2$ in (3.4). So the homogeneous steady state is stable against large wavenumber perturbations. $\qquad\square$

Note that assuming $d_2 = 0$ instead of $d_1 = 0$ in the final step of the proof would lead to $\lambda_0 = a_4 > 0$ under assumption $A2$ in (3.4). Hence, the homogeneous steady state would be unstable against 'half' of the large wavenumber perturbations and we therefore assume $d_2 > 0$.

3.B Dispersion relations for striped patterns

In this appendix we briefly outline the characterization of the spectrum of striped patterns via Floquet-Bloch decomposition. This theory may be viewed as a substitute for the Fourier transform when dealing with periodic structures. Here it is equivalent to an Evans-function formulation using spatial dynamics, which we exploit in Section 3.3.2.

Let $(u_*, v_*)(t, x, y)$ denote a striped pattern of (3.2) that is L-periodic in x, so wavenumber $\kappa = 2\pi/L$, constant in y and travels with constant speed s. Its spectral stability is determined by the spectrum of the linear operator arising from the linearization of (3.2) in a comoving frame $\xi = x - st$ evaluated in (u_*, v_*). Applying a Fourier transform in the y-direction with wavenumber ℓ we obtain the differential operator with periodic coefficients

$$M(\partial_\xi, \xi) = \begin{pmatrix} d_1(\partial_\xi^2 - \ell^2) + (c_1 + s)\partial_\xi + a_1(\xi) & a_2(\xi) \\ a_3(\xi) & d_2(\partial_\xi^2 - \ell^2) + (c_2 + s)\partial_\xi + a_4(\xi) \end{pmatrix}$$

whose spectrum is the union of spectra of the Bloch-operators $M_{\mathrm{per}}(\gamma, \xi) := M(\partial_\xi - \log(\gamma)/L, \xi)$, with γ on the unit circle so $\log(\gamma) \in (-\pi\mathrm{i}, \pi\mathrm{i}]$, posed on $[0, 1]$ with periodic boundary conditions [147, 157]. Hence, the spectrum is determined by the family of eigenvalue problems $M_{\mathrm{per}}(\gamma, \xi) - \lambda \mathrm{Id} = 0$. The solutions $\lambda(\gamma)$ are referred to as γ-eigenvalues, see Section 3.3.2. Abstractly written, in terms of the period-map $\Phi(\lambda, \ell)$ of the evolution of this ODE for $\gamma = 1$, the expression

$$d(\lambda, \gamma, \ell) = \det\left(\Phi(\lambda, \ell) - \gamma\right), \tag{3.B.1}$$

is the dispersion relation analogous to the case of homogeneous steady states, which is holomorphic in λ, γ and ℓ. [147]

The cases that are traced by numerical continuation in Section 3.3.3 are $\gamma = \pm 1$, the corresponding eigenfunctions (perturbations) have distinct periodicity properties. We first restrict to $\ell = 0$, so perturbations $(\tilde{u}, \tilde{v})$ that are constant in the y-direction. Suppose that $(\tilde{u}, \tilde{v})(\xi)$ solves (3.B.1), then

$$\tilde{u}\left(\xi + \frac{2\pi}{\kappa}\right) = \gamma \tilde{u}(\xi) \tag{3.B.2}$$

and similarly for $\tilde{v}$.

From this it is clear that for $\gamma = 1$ the wavenumber of the perturbation is $\tilde{\kappa} = \kappa$. One of the perturbations corresponding to a solution of (3.B.1)

for $\gamma = 1$ is the translation mode with eigenvalue $\lambda = 0$. The solutions to (3.B.1) consist of curves of spectrum, where $\mathrm{Re}(\lambda)$ is invariant with respect to complex conjugation of γ, which leads to genericity of the aforementioned sideband instability where the curve of $\mathrm{Re}(\lambda)$ locally changes from concave to convex at $\lambda = 0$.

For $\gamma = -1$ it holds that $\tilde{\kappa} = \kappa/2$, so the perturbation has twice the wavelength of the underlying striped pattern. This links to spatial *period doubling* relevant in [180].

Perturbations of striped patterns with non-trivial y-dependence are represented by products of a perturbation in x and a perturbation in y, as treated in Section 3.3.1.

3.C No advection: existence of long wavelength patterns

The existence of stationary spatially periodic patterns for the scaled Gray-Scott model (3.43) in 1D follows directly from [45, Theorem 2.2] (which is itself based on [49, Theorem 4.2]).

Theorem 3.4. *There exist $\epsilon_0, \delta_0 > 0$ such that for every $0 < \epsilon < \epsilon_0$ and $0 < \delta < \epsilon\delta_0$, (3.43) has a family of stationary spatially periodic solutions $(U_\mu(\xi), V_\mu(\xi))$, parameterized by $\mu > 1$. Each periodic solution has a well-defined wavelength $\mathcal{T}(\mu)$ in the ξ-direction, at leading order given by*

$$\mathcal{T}(\mu) = \frac{2}{\epsilon\delta} \log \frac{\mu + 1}{\sqrt{\mu^2 - 1}}. \tag{3.C.1}$$

A periodic solution $(U_\mu(\xi), V_\mu(\xi))$ can be translated (in the ξ-direction) in such a way that it is symmetric w.r.t. $\xi = 0$ on a fundamental ξ-interval $[-\frac{1}{2}\mathcal{T}(\mu), \frac{1}{2}\mathcal{T}(\mu)]$. For such a solution, on a fast subinterval $\mathcal{I}_f = [-\frac{1}{\sqrt{\varepsilon}}, \frac{1}{\sqrt{\varepsilon}}] \subset [-\frac{1}{2}\mathcal{T}(\mu), \frac{1}{2}\mathcal{T}(\mu)]$, $U_\mu(\xi) \equiv 3\mu$ is constant while

$$V_\mu(\xi) = \frac{1}{2\mu}\mathrm{sech}^2\left(\frac{1}{2}\xi\right)$$

is the homoclinic solution of the fast reduced limit problem

$$V_{\xi\xi} - V + 3\mu V^2 = 0,$$

both up to corrections of $\mathcal{O}(\varepsilon)$. On the slow subintervals $[-\frac{1}{2}\mathcal{T}(\mu), \frac{1}{2}\mathcal{T}(\mu)]\backslash\mathcal{I}_f$, $V_\mu(\xi) \equiv 0$ up to exponentially small corrections, and $U_\mu(\xi)$ is at leading order given by a hyperbolic cosine solution of the slow reduced limit problem

$$U_{\xi\xi} - \varepsilon^2\delta^2 U + \varepsilon^3\delta = 0.$$

Note that the earlier versions of this theorem concern special cases of the present theorem, since the choices of parameters A, B, D from (3.39) are less general than here [45, 49]. This does however not influence the proof of the result that can be directly copied from [49]. Note also that the limit $\mu \downarrow 1$, i.e. $\mathcal{T}(\mu) \to \infty$, reproduces the existence of the well-known solitary homoclinic pulse solution of the Gray-Scott model, see [45, 49, 101–103] and the references therein. Of course the present result can be 'translated' directly into an existence result for periodic patterns in the original model (3.1), under the assumption on the parameters (a, m, d) of (3.1) that

$$\varepsilon = \frac{a}{m} < \varepsilon_0 \text{ and } \frac{\delta}{\varepsilon} = \frac{m\sqrt{m}}{a^2 d} < \delta_0 \qquad (3.\text{C}.2)$$

and (3.40), (3.44) hold for certain $\varepsilon_0, \delta_0 > 0$. We refrain from giving a fully detailed rewritten version of Theorem 3.4 in terms of (3.1).

Since existence result Theorem 3.4 only establishes the existence of long wave length spatially periodic patterns, the results obtained in this section are only valid for wave number κ small enough, i.e. in regions of the Busse balloon sufficiently close to the homoclinic limit $\kappa \to 0$.

The quantitative aspects of Theorem 3.4 may be used to analytically derive asymptotically accurate approximations of the right boundary of the Busse balloon near $\kappa = 0$, see Figure 3.1. This boundary has the character of a saddle-node bifurcation, and it is associated to the case in which ε becomes so large that the pulse self-replication mechanism is triggered, see [45, 199] and the references therein. It is in fact quite surprising that the present theory appears to be valid in Figure 3.1 where $a \approx 0.68$ at this boundary, which implies that $\varepsilon = \frac{a}{m} \approx 1.5$ for $m = 0.45$. Note that this agrees completely with the critical saddle-node/self-replication value of ε as can be deduced from [45], that was obtained by careful numerical experiments on the critical magnitude of ε for which the methods developed there – and used here – are valid.

3.D Proof of Theorem 3.3

We do not intend to present the proof of Theorem 3.3 (Section 3.3.2) in its full analytical detail: we will sketch the main ideas following the Evans function approach as developed in [46,47]. To facilitate the exposition we also impose another (formal) conditions on the relative magnitude of parameter D compared to the asymptotically small parameters ε and δ introduced in (3.44): $D \ll \epsilon^2$. Thus, we assume throughout this proof that,

$$\epsilon^2 \delta^2 \ll D \ll \epsilon^2 \ll 1. \tag{3.D.1}$$

This additional condition is not essential to the validity of the instability result.

Since $V_\mu(\xi)$ is exponentially small outside the fast region $\mathcal{I}_f$ (Theorem 3.4), it immediately follows that the matrix $\mathcal{A}_\mu(\xi; \lambda, \hat{\ell})$ is exponentially close to the constant coefficient limit

$$\mathcal{A}_\mu^\infty(\lambda, \hat{\ell}) = \lim_{\xi \to \pm\infty} \mathcal{A}_\mu(\xi; \lambda, \hat{\ell}) = \begin{pmatrix} 0 & \varepsilon & 0 & 0 \\ \frac{D}{\varepsilon}(\hat{\ell}^2 + \lambda) - \varepsilon\delta^2 & 0 & 0 & 0 \\ 0 & 0 & 0 & 1 \\ 0 & 0 & 1 + \lambda + D\hat{\ell}^2 & 0 \end{pmatrix} \tag{3.D.2}$$

outside $\mathcal{I}_f$. Note that in a rigorous framework, the limit $\xi \to \pm\infty$ should be replaced by $\xi \to \pm\frac{1}{2}\mathcal{T}(\mu)$ – which will not have a leading order effect on the outcome of the analysis (as discussed briefly in Section 3.3.2). This matrix has eigenvalues $\mathrm{Re}\left(\Lambda_{\mu,1}(\lambda, \hat{\ell})\right) > \mathrm{Re}\left(\Lambda_{\mu,2}(\lambda, \hat{\ell})\right) > \mathrm{Re}\left(\Lambda_{\mu,3}(\lambda, \hat{\ell})\right) > \mathrm{Re}\left(\Lambda_{\mu,4}(\lambda, \hat{\ell})\right)$,

$$\begin{aligned} \Lambda_{\mu,1,4}(\lambda, \hat{\ell}) &= \pm\sqrt{1 + \lambda + D\hat{\ell}^2} &= \pm\sqrt{1 + \lambda} + \mathcal{O}(D), \\ \Lambda_{\mu,2,3}(\lambda, \hat{\ell}) &= \pm\sqrt{D}\sqrt{\lambda + \hat{\ell}^2 - \frac{\varepsilon^2\delta^2}{D}} &= \pm\sqrt{D}\sqrt{\lambda + \hat{\ell}^2} + \mathcal{O}(\frac{\varepsilon^2\delta^2}{D}), \end{aligned} \tag{3.D.3}$$

under the assumptions in (3.D.1) and for $\hat{\ell}, |\lambda| = \mathcal{O}(1)$, and associated eigenvectors

$$\begin{aligned} E_{\mu,1,4}\left(\lambda, \hat{\ell}\right) &= \left(0, 0, 1, \pm\sqrt{1 + \lambda} + \mathcal{O}(D)\right) \\ E_{\mu,2,3}\left(\lambda, \hat{\ell}\right) &= \left(1, \pm\sqrt{D}\sqrt{\lambda + \hat{\ell}^2} + \mathcal{O}\left(\frac{\varepsilon^2\delta^2}{D}\right), 0, 0\right). \end{aligned} \tag{3.D.4}$$

By the theory developed in [46,47], linear system (3.48) has 4 independent

solutions $\phi_{\mu,j}(\xi; \lambda, \hat{\ell})$, such that

$$
\begin{aligned}
\lim_{\xi \to -\infty} \phi_{\mu,j}\left(\xi; \lambda, \hat{\ell}\right) e^{-\Lambda_{\mu,j}(\lambda,\hat{\ell})\xi} &= E_{\mu,j}\left(\lambda, \hat{\ell}\right), j = 1, 2 \\
\lim_{\xi \to \infty} \phi_{\mu,j}\left(\xi; \lambda, \hat{\ell}\right) e^{-\Lambda_{\mu,j}(\lambda,\hat{\ell})\xi} &= E_{\mu,j}\left(\lambda, \hat{\ell}\right), j = 3, 4.
\end{aligned}
\tag{3.D.5}
$$

This especially implies

$$
\lim_{\xi \to -\infty} \phi_{\mu,1,2}(\xi; \lambda, \hat{\ell}) = (0, 0, 0, 0) \text{ and } \lim_{\xi \to \infty} \phi_{\mu,3,4}(\xi; \lambda, \hat{\ell}) = (0, 0, 0, 0);
$$

(3.D.5) determines $\phi_{\mu,1,2}(\xi; \lambda, \hat{\ell}) = 0$ uniquely, and since $\mathcal{A}_\mu(\xi; \lambda, \hat{\ell})$ is exponentially close to $\mathcal{A}_\mu^\infty(\lambda, \hat{\ell})$, the *fast transmission function* $t_{\mu,f}(\lambda, \hat{\ell}) : \mathbb{C} \times \mathbb{R} \to \mathbb{C}$ can be defined by

$$
\lim_{\xi \to \infty} \phi_{\mu,1}\left(\xi; \lambda, \hat{\ell}\right) e^{-\Lambda_{\mu,1}(\lambda,\hat{\ell})\xi} = t_{\mu,f}\left(\lambda, \hat{\ell}\right) E_{\mu,1}\left(\lambda, \hat{\ell}\right), \tag{3.D.6}
$$

where for any given $\mu > 1$ and $\hat{\ell} \in \mathbb{R}$, $t_{\mu,f}(\lambda, \hat{\ell})$ is analytic as a function of λ. [46, 47]

As a direct application of the methods of [46, 47], it can also be shown that for $\lambda, \hat{\ell}$ such that $t_{\mu,f}(\lambda, \hat{\ell}) \neq 0$, there is a uniquely determined function $\phi_{\mu,2}(\xi; \lambda, \hat{\ell})$ for which

$$
\lim_{\xi \to \infty} \phi_{\mu,2}\left(\xi; \lambda, \hat{\ell}\right) e^{-\Lambda_{\mu,1}(\lambda,\hat{\ell})\xi} = (0, 0, 0, 0), \tag{3.D.7}
$$

i.e. there is a unique $\phi_{\mu,2}(\xi; \lambda, \hat{\ell})$ that does not grow with the fast rate $\Lambda_{\mu,1}(\lambda, \hat{\ell})$ beyond the fast interval $\mathcal{I}_f$. As a consequence, the *slow transmission function* $t_{\mu,s}(\lambda, \hat{\ell})$ can be defined by

$$
\lim_{\xi \to \infty} \phi_{\mu,2}\left(\xi; \lambda, \hat{\ell}\right) e^{-\Lambda_{\mu,2}(\lambda,\hat{\ell})\xi} = t_{\mu,s}\left(\lambda, \hat{\ell}\right) E_{\mu,2}\left(\lambda, \hat{\ell}\right), \tag{3.D.8}
$$

under the assumption that $t_{\mu,f}(\lambda, \hat{\ell}) \neq 0$.

For this choice of solutions $\phi_{\mu,j}(\xi; \lambda, \hat{\ell})$ of (3.48), we once again follow [46, 47] and define the Evans function $\mathcal{D}_\mu(\lambda, \hat{\ell})$ by

$$
\mathcal{D}_\mu\left(\lambda, \hat{\ell}\right) = \det\left[\phi_{\mu,1}\left(\xi; \lambda, \hat{\ell}\right), \phi_{\mu,2}\left(\xi; \lambda, \hat{\ell}\right), \phi_{\mu,3}\left(\xi; \lambda, \hat{\ell}\right), \phi_{\mu,4}\left(\xi; \lambda, \hat{\ell}\right)\right].
$$
$$\tag{3.D.9}$$

Note that this definition is only valid for λ not in the essential spectrum associated to (3.48) – again seen as being defined on all of $\mathbb{R}$ (instead of

on $[-\frac{1}{2}\mathcal{T}(\mu), \frac{1}{2}\mathcal{T}(\mu)]$), so that the essential spectrum coincides with all $\lambda = \lambda(\hat{\ell}) \in \mathbb{C}$ for which $\mathcal{A}_\mu^\infty(\lambda, \hat{\ell})$ has an eigenvalue $\Lambda_{\mu,j}(\lambda, \hat{\ell}) \in i\mathbb{R}$. Since the trace $\mathrm{tr}\left(\mathcal{A}_\mu(\xi; \lambda, \hat{\ell})\right) = 0$ (see (3.49)), $\mathcal{D}_\mu(\lambda, \hat{\ell})$ does not depend on ξ and $\sum_{i=j}^{4} \Lambda_{\mu,j}(\lambda, \hat{\ell}) \equiv 0$, therefore

$$
\begin{aligned}
\mathcal{D}_\mu\left(\lambda, \hat{\ell}\right) &= \lim_{\xi \to \infty} \det\left[\phi_{\mu,1}\left(\xi; \lambda, \hat{\ell}\right), \phi_{\mu,2}\left(\xi; \lambda, \hat{\ell}\right), \phi_{\mu,3}\left(\xi; \lambda, \hat{\ell}\right), \phi_{\mu,4}\left(\xi; \lambda, \hat{\ell}\right)\right] \\
&= \lim_{\xi \to \infty} \det\left[\phi_{\mu,1}(\xi) e^{-\Lambda_{\mu,1}\xi}, \phi_{\mu,2}(\xi) e^{-\Lambda_{\mu,2}\xi}, \phi_{\mu,3}(\xi) e^{-\Lambda_{\mu,3}\xi}, \phi_{\mu,4}(\xi) e^{-\Lambda_{\mu,4}\xi}\right] \\
&= \det\left[t_{\mu,f}(\lambda, \varepsilon) E_{\mu,1}(\lambda, \varepsilon), t_{\mu,s}(\lambda, \varepsilon) E_{\mu,2}(\lambda, \varepsilon), E_{\mu,3}(\lambda, \varepsilon), E_{\mu,4}(\lambda, \varepsilon)\right] \\
&= 4\sqrt{D} t_{\mu,f}\left(\lambda, \hat{\ell}\right) t_{\mu,s}\left(\lambda, \hat{\ell}\right) \sqrt{(1+\lambda)\left(\lambda + \hat{\ell}^2\right)}, \quad (3.D.10)
\end{aligned}
$$

at leading order by (3.D.3), (3.D.4), (3.D.5), (3.D.6) and (3.D.8).

For any given $\mu > 1$ and $\hat{\ell} \in \mathbb{R}$, the zeroes of $\mathcal{D}_\mu(\lambda, \hat{\ell})$ coincide (at leading order) with the eigenvalues of (3.48), counting multiplicities [46, 47]. Moreover, under the assumptions in (3.D.1) and for $\hat{\ell} = \mathcal{O}(1)$, it follows by [46, 47] that the zeroes $\lambda_{\mu,f,j}$ of the fast component $t_{\mu,f}(\lambda, \hat{\ell})$ of the decomposition of the Evans function $\mathcal{D}_\mu(\lambda, \hat{\ell})$ (see (3.D.10)) are at leading order given by the eigenvalues

$$
\lambda_{\mu,f,0} = \frac{5}{4}, \ \lambda_{\mu,f,1} = 0, \ \lambda_{\mu,f,2} = -\frac{3}{4}, \quad (3.D.11)
$$

of the fast reduced stability problem

$$
(\mathcal{L}_f - \lambda)v = v_{\xi\xi} + \left[3\mathrm{sech}^2\frac{1}{2}\xi - (1 + \lambda)\right]v = 0, \quad (3.D.12)
$$

that can be obtained from the v-equation in (3.47) by using the leading order approximations of $U_\mu(x)$ and $V_\mu(\xi)$ in $\mathcal{I}_f$ (Theorem 3.4), and setting $u \equiv 0$ – which is natural by (3.D.6), (3.D.4) and the fact that $\phi_{\mu,1}(\xi; \lambda, \hat{\ell})$ does not have any leading order slow components for $\xi < 0$.

Since $t_{\mu,s}(\lambda, \hat{\ell})$ is meromorphic and has a pole at $\lambda_{\mu,f,0}$ – as we will show below – this result does not establish the instability of $(U_\mu(\xi), V_\mu(\xi))$. In fact, this zero-pole cancellation mechanism is called 'the resolution of the NLEP paradox'. [46, 47]

Beyond the fast interval $\mathcal{I}_f$, $\phi_{\mu,2}(\xi; \lambda, \hat{\ell})$ is – up to exponentially small corrections – a solution of the constant coefficient problem $\dot{\phi} = \mathcal{A}_\mu^\infty(\lambda, \hat{\ell})\phi$ that does not have a fast growing component associated to $\Lambda_{\mu,1}(\lambda, \hat{\ell})$ and

$E_{\mu,1}(\lambda,\hat{\ell})$ – see (3.D.7). Therefore, $\phi_{\mu,2}(\xi;\lambda,\hat{\ell})$ is for $\xi > 0$ approximated by

$$\phi_{\mu,2}(\xi;\lambda,\hat{\ell}) = t_{\mu,s}(\lambda,\hat{\ell})e^{\Lambda_{\mu,2}(\lambda,\hat{\ell})\xi}E_{\mu,2}(\lambda,\hat{\ell}) + \tilde{t}_{\mu,s}(\lambda,\hat{\ell})e^{\Lambda_{\mu,3}(\lambda,\hat{\ell})\xi}E_{\mu,3}(\lambda,\hat{\ell}),$$
$$(3.D.13)$$

where $\tilde{t}_{\mu,s}(\lambda,\hat{\ell})$ is a second slow transmission function that measures the slow decay of $\phi_{\mu,2}(\xi;\lambda,\hat{\ell})$ beyond $\mathcal{I}_f$ – see also (3.D.8). By construction, $\phi_{\mu,2}(\xi;\lambda,\hat{\ell})$ is for $\xi < 0$ outside $\mathcal{I}_f$ approximated by

$$\phi_{\mu,2}(\xi;\lambda,\hat{\ell}) = e^{\Lambda_{\mu,2}(\lambda,\hat{\ell})\xi}E_{\mu,2}(\lambda,\hat{\ell}) \qquad (3.D.14)$$

by (3.D.5).

Under the assumptions (3.D.1), it follows by (3.47) that the u-component of a solution $\phi(\xi)$ of (3.48) remains constant at leading order in the fast region $\mathcal{I}_f$, which implies by combining (3.D.13), (3.D.14) and (3.D.4) that

$$t_{\mu,s}(\lambda,\hat{\ell}) + \tilde{t}_{\mu,s}(\lambda,\hat{\ell}) = 1 \qquad (3.D.15)$$

at leading order. On the other hand, a similar comparison between (3.D.14) for $\xi < 0$ and (3.D.13) for $\xi > 0$ implies that the passage of $\phi_{\mu,2}(\xi;\lambda,\hat{\ell})$ over $\mathcal{I}_f$ must have a net effect on the p-component $p_{\mu,2}(\xi;\lambda,\hat{\ell})$ of $\phi_{\mu,2}(\xi;\lambda,\hat{\ell})$ at leading order given by

$$\Delta_s p_{\mu,2} = \lim_{\xi\downarrow\frac{1}{\sqrt{\varepsilon}}} p_{\mu,2}(\xi;\lambda,\hat{\ell}) - \lim_{\xi\uparrow\frac{-1}{\sqrt{\varepsilon}}} p_{\mu,2}(\xi;\lambda,\hat{\ell})$$
$$= \frac{\sqrt{D}}{\varepsilon}\left((t_{\mu,s}(\lambda,\hat{\ell})\sqrt{\lambda+\hat{\ell}^2} - \tilde{t}_{\mu,s}(\lambda,\hat{\ell})\sqrt{\lambda+\hat{\ell}^2}) - \sqrt{\lambda+\hat{\ell}^2}\right)$$
$$(3.D.16)$$
$$= -2\frac{\sqrt{D}}{\varepsilon}\left(1 - t_{\mu,s}(\lambda,\hat{\ell})\right)\sqrt{\lambda+\hat{\ell}^2}$$

by (3.D.15).

The net effect originates from the total change over $p_{\mu,2}(\xi;\lambda,\hat{\ell})$ in $\mathcal{I}_f$, which is by (3.48) and the explicit approximations of Theorem 3.4 given by

$$\Delta_f p_{\mu,2} = \int_{-\frac{1}{\sqrt{\varepsilon}}}^{\frac{1}{\sqrt{\varepsilon}}} p(\xi)\,d\xi$$
$$= \varepsilon \int_{-\infty}^{\infty}\left(V_\mu^2(\xi)u + 2U_\mu(\xi)V_\mu(\xi)v\right)\,d\xi \qquad (3.D.17)$$
$$= \varepsilon \int_{-\infty}^{\infty}\left(\frac{1}{4\mu^2}\operatorname{sech}^4\tfrac{1}{2}\xi + 3v_{in,\mu}(\xi;\lambda)\operatorname{sech}^2\tfrac{1}{2}\xi\right)\,d\xi$$

at leading order, by (3.D.1). Here we have used that the u-component of $\phi_{\mu,2}(\xi; \lambda, \hat{\ell})$ is at leading order constant and equal to 1 in $\mathcal{I}_f$ and $v_{in,\mu}(\xi; \lambda)$ is defined as the unique, bounded (even) solution of

$$v_{\xi\xi} + \left[3\operatorname{sech}^2 \frac{1}{2}\xi - (1 + \lambda) \right] v = -\frac{1}{4\mu^2} \operatorname{sech}^4 \frac{1}{2}\xi, \qquad (3.D.18)$$

i.e.

$$v_{in,\mu}(\xi; \lambda) = (\mathcal{L}_f - \lambda)^{-1} \left(-\frac{1}{4\mu^2} \operatorname{sech}^4 \frac{1}{2}\xi \right) \qquad (3.D.19)$$

by (3.D.12), the leading order approximation of the fast v-equation of (3.47) – that at leading order decouples from the system.

Combining (3.D.16) and (3.D.17) yields an explicit expression for the slow component of the decomposition of the Evans function $\mathcal{D}_\mu(\lambda, \hat{\ell})$ (see (3.D.10))

$$t_{\mu,s}(\lambda, \hat{\ell}) = 1 + \frac{\varepsilon^2}{2\sqrt{D}\sqrt{\lambda + \hat{\ell}^2}} \left[\frac{2}{3\mu^2} + 3 \int_{-\infty}^{\infty} v_{in,\mu}(\xi; \lambda) \operatorname{sech}^2 \frac{1}{2}\xi \, d\xi \right] \quad (3.D.20)$$

at leading order. Note that it immediately follows from the definition (3.D.19) of $v_{in,\mu}(\xi; \lambda)$ that $t_{\mu,s}(\lambda, \hat{\ell})$ has (simple) poles at the zeroes $\lambda_{\mu,f,0}$ and $\lambda_{\mu,f,2}$ of $t_{\mu,f}(\lambda, \hat{\ell})$, i.e. at the even eigenvalues (3.D.11) of $\mathcal{L}_f$. Hence these eigenvalues do not correspond to zeroes of $\mathcal{D}_\mu(\lambda, \hat{\ell})$ and thus not to spectrum associated to the stability of $U_\mu(\xi), V_\mu(\xi)$. (Since the eigenfunction of (3.D.12) associated to $\lambda_{\mu,f,1} = 0$ is odd and the right-hand side of (3.D.18) even as function of ξ, $\lambda_{\mu,f,1} = 0$ does persist as eigenvalue of (3.48), see [46,47]). An (eigenvalue, eigenfunction) pair of (3.48) is obtained by setting $t_{\mu,s}(\lambda, \hat{\ell}) = 0$ – in which case $\phi_{\mu,2}(\xi; \lambda, \hat{\ell})$ decays in both limits $\xi \to \pm\infty$ (see (3.D.13) and (3.D.14)) – i.e. by solving,

$$-2\sqrt{\lambda + \hat{\ell}^2} = \frac{\varepsilon^2}{2\sqrt{D}} \left[\frac{2}{3\mu^2} + 3 \int_{-\infty}^{\infty} v_{in,\mu}(\xi; \lambda) \operatorname{sech}^2 \frac{1}{2}\xi \, d\xi \right], \qquad (3.D.21)$$

Since the right-hand side has a simple pole near $\lambda_{\mu,f,0} = \frac{5}{4}$ it immediately follows that there must be a solution of (3.D.21) near $\lambda = \frac{5}{4}$ if $\frac{\varepsilon^2}{\sqrt{D}}$ is small enough compared to the left-hand side of (3.D.21). Note that, this expands and confirms the arguments in [45] about the instability of spatially periodic patterns by setting $\hat{\ell} = 0$ (in the more special scaling there).

In the one-dimensional $\hat{\ell} = 0$ setting, the patterns $(U_\mu(\xi), V_\mu(\xi))$ may become stable as $\frac{\varepsilon^2}{\sqrt{D}}$ grows in magnitude, i.e. becomes $\mathcal{O}(1)$ – as is shown

in [45]. This mechanism is counteracted in the present two-dimensional setting by the appearance of $\hat{\ell}^2$ in the left-hand side of (3.D.21): if $\hat{\ell}$ is such that $\sqrt{\lambda + \hat{\ell}^2}$ is large enough compared to $\frac{\varepsilon^2}{\sqrt{D}}$, the above argument can still be applied, leading to the zeroes $\lambda_{\mathrm{pole}}(\mu, \hat{\ell})$ as in Theorem 3.3 for $\hat{\ell}$ large enough and not too close to 0 – as in the statement of Theorem 3.3.

In the above derivation procedure it is assumed that $D\hat{\ell}^2$ is small enough: it has been neglected as a higher order effect in the reduction of the fast v-equation of (3.47) to (3.D.18). This implies that the left-hand side of (3.D.21) may grow to size $\frac{L}{\sqrt{D}}$ for L small enough (but a priori not beyond that). Comparing this to the magnitude of the right-hand side – that is of order $\frac{\varepsilon^2}{\sqrt{D}}$ – implies that the instability argument can be applied as long as ε is small enough – which also is the assumption under which the existence of the spatially periodic stripes has been established in Theorem 3.4. $\qquad\square$

4 Effects of nonlocal grazing on dryland vegetation patterns

4.1 Introduction

Environmental stress, e.g. due to climate change or increased grazing, drives desertification. Annual mean precipitation is likely to decrease in many arid and semi-arid regions [87]. Contrary to climate change, grazing can in principle be managed locally and directly, which creates the opportunity to intervene. Timely measures that decrease the grazing pressure on ecosystems may help prevent regime shifts to a degraded bare desert state [149,163]. For this, expanding the understanding of grazing systems would be very useful.

A complexifying property of drylands is that spatially periodic vegetation patterns may emerge, even though the abiotic environment is (approximately) spatially homogeneous. The widespread occurrence of periodic vegetation patterns has been confirmed at the interface between arid and semi-arid regions [36]. A widely accepted pattern forming mechanism is the increased infiltration at vegetated soil (short range facilitation), in combination with overland redistribution of water during rain showers to the vegetated patches, where the soil conditions favor water infiltration (long range competition) [150]. This mechanism is present in many spatially extended arid ecosystem models, see e.g. [70, 79, 97, 148, 156].

Figure 4.1 shows a simulation of the desertification process in one space dimension x for one of these models, the extended Klausmeier model [97,180].[1] For large values of the rainfall a, the system resides in a stable homogeneously vegetated state. As rainfall decreases to a value below $a = 3$, the homogeneous state becomes Turing unstable [190]. A vegetation pattern forms with a certain wavelength, which remains the same for a range of a. Then a cascade of transitions to patterns with larger and larger wavelengths follows [180]. Finally, the system transitions from a large wavelength pattern

---

[1]With [180] corresponding to Chapter 2.
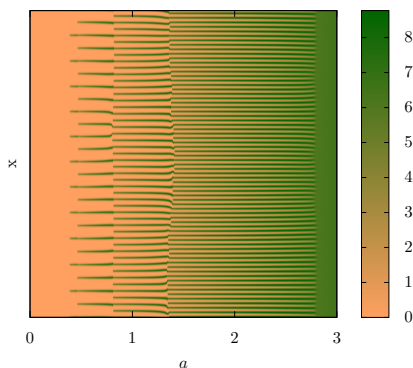
Figure 4.1: Desertification process driven by decreasing rainfall a ($\frac{da}{dt} = -10^{-4}$) in the absence of grazing, starting with a spatially homogeneous vegetation at $a = 3$, showing the evolution of the distribution of vegetation in a single space dimension x. The simulation is based on the extended Klausmeier model, see Section 4.5 for further details.

to the bare desert state and the desertification process is completed. This final transition is in accordance with (an extension of) one of Ni's conjectures [133]: the last patterns to destabilize have large wavelengths.

We aim to study the influence of grazing on this desertification process: on the pattern formation, pattern adaptation and the final transition to a bare desert state.

The most common way of incorporating senescence of vegetation n, in reaction-diffusion type arid ecosystem modeling, is by including a linear death term $-mn$, with m a constant parameter, see [70, 79, 97, 125, 135, 148, 156, 175, 202] among others. Occurrence of grazing has been viewed as included in the term $-mn$ [70, 125, 202], through a higher value of the coefficient m [156]. Here we analyze a refinement to this modeling by taking into account the nonlocal coupling grazing asserts on the vegetation [196]: the availability of (superior) forage elsewhere decreases foraging at a given location.

In Section 4.2 we account for the nonlocal coupling asserted by the grazing by combining the concepts of ideal free distribution [65], functional and numerical response [80, 181]. For this, plant death mn is split into the usual local linear term m_0n (non-grazing related senescence) and a nonlocal coupling for modeling grazing:

$$mn = m_0n + \text{grazing}. \tag{4.1}$$

The grazing at any location will depend on the overall distribution of the vegetation. For this we assume that herbivore dynamics is fast compared to biomass evolution.

The ideal free distribution [65] is used to determine the spatial distribution of herbivores, which means that herbivores spread out such that the suitability of all locations is the same. There have been recent studies on (individual) herbivore foraging behavior in heterogeneous environments, see e.g. [31,66] and the references therein, which extend this by also taking into account finite animal movement speed and incomplete knowledge of the resource distribution. We note that on the population level, all individual herbivores only need to comply with the ideal free distribution locally to enforce an ideal free distribution globally. We introduce a parameter j that models the preference of herbivores for the more vegetated locations.

The functional and numerical response [80,181] of herbivores on available forage will be determined under simple assumptions both in the context of *sustained* grazing and *natural* grazing. In a system with sustained grazing we assume that the number of herbivores is kept constant, by always supplying supplementary food if necessary. For natural grazing we assume that supplementary food is never provided, so that herbivores need to completely sustain themselves. These cases are two extremes.

Section 4.3 incorporates the derived grazing terms in the two-component (surface water, plant biomass) extended Klausmeier model. This model has been used to study the desertification process driven by decreasing rainfall a both in one space dimension [180] and in two space dimensions [176][2], but in the absence of nonlocal coupling caused by grazing.

We restrict attention to sustained grazing with $j = 2$ and natural grazing with $j = 1$. These choices will allow for a direct comparison with the case without grazing, because the dependence on grazing of the homogeneously vegetated states themselves can in these cases be absorbed by the rainfall parameter.

In Section 4.4 we perform a linear stability analysis about the homogeneous steady state from where the desertification process starts, for the specific choices of grazing.

We show that for sufficiently severe sustained grazing with $j = 2$, the ho-

---

[2]With [176] corresponding to Chapter 3.

mogeneous steady state is destabilized by a Hopf instability before patterns form (at the Turing instability), which is in line with Result 1 below. In this case complete desertification is immediate and vegetation patterns are omitted. For natural grazing with $j = 1$ this is not the case: the homogeneous steady state generally becomes more susceptible to Turing instability as grazing becomes more severe.

Section 4.5 presents simulations for the same specific choices of grazing as in the previous section, all with decreasing rainfall as in Figure 4.1. For sustained grazing with $j = 2$ we perform a sequence of simulations with larger and larger numbers of herbivores, which increases the grazing pressure on all vegetation distributions proportionally. Not only do these simulations show that vegetation patterns can be suppressed (Result 1 below), but also that in the desertification process the large wavelength patterns are skipped (Result 2 below). For natural grazing with $j = 1$, the influence of increasing the grazing pressure on all vegetation distributions proportionally is studied with simulations. For this case we also vary herbivore persistence, which is herbivore ability to survive at low levels of available forage. The simulations show jumps from high to low forage states that become more dramatic if natural grazing is set to be more severe (Result 3 below).

Concerning grazing in the extended Klausmeier model, we have the following main results:

1. A strong preference of herbivores for locations with large available forage ($j > 1$) may suppress vegetation patterns altogether (as a manifestation of the tall poppy syndrome, Corollary 4.1 & Figure 4.6(d));

2. Sustained grazing impedes the existence of large wavelength patterns, causing a violation of Ni's conjecture (Figure 4.6, see also Section 4.6.1);

3. Natural grazing may create a dichotomy of high forage and low forage system states, with large respectively small numbers of herbivores. (Figure 4.8).

All these results likely hold for implementations of the derived grazing terms in other arid ecosystem models, as we discuss at the end of Section 4.2.

Result 1 has profound consequences for the desertification process, since in this case vegetation patterning will not always precede the transition to the bare desert state, so vegetation patterns are not an early warning signal

for complete land degradation. Result 2 means that, in case of a coarsening cascade of vegetation patterns, the penultimate state in the desertification process need not have a long wavelength; together with Result 3 it implies that

4. both sustained and natural grazing open up the possibility of a dramatic sudden regime shift [149, 163].

For sustained grazing the shift will be towards the bare desert state [196]. For natural grazing the regime shift will result in a low forage state.

We conclude that the proposed grazing model refinements dramatically alter the desertification process, but this alteration depends strongly on what model refinement is implemented.

Remark 4.1. *In this chapter we use as a domain a one-dimensional bounded interval with length L, though all ideas can be transported to two-dimensional or unbounded domains (by using an integration kernel for the grazing terms). As patterns in one space dimension correspond to banded vegetation in two space dimensions, we will refer to parts of the domain as areas.*

4.2 Modeling of grazing

In this section we develop nonlocal terms to model grazing. Modeling assumptions lead to Holling type II (sustained) and type III (natural) grazing response functions [80]. We model grazing by dissecting it in three parts and determining each part separately, as follows:

$$\text{grazing} = \text{spatial distribution} \times \text{functional response} \times \text{numerical response}$$
(4.2)

where we distinguish

- spatial distribution: spatial probability distribution of a single herbivore as a function of the distribution of the vegetation, assuming an ideal free distribution [65],
- functional response [80,181]: consumption rate of a single herbivore as a function of available forage,
- numerical response [80, 181]: number of herbivores as a function of available forage.

Combining these concepts in this way is, as far as we know, a novel approach.

4.2.1 Ideal free distribution

An inhomogeneous distribution of biomass $n(x)$ leads to an inhomogeneous distribution of herbivores. Assuming that the system is in a steady state, we want to determine an ideal free distribution [65] of herbivores, which we express as the probability distribution of the location of a single herbivore. For this we need to make assumptions on the suitability S of a location. As the suitability is set to decrease with the density of herbivores, the ideal free distribution is attained if the suitability of all (occupied) locations is equal [65].

We set the suitability S of a location x to be solely determined by the effective foraging potential which we assume to be of the form $n^j(x)$ $(j > 0)$ divided by the herbivore density $\phi(x)$ among whom this forage is shared: $S(n, \phi) := n^j/\phi$. The ideal free distribution is attained if S is constant, so that the density of herbivores ϕ is proportional to n^j and the probability distribution of a single herbivore is given by

$$\frac{n^j(x)}{\int_0^L n^j(x)\ dx}, \tag{4.3}$$

where the denominator takes care of the normalization.

If $j = 1$, S is proportional to the local biomass. If only the amount of vegetation and not its spatial distribution affect total herbivory, then this is the natural choice for j.

Locations with large amounts of forage provide herbivores the opportunity to graze more efficiently, since it allows for a significant overlap of the searching and handling of forage [182]. Thus the attractivity of a vegetation patch may be superlinear in n, resulting in a suitability with $j > 1$. In this case a distribution of vegetation concentrated in patches can be grazed more than the same amount of biomass being smeared out equally over the whole domain.

If plants become less susceptible to herbivory as they grow [165], e.g. because of decreased palatability, then attractiveness of large vegetation patches may be less than proportional to the amount of biomass. This corresponds to a suitability with $0 < j < 1$. In this case a homogeneous distribution of vegetation will provide the most forage.

The effective forage potential of a vegetation distribution should reflect the (un)attractiveness of patches of vegetation, through the parameter j.

We define as *measures of forage* per unit area

$$I_j(n) := \frac{1}{L} \int_0^L n^j(x) \, dx, \qquad (4.4)$$

with $j > 0$. Which measure of forage is relevant relates to the utilization and foraging behavior of the herbivores. From the subsequent derivation it will follow that the grazing rate $(= \frac{\text{grazing}}{n})$ is constant ('flat rate') if $j = 1$, so equal for densely and scarcely vegetated locations. A value $j > 1$ will make for a grazing rate that itself grows with increasing n ('progressive rate').

Substituting definition (4.4) into (4.3), the probability distribution of a single herbivore can be written as

$$\frac{n^j}{LI_j(n)}. \qquad (4.5)$$

4.2.2 Sustained grazing

Although (for steady vegetation distributions) the spatial distribution of herbivores is constant on the population level, individual herbivores will still move around, so that the functional response of herbivores is affected by time spend moving and searching [64] (without handling [182]). Assuming that herbivores spend a fixed amount of time on foraging, the total individual forage of herbivores can be described by a Holling functional response type II [80]. For a system with sustained grazing, a constant effective herbivore number has been regarded as a good approximation of reality [134, 196], any grazing deficiency will be compensated by supplementary food. We denote the imposed number of herbivores per unit area by h_{imp}.

From the previous discussion on sustained grazing we deduce two assumptions:

- the functional response is of type II;
- the numerical response is constant and equals $h_{\text{imp}}L$.

The functional response depends on the available forage, which is measured by $I_j(n)$ (4.4). For large $I_j(n)$, intake of the herbivores satiates at a maximal consumption rate c_{max}. The type II functional response is given by

$$\frac{c_{\text{max}}I_j(n)}{I_h + I_j(n)},$$

where I_h is the value of $I_j(n)$ where half of the maximum consumption rate is lost through searching.

Applying equation (4.2) with (4.5) in the setting with sustained grazing yields

$$\text{grazing} = \frac{n^j}{LI_j(n)} \times \frac{c_{\max}I_j(n)}{I_h + I_j(n)} \times h_{\text{imp}}L = \frac{m_{\text{sus}}}{I_h + I_j(n)}n^j \qquad (4.6)$$

with $m_{\text{sus}} := c_{\max}h_{\text{imp}}$ the maximum rate of intake on the population level, per unit area.

The *total amount of grazing* for sustained grazing is given by

$$G_{j,\text{sus}}(n) := \int_0^L \frac{m_{\text{sus}}}{I_h + I_j(n)}n^j dx = \frac{m_{\text{sus}}LI_j(n)}{I_h + I_j(n)}. \qquad (4.7)$$

The *grazing pressure*, defined as total intake $G_{j,\text{sus}}(n)$ divided by the total forage mass $LI_j(n)$ [2], is given by

$$g_{j,\text{sus}}(n) := \frac{G_{j,\text{sus}}(n)}{LI_j(n)} = \frac{m_{\text{sus}}}{I_h + I_j(n)}, \qquad (4.8)$$

so that (4.6) can be concisely written as

$$\text{grazing} = g_{j,\text{sus}}(n) \cdot n^j. \qquad (4.9)$$

4.2.3 Natural grazing

In a natural setting, given an amount of forage $I_j(n)$ (4.4), part of the herbivores will be able to sustain themselves by acquiring sufficient grazing intake for maintenance, e.g. by increasing foraging time. Other herbivores will disappear from the domain, e.g. due to death or emigration, relieving the remaining herbivores of high competition for suitable forage. Thus in this case the consumption of the remaining individuals is approximately constant at a sufficient sustenance level c_{suf}, but at the expense of a numerical response. As the available forage $I_j(n)$ decreases it may hardly be able to support any wildlife, even before all biomass has disappeared. At the other side of the spectrum where forage is abundant, the number of herbivores is assumed to be delimited by other factors, e.g. due to top-down control by predation.

We summarize this discussion on natural systems by listing two assumptions:

- the functional response is constant and equals c_{suf};

- the numerical response is sigmoid (corresponding to type III).

We model the numerical response by the sigmoid function

$$\frac{h_{\max} L I_j(n)^2}{I_h{}^2 + I_j(n)^2},$$

where I_h in this case represents the value of $I_j(n)$ where half of the maximal number of herbivores $h_{\max} L$ remain.

Applying equation (4.2) with (4.5) in the natural setting now yields

$$\text{grazing} = \frac{n^j}{L I_j(n)} \times c_{\text{suf}} \times \frac{h_{\max} L I_j(n)^2}{I_h{}^2 + I_j(n)^2} = \frac{m_{\text{nat}} I_j(n)}{I_h{}^2 + I_j(n)^2} n^j \tag{4.10}$$

with $m_{\text{nat}} := c_{\text{suf}} h_{\max}$ the maximum rate of intake on the population level, per unit area.

The *total grazing* is given by

$$G_{j,\text{nat}} := \int_0^L \frac{m_{\text{nat}} I_j(n)}{I_h{}^2 + I_j(n)^2} n^j \, dx = \frac{m_{\text{nat}} L I_j(n)^2}{I_h{}^2 + I_j(n)^2} \tag{4.11}$$

so that we identify the *grazing pressure* being

$$g_{j,\text{nat}}(n) := \frac{G_{j,\text{nat}}}{L I_j(n)} = \frac{m_{\text{nat}} I_j(n)}{I_h{}^2 + I_j(n)^2} \tag{4.12}$$

and (4.10) becomes

$$\text{grazing} = g_{j,\text{nat}}(n) \cdot n^j. \tag{4.13}$$

4.2.4 Comparison of sustained and natural grazing

We make a comparison of the total grazing (4.7), (4.11) and grazing pressure (4.9), (4.13) functions in the sustained and natural setting. In (4.14) the asymptotic behavior of the grazing functions is shown and we see that at $I_j(n) = I_h$ for both types of grazing intake is precisely half of the maximum intake on the population level.

	$G_{j,\text{sus}}$	$G_{j,\text{nat}}$	$g_{j,\text{sus}}$	$g_{j,\text{nat}}$
$I_j(n) \to 0$	$G_{j,\text{sus}} \to 0$	$G_{j,\text{nat}} \to 0$	$g_{j,\text{sus}} \to \frac{m_{\text{sus}}}{I_h}$	$g_{j,\text{nat}} \to 0$
$I_j(n) = I_h$	$G_{j,\text{sus}} = \frac{m_{\text{sus}} L}{2}$	$G_{j,\text{nat}} = \frac{m_{\text{nat}} L}{2}$	$g_{j,\text{sus}} = \frac{m_{\text{sus}}}{2 I_h}$	$g_{j,\text{nat}} = \frac{m_{\text{nat}}}{2 I_h}$
$I_j(n) \to \infty$	$G_{j,\text{sus}} \to m_{\text{sus}} L$	$G_{j,\text{nat}} \to m_{\text{nat}} L$	$g_{j,\text{sus}} \to 0$	$g_{j,\text{nat}} \to 0$

$$\tag{4.14}$$

Regardless the setting, in a regime of abundant vegetation total grazing converges to the maximal overall intake rate mL and grazing pressure diminishes. Also, as available forage $I_j(n)$ becomes smaller but $I_j(n) > I_h$, the grazing pressure monotonically increases. The main difference between the sustained and natural setting occurs when $I_j(n)$ decreases below I_h, since then in the sustained setting grazing pressure increases more and more (due to constant herbivore numbers, with a type II functional response) whereas in the natural setting herbivore numbers start reducing so fast (sigmoid response) that the grazing pressure starts to become smaller again from $I_j(n)$ below I_h onward. This is reflected by the sigmoid form of the total grazing $G_{j,\mathrm{nat}}$, see Figure 4.2.

Remark 4.2. *Since the sustained and natural grazing functions (with $m_{\mathrm{sus}} = m_{\mathrm{nat}}$ and the same value of j) are almost equal for $I_j(n) \gg I_h$, in this regime the same dynamics are likely to occur for sustained and natural grazing.*

With the proposed grazing functions set, we return to the main results of the introduction to see how they fit.

1. The grazing rate $(= \frac{\mathrm{grazing}}{n} = g_j n^{j-1})$ is an increasing function of n for $j > 1$ ('progressive'), so that locations with relatively large biomass bear a large grazing rate and locations with small biomass bear a small grazing rate. If this difference is large enough, this may lead to levelling out of vegetation distributions resulting in a spatially homogeneous vegetation.

2. For sustained grazing, periodic vegetation patterns with large wavelength have low available forage $I_j(n)$ and thus are subjected to a large grazing pressure, see Figure 4.2(b).

3. For natural grazing, states with intermediate amounts of forage $I_j(n) = I_h$ experience the heighest levels of grazing pressure, Figure 4.2(b). A small I_h corresponds to persistent herbivores, so the available forage $I_j(n)$ of possibly inadmissible states is influenced by herbivore persistence, creating a dichotomy of higher forage and lower forage states.

4.3 Incorporation of grazing in the extended Klausmeier model

As announced in the introduction, we analyze the proposed nonlocal grazing terms within an extended Klausmeier model [176, 180]. On flat ground, in
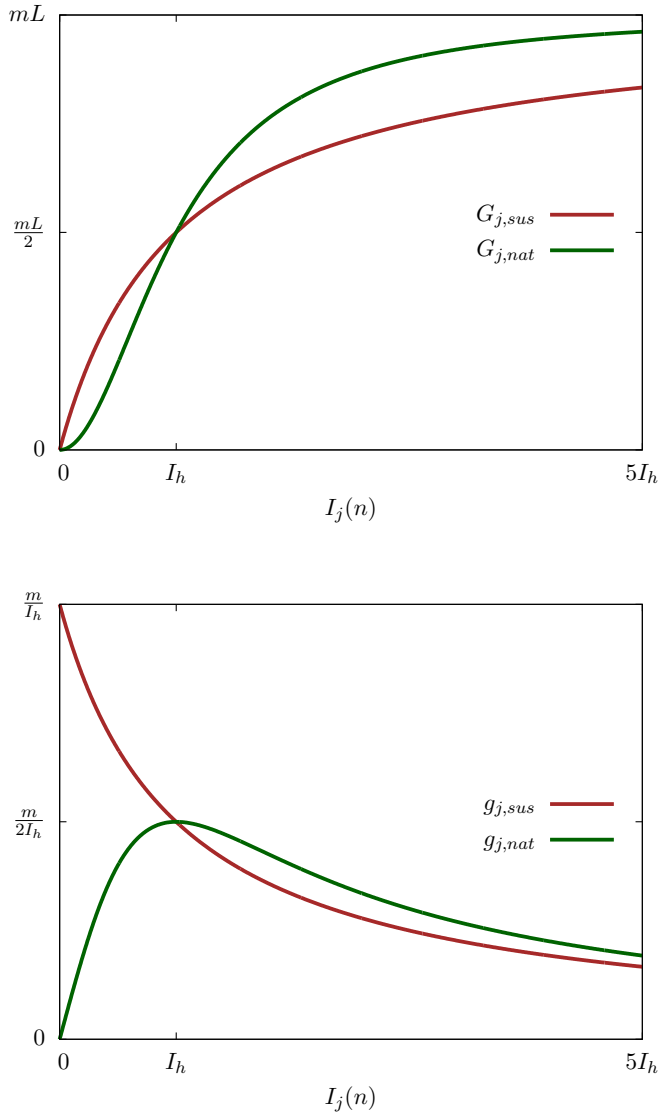
Figure 4.2: Grazing as a function of available forage $I_j(n)$. Here I_h designates the amount of forage where the total grazing is half the maximum value and $m = m_{\text{sus}}$ or m_{nat} respectively. Note that the graphs do not depend on j. Top panel: in both cases the total grazing G converges to mL as forage becomes more and more abundant and diminishes if vegetation becomes scarce. Bottom panel: in both cases the grazing pressure g is (approximately) inversely proportional to available forage in case of abundant forage. The function $g_{j,\text{sus}}$ monotonically increases to m/I_h as all vegetation disappears; in contrast $g_{j,\text{nat}}$ initially increases to a maximum at $I_j(n) = I_h$ but then converges to zero for ever smaller forage amount.

dimensionless form, it is given by

$$w_t = d_1 w_{xx} + f(w, n),$$
$$n_t = d_2 n_{xx} + g(w, n) \tag{4.15}$$

where the reaction terms are given by

$$f(w, n) = a - w - wn^2,$$
$$g(w, n) = -mn + wn^2. \tag{4.16}$$

As mentioned in the introduction, we choose a finite but large domain $[0, L]$, with Neumann or periodic boundary conditions. The second order derivatives w_{xx} and n_{xx} model water diffusion and plant dispersal, with water diffusion being faster so $d_1 \gg d_2$ (although in the original Klaumeier model [97], extensively analyzed in [173] and references therein, it holds that $d_1 = 0$). The parameter $a \geq 0$ models rainfall and may change as a function of time due to a changing climate; $-w$ models evaporation, m is an effective death rate and the terms $\pm wn^2$ model water uptake by the vegetation.

Remark 4.3. *When having to fix parameters, we do so in accordance with those employed in previous studies [97, 176, 180]:* $d_1 = 500$, $d_2 = 1$ *and* $m_0 = 0.45$.

As discussed in the introduction we now restrict to certain types of grazing that allow for a straightforward comparison with the case without grazing. Specifically, we choose $I_h = 1$ and sustained grazing with $j = 2$ or natural grazing with $j = 1$. It is of notational convenience that we now treat both types of grazing at once, we assume that either one has been set to zero. The realization of (4.1) with (4.9) and (4.13) is

$$mn = m_0 n + g_{2,\mathrm{sus}}(n) \cdot n^2 + g_{1,\mathrm{nat}}(n) \cdot n$$
$$= m_0 n + \frac{m_{\mathrm{sus}}}{1 + I_2(n)} n^2 + \frac{m_{\mathrm{nat}} I_1(n)}{1 + (I_1(n))^2} n \tag{4.17}$$

where $m_0 > 0$, $m_{\mathrm{sus}}, m_{\mathrm{nat}} \geq 0$ (and $m_{\mathrm{sus}} m_{\mathrm{nat}} = 0$). By substituting (4.17) in (4.16), grazing is incorporated in the extended Klausmeier model.

4.4 Linear analysis of pattern formation with grazing

The grazing terms can alter both the homogeneous steady state solutions and their stability. In Section 4.3 we have restricted our attention to choices

for which the effect on the homogeneous steady states can be absorbed in the rainfall parameter, as we show in Section 4.4.1.

Next we focus on stability of the homogeneous steady states. Through a linear stability analysis, we identify possible scenarios for destabilization of a homogeneously vegetated state in the presence of grazing, which could result in vegetation pattern formation but could also lead to immediate desertification.

4.4.1 Homogeneous steady states

As in previous papers [176,180], when looking for homogeneous steady states we set $f(w, n) = g(w, n) = 0$ (see (4.16)) and obtain:

$$a - w - wn^2 = 0,$$
$$-mn + wn^2 = 0.$$

One solution is given by $n_\text{bare} = 0$ and consequently $w_\text{bare} = a$, which corresponds to the bare desert state.

Otherwise

$$m = wn,$$
$$w = \frac{a}{1 + n^2} \tag{4.18}$$

so that

$$m = \frac{an}{1 + n^2}. \tag{4.19}$$

Because $I_1(n) = n$ and $I_2(n) = n^2$, (4.17) simplifies to

$$m = m_0 + \frac{m_\text{sus} + m_\text{nat}}{1 + n^2} n. \tag{4.20}$$

Substituting this into (4.19) we obtain

$$m_0 = \frac{(a - m_\text{sus} - m_\text{nat})n}{1 + n^2}.$$

Setting $\bar{a} := a - m_\text{sus} - m_\text{nat}$ this leads to

$$m_0(1 + n^2) = \bar{a}n \tag{4.21}$$

which is a quadratic equation in n having solutions

$$n_\pm(\bar{a}, m_0) = \frac{\bar{a} \pm \sqrt{\bar{a}^2 - 4m_0^2}}{2m_0} \qquad (\bar{a} \geq 2m_0). \tag{4.22}$$
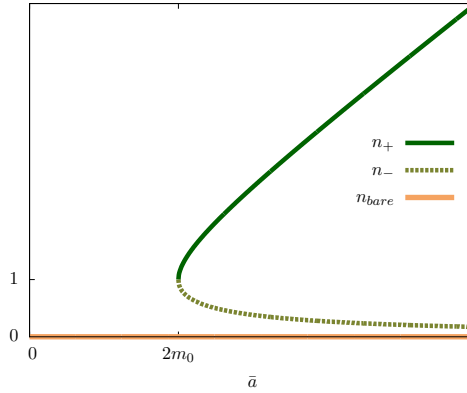
Figure 4.3: Homogeneous steady states of the extended Klausmeier model. For sustained grazing with $j = 2$ or natural grazing with $j = 1$, the grazing is absorbed into the rainfall a, together $\bar{a}$. In this case, the homogeneous steady states depend on $\bar{a}$ identically as they depend on a in the case without grazing ([180], Figure 2.8).

This shows that a fold or saddle-node bifurcation occurs at

$$\bar{a} = 2m_0, \tag{4.23}$$

or $a = 2m_0 + m_{\text{sus}} + m_{\text{nat}}$. The other component $w_\pm$ can be computed from (4.22) and any of the equations (4.18).

Remark 4.4. *We started out with independent parameters $a, m_0, m_{\text{sus}}, m_{\text{nat}}$ and introduced $\bar{a}$ as a dependent parameter. Since $n_\pm$ only directly depends on $\bar{a}$ and m_0, for the continuation of this section it will be easier to view $\bar{a}$ as an independent parameter and have a depend on $\bar{a}, m_{\text{sus}}, m_{\text{nat}}$.*

Remark 4.5. *The choice of $I_h = 1$ and the restriction to sustained grazing with $j = 2$ and natural grazing with $j = 1$ means that when $I_2(n)$ respectively $I_1(n)$ has decreased to 1, the total sustained grazing $G_{2,\text{sus}}$ respectively total natural grazing $G_{1,\text{nat}}$ have decreased to half the maximum total grazing. If destabilization of (w_+, n_+) for sustained grazing with $j = 2$ occurs for $n_+^2 = I_2(n_+) \gg 1$, then this likely also occurs for natural grazing, see Remark 4.2. Vice versa if (w_+, n_+) destabilizes for natural grazing with $j = 1$ when $n_+ = I_1(n_+) \gg 1$, then this likely also occurs for sustained grazing.*

4.4.2 Linearization of kinetics about $(w_\pm, n_\pm)$

We compute the linearization of the reaction terms about the homogeneous steady states $(w_\pm, n_\pm)$. To reduce notational burden, we abbreviate $(w_\pm, n_\pm)$ by (w, n) since we now only focus on these system states. As notation for the derivatives we introduce

$$
\begin{aligned}
a_1 :=& \frac{\partial f}{\partial w}(w, n) = -1 - n^2, \\
a_2 :=& \frac{\partial f}{\partial n}(w, n) = -2wn, \\
a_3 :=& \frac{\partial g}{\partial w}(w, n) = n^2, \\
a_4 :=& \frac{\partial g}{\partial n}(w, n) = -\frac{\partial(m(n)n)}{\partial n} + 2wn.
\end{aligned}
\tag{4.24}
$$

We note that a_1 and a_3 only depend on n. We view $n_\pm(\bar{a}, m_0)$ as independent of m_{sus} and m_{nat}, see Remark 4.4. This also makes a_1 and a_3 independent of these parameters. The function a_2 does depend on m_{sus} and m_{nat} through w. By (4.16) and (4.17), $g(w, n) = -m_0 n - g_{2,\text{sus}}(n) \cdot n^2 - g_{1,\text{nat}}(n) \cdot n + wn^2$, so

$$
\begin{aligned}
a_4 =& -m_0 - \frac{\partial g_{2,\text{sus}}(n)}{\partial n} n^2 - \frac{2m_{\text{sus}}n}{1 + n^2} - \frac{\partial g_{1,\text{nat}}(n)}{\partial n} n - \frac{m_{\text{nat}}n}{1 + n^2} + 2wn \\
=& m_0 - \frac{\partial g_{2,\text{sus}}(n)}{\partial n} n^2 - \frac{\partial g_{1,\text{nat}}(n)}{\partial n} n + \frac{m_{\text{nat}}n}{1 + n^2}
\end{aligned}
\tag{4.25}
$$

where we used (4.18) and (4.20). Since $g_{2,\text{sus}}$ and $g_{1,\text{nat}}$ contain integrals, their differentation requires a bit more attention, for this we rely on outcomes of the more general linearization computations in Appendix 4.A.

Given a perturbation $(\tilde{w}(x), \tilde{n}(x))$ we may split it in a homogeneous and inhomogeneous part:

$$
\begin{aligned}
(\tilde{w}, \tilde{n})_{\text{hom}} :=& \left(\int_0^L \tilde{w} \, dx, \int_0^L \tilde{n} \, dx \right), \\
(\tilde{w}, \tilde{n})_{\text{inh}} :=& (\tilde{w}, \tilde{n}) - (\tilde{w}, \tilde{n})_{\text{hom}}.
\end{aligned}
$$

For the inhomogeneous part it follows from (4.25), (4.A.5) and (4.A.6), since $\beta_0 = 0$, that

$$
a_{4,\text{inh}} = m_0 + \frac{m_{\text{nat}}n}{1 + n^2},
\tag{4.26}
$$

which does not depend on m_{sus}. For spatially homogeneous perturbations, it follows that

$$
\begin{aligned}
a_{4,\text{hom}} =& m_0 - \frac{-m_{\text{sus}}}{(1+n^2)^2} \cdot 2n \cdot n^2 - m_{\text{nat}}\frac{1-n^2}{(1+n^2)^2}n + \frac{m_{\text{nat}}n}{1+n^2} \\
=& m_0 + \frac{2(m_{\text{sus}}+m_{\text{nat}})n^3}{(1+n^2)^2}.
\end{aligned}
$$

For the stability against homogeneous perturbations,

$$
A_{\text{hom}} := \begin{pmatrix} a_1 & a_2 \\ a_3 & a_{4,\text{hom}} \end{pmatrix} = \begin{pmatrix} -1-n^2 & -2m_0 - \frac{2(m_{\text{sus}}+m_{\text{nat}})n}{1+n^2} \\ n^2 & m_0 + \frac{2(m_{\text{sus}}+m_{\text{nat}})n^3}{(1+n^2)^2} \end{pmatrix}
$$

is relevant. We calculate the determinant

$$
\begin{aligned}
\det(A_{\text{hom}}) =& a_1 a_{4,\text{hom}} - a_2 a_3 \\
=& (-1-n^2)\left(m_0 + \frac{2(m_{\text{sus}}+m_{\text{nat}})n^3}{(1+n^2)^2}\right) \\
&+ \left(2m_0 + \frac{2(m_{\text{sus}}+m_{\text{nat}})n}{1+n^2}\right)n^2 \\
=& m_0(n^2-1)
\end{aligned}
$$

which does not depend on m_{sus} and m_{nat} (since n only depends on $\bar{a}$ and m_0, Remark 4.4). We note that $n_- < 1$ so then $\det(A_{\text{hom}}) < 0$, so (w_-, n_-) is unstable. On the other hand $n_+ > 1$ implies $\det(A_{\text{hom}}) > 0$, so that stability of (w_+, n_+) against homogeneous perturbations depends on the sign of the trace, where a change in sign signals a Hopf instability. From now on we focus on (w_+, n_+).

4.4.3 Hopf instability of (w_+, n_+)

Here (w, n) denotes (w_+, n_+). It holds that

$$
\begin{aligned}
\text{tr}(A_{\text{hom}}) =& a_1 + a_{4,\text{hom}} \\
=& -(1+n^2) + m_0 + \frac{2(m_{\text{sus}}+m_{\text{nat}})n^3}{(1+n^2)^2}
\end{aligned} \tag{4.27}
$$

which by equation (4.21) becomes

$$
\text{tr}(A_{\text{hom}}) = -\frac{\bar{a}n}{m_0} + m_0 + \frac{2(m_{\text{sus}}+m_{\text{nat}})m_0^2 n}{\bar{a}^2}. \tag{4.28}
$$

At the Hopf instability threshold it holds that $\mathrm{tr}(A_{\mathrm{hom}}) = 0$, so

$$\left(\bar{a}^3 - 2m_0^3(m_{\mathrm{sus}} + m_{\mathrm{nat}})\right) n = m_0^2 \bar{a}^2. \tag{4.29}$$

We compute $\mathrm{tr}(A_{\mathrm{hom}})$ on the fold bifurcation, where $\bar{a} = 2m_0$ (by (4.23)) and $n = 1$. Inserting this in (4.28) yields

$$\mathrm{tr}(A_{\mathrm{hom}}) = -2 + m_0 + \frac{1}{2}(m_{\mathrm{sus}} + m_{\mathrm{nat}})$$

$$\begin{cases} < 0 & \text{if } m_0 < 2 - \frac{1}{2}(m_{\mathrm{sus}} + m_{\mathrm{nat}}) & \text{(Hopf stable)} \\ > 0 & \text{if } m_0 > 2 - \frac{1}{2}(m_{\mathrm{sus}} + m_{\mathrm{nat}}) & \text{(Hopf unstable)} \end{cases} \tag{4.30}$$

so the Hopf instability locus on the fold moves to smaller values of m_0 for increasing m_{sus} or m_{nat}, and exists only for $m_{\mathrm{sus}} + m_{\mathrm{nat}} < 4$ (since $m_0 > 0$).

Since $\lim_{\bar{a} \to \infty} n = \infty$ but $n < \frac{\bar{a}}{m_0}$, it holds that for fixed $m_0 > 0$ and $m_{\mathrm{sus}}, m_{\mathrm{nat}} \geq 0$

$$\lim_{\bar{a} \to \infty} \mathrm{tr}(A_{\mathrm{hom}}) = -\infty. \tag{4.31}$$

Lemma 4.1 (Hopf curve monotonicity). *No Hopf instabilities exist for triplets* $(m_0, m_{\mathrm{sus}}, m_{\mathrm{nat}})$ *with* $m_0 < 2 - \frac{1}{2}(m_{\mathrm{sus}} + m_{\mathrm{nat}})$. *For triplets with* $m_0 \geq \max\left\{0, 2 - \frac{1}{2}(m_{\mathrm{sus}} + m_{\mathrm{nat}})\right\}$, *there exists a unique Hopf instability; it moves to higher values of* $\bar{a}$ *for increasing* m_0, m_{sus} *or* m_{nat}.

Proof. Dividing (4.29) by $\bar{a}^2$ we obtain

$$\frac{\bar{a}^3 - 2m_0^3(m_{\mathrm{sus}} + m_{\mathrm{nat}})}{\bar{a}^2} n = m_0^2. \tag{4.32}$$

Define

$$D_- := \left\{(\bar{a}, m_0, m_{\mathrm{sus}}, m_{\mathrm{nat}}) : \bar{a}^2 - 2m_0^3(m_{\mathrm{sus}} + m_{\mathrm{nat}}) \leq 0\right\},$$
$$D_+ := \left\{(\bar{a}, m_0, m_{\mathrm{sus}}, m_{\mathrm{nat}}) : \bar{a}^2 - 2m_0^3(m_{\mathrm{sus}} + m_{\mathrm{nat}}) > 0\right\}.$$

Since the right-hand side of (4.32) is positive, it can't have solutions on D_-, so we restrict attention to D_+.

On D_+ the left-hand side is a monotonically increasing function of $\bar{a}$ and the right-hand side is independent of $\bar{a}$, so that for each combination $m_0 > 0$, $m_{\mathrm{sus}}, m_{\mathrm{nat}} \geq 0$ there can be at most one Hopf instability. By (4.30) and (4.31) a unique Hopf instability exists only for $m_0 > 2 - \frac{1}{2}(m_{\mathrm{sus}} + m_{\mathrm{nat}})$ (and $m_0 > 0$).

On D_+, for each fixed $\bar{a}$, the left-hand side is a decreasing function of m_0, m_{sus} and m_{nat}, since n is a decreasing function of m_0 for each fixed $\bar{a}$. The right-hand side is a non-decreasing function of m_0, m_{sus} and m_{nat}. So the Hopf instability moves to a higher value of $\bar{a}$ for larger m_0, m_{sus} or m_{nat}.

$\square$

Since m_{sus} and m_{nat} are interchangeable in (4.28), (w, n) becomes equally more susceptible to Hopf instability in case of increased sustained grazing with $j = 2$ or increased natural grazing with $j = 1$. The Hopf instabilities for various values of $m_{\mathrm{sus}}, m_{\mathrm{nat}}$ for a realistic choice of parameters are plotted in Figure 4.4, illustrating that the Hopf instability curve moves to larger $\bar{a}$ for increasing m_{sus} or m_{nat}.

4.4.4 Turing instability of (w_+, n_+)

We again denote (w_+, n_+) by (w, n). Regarding a possible Turing instability we look at spatially inhomogeneous perturbations, with linearization given by

$$
\begin{aligned}
A_{\mathrm{inh}}(\bar{a}, m_0, m_{\mathrm{sus}}, m_{\mathrm{nat}}) &:= \begin{pmatrix} a_1 & a_2 \\ a_3 & a_{4,\mathrm{inh}} \end{pmatrix} \\
&= \begin{pmatrix} -1 - n^2 & -2m_0 - \frac{2(m_{\mathrm{sus}} + m_{\mathrm{nat}})n}{1 + n^2} \\ n^2 & m_0 + \frac{m_{\mathrm{nat}} n}{1 + n^2} \end{pmatrix},
\end{aligned} \tag{4.33}
$$

see (4.24) and (4.26). We compute

$$
\begin{aligned}
\det(A_{\mathrm{inh}}) &= a_1 a_{4,\mathrm{inh}} - a_2 a_3 \\
&= (-1 - n^2)\left(m_0 + \frac{m_{\mathrm{nat}} n}{1 + n^2} \right) + \left(2m_0 + 2n\frac{m_{\mathrm{sus}} + m_{\mathrm{nat}}}{1 + n^2} \right) n^2 \\
&= (n^2 - 1)m_0 + \frac{-m_{\mathrm{nat}} n - m_{\mathrm{nat}} n^3 + 2n^3(m_{\mathrm{sus}} + m_{\mathrm{nat}})}{1 + n^2} \\
&= (n^2 - 1)m_0 + \frac{2m_{\mathrm{sus}} n^3 + m_{\mathrm{nat}} n(n^2 - 1)}{1 + n^2} > 0
\end{aligned}
$$

and define

$$
\mathrm{Tur}(\bar{a}, m_0, m_{\mathrm{sus}}, m_{\mathrm{nat}}) := \Gamma - 2\sqrt{d_1 d_2 \det(A_{\mathrm{inh}})}, \tag{4.34}
$$

where $\Gamma := d_1 a_{4,\mathrm{inh}} + d_2 a_1$, with d_1 and d_2 the diffusion constants.

The homogeneous steady state is Turing unstable if Tur > 0 and Turing stable if Tur < 0, see [176]. Note that these results follow from analysis of the continuous spectrum that relates to unbounded domains, in case of a (large) finite domain the instability is delayed (by a negligible amount).

Like for the Hopf instability we investigate Turing (in)stability on the fold bifurcation, where $\bar{a} = 2m_0$ (4.23) and $n = 1$. Substitution in (4.34) yields

$$
\text{Tur} = d_1 \left(m_0 + \frac{m_{\text{nat}}}{2} \right) - 2d_2 - 2\sqrt{d_1 d_2 m_{\text{sus}}}
$$

$$
\begin{cases}
< 0 & \text{if } m_0 < 2\frac{d_2}{d_1} + 2\sqrt{\frac{d_2}{d_1} m_{\text{sus}}} - \frac{m_{\text{nat}}}{2} & \text{(Turing stable)} \\
> 0 & \text{if } m_0 > 2\frac{d_2}{d_1} + 2\sqrt{\frac{d_2}{d_1} m_{\text{sus}}} - \frac{m_{\text{nat}}}{2} & \text{(Turing unstable)}.
\end{cases}
$$
$$(4.35)$$

Lemma 4.2 (Turing curve monotonicity). *No Turing instabilities exist for triplets $(m_0, m_{\text{sus}}, m_{\text{nat}})$ with $m_0 < 2\frac{d_2}{d_1} + 2\sqrt{\frac{d_2}{d_1} m_{\text{sus}}} - \frac{m_{\text{nat}}}{2}$. For triplets $(m_0, m_{\text{sus}}, m_{\text{nat}})$ with $m_0 \geq \max \left\{ 2\frac{d_2}{d_1} + 2\sqrt{\frac{d_2}{d_1} m_{\text{sus}}} - \frac{m_{\text{nat}}}{2} \right\}$ there exists a unique Turing instability; it moves to higher values of $\bar{a}$ for increasing m_0.*

Proof. This monotonicity was already shown in [176] in the absence of nonlocal grazing terms ($m_{\text{sus}} = m_{\text{nat}} = 0$), we will apply the framework provided there to also apply it to the cases with grazing. It is sufficient to show that

$$
\text{sgn} \frac{\partial a_1}{\partial \bar{a}} = \text{sgn} \frac{\partial a_{4,\text{inh}}}{\partial \bar{a}} = \text{sgn} \left(-\frac{\partial \det(A_{\text{inh}})}{\partial \bar{a}} \right) = -1
$$

which means that increasing $\bar{a}$ acts stabilizing and

$$
\text{sgn} \frac{\partial a_1}{\partial m_0} = \text{sgn} \frac{\partial a_{4,\text{inh}}}{\partial m_0} = \text{sgn} \left(-\frac{\partial \det(A_{\text{inh}})}{\partial m_0} \right) = 1
$$

which means that increasing m_0 acts destabilizing.

Since a_1 is unaffected by the grazing terms, we only compute

$$\frac{\partial a_{4,\text{inh}}}{\partial \bar{a}} = m_{\text{nat}} \frac{1 - n^2}{(1 + n^2)^2} \frac{\partial n}{\partial \bar{a}} < 0$$

$$\frac{\partial a_{4,\text{inh}}}{\partial m_0} = 1 + m_{\text{nat}} \frac{1 - n^2}{(1 + n^2)^2} \frac{\partial n}{\partial m_0} > 0$$

$$\frac{\partial \det(A_{\text{inh}})}{\partial \bar{a}} = 2 m_0 n \frac{\partial n}{\partial \bar{a}} + \frac{m_{\text{sus}} \left(n^4 + 6n^2\right) + m_{\text{nat}} \left(n^4 + 3n^2 - 1\right)}{(1 + n^2)^2} \frac{\partial n}{\partial \bar{a}} > 0$$

$$\frac{\partial \det(A_{\text{inh}})}{\partial m_0} = 2 m_0 n \frac{\partial n}{\partial m_0} + n^2 - 1$$
$$+ \frac{m_{\text{sus}} \left(n^4 + 6n^2\right) + m_{\text{nat}} \left(n^4 + 3n^2 - 1\right)}{(1 + n^2)^2} \frac{\partial n}{\partial m_0} < 0$$

where the final estimate follows from the estimate $\frac{\partial n}{\partial m_0} \leq -\frac{a}{m_0^2}$ as in [176].

Since for $m_0 < 2\frac{d_2}{d_1} + 2\sqrt{\frac{d_2}{d_1} m_{\text{sus}}} - \frac{m_{\text{nat}}}{2}$, (w, n) was already Turing stable on the fold $\bar{a} = 2m_0$, it remains stable for all $\bar{a} > 2m_0$. The linear results on pattern formation from [176] apply, in particular that for fixed $m_{\text{sus}}, m_{\text{nat}} \geq 0$ and $m_0 \geq 2\frac{d_2}{d_1} + 2\sqrt{\frac{d_2}{d_1} m_{\text{sus}}} - \frac{m_{\text{nat}}}{2}$, the unique $\bar{a}$-value of the Turing instability locus monotonically increases as m_0 increases. $\qquad\square$

Sustained grazing with $j = 2$

The previous result Lemma 4.2 automatically leads to the simple consequence that a desertification process without Turing patterns is promoted by increasing m_{sus}.

Corollary 4.1. *Let $m_{\text{nat}} = 0$ and m_{sus} be fixed. If*

$$m_0 < 2\frac{d_2}{d_1} + 2\sqrt{\frac{d_2}{d_1} m_{\text{sus}}},$$

then (w, n) doesn't become Turing unstable as $\bar{a}$ decreases.

We now study further how sustained grazing with $j = 2$ affects the Turing instability. We do some preparatory work. First we compute the component-wise derivative of A_{inh} (4.33) with respect to m_{sus}:

$$\frac{\partial A_{\text{inh}}}{\partial m_{\text{sus}}} = \begin{pmatrix} 0 & \frac{-2n}{1+n^2} \\ 0 & 0 \end{pmatrix} \tag{4.36}$$

Now the first and second derivatives of Tur against any $m_\bullet$, be it m_{sus} or m_{nat}, are given by

$$\frac{\partial \mathrm{Tur}}{\partial m_\bullet} = \frac{\partial \Gamma}{\partial m_\bullet} - \sqrt{\frac{d_1 d_2}{\det(A_{\mathrm{inh}})}} \frac{\partial \det(A_{\mathrm{inh}})}{\partial m_\bullet}, \tag{4.37}$$

$$\frac{\partial^2 \mathrm{Tur}}{\partial m_\bullet{}^2} = \frac{\partial^2 \Gamma}{\partial m_\bullet{}^2} + \frac{\sqrt{d_1 d_2}}{2 \left(\det(A_{\mathrm{inh}})\right)^{\frac{3}{2}}} \frac{\partial \det(A_{\mathrm{inh}})}{\partial m_\bullet} - \sqrt{\frac{d_1 d_2}{\det(A_{\mathrm{inh}})}} \frac{\partial^2 \det(A_{\mathrm{inh}})}{\partial m_\bullet{}^2}. \tag{4.38}$$

Lemma 4.3. *The Turing unstable region in $(m_0, \bar{a})$-space becomes smaller as m_{sus} increases.*

Proof. From (4.36) we see that

$$\frac{\partial \det(A_{\mathrm{inh}})}{\partial m_{\mathrm{sus}}} = -\frac{\partial a_2}{\partial m_{\mathrm{sus}}} a_3 = \frac{2n}{1+n^2} n^2 = \frac{2n^3}{1+n^2} > 0,$$
$$\frac{\partial \Gamma}{\partial m_{\mathrm{sus}}} = 0,$$

which together with (4.37) leads to $\frac{\partial \mathrm{Tur}}{\partial m_{\mathrm{sus}}} < 0$, so that the Turing unstable region becomes smaller as m_{sus} increases. $\square$

The range in m_0 for which the Turing instability is not the primary destabilization mechanism may be larger than the lower bound presented in Corollary 4.1, since the increase of m_{sus} pushes the Turing instability to the background (Lemma 4.3) but promotes the Hopf instability (Lemma 4.1). So after the Turing instability emerges from the fold it may still need to overtake the Hopf instability as primary destabilization mechanism, see Figure 4.4.

Natural grazing with $j = 1$

For linear ($j = 1$) natural grazing, it is not as clear how the Turing instability is affected. The component-wise derivative

$$\frac{\partial A_{\mathrm{inh}}}{\partial m_{\mathrm{nat}}} = \begin{pmatrix} 0 & \frac{-2n}{1+n^2} \\ 0 & \frac{n}{1+n^2} \end{pmatrix}. \tag{4.39}$$

of (4.33) yields

$$\frac{\partial \det(A_{\text{inh}})}{\partial m_{\text{nat}}} = a_1 \frac{\partial a_4}{\partial m_{\text{nat}}} - \frac{\partial a_2}{\partial m_{\text{nat}}} a_3 = (-1 - n^2)\frac{n}{1 + n^2} + \frac{2n}{1 + n^2}n^2$$

$$= \frac{n^3 - n}{1 + n^2} > 0, \tag{4.40}$$

$$\frac{\partial \Gamma}{\partial m_{\text{nat}}} = d_1 \frac{\partial a_{4,\text{inh}}}{\partial m_{\text{nat}}} = \frac{d_1 n}{1 + n^2} > 0,$$

and with (4.37) it follows that

$$\frac{\partial \text{Tur}}{\partial m_{\text{nat}}} = \frac{d_1 n}{1 + n^2} - \sqrt{\frac{d_1 d_2}{\det(A_{\text{inh}})}}\frac{n^3 - n}{1 + n^2}$$

$$= \frac{\sqrt{d_1 d_2}n}{1 + n^2}\left(\sqrt{\frac{d_1}{d_2}} - \frac{n^2 - 1}{\sqrt{\det(A_{\text{inh}})}}\right),$$

and when assuming that $m_{\text{sus}} = 0$,

$$\frac{\partial \text{Tur}}{\partial m_{\text{nat}}} = \frac{\sqrt{d_1 d_2}n}{1 + n^2}\left(\sqrt{\frac{d_1}{d_2}} - \sqrt{\frac{n^2 - 1}{m_0 + \frac{m_{\text{nat}}}{1 + n^2}}}\right).$$

This implies that the derivative tends to be positive for $n \gtrsim 1$ but becomes negative for $n \gg 1$. Indeed, it can only be negative if $n^2 > \frac{d_1}{d_2}m_0$, which for $d_1 = 500$, $d_2 = 1$ and $m_0 = 0.45$ (Remark 4.3) leads to $n > 15$ so that through (4.22), $\bar{a} > 6$ is necessary. Thus we conclude that, in this case, for $\bar{a} \leq 6$ the Turing unstable region becomes larger, which is in agreement with Figure 4.4. Together with the monotonicity result Lemma 4.2, this does restrict the Turing instability location for $\bar{a} > 6$.

It is possible to prove a more general result based on the second derivative of Tur with respect to m_{nat}.

Lemma 4.4. *Any region in $(m_0, \bar{a})$-space that becomes Turing unstable due to an increase of m_{nat} will remain unstable as m_{nat} increases further.*

Proof. It holds that

$$\frac{\partial^2 \det(A_{\text{inh}})}{\partial m_{\text{nat}}^2} = 0,$$

$$\frac{\partial^2 \Gamma}{\partial m_{\text{nat}}^2} = 0.$$

which after substitution together with (4.40) into (4.38) yields $\frac{\partial^2 \text{Tur}}{\partial m_{\text{nat}}^2} > 0$. $\square$

4.5 Simulations with grazing and decreasing rainfall

In this section we show the results of simulations of the extended Klausmeier model (4.15) with grazing incorporated (Section 4.3) to see how the presence of grazing terms changes the desertification process under decreasing rainfall. For this we fix parameters to the values $d_1 = 500$, $d_2 = 1$ and $m_0 = 0.45$ (Remark 4.3). Application of noise tends to decrease the delay in destabilization and the jump in wavenumber at transition [180], in all simulations we apply white multiplicative noise of small amplitude 0.05% (on both the water and the biomass component) at every integer t. Also the rate of change of rainfall a has an influence [180], here we fix $\frac{\partial a}{\partial t} = -10^{-4}$. As initial condition we take the homogeneously vegetated state at a rainfall level where it is still stable. The spatial domain size is 1000, with periodic boundary conditions.

4.5.1 Varying maximum sustained intake

For the simulations presented in this subsection we vary the maximum sustained intake m_{sus} while fixing $I_h = 1$ and $j = 2$. This corresponds to the grazing pressures plotted in Figure 4.5(a). From these plots it is visible that especially for small $I_2(n)$, which encompass patterns with a (very) long wavelength, the grazing pressure becomes exceedingly large. On the other end, from the linear analysis performed in Section 4.4.4 we know that the Turing instability may be delayed (in $\bar{a}$), or even suppressed, by increasing m_{sus} with $j = 2$.

Together with Figure 4.1, the panels in Figure 4.6 show the influence of increasing the maximal intake on the population level (per unit area) m_{sus} on the desertification process driven by decreasing rainfall. We see that the Turing instability occurs at higher values of a, but lower values of $\bar{a} = a - m_{\text{sus}}$, for larger m_{sus}. This is consistent with Lemma 4.3. For the highest value $m_{\text{sus}} = 8$, no Turing patterns form, which is consistent with Figure 4.4 from which it can be read of that, at $m_0 = 0.45$, the Hopf instability occurs at a higher value of $\bar{a}$ (thus also a) than the Turing instability. This is in accordance with main Result 1 of Section 4.1.R

From the simulations it is also visible that for $m_{\text{sus}} \geq 2$, the final transition of the system from a vegetated state to the bare desert state occurs at a relatively small wavelength (large wavenumber) compared to the simulation without grazing (Figure 4.1). This is in supports of main Result 3. In terms
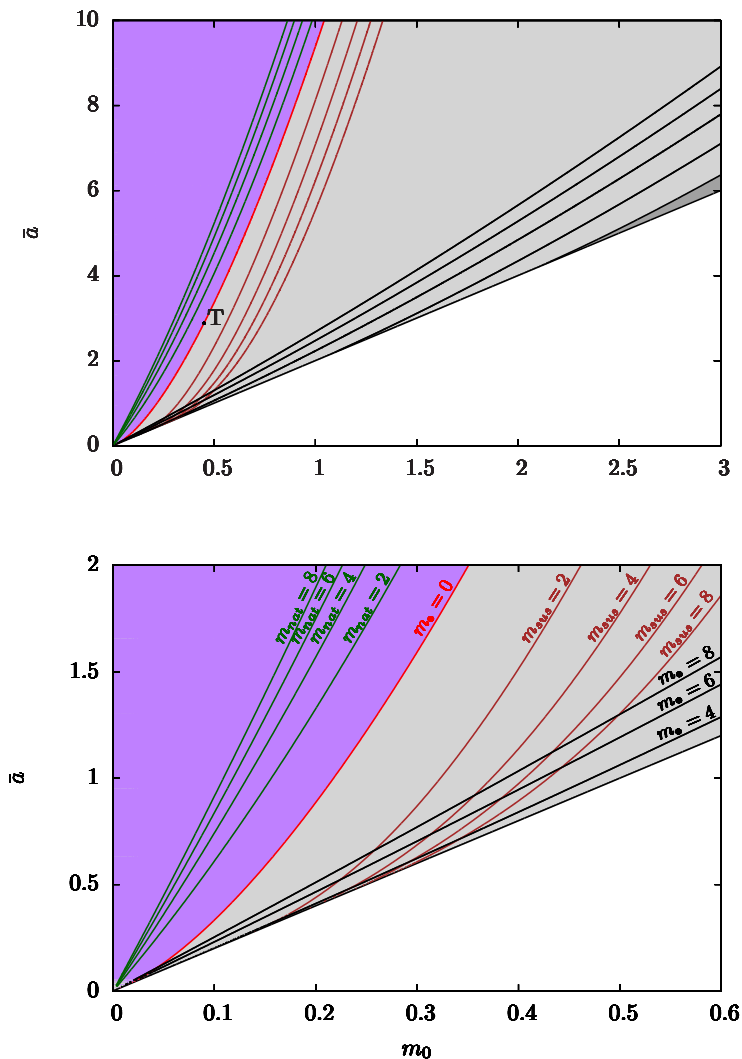
Figure 4.4: The bottom panel is a zoom of the top panel, both showing the influence of grazing on Turing and Hopf instability curves for $d_1 = 500$ and $d_2 = 1$ (Remark 4.3). The red curve is the Turing instability locus without grazing and the purple region is the corresponding Turing stable region. The black line $\bar{a} = 2m_0$, on the boundary of the white region where $(w_\pm, n_\pm)$ does not exist, is the fold bifurcation. Green curves represent Turing instabilities for natural grazing with $j = 1$, $I_h = 1$, L-R: $m_{\text{nat}} = 8, 6, 4, 2$. Brown curves are Turing instabilities for sustained grazing with $j = 2$, $I_h = 1$, L-R: $m_{\text{sus}} = 2, 4, 6, 8$. Black curves show Hopf instability curves, T-B: $m_\bullet = 8, 6, 4, 2, 0$, with $m_\bullet = m_{\text{sus}}$ or m_{nat}. Dark-grey region corresponds to Hopf unstable region in absence of grazing, $m_\bullet = 0$. The point with label T is the locus of the Turing instability for $m_0 = 0.45$, $m_{\text{sus}} = m_{\text{nat}} = 0$.
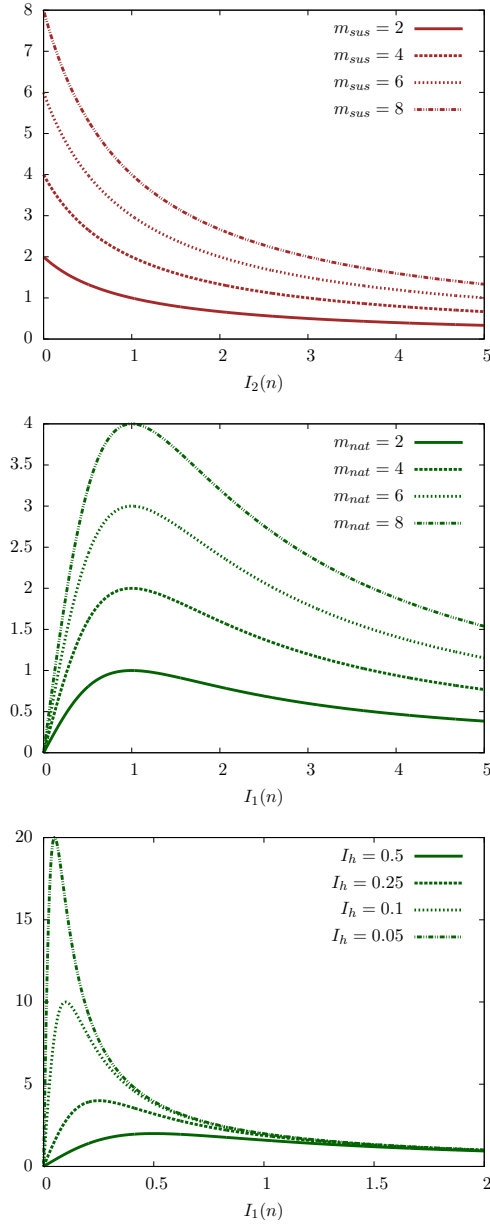
Figure 4.5: Grazing pressures as a function of available forage $I_j(n)$ for the simulations shown in this section. In all cases the grazing pressure monotonically changes for all values of forage. Top panel: sustained grazing with $j = 2$ for $I_h = 1$, varying m_{sus}. Middle panel: natural grazing with $j = 1$ for $I_h = 1$, varying m_{nat}. Bottom panel: natural grazing with $j = 1$ for $m_{\text{nat}} = 2$, varying I_h.

(a) $\overset{a}{m}_{\text{sus}} = 2$

(b) $\overset{a}{m}_{\text{sus}} = 4$

(c) $\overset{a}{m}_{\text{sus}} = 6$

(d) $\overset{a}{m}_{\text{sus}} = 8$

(e)
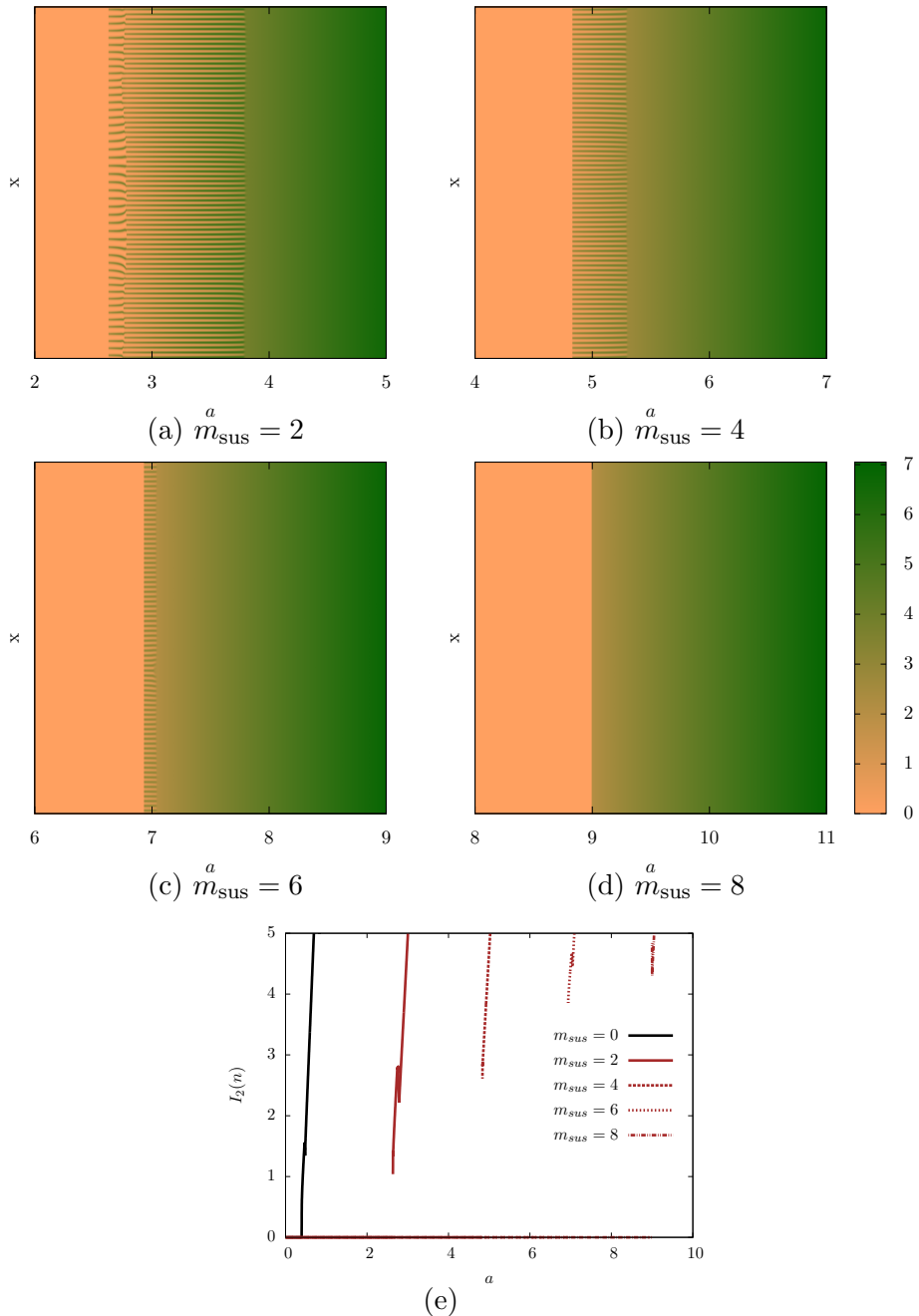
Figure 4.6: Influence of the maximum rate of intake $m_{\text{sus}} = 2, 4, 6, 8$ of sustained grazing with superlinear grazing $j = 2$ on the evolution of vegetation with a slowly decreasing rainfall parameter a, $\frac{\partial a}{\partial t} = -10^{-4}$, and $I_h = 1$. The colorbar besides panel (d) holds for all simulations in this figure. Panel (e) shows the evolution of forage per unit area $I_2(n)$ in the final stages, with very fast jumps to the bare desert state.

of loss of available forage, the final transition to the bare desert state becomes more dramatic as m_{sus} increases, as depicted in Figure 4.6(e) (Result 4, Section 4.1).

4.5.2 Varying maximum natural intake

For the following simulations we vary m_{nat}, while $I_h = 1$ and $j = 1$. Figure 4.5(b) shows that for the simulations shown in this subsection, distributions with $I_1(n) = I_h = 1$ are penalized the most compared to the simulation without grazing in Figure 4.1. This feeds the expectation that transitions from vegetation pattern with large $I_1(n)$ to small $I_1(n)$ occur and the jumps in available forage at these transitions becomes larger as m_{nat} increases. Since in general $g_{j,\mathrm{nat}} \to 0$ as $I_j(n) \to 0$, the destabilization of patterns with low $I_1(n)$ will not occur significantly earlier in a. As a result, the system spends more time residing in vegetation patterns with long wavelength (low wavenumber) as m_{nat} increases, which is confirmed by the simulations in Figure 4.7.

The value of a at the Turing instability, where pattern formation occurs, increases faster than m_{nat} increases. This corresponds to an increasing $\bar{a} = a - m_{\mathrm{nat}}$, which is in line but goes beyond what was shown in Section 4.4.4.

4.5.3 Varying natural herbivore persistence

In the final simulations we vary the herbivore peristence I_h in a natural grazing setting where $m_{\mathrm{nat}} = 2$ and $j = 1$. In Figure 4.5(c) we see that increasing the persistence of herbivores, by decreasing I_h, has a dramatic effect on the grazing pressure on vegetation with small $I_1(n)$ and barely any effect on vegetation with large $I_1(n)$. The panels in Figure 4.8 together with Figure 4.7(a) show how persistence affects the desertification process under decreasing rainfall.

Because we already saw in Figure 4.7(a) that pattern formation at the Turing instability occurs for $n \gg 1$, and persistence does not really affect grazing pressure at this level of available forage $I_j(n)$, it comes as no surprise that the location of the Turing instability in a is not different for different values of I_h (Figure 4.8).

From Figure 4.2(b) we recall that I_h determines at what intermediate value of available forage the grazing pressure is maximal. The smaller I_h,

(a) $m_\mathrm{nat} = 2$

(b) $m_\mathrm{nat} = 4$

(c) $m_\mathrm{nat} = 6$

(d) $m_\mathrm{nat} = 8$

(e)
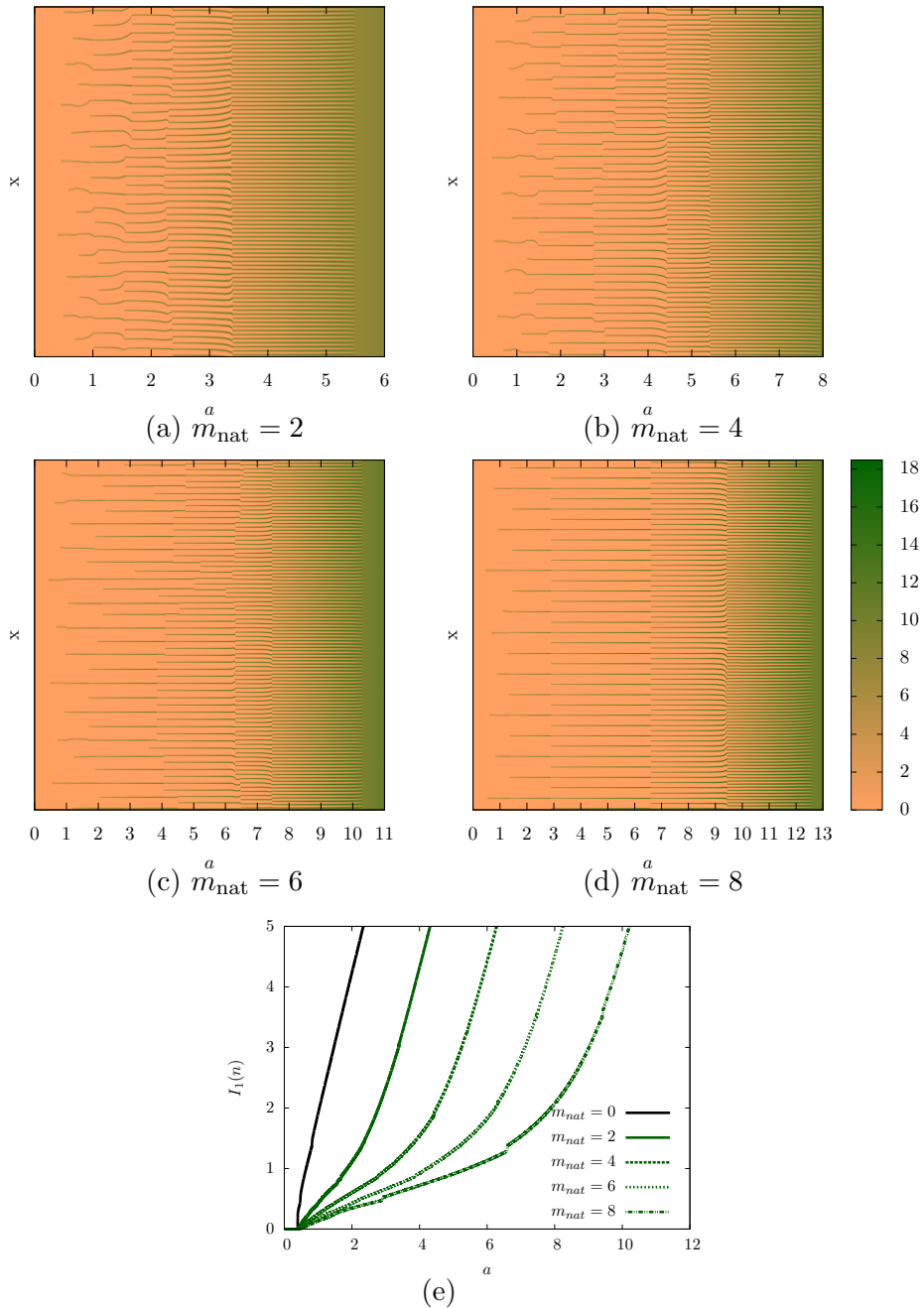
Figure 4.7: Influence of the maximum natural intake of natural grazing $m_\mathrm{nat} = 2, 4, 6, 8$ with linear foraging potential ($j = 1$) on vegetation evolution with slowly decreasing rainfall a, $\frac{da}{dt} = -10^{-4}$, and $I_h = 1$. The colorbar besides panel (d) holds for all the simulations in this figure. Panel (e) shows the evolution of forage per unit area $I_1(n)$ in the final stages.

the more dramatic the regime shift from high to low forage is. In Figure 4.8(d), near $a = 3$ a large majority of the vegetation patches disappears, which is also visible as a very fast jump in available forage (Results 3 and 4 of Section 4.1).

Hysteresis is expected to occur when returning from a vegetation pattern with small available forage to a vegetation pattern with large available forage, since intermediate patterns - that the system would reside in on its journey otherwise - are inadmissible. This hysteresis will therefore probably be stronger then reported for systems without explicit grazing [172, 180].

4.6 Discussion and outlook

The effects of grazing on system stability has already been studied for a nonspatial model in [134]. In another nonspatial model [194], soil degradation together with a vegetation dependent herbivore population allows for the possibility of irreversible vegetation change; analysis suggests this is less likely to occur for a natural herbivore population than for human controlled populations. In [196] it is shown that reduced plant cover results in focusing of herbivore grazing on the remaining vegetation, which may lead to the collapse of the entire vegetation [149].

The results in this chapter are in line with these previous model studies. In the simulations (Section 4.5), critical transitions have been shown to occur for both sustained and natural grazing (Result 4). The human controlled case in [196] corresponds to sustained grazing, where the vegetation change leads to the bare desert state, a transition that is irreversible. The prediction of these regime shifts by finding early-warning signals is of great interest [163], e.g. for conservation and management purposes.

We assumed throughout that herbivore dynamics is fast compared to biomass evolution. This assumption may not hold at the very fast transitions in the simulations of Figure 4.8(c) and (d); in that case herbivore population decrease may not keep up with forage decrease, which is expected to lead to an even more dramatic downfall of biomass [178].

We continue by putting forward some promising directions for future analysis and briefly discuss some possible model extensions.
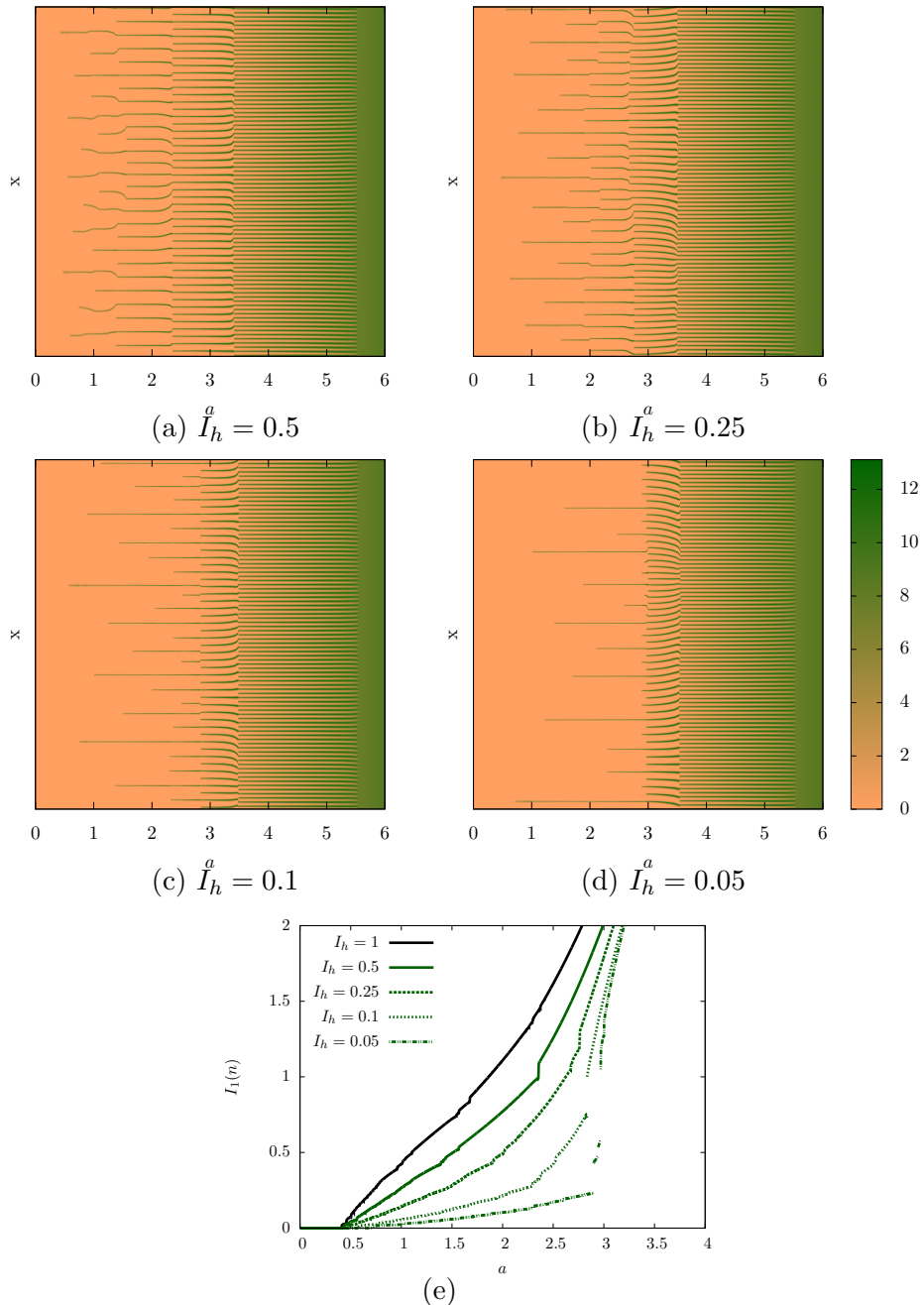
Figure 4.8: Influence of the persistence of natural grazing $I_h = 0.5, 0.25, 0.1, 0.05$ with linear foraging potential $(j = 1)$ on vegetation evolution with slowly decreasing rainfall a, $\frac{da}{dt} = -10^{-4}$, and $m_{\mathrm{nat}} = 2$. The colorbar besides panel (d) holds for all the simulations in this figure. Panel (e) shows the evolution of forage per unit area $I_1(n)$ in the final stages, with very fast jumps in the regimes with larger persistence.

4.6.1 Analysis

Construction of Busse balloons

Ultimately, the computation of overviews of stable periodic vegetation patterns, called Busse balloons [21, 176, 180, 199], would provide further insight in the influence of grazing on desertification scenarios. A Busse balloon is a representation of stable periodic patterns by a parameter-wavenumber pair. The computation requires the implementation of the linearizations of the grazing terms computed in Appendix 4.A in continuation software.

In this context, we translate the main results from the introduction into the following hypotheses on the Busse balloon.

1. Progressive rate grazing, where $j > 1$, leads to deflation of the Busse balloon.

2. Sustained grazing leads to Busse balloon lift-off. Without grazing the Busse balloon is connected to the x-axis through the existence of stable large wavelength patterns.

3. Natural grazing may split the Busse balloon in two disjoint parts. This may occur if states with intermediate available forage, which become inadmissible due to large grazing pressure, form a connected region in (rainfall, wavenumber)-space.

Concerning hypothesis 1, it would be interesting to see what destabilization mechanism is responsible for the deflation of the Busse balloon. The boundary of the Busse balloon has been found to be given primarily by a sideband instability [180, 199], although for small wavenumbers (large wavelengths) the boundary is given by a Hopf instabilities [51, 199]. Since the destabilization of the homogeneous steady state (w_+, n_+) can become dominated by Hopf instabilities (Section 4.4.4), the same could hold for periodic patterns and a larger part of the boundary of the Busse balloon may consist of Hopf instabilities. In case of a supercritical Hopf instability, the emergence of a limit cycle could act as an early warning signal.

Singular perturbation theory for sustained grazing: obstruction of existence of large wavelength patterns

We briefly sketch how sustained grazing may obstruct the existence of a large wavelength (small wavenumber) patterns, namely that of a single patch, within the extended Klausmeier model (4.15). We start out with the case

$j = 2$.

We view the limit $L \to \infty$, in which the single patch converges to a homoclinic state. In this limit the measure of forage per unit area of the pulse n, $I_2(n)$ (4.4), converges to 0. Thus the grazing pressure $g_{2,\text{sus}}$ (4.8) converges to $\frac{m_{\text{sus}}}{I_h}$. If the loss in vegetation through grazing is larger than the growth through the water uptake,

$$g_{2,\text{sus}} n^2 = \frac{m_{\text{sus}}}{I_h} n^2 > w n^2,$$

then the homoclinic pulse can't be a steady state. Since $w \leq a$ uniformly, it follows that for $a < \frac{m_{\text{sus}}}{I_h}$ the homoclinic pulse does not exist.

For $j = 1$, the nonlocal grazing contributes on the level of the linear death $-m_0 n$. By moving to the homoclinic limit the effective linear death rate becomes $m_0 + \frac{m_{\text{sus}}}{I_h}$.

Much more sophisticated results should be available for both the case $j = 1$ and $j = 2$ by making use of the singular perturbed nature of (4.15), which originates from the fact that $d_1 \gg d_2$. Large wavelength vegetation patterns consist of localized pulses. These pulses can be constructed by using geometric singular perturbation theory [45, 50].

4.6.2 Modeling

Slope and two space dimensions

The analysis here has been restricted to a finite domain in one space dimension without a slope. Future research in two dimensions with downslope water advection could show how grazing affects the stability of vegetation bands [176].

Combination of functional and numerical response

The division between sustained and natural grazing is a division between two extremes. Most populations of herbivores will exhibit both a functional and a numerical response. This may result in a response (4.2) that is the product of a Holling type II functional response and a type III numerical response, again yielding a sigmoid total grazing curve (albeit not of type III).

Palatability

Grazing resistance mechanisms of vegetation include grazing tolerance (large regrowth rates) and grazing avoidance (accessibility and palatability) [40]. In semi-arid rangelands, deterioration of rangelands is shown by replacement of palatable by unpalatable grasses [9]. Experiments confer that selective defoliation of palatable species could lead to their replacement by unpalatable species in grasslands [129]. On a Mongolia study location it was found that sites with a large grazing pressure developed a periodic pattern of unpalatable plants, whereas sites with less grazing pressure have a homogeneous vegetation cover and are dominated by palatable plants [136].

In arid ecosystem modeling it is rather common to make no distinction between plant species with different functional traits, e.g. palatability. It is thus assumed that all the present vegetation is equally available for consumption [134], a notable exception being [69]. A future distinction between palatable and unpalatable vegetation may retrieve the transition from spatially homogeneous predominantly palatable vegetation to an unpalatable periodic vegetation pattern in Mongolia [136]. Also the Holling functional response may change from type II to type III [80], as herbivores may need to learn to distinguish palatable plants in between unpalatable plants.

An increasing percentage of unpalatable vegetation may be an early warning signal for desertification, specific for increased environmental stress due to an increased grazing pressure. Reduced grazing pressure does not promptly lead to the palatable species recovering dominance [204]. The replacement of palatable by unpalatable species is not visible as a collapse in ecosystem biomass, although the economic service provided by the ecosystem does drop dramatically.

4.A General linearization of nonlocal grazing terms

For reference, we compute the linearization of the grazing terms (4.9) and (4.13). These are of use when determining the stability of system states. We start out by linearizing about arbitrary system states and end by simplifying to spatially homogeneous states.

It holds that, for general $j \geq 1$, the *Gâteaux differential* of I_j is given by

$$
\begin{aligned}
dI_j(n, \tilde{n}) &= \lim_{h \to 0} \frac{I_j(n + h\tilde{n}) - I_j(n)}{h} \\
&= \lim_{h \to 0} \frac{\int_0^L \int_0^1 \frac{d}{ds}(n + hs\tilde{n})^j \, ds \, dx}{Lh} \\
&= \lim_{h \to 0} \frac{1}{L} \int_0^L \int_0^1 j(n + hs\tilde{n})^{j-1} \tilde{n} \, ds \, dx \\
&= \frac{j}{L} \int_0^L n^{j-1} \tilde{n} \, dx
\end{aligned}
\tag{4.A.1}
$$

where we have ignored technical details for interchanging limit and integral.

Now we differentiate $g_{j,\text{sus}}$ and $g_{j,\text{nat}}$:

$$
\begin{aligned}
dg_{j,\text{sus}}(n, \tilde{n}) &= \lim_{h \to 0} \frac{g_{j,\text{sus}}(n + h\tilde{n}) - g_{j,\text{sus}}(n)}{h} \\
&= \lim_{h \to 0} \frac{\frac{m_{\text{sus}}}{I_h + I_j(n + h\tilde{n})} - \frac{m_{\text{sus}}}{I_h + I_j(n)}}{h} \\
&= \frac{-m_{\text{sus}}}{I_h + I_j(n)} \lim_{h \to 0} \frac{1}{I_h + I_j(n + h\tilde{n})} \frac{I_j(n + h\tilde{n}) - I_j(n)}{h} \\
&= \frac{-m_{\text{sus}}}{(I_h + I_j(n))^2} dI_j(n, \tilde{n}),
\end{aligned}
\tag{4.A.2}
$$

$$
\begin{aligned}
dg_{j,\text{nat}}(n, \tilde{n}) &= \lim_{h \to 0} \frac{g_{j,\text{nat}}(n + h\tilde{n}) - g_{j,\text{nat}}(n)}{h} \\
&= \lim_{h \to 0} \frac{\frac{m_{\text{nat}} I_j(n + h\tilde{n})}{I_h^2 + I_j(n + h\tilde{n})^2} - \frac{m_{\text{nat}} I_j(n)}{I_h^2 + I_j(n)^2}}{h} \\
&= \frac{m_{\text{nat}}}{I_h^2 + I_j(n)^2} \lim_{h \to 0} \frac{I_h^2 - I_j(n) I_j(n + h\tilde{n})}{I_h^2 + I_j(n + h\tilde{n})^2} \frac{I_j(n + h\tilde{n}) - I_j(n)}{h} \\
&= m_{\text{nat}} \frac{I_h^2 - I_j(n)^2}{\left(I_h^2 + I_j(n)^2\right)^2} dI_j(n, \tilde{n}).
\end{aligned}
\tag{4.A.3}
$$

4.A.1 Spatially homogeneous states

Restricting to spatially homogeneous states, denoted by $n_\pm$, the Gâteaux differential of I_j (4.A.1) simplifies to

$$dI_j(n_\pm, \tilde{n}) = \frac{jn_\pm^{j-1}}{L} \int_0^L \tilde{n} \, dx. \tag{4.A.4}$$

Depending on the boundary conditions we can choose an appropriate basis for the perturbations.

Neumann boundary conditions

A basis of $L^2[0, L]$ with Neumann boundary conditions is given by the functions $\tilde{n}_k(x) = \cos(kx)$ with k an integer multiple of $\frac{\pi}{L}$. Substitution in (4.A.4) yields

$$dI_j(n_\pm, \cos(kx)) = \begin{cases} jn_\pm^{\,j-1} & \text{if } k = 0 \\ 0 & \text{if } k \neq 0 \end{cases}$$

Thus the linearization acts differently on spatially homogeneous and spatially inhomogeneous perturbations.

Any perturbation $\tilde{n}$ can be written as a linear combination $\tilde{n} = \sum_{k=0}^{\infty} \beta_k \tilde{n}_k$. Substitution into (4.A.2) and (4.A.3) yields

$$dg_{j,\text{sus}}(n_\pm, \tilde{n}) = \beta_0 \frac{-m_{\text{sus}}}{(I_h + n_\pm{}^j)^2} jn_\pm{}^{j-1}, \tag{4.A.5}$$

$$dg_{j,\text{nat}}(n_\pm, \tilde{n}) = \beta_0 m_{\text{nat}} \frac{I_h{}^2 - n_\pm{}^{2j}}{(I_h{}^2 + n_\pm{}^{2j})^2} jn_\pm{}^{j-1}. \tag{4.A.6}$$

Periodic boundary conditions

For periodic boundary conditions a basis is given by functions $\cos(kx)$ and $\sin(kx)$, but now k is an integer multiple of $\frac{2\pi}{L}$, leading to the same results (4.A.5) and (4.A.6) since also $dI_j(n_\pm, \sin(kx))$ vanishes (for k an integer multiple of $\frac{2\pi}{L}$).

5 Quasilinear parabolic reaction-diffusion systems: user's guide to well-posedness, spectra and stability of travelling waves

This paper is concerned with quasilinear parabolic reaction-diffusion-advection systems on extended domains. Frameworks for well-posedness in Hilbert spaces and spaces of continuous functions are presented, based on known results using maximal regularity. It is shown that spectra of travelling waves on the line are meaningfully given by the familiar tools for semilinear equations, such as dispersion relations, and basic connections of spectra to stability and instability are considered. In particular, a principle of linearized orbital instability for manifolds of equilibria is proven. Our goal is to provide easy access for practitioners to these rigorous aspects. As a guiding example the Gray-Scott-Klausmeier model for vegetation-water interaction is considered in detail, which is a rescaling of the extended Klausmeier model considered in earlier chapters.

5.1 Introduction

In this paper we present rigorous frameworks for well-posedness, spectra and nonlinear stability of travelling wave solutions (pulses, fronts and wavetrains) of quasilinear parabolic reaction-diffusion systems of the form

$$u_t = (a(u)u_x)_x + f(u, u_x), \qquad t > 0, \qquad x \in \mathbb{R}, \qquad (5.1.1)$$

with unknown $u(t,x) \in \mathbb{R}^N$. The nonlinearities a, f are smooth and $a(u) \in \mathbb{R}^{N \times N}$ is strongly elliptic in the domain of interest, but does not have to be symmetric. We further consider a variant of (5.1.1) in higher space dimensions $x \in \mathbb{R}^n$ up to $n = 3$. The nonlinearities may also depend explicitly on x in an appropriate way.

Quasilinear reaction-diffusion systems arise as models in various contexts due to nonlinear fluxes, density dependent diffusion, self or cross diffusion, see e.g. [3, 152, 153]. For pattern formation problems it is natural to consider an extended domain and to neglect the influence of boundary conditions. Travelling waves, i.e., solutions of (5.1.1) constant in a co-moving frame $\xi = x - ct$ with speed $c \in \mathbb{R}$ having constant or periodic asymptotic states, are among the simplest interesting reaction-diffusion patterns and are observed for different types of quasilinear systems, see, e.g., [82, 104, 117, 126, 131, 169, 205].

For semilinear parabolic problems on the line it is well-known that e.g. H^1 or BUC^1 are suitable phase spaces for well-posedness in a perturbative setting [27, 78]. The corresponding spectrum of the linearization is characterized in terms of the dispersion relation and the Evans function [63, 157]. In some situations, in particular when the essential spectrum does not touch the imaginary axis, nonlinear (orbital) stability of a wave can directly be deduced by a principle of linearized stability [78, 166]. An excellent reference for the spectrum and stability of nonlinear waves in the semilinear context is [90]. We also mention the abstract solution theory in Sobolev spaces [112], which can be used for fluid problems in unbounded domains, e.g., [14, 191].

For quasilinear models an analogous unified framework for well-posedness, spectra and stability of waves seems less known. It seems that the majority of concrete well-posedness results in the literature concerns bounded domains. Moreover, when the general results are formulated abstractly or under abstract conditions, a user needs to search for suitable function spaces and verify hypotheses that lead astray (even though some examples provide guidelines).

However, the spectrum of the linearization in a travelling wave can only be meaningfully determined based on a well-posedness setting. For instance, a Turing-instability determined via the usual dispersion relation lacks a basis without a consistent phase space. Conveniently, the pattern forming nature of a Turing-instability can be identified ad hoc since the existence of travelling wave patterns is an ODE problem. Well-posedness is, however, required to prove that a spectrally unstable solution indeed is unstable under the nonlinear evolution. Such a result then justifies the computation of stability boundaries by the spectrum as in [147, 199] (see also §5.5).

The purpose of this paper is to present rigorous settings for quasilinear parabolic problems in the travelling wave context as described above. We aim for a presentation accessible to practitioners, in the spirit of [27, 78, 157] for semilinear problems. To this end we bring together and apply to (5.1.1) mostly abstract results from the different fields involved in well-posedness, spectra and stability. This puts the naively expected analogy to the semilinear case on firm grounds. For quasi-linear systems, new difficulties mainly arise on a technical level concerning well-posedness and nonlinear stability. Most importantly, a variation-of-constants formula is not available. Further, when dealing with quasi-linear problems one has to take into account all available regularity as prescribed by sharp trace results such that in general one cannot take fractional power domains as a phase space for the solution semiflow. Instead one has to work with real interpolations spaces (see section 5.2.1) or the domain of the linearized operator itself. However, in the end it turns out that the familiar spaces H^2 and BUC^2 are possible phase spaces and that the spectral theory and the sufficient conditions for nonlinear stability are analogous to the semilinear case, at least in noncritical cases.

There are several abstract settings for well-posedness of general quasilinear parabolic problems available in the literature (see [3, 6, 29, 75, 91, 99, 114, 143, 206], and [5] as well as §5.2.3 for a selective overview). These have advantages and disadvantages depending on the present context, and the geometric (qualitative) theory is more or less developed in each case. On the other hand, solutions may be constructed by fixed point arguments tailor-made for the issues under investigation (e.g. [210]). The (real) viscous conservation laws are an important and well studied class of quasilinear problems, where well-posedness results exploit the additional structure [93]. We refer to the survey [211] and the references therein.

Our focus lies on the approach of [28, 99, 143] based on maximal L^p - regu-

larity, but we also highlight the approach of [114] based on maximal Hölder regularity. Besides reaction-diffusion problems, the approach of [28, 99, 143] and its extensions apply successfully to the local theory of free boundary problems and to general parabolic problems with nonlinear boundary conditions. Here the geometric theory is well-developed and still advances, especially for the needs in the context of free boundary problems. The approach of [114] also applies to fully nonlinear problems.

Recently, in [144, 145] the principle of linearized orbital stability with asymptotic phase for manifolds of equilibria has been established in the quasilinear case, for any sufficiently strong well-posedness setting (see e.g. [78, Section 5.1] for the semilinear case). It in particular applies to the orbital stability of pulses and fronts for (5.1.1) in both approaches mentioned before. The conclusion from arbitrary unstable spectrum to nonlinear orbital instability of a manifold of equilibria does not seem to exist in the literature. Refining arguments from [78, Theorem 5.1.5] and [168] for single equilibria, we close this gap in the present paper. This might be of interest also in other contexts, where families of equilibria occur.

In more detail, our considerations may be summarized as follows.

- In one space dimension, $x \in \mathbb{R}$, a possible phase space for the evolution under (5.1.1) of localized perturbations from travelling wave and other pattern type solutions is the Sobolev space H^2 (Theorem 5.4). For non-localized perturbations BUC^2 (C^2–functions, bounded and uniformly continuous with all derivatives) is a possible phase space (Theorem 5.7).

- For space dimensions $x \in \mathbb{R}^n$ with $n \leq 3$ other possible phase spaces are certain Besov spaces, (real) interpolating between L^2 and the Sobolev space H^2 (Theorem 5.5). Here the linearization can directly be considered on L^2.

- The 'spatial dynamics' spectral theory developed for semilinear parabolic systems on the line applies also in the quasilinear case, which allows to compute the spectrum of travelling waves in a familiar way (see §5.3.3). In particular, the spectrum is independent of the chosen setting (Proposition 1).

- The well-known nonlinear stability result with asymptotic phase for travelling waves with simple zero eigenvalue applies in these settings (Proposition 2, as a direct consequence of [144, 145]).

- Without assuming a spectral gap or an unstable eigenvalue, it is shown

that an unstable spectrum implies orbital instability of pulses and fronts (Theorem 5.8) and instability of wavetrains (Proposition 3). Here we rely on a general result on orbital instability of manifolds of equilibria (Lemma 5.1).

We emphasize that the divergence form (5.1.1) is only assumed in view of applications. In a smooth setting, the equation $u_t = a(u)u_{xx} + f(u, u_x)$ can be cast into divergence form by a suitable redefinition of a and f.

We believe that also the more general results in [158] on spectra of modulated travelling waves carry over to the quasilinear case, but we do not enter into details here. Also the nonlinear stability of wavetrains is not considered. This is a delicate issue since zero always lies in the essential spectrum. Hence, the best one can hope for is heat-equation-like decay. Under certain assumptions this has been established for the semilinear reaction-diffusion case in [52, 166]. A special quasilinear case, more precisely the quasilinear IBL model, is considered in [77]. Also for viscous shocks the spectrum touches the origin and stability in weighted spaces can be established. We refer to [212], the survey [211] and the references therein, as well as to [15] for more recent results.

In §5.5 we illustrate our general considerations by means of the Gray-Scott-Klausmeier vegetation-water interaction model [97], for $x \in \mathbb{R}$ given by

$$
\begin{aligned}
w_t &= (w^2)_{xx} + Cw_x + A(1 - w) - wv^2, \\
v_t &= Dv_{xx} - Bv + wv^2,
\end{aligned}
\tag{5.1.2}
$$

with constants $A, B \geq 0$, $C \in \mathbb{R}$ and $D > 0$. This system is the original motivation for the present study. It is quasilinear due to the porous medium term $(w^2)_{xx} = 2(ww_{xx} + (w_x)^2)$ and is therefore parabolic only in the regime $w > 0$, in which (5.1.2) supports a large family of travelling waves (see [199] and §5.5).

This paper is organized as follows. In §5.2 different well-posedness setting results for (5.1.1) are treated, §5.3 is devoted to the spectrum of the linearization in travelling waves. The connection to nonlinear stability and instability is considered in §5.4. In §5.5 we expand the discussion of (5.1.2) and illustrate the application of the general results. For the sake of self-containedness we prove some technical results in the appendix.

Notation. All Banach spaces are real, and we consider complexifications if necessary. We write $\mathscr{L}(X_1, X_0)$ for the bounded linear operators between Banach spaces X_0, X_1, and $\mathscr{L}(X_0) = \mathscr{L}(X_0, X_0)$. The usual

Sobolev spaces based on $L^p(\mathbb{R}^n)$ are denoted by $H^{k,p}$, and $H^k = H^{k,2}$. By $\mathrm{BC}^k = \mathrm{BC}^k(\mathbb{R}^n)$ and $\mathrm{BUC}^k = \mathrm{BUC}^k(\mathbb{R}^n)$ we denote the Banach space of bounded C^k-functions and of bounded C^k-functions such that all derivatives up to order k are uniformly continuous, respectively.

5.2 Frameworks for well-posedness

We formulate the abstract well-posedness results based on maximal regularity and present three concrete frameworks for quasilinear reaction-diffusion systems. In one space dimension we obtain well-posedness in H^2 and in BUC^2, and in space dimensions less than or equal to three we have well-posedness in certain Besov spaces. More general problems and further settings are briefly discussed at the end of this section.

5.2.1 Well-posedness based on maximal L^p-regularity

We formulate the results of [99, 143] for abstract quasilinear parabolic problems of the form

$$\partial_t u = A(u)u + F(u), \quad t > 0, \qquad u(0) = u_0, \tag{5.2.1}$$

in a Hilbert space setting. Let X_0, X_1 be Hilbert spaces with X_1 continuously and densely embedded into X_0. Roughly speaking, X_0 is the base space for (5.2.1) and $A(u(t))$ is an unbounded linear operator on X_0 with domain X_1. It turns out that on this abstract level the phase space of the solution semiflow for (5.2.1) acts is a real interpolation space,

$$\mathcal{X} = (X_0, X_1)_{1-1/p,p}, \qquad p \in (1, \infty),$$

between X_0 and X_1. For a definition and the properties of these spaces we refer to the textbooks [18, 115, 188]. At this point we only note that $X_1 \subset \mathcal{X} \subset X_0$ and that $\mathcal{X}$ is in general *not* a Hilbert space, with exceptions for $p = 2$. Fortunately, explicit characterizations of $\mathcal{X}$ are possible in the concrete settings that we shall use later, e.g., $H^1 = (L^2, H^2)_{1/2,2}$. The real interpolation spaces are the analogue to the fractional power domains in the

semilinear theory [27, 78]. These two types of intermediate spaces between X_0 and X_1 differ, in general (again with exceptions for $p = 2$), but are closely related (see, e.g., [115, Proposition 4.1.7]).

Recall from [60, 114] that a densely defined operator B on X_0 generates a strongly continuous analytic semigroup if and only if $\|\lambda(\lambda - B)^{-1}\|_{\mathscr{L}(X_0)}$ is uniformly bounded for λ in a left open sector in $\mathbb{C}$.

As a consequence of the results in [99, 143] we have

Theorem 5.1. *Let $p \in (1, \infty)$ and $X_1 \subset \mathcal{X} \subset X_0$ be as above. Assume there is an open set $\mathcal{V} \subseteq \mathcal{X}$ such that*

- *$F : \mathcal{V} \to X_0$ and $A : \mathcal{V} \to \mathscr{L}(X_1, X_0)$ are Lipschitz on bounded sets;*
- *for each $w_0 \in \mathcal{V}$, the operator $A(w_0)$ with domain X_1 generates a strongly continuous analytic semigroup on X_0.*

Then (5.2.1) is locally well-posed in $\mathcal{V}$, with solutions in a strong L^p-sense.

More precisely, the theorem yields solvability of (5.2.1) as follows. For each initial value $u_0 \in \mathcal{V}$ there is a maximal existence time $t^+(u_0) > 0$ and a unique solution $u = u(\cdot; u_0) \in C([0, t^+(u_0)), \mathcal{V})$ of (5.2.1), such that $u \in H^{1,p}(J, X_0) \cap L^p(J, X_1)$ for time intervals $J = (0, T)$ with $T < t^+(u_0)$. Here $H^{1,p}(J, X_0)$ denotes a vector-valued Sobolev space, which is defined as in the scalar case. Furthermore, $t^+(u_0)$ is finite only if either $\mathrm{dist}(u(t; u_0), \partial \mathcal{V}) \to 0$ or $\|u(t; u_0)\|_{\mathcal{X}} \to \infty$ as $t \to t^+(u_0)$. The map $t^+ : \mathcal{V} \to (0, \infty]$ is lower semicontinuous, and the local solution semiflow, $(t, u_0) \mapsto u(t; u_0)$, is continuous with values in $\mathcal{V} \subseteq \mathcal{X}$. If F and A are smooth, then the semiflow enjoys smoothness properties as well. We demonstrate this in Proposition 4 in the appendix for a neighbourhood of a steady state.

Note that if $A(w_0)$ generates an analytic semigroup for $w_0 \in \mathcal{X}$, then the Lipschitz property of A as in the theorem combined with well-known perturbation results for semigroups (see [114, Proposition 2.4.2]) imply that this is true for any $A(\tilde{w}_0)$ with $\tilde{w}_0$ in a small neighbourhood of w_0. This gives a candidate for $\mathcal{V}$.

To verify the assumptions in [99, Section 2], [143, Theorem 3.1] and prove Theorem 5.1 we only need to know that $-A(w_0)$ has for each $w_0 \in \mathcal{V}$ the property of maximal L^p-regularity on finite time intervals J. But in *Hilbert spaces* this already follows from the assumed generator property of $A(w_0)$. Indeed, by [55, Theorems 3.3, 7.1] it suffices to consider the case $p = 2$, $J = \mathbb{R}_+$ and that the semigroup generated by $A(w_0)$ is exponentially

decaying. In this situation maximal L^2-regularity follows from [33] (see also [143, Theorem 1.6] for the short proof using Plancherel's theorem).

One space dimension: well-posedness in H^2

For $u(t,x) \in \mathbb{R}^N$ we apply the abstract result Theorem 5.1 to the reaction-diffusion system

$$u_t = (a(u)u_x)_x + f(u, u_x), \qquad t > 0, \qquad x \in \mathbb{R}. \qquad (5.2.2)$$

To obtain a simple setting with familiar function spaces which is at the same time directly linked to L^2-spectral theory, we work with $X_0 = H^1 = H^1(\mathbb{R})^N$ as a base space. In one space dimension (and only there) this is possible since H^1 is an algebra, i.e., $uw \in H^1$ and $\|uv\|_{H^1} \leq C\|u\|_{H^1}\|v\|_{H^1}$ for $u, w \in H^1$.

We start with the case when the nonlinearities in (5.2.2) are everywhere defined. We emphasize that a does not have to be symmetric, and that a, f may be less regular than actually stated.

Theorem 5.2. *Assume $a : \mathbb{R}^N \to \mathbb{R}^{N \times N}$ is C^4 such that $a(\zeta) \in \mathbb{R}^{N \times N}$ is positive definite for each $\zeta \in \mathbb{R}^N$, and that $f : \mathbb{R}^N \times \mathbb{R}^N \to \mathbb{R}^N$ is C^3 with $f(0,0) = 0$.*

Then (5.2.2) is locally well-posed in the phase space $\mathcal{X} = H^2$. The solutions belong to $H^1(J, H^1(\mathbb{R})) \cap L^2(J, H^3(\mathbb{R})) \cap C(\overline{J}, H^2(\mathbb{R}))$ on time intervals $J = (0, T)$ away from the maximal existence time.

Proof. We choose $X_0 = H^1$, $X_1 = H^3$ and $p = 2$. Then $\mathcal{X} = (H^1, H^3)_{1/2,2} = H^2$, see [188, Remark 2.4.2/2]. Define the superposition (Nemytskii) operators A and F by $A(u)v = (a(u)v_x)_x$ and $F(u) = f(u, u_x)$. Then $F : H^2 \to H^1$ and $A : H^2 \to \mathscr{L}(H^3, H^1)$ are Lipschitz on bounded sets by Lemma 5.2. For the generator property, let $w_0 \in H^2$ be arbitrary. Denote by A_{L^2} the realization of $A(w_0)$ on L^2, with domain H^2. Since $w_0, a(w_0) \in \mathrm{BC}^1$ by Sobolev's embedding $H^1 \subset \mathrm{BC}$, it follows from [7, Corollary 9.5] that the operator A_{L^2} generates an analytic C_0-semigroup on L^2. Next, let A_{H^1} be the realization of $A(w_0)$ on H^1, i.e., the restriction of A_{L^2} to H^1. Since $H^1 = (L^2, H^2)_{1/2,2}$ (see again [188]), it follows from [115, Theorem 5.2.1] that A_{H^1} with domain $D(A_{H^1}) = \{u \in H^2 : A_{L^2}u \in H^1\}$ generates an analytic C_0-semigroup as well. Using the algebra property of H^1, it is elementary to check that $D(A_{H^1}) = H^3$ (see the proof of Lemma 5.4 in the appendix). Thus Theorem 5.1 applies. $\qquad \square$

Remark 5.3. *Employing, e.g.,* Angenent's parameter trick *(see [143, Theorem 5.1] and [62]), one can show that for smooth nonlinearities the solutions of* (5.2.2) *are smooth in space and time.*

When investigating the stability of a non-localized travelling wave with respect to localized perturbations, one is lead to a variant of (5.2.2) with x-dependent nonlinearities. Furthermore, in many situations the nonlinearities are not everywhere defined on $\mathbb{R}^N$, or the leading coefficient a is positive definite only in a subset of $\mathbb{R}^N$. For instance, this is the case for the Gray-Scott-Klausmeier model (5.1.2), where the focus lies on perturbations of travelling wave solutions in the parabolic regime $w > 0$.

For a general formulation, let $\overline{u} \in \mathrm{BC}^2(\mathbb{R}, \mathbb{R}^N)$ be a steady state of (5.2.2), i.e.,

$$(a(\overline{u})\overline{u}_x)_x + f(\overline{u}, \overline{u}_x) = 0. \tag{5.2.3}$$

Then $\overline{u} + u$ solves (5.2.2) for a perturbation u if and only if u solves

$$u_t = (a(\overline{u} + u)u_x)_x + (a(\overline{u} + u)\overline{u}_x)_x + f(\overline{u} + u, \overline{u}_x + u_x). \tag{5.2.4}$$

For this perturbative setting we have the following variant of Theorem 5.2. Here and in the following, the image of $\overline{u}$ is meant to be the set $\{\overline{u}(x) \; : \; x \in \mathbb{R}\}$.

Theorem 5.4. *Let* $\overline{u} \in \mathrm{BC}^2(\mathbb{R}, \mathbb{R}^N)$ *satisfy* (5.2.3), *and let* $U_1, U_2 \subseteq \mathbb{R}^N$ *be open neighbourhoods of the closure of the images of* $\overline{u}$ *resp.* $\overline{u}_x$. *Assume* $a : U_1 \to \mathbb{R}^{N \times N}$ *is* C^4 *such that* $a(\zeta)$ *is positive definite for any* $\zeta \in U_1$, *and* $f : U_1 \times U_2 \to \mathbb{R}^N$ *is* C^3.

Then there is an open neighbourhood $\mathcal{V}$ *of the zero function in* H^2 *such that* (5.2.4) *is locally well-posed in* $\mathcal{V}$. *If* $U_1 = U_2 = \mathbb{R}^N$, *then one can take* $\mathcal{V} = H^2$.

Proof. Let again $X_0 = H^1$, $X_1 = H^3$ and $p = 2$, such that $\mathcal{X} = H^2$. Define

$$A(u)v = (a(\overline{u} + u)v_x)_x, \quad F(u) = (a(\overline{u} + u)\overline{u}_x)_x + f(\overline{u} + u, \overline{u}_x + u_x). \tag{5.2.5}$$

Using $F(0) = 0$, Lemma 5.2 yields $\mathcal{V} \subseteq H^2$ such that $F : \mathcal{V} \to H^1$ and $A : \mathcal{V} \to \mathscr{L}(H^3, H^1)$ are Lipschitz on bounded sets. If $\mathcal{V}$ is sufficiently small, then for each $w_0 \in \mathcal{V}$ the leading coefficient $a(\overline{u} + w_0)$ of $A(w_0)$ is positive definite, uniformly in $x \in \mathbb{R}$. Thus as in the proof of Theorem 5.2 it follows from [7, Corollary 9.5] and an interpolation argument that $A(w_0)$ with domain H^3 has the required generator property on H^1 to apply Theorem 5.1. □

5 Quasilinear parabolic reaction-diffusion systems

Well-posedness in space dimensions $n \leq 3$

For simplicity, on $\mathbb{R}^n$ we consider quasilinear reaction-diffusion-advection problems (using sum convention)

$$u_t = \partial_i(a_{ij}(u)\partial_j u) + c_i\partial_i u + f(u), \qquad x \in \mathbb{R}^n. \qquad (5.2.6)$$

Here, essentially, $a_{ij} : \mathbb{R}^N \to \mathbb{R}^{N \times N}$, $c_i \in \mathbb{R}^{N \times N}$ for $i,j = 1,...,n$ and $f : \mathbb{R}^N \to \mathbb{R}^N$. The approach of the previous subsection works in any dimension if one takes $X_0 = H^k(\mathbb{R}^n)$ with $k > \frac{n}{2}$ as a base space, since then H^k is an algebra and the superposition operators are Lipschitz as before.

We present another functional analytic setting with $X_0 = L^2$ as a base space, for which Theorem 5.1 applies to (5.2.6) in space dimensions $n \leq 3$. The price one has to pay in the maximal L^p-regularity approach is that the phase space $\mathcal{X} = (L^2, H^2)_{1-1/p,p}$ becomes slightly more complicated to describe. It is the N-fold product $B_{2,p}^s$ of a *Besov space* $B_{2,p}^s(\mathbb{R}^n)$, with $s > 0$ and $p \in (1, \infty)$. For $s \notin \mathbb{N}$, it follows from [189, Theorem 2.6.1] that an equivalent norm for this space is given by

$$\|u\|_{B_{2,p}^s} = \|u\|_{H^k} + \sum_{|\alpha| \leq k} \left(\int_{|h| \leq 1} |h|^{-(s-k)p-n} \|D^\alpha u(\cdot + h) - D^\alpha u(\cdot)\|_{L^2}^p \, dh \right)^{1/p},$$

where k is the largest integer smaller than s. The Besov spaces are closely related to the more common Bessel-potential spaces H^s. For any $\varepsilon > 0$ we have the dense inclusions $H^{s+\varepsilon} \subset B_{2,p}^s \subset H^{s-\varepsilon}$. However, $B_{2,p}^s = H^s$ if and only if $p = 2$, and furthermore $B_{2,p}^s$ is a Hilbert space only for $p = 2$. Essential for the applications are the Sobolev embeddings

$$B_{2,p}^s(\mathbb{R}^n) \subset \mathrm{BC}(\mathbb{R}^n) \quad \text{for } s > \frac{n}{2}, \quad B_{2,p}^s(\mathbb{R}^n) \subset L^q(\mathbb{R}^n) \quad \text{for } s \geq \frac{n}{2} - \frac{n}{q} > 0.$$
$$(5.2.7)$$

These are a consequence of $B_{2,p}^s \subset H^{s-\varepsilon}$ and the corresponding embeddings for the H-spaces. For these and many more properties of B-spaces we refer to [188].

As above we consider a perturbative setting. Analogous to (5.2.4), for perturbations u of a steady state $\overline{u} \in \mathrm{BC}^2(\mathbb{R}^n, \mathbb{R}^N)$ of (5.2.6), one is lead to

$$\partial_t u = \partial_i(a_{ij}(\overline{u} + u)\partial_j u) + \partial_i(a_{ij}(\overline{u} + u)\partial_j\overline{u}) + c_i\partial_i(u + \overline{u}) + f(\overline{u} + u). \quad (5.2.8)$$

Note that the following well-posedness result in particular applies to (5.2.6) when setting $\overline{u} = 0$ and assuming $f(0) = 0$. Again no symmetry properties of the diffusion coefficients (a_{ij}) are required.

Theorem 5.5. *Let $n = 1, 2, 3$. Let $\overline{u} \in \mathrm{BC}^2(\mathbb{R}^n, \mathbb{R}^N)$ be a steady state of (5.2.6), and let $U \subseteq \mathbb{R}^N$ be an open neighbourhood of the closure of its image. For all $i, j = 1, ..., n$, assume that $c_i \in \mathbb{R}^{N \times N}$ is constant, that $a_{ij} : U \to \mathbb{R}^{N \times N}$ and $f : U \to \mathbb{R}^N$ are C^2, and that $a_{ij}(\zeta)$ is positive definite for any $\zeta \in U$.*

Then for all sufficiently large $p \in (2, \infty)$ there is an open neighbourhood $\mathcal{V}$ of the zero function in $B_{2,p}^{2-2/p} = B_{2,p}^{2-2/p}(\mathbb{R}^n)^N$ such that (5.2.8) is locally well-posed in $\mathcal{V}$. The solutions belong to $H^{1,p}(J, L^2) \cap L^p(J, H^2) \cap C(\overline{J}, \mathcal{V})$ on time intervals J away from the maximal existence time. If $U = \mathbb{R}^N$, then one can take $\mathcal{V} = B_{2,p}^{2-2/p}$.

Proof. The choice $X_0 = L^2$ and $X_1 = H^2$ leads to

$$B_{2,p}^{2-2/p} = \mathcal{X} = (X_0, X_1)_{1-1/p,p} \text{ for } p \in (1, \infty),$$

see [188, Remark 2.4.2/4]. Let $A(u)v = \partial_i(a_{ij}(\overline{u} + u)\partial_j v)$, and denote by $F(u)$ the remaining terms on the right-hand side of (5.2.8). The Lipschitz properties of A and F on a neighbourhood $\mathcal{V}$ of zero follow from Lemma 5.3. For $w_0 \in \mathcal{V}$ the operator $A(w_0)$ is elliptic, the coefficients are bounded and the leading coefficient is uniformly Hölder continuous, since $B_{2,p}^{2-2/p}$ even embeds into BC^σ for some $\sigma > 0$ if $n \le 3$ and p is large, see [188, Theorem 2.8.1]. Now the generator property on L^2 follows again from [7, Corollary 9.5]. □

5.2.2 Well-posedness based on maximal Hölder regularity

We formulate the well-posedness result of [114, Chapter 8] for abstract quasilinear parabolic problems

$$\partial_t u = A(u)u + F(u), \quad t > 0, \qquad u(0) = u_0. \tag{5.2.9}$$

The approach of [114] is based on maximal Hölder regularity (see also [4, Chapter III.2] for the general linear theory). It also covers fully nonlinear problems and does not take into account the quasilinear structure of (5.2.9). It has the big advantage to be applicable in arbitrary Banach spaces X_0, while in applications maximal L^p-regularity is usually restricted to reflexive Banach spaces, excluding spaces of continuous functions. Moreover, the phase space equals the domain of the linearized operator, which is usually easier to describe than an interpolation space.

The following well-posedness result for (5.2.9) is a consequence of [114, Theorem 8.1.1, Proposition 8.2.3, Corollary 8.3.3].

Theorem 5.6. *Let X_0, X_1 be arbitrary Banach spaces such that X_1 is continuously and densely embedded in X_0. Let $\mathcal{V} \subseteq \mathcal{X} := X_1$ be open, define $\mathcal{F}(u) = A(u)u + F(u)$ and suppose that*

- *$\mathcal{F} \in C^1(\mathcal{V}, X_0)$ with locally Lipschitz derivative;*
- *for each $w_0 \in \mathcal{V}$, the operator $\mathcal{F}'(w_0)$ with domain X_1 generates a strongly continuous analytic semigroup on X_0 and $\|u\|_{X_0} + \|\mathcal{F}'(w_0)u\|_{X_0}$ defines an equivalent norm on X_1.*

Then (5.2.9) is locally well-posed in $\mathcal{V}$, and solutions are classical in time.

As already mentioned, the phase space $\mathcal{X}$ is now a subset of X_1 and not of an intermediate space between X_0 and X_1. Well-posedness is similar as for Theorem 5.1. The maximal existence time is lower semicontinuous and the solution semiflow is continuous with values in $\mathcal{V}$. For each $\alpha \in (0, 1)$ and an initial value $u_0 \in \mathcal{V}$, one obtains a unique maximal solution u of (5.2.9) such that $u \in \mathrm{BUC}_\alpha^{1+\alpha}([0, T], X_0) \cap \mathrm{BUC}_\alpha^\alpha([0, T], X_1)$ for $T < t^+(u_0)$. Here $\mathrm{BUC}_\alpha^\alpha$ is a weighted Hölder space, see [4, Chapter III.2] and [145, Example 3]. (It is slightly confusing that these spaces differ from the ones in [114] denoted by C_α^α, but $\mathrm{BUC}_\alpha^\alpha$ is indeed the regularity obtained in [114, Theorem 8.1.1]).

Theorem 5.6 applies to (5.2.2), (5.2.4) and (5.2.8) under similar assumptions as in the Theorems 5.2, 5.4 and 5.5, with different phase spaces. In particular, instead of a Besov space one obtains H^2 as a phase space in the setting of Theorem 5.5. We do not formulate the precise results and rather consider a setting for reaction-diffusion systems which is not covered by the approach of Theorem 5.1.

One space dimension: well-posedness in BUC^2

We reconsider the case of one space dimension, i.e., for $u(t, x) \in \mathbb{R}^N$ the problem

$$u_t = (a(u)u_x)_x + f(u, u_x), \qquad t > 0, \qquad x \in \mathbb{R}. \qquad (5.2.10)$$

We present a setting in which non-localized perturbations of steady states can be treated. For $k \in \mathbb{N}_0$, denote by $\mathrm{BUC}^k = \mathrm{BUC}^k(\mathbb{R}, \mathbb{R}^N)$ the Banach space of bounded uniformly continuous functions, endowed with the usual C^k-norm. It is shown in [114] that a scalar second order elliptic operator on

$\mathrm{BUC} = \mathrm{BUC}^0$ behaves well and generates an analytic semigroup. This is the main ingredient to apply Theorem 5.6 as follows. The triangular structure of a is assumed for simplicity.

Theorem 5.7. *Let $\overline{u} \in \mathrm{BUC}^2(\mathbb{R}, \mathbb{R}^N)$ be a steady state of (5.2.10) and let $U_1, U_2 \subseteq \mathbb{R}^N$ be open neighbourhoods of the closure of image of $\overline{u}$ resp. $\overline{u}_x$. Assume $a : U_1 \to \mathbb{R}^{N \times N}$ and $f : U_1 \times U_2 \to \mathbb{R}^N$ are C^2, such that*

- *for each $\zeta \in U_1$ the matrix $a(\zeta)$ is triangular, and the diagonal entries of a are positive and bounded away from zero uniformly.*

Then there is an open neighbourhood $\mathcal{V}$ of $\overline{u}$ in BUC^2 such that (5.2.10) is locally well-posed in $\mathcal{V}$. One can take $\mathcal{V} = \mathrm{BUC}^2$ if $U_1 = U_2 = \mathbb{R}^N$.

Proof. Choose an open set $V \subset \mathbb{R}^N$ that contains the image of $\overline{u}$ and satisfies $\overline{V} \subset U$. Define $\mathcal{V}$ as the set of all $w_0 \in \mathrm{BUC}^2$ with image contained in V. Then $\mathcal{F}(u) = (a(u)u_x)_x + f(u, u_x)$ defines a superposition operator $\mathcal{F} : \mathcal{V} \to \mathrm{BUC}$. It is straightforward to check that $\mathcal{F} \in C^1(\mathcal{V}, \mathrm{BUC})$. At $w_0 \in \mathcal{V}$ we have

$$\mathcal{F}'(w_0)v = (a(w_0)v_x)_x + (a'(w_0)[(w_0)_x, v])_x + cv_x + f'(w_0)v, \qquad v \in \mathrm{BUC}^2,$$

and $\mathcal{F}' : \mathcal{V} \to \mathscr{L}(\mathrm{BUC}^2, \mathrm{BUC})$ is locally Lipschitz. For the generator property, let $w_0 \in \mathcal{V}$ be given. By [114, Corollary 3.1.9], each of the scalar-valued operators $v \mapsto a_{ii}(w_0)v_{xx}$ with domain BUC^2 generates an analytic C_0- semigroup on BUC, where a_{ii} are for $i = 1, ..., N$ the diagonal entries of a. Using the matrix generator result [132, Corollary 3.3] and the triangular structure of a, we conclude that the principle part $v \mapsto a(w_0)v_{xx}$ of $\mathcal{F}'(w_0)$ is a generator on $\mathrm{BUC}(\mathbb{R}, \mathbb{R}^N)$, with domain $\mathrm{BUC}^2(\mathbb{R}, \mathbb{R}^N)$. The remaining lower order terms preserve this property. The equivalence of the graph norm of $\mathcal{F}'(w_0)$ and the C^2-norm follows from the boundedness of the coefficients and the open mapping theorem. Therefore Theorem 5.6 applies to (5.2.10). $\qquad \square$

5.2.3 More general problems and other frameworks

The above results also hold for smooth x-dependent nonlinearities, provided the principal term a is positive definite uniformly in x. Also non-autonomous and nonlocal problems can be treated, see [5, 6, 114, 143]. Only the mapping properties of the superposition operators and the generator properties of the linearization are relevant. Both frameworks cover general quasilinear systems in any dimension if one works with $X_0 = L^q$ for large q as a base

space, since then the superposition operators are well-defined by Sobolev embeddings. Theorem 5.6 also allows to work in spaces of Hölder continuous functions, L^∞ or subspaces of BUC like C_0 or $C(\overline{\mathbb{R}})$, based on the analytic generator results of [114] and [60, Section VI.4].

A framework with spatial weights might also be of interest, for instance, to force some decay of solutions [210] or to treat singular terms [126]. Here in particular weights with exponential growth are straightforward to treat, as the generator results can be obtained from the unweighted case by a simple similarity transformation. Concerning weights, we also mention that the approach of [112] has proven useful for quasi-linear parabolic problems in weighted spaces; see [14, 77, 191]. Invariant manifolds for quasi-linear parabolic systems with nonlinear boundary conditions on bounded or exterior domains are constructed, e.g., in [106, 107, 177]; see also the references given there.

Besides the above approaches based on maximal L^p- and Hölder regularity there is a similar abstract approach based on continuous regularity [8, 29]. Completely different frameworks for problems in weaker settings on bounded domains with boundary conditions are presented in [3, 75]. They should also be applicable to problems on $\mathbb{R}^n$. Finally, the pioneering work of [105] should be mentioned. For a comprehensive overview of possible settings for quasilinear parabolic problems we refer to [5].

5.3 Stability and spectra of travelling waves

While travelling waves also occur in higher space dimensions, we restrict here to $x \in \mathbb{R}$.

Throughout, let $u_*(t, x) = \overline{u}(x - ct)$ be a travelling wave solution of

$$u_t = (a(u)u_x)_x + f(u, u_x), \qquad x \in \mathbb{R},$$

with speed $c \in \mathbb{R}$ and profile $\overline{u} \in \mathrm{BC}^\infty(\mathbb{R}, \mathbb{R}^N)$ solving the ordinary differential equation (5.2.3). We assume that a, f are C^∞ and that a is uniformly positively definite in a vicinity of the image of $\overline{u}$. Suitable finite regularity of $\overline{u}, a, f$ suffices for each of the following results and we assume infinite smoothness only for the sake of a simple exposition. We further assume that $\overline{u}$ is constant or periodic at infinity and that the asymptotic states are approached exponentially. A travelling wave is called a *pulse* or a *front* if the asymptotic states are equal or different homogeneous equilibria, respectively.

A *wavetrain* is a periodic travelling wave, and we refer to travelling waves with at least one periodic asymptotic state as *generalized* fronts or pulses.

5.3.1 Stability in a perturbative setting

The evolution of perturbations u of u_* is governed by

$$u_t = (a(\overline{u}+u)u_x)_x + (a(\overline{u}+u)\overline{u}_x)_x + c(\overline{u}_x + u_x) + f(\overline{u}+u, \overline{u}_x + u_x), \quad (5.3.1)$$

where the co-moving frame $x - ct$ is again denoted by x. By translation invariance of the underlying equation, stability must be considered with respect to the family of translates

$$S = \{\overline{u}(\cdot + \tau) - \overline{u} : \tau \in \mathbb{R}\}.$$

The Theorems 5.4, 5.5 and 5.7 guarantee local well-posedness of (5.3.1) for initial data from $\mathcal{X} = H^2$, $\mathcal{X} = B_{2,p}^{2-2/p}$ or $\mathcal{X} = \mathrm{BUC}^2$ sufficiently close to S (note that in Theorem 5.5 it is actually assumed that f is independent of u_x). Even though $H^2 \subset B_{2,p}^{2-2/p}$ we distinguish between these cases, because of the different corresponding base spaces H^1 and L^2, and to highlight that a pure Sobolev space setting suffices for (5.3.1). For $\mathcal{X} = \mathrm{BUC}^2$, or in case of a pulse, one could equivalently consider (5.3.1) with $\overline{u}$ replaced by zero, in a neighbourhood of $\{\overline{u}(\cdot + \tau) : \tau \in \mathbb{R}\}$.

If u_* is a pulse or a front, then S is in each setting a family of equilibria of (5.3.1).

Definition 5.1. *A pulse or front solution u_* is called* orbitally stable*, if for $\epsilon > 0$ there is $\delta > 0$ such that for $u_0 \in \mathcal{X}$ with $\mathrm{dist}_{\mathcal{X}}(u_0, S) \leq \delta$ the corresponding solution u of (5.3.1) exists globally in time and satisfies $\mathrm{dist}_{\mathcal{X}}(u(t), S) \leq \epsilon$ for all $t > 0$. u_* is called* orbitally stable with asymptotic phase*, if it is orbitally stable and if for each $u_0 \in \mathcal{X}$ sufficiently close to S there is τ_∞ such that the corresponding solution of (5.3.1) converges to $\overline{u}(\cdot + \tau_\infty) - \overline{u}$ as $t \to \infty$. u_* is* orbitally unstable *if it is not orbitally stable.*

For a wavetrain, translates of the profile cannot be realized by localized perturbations. Thus only for $\mathcal{X} = \mathrm{BUC}^2$ orbital stability as above can be considered. For localized perturbations, i.e., $\mathcal{X} = H^2$ or $\mathcal{X} = B_{2,p}^{2-2/p}$, stability of a wavetrain is understood with respect to stability of the zero solution of (5.3.1).

5.3.2 The spectrum of the linearization

The linearization $\mathcal{L}$ of the right-hand side of (5.3.1) in $u = 0$ is

$$\mathcal{L}\varphi = \alpha\varphi_{xx} + \beta\varphi_x + \gamma\varphi, \qquad (5.3.2)$$

with smooth coefficients $\alpha(x), \beta(x), \gamma(x) \in \mathbb{R}^{N \times N}$ given by

$$\alpha = a(\overline{u}), \qquad \beta = a'(\overline{u})[\overline{u}_x, \cdot] + a'(\overline{u})[\cdot, \overline{u}_x] + c + \partial_2 f(\overline{u}, \overline{u}_x),$$

$$\gamma = a''(\overline{u})[\overline{u}_x, \cdot, \overline{u}_x] + a'(\overline{u})[\cdot, \overline{u}_{xx}] + \partial_1 f(\overline{u}, \overline{u}_x).$$

Depending on the chosen well-posedness framework, the operator $\mathcal{L}$ is considered on $X_0 = H^1$, L^2 or BUC, with domain H^3, H^2 or BUC^2, where we write $\mathcal{L}_{X_0}$ for a realization. The *spectrum* of $\mathcal{L}_{X_0}$ is the set of $\lambda \in \mathbb{C}$, where $\mathcal{L}_{X_0} - \lambda$ is not boundedly invertible. It is denoted by $\operatorname{spec}\mathcal{L}_{X_0}$.

As in the approach surveyed in [157], we distinguish between the *point spectrum*, i.e., $\lambda \in \operatorname{spec}\mathcal{L}_{X_0}$ such that $\mathcal{L}_{X_0} - \lambda$ is a Fredholm operator of index zero, and its complement within the spectrum, called the *essential spectrum*. We will see that point and essential spectrum are independent of the chosen framework and that the familiar spectral theory for ordinary differential operators based on exponential dichotomies, as described in [157], applies to $\mathcal{L}$.

Usually, the *set of eigenvalues* of $\mathcal{L}_{X,0}$ is called the point spectrum. Note that, with the above definition, eigenvalues can be contained in the essential spectrum. Moreover, eigenvalues are not independent of the setting. For instance, the operator $\partial_x - i$ has a zero eigenvalue with eigenfunction $\phi(x) = e^{ix}$ on BUC, but it is injective on L^2 and H^1. Of course this does not contradict Proposition 1 on kernel dimensions below since the operator is not Fredholm.

Since it is assumed that a is positive definite in a neighbourhood of the image of $\overline{u}$, the multiplication by α^{-1} is an isomorphism in each setting. Thus the invertibility and Fredholm properties of $\mathcal{L} - \lambda$ are the same as for

$$\tilde{\mathcal{L}}(\lambda) = \alpha^{-1}(\mathcal{L} - \lambda) = \partial_{xx} + \alpha^{-1}\beta\partial_x + \alpha^{-1}(\gamma - \lambda),$$

which has constant leading order coefficients. As before we write $\tilde{\mathcal{L}}_{X_0}(\lambda)$ for a realization of $\tilde{\mathcal{L}}(\lambda)$. The key to the spectral properties of $\tilde{\mathcal{L}}(\lambda)$ is the corresponding first order operator

$$\tilde{\mathcal{T}}(\lambda) = \partial_x - A(\cdot, \lambda), \qquad A(x, \lambda) = \begin{pmatrix} 0 & -1 \\ \alpha^{-1}(x)(\gamma(x) - \lambda) & \alpha^{-1}(x)\beta(x) \end{pmatrix},$$

which is obtained from rewriting $\tilde{\mathcal{L}}(\lambda) = 0$ into a first order ODE. Hence $A(x, \lambda)$ is a $(2N \times 2N)$-matrix. We write $\tilde{\mathcal{T}}_{L^2}(\lambda)$ and $\tilde{\mathcal{T}}_{BUC}(\lambda)$ for the realization of $\tilde{\mathcal{T}}(\lambda)$ on $L^2(\mathbb{R}, \mathbb{C}^{2N})$ and $\mathrm{BUC}(\mathbb{R}, \mathbb{C}^{2N})$ with natural domains, respectively.

The following result is rather folklore, but does not seem to be explicitly stated in the literature. The equality of spectra for realizations on L^p, $1 \le p < \infty$ and the space C_0 of continuous functions vanishing at infinity follows from [146, Corollary 4.6]. For the more general theory of dichotomies and spectral mapping results on these spaces we refer to the monograph [26].

Proposition 1. *The following assertions are true, where $\lambda \in \mathbb{C}$.*

- *The spectrum, the point spectrum and the essential spectrum of $\mathcal{L}_{H^1}$, $\mathcal{L}_{L^2}$ and $\mathcal{L}_{\mathrm{BUC}}$ all coincide, respectively.*
- *The operator $\mathcal{L}_{L^2} - \lambda$ is invertible if and only if $\tilde{\mathcal{T}}_{L^2}(\lambda)$ is invertible.*
- *The operator $\mathcal{L}_{L^2} - \lambda$ is Fredholm if and only if $\tilde{\mathcal{T}}_{L^2}(\lambda)$ is Fredholm. In this case the Fredholm indices coincide, as well as the dimension of the kernels.*

Proof. Lemma 5.4 provides an isomorphism T from H^1 to L^2 and from H^3 to H^2 such that $\mathcal{L}_{H^1} = T^{-1}\mathcal{L}_{L^2}T$. Thus $\mathcal{L}_{H^1} - \lambda$ and $\mathcal{L}_{L^2} - \lambda$ have for each $\lambda \in \mathbb{C}$ the same invertibility and Fredholm properties. It remains to compare $\mathcal{L}_{L^2} - \lambda$ and $\mathcal{L}_{\mathrm{BUC}} - \lambda$. Since α is boundedly invertible, these operators have the same invertibility and Fredholm properties as $\tilde{\mathcal{L}}_{L^2}(\lambda)$ and $\tilde{\mathcal{L}}_{\mathrm{BUC}}(\lambda)$, respectively. It follows from [160, Theorem A.1] that their Fredholm properties are the same as those of $\tilde{\mathcal{T}}_{L^2}(\lambda)$ and $\tilde{\mathcal{T}}_{\mathrm{BUC}}(\lambda)$, respectively. It is further clear that the dimensions of the kernels coincide in both settings. Now in [17, Theorem 1.2] it is shown that the Fredholm properties of $\tilde{\mathcal{T}}_{L^2}(\lambda)$ are characterized by exponential dichotomies of the ODE $v' = A(\cdot, \lambda)v$ on both half-lines, and that in this case the dimension of the kernel of $\tilde{\mathcal{T}}_{L^2}(\lambda)$ only depends on the image of the dichotomies. This characterization is also true for $\tilde{\mathcal{T}}_{\mathrm{BUC}}(\lambda)$ with the same formula for the dimension of the kernel, see [137, Lemma 4.2] and [138]. Hence the invertibility and Fredholm properties of $\tilde{\mathcal{T}}_{L^2}(\lambda)$ and $\tilde{\mathcal{T}}_{\mathrm{BUC}}(\lambda)$ coincide, and if the operators are Fredholm, then the dimensions of the kernels coincide. This carries over to $\mathcal{L}_{L^2} - \lambda$ and $\mathcal{L}_{\mathrm{BUC}} - \lambda$ by the above considerations and shows the assertions. □

We finally remark that also for the realization of $\tilde{\mathcal{T}}(\lambda)$ on L^q with any $1 < q < \infty$ the Fredholm properties are characterized by exponential dichotomies (see [17, p. 94]). Together with the arguments for [160, The-

orem A.1], an appropriate generalization of Lemma 5.4 and interpolation. This shows that the spectrum of $\mathcal{L}$ is independent of its realization on any of the spaces $H^{s,q}$ and $B^s_{q,r}$, where $s \geq 0$ and $1 \leq r \leq \infty$.

5.3.3 Computation of the spectrum

The invertibility and Fredholm properties of $\tilde{\mathcal{T}}(\lambda)$, and thus the characterization of point and essential spectrum of $\mathcal{L}$, are described in terms of exponential dichotomies in [157, Section 3.4]. This is independent of the variable leading order coefficients of $\mathcal{L}$ due to its quasilinear origin, and thus the same as for semilinear reaction-diffusion systems. We briefly describe the main points for each type of wave. A detailed discussion can also be found in [90, Chapter 3].

For a *homogeneous steady state* the point spectrum of the constant coefficient operator $\mathcal{L}$ is empty. Since the Fourier transform is an isomorphism on L^2, the (essential) spectrum can be determined by transforming $\mathcal{L}$ to

$$\widehat{\mathcal{L}}(\kappa) = -\alpha\kappa^2 + \mathrm{i}\beta\kappa + \gamma \in \mathbb{C}^{N \times N}, \qquad \kappa \in \mathbb{R}.$$

Now we have $\lambda \in \operatorname{spec} \mathcal{L}$ if and only if

$$d(\lambda, \kappa) := \det(\widehat{\mathcal{L}}(\kappa) - \lambda) = \det(A(\lambda) - \mathrm{i}\kappa) = 0$$

for some κ, which is called the dispersion relation for $\mathcal{L}$. The latter also means that $A(\lambda)$ is a non-hyperbolic matrix. Thus here it is straightforward to determine the spectrum, at least for N not too large.

For *pulses and fronts*, replacing the variable coefficients of $\mathcal{L}$ by their values at $\pm\infty$ leads to constant coefficient operators $\mathcal{L}^\pm$ whose spectrum is determined as just described. For pulses the essential spectrum of $\mathcal{L}$ already coincides with $\operatorname{spec} \mathcal{L}^\pm$. For fronts, $\operatorname{spec} \mathcal{L}^\pm$ equals the boundary of the essential spectrum of $\mathcal{L}$, which is usually already sufficient to know for stability issues. This is related to the fact that the replacement by the values at infinity is a relatively compact perturbation of $\mathcal{L}$, which leaves Fredholm properties invariant (see [92, Theorem IV.5.26]). The point spectrum of a pulse or a front is determined by detecting intersections of the stable and unstable subspaces of $v' = A(\cdot, \lambda)v$. Here the *Evans function* [1, 63] is a powerful tool and we refer to the survey [157, Section 4] and the references therein.

For a *wavetrain*, i.e., when $\overline{u}$ is periodic with wavelength (period) $L > 0$, the coefficients of $\mathcal{L}$ are periodic. The point spectrum is empty. Instead of

the Fourier transform, here the Floquet-Bloch transform applies and yields (see [128, Theorem A.4], also for higher space dimensions)

$$\operatorname{spec} \mathcal{L} = \overline{\cup_{\kappa \in [0, 2\pi/L)} \operatorname{spec} \hat{B}(\kappa)}. \qquad (5.3.3)$$

For $\kappa \in [0, 2\pi/L)$ the operator $\hat{B}(\kappa) : H^2_{\mathrm{per}}(0, L) \subset L_{2,\mathrm{per}}(0, L) \to L_{2,\mathrm{per}}(0, L)$ with periodic boundary conditions is given by

$$\hat{B}(\kappa)U = \mathrm{e}^{-\mathrm{i}\kappa x} \mathcal{L}[\mathrm{e}^{\mathrm{i}\kappa x} U] = \widehat{\mathcal{L}}(\mathrm{i}\kappa + \partial_x)U,$$

where $\widehat{\mathcal{L}}(\cdot)$ is the formal operator symbol of $\mathcal{L}$. Since $\operatorname{spec} \hat{B}(\kappa)$ only consists of eigenvalues, its spectrum is fully determined by the solvability of the family of boundary value problems

$$\widehat{\mathcal{L}}(\mathrm{i}\kappa + \partial_x)U = \lambda U, \qquad U(0) = U(L).$$

In fact, also multiplicity of eigenvalues is determined via Jordan chains as in [1, 157]. Notably, the spectrum again comes in curves; now an infinite countable union since the eigenvalue problem for each κ still concerns an unbounded operator (rather than a matrix in case of a homogeneous steady state).

Via $V = \mathrm{e}^{\mathrm{i}\kappa x} U$, the boundary value problem formulation is equivalent to

$$\widehat{\mathcal{L}}(\partial_x)V = \lambda V, \qquad V(0) = \mathrm{e}^{-\mathrm{i}\kappa L} V(L).$$

By Floquet theory, this precisely means that the period map $\Pi(\lambda)$ of the evolution operator for the ODE $\widehat{\mathcal{L}}(\partial_x)U = \lambda U$ possesses an eigenvalue (a Floquet multiplier) $\mathrm{e}^{\mathrm{i}\kappa L}$. Hence, also here a (linear) dispersion relation can be defined by

$$d(\lambda, \kappa) = \det \left(\Pi(\lambda) - \mathrm{e}^{\mathrm{i}\kappa L} \right) = 0,$$

which precisely characterizes the spectrum. An important difference to the case of homogeneous steady states is that $\lambda = 0$ always lies in the essential spectrum: x-independent coefficients of (5.3.1) yield a trivial zero Floquet exponent, which implies that $d(0, 0) = 0$. Indeed, $\hat{B}(0)\overline{u}_x = 0$ in this translation symmetric case.

Finally, in case of a *generalized wave train*, the boundary of the essential spectrum of $\mathcal{L}$ is as above obtained by replacing the coefficients of $\mathcal{L}$ with its periodic limits at $\pm\infty$, and considering the dispersion relation. The point spectrum is also given by an Evans-function, see [159, Section 4] (here also the more general case of time periodic solutions, so-called defects, is treated).

5.4 Nonlinear stability and instability

For the nonlinearities a, f and a travelling wave solution $u_*(t, x) = \overline{u}(x - ct)$ of (5.1.1) we make the same assumptions as in the previous section. We consider (5.3.1)

$$u_t = (a(\overline{u} + u)u_x)_x + (a(\overline{u} + u)\overline{u}_x)_x + c(\overline{u}_x + u_x) + f(\overline{u} + u, \overline{u}_x + u_x)$$

in any of the well-posedness settings in a neighbourhood of

$$S = \{\overline{u}(\cdot + \tau) - \overline{u} : \tau \in \mathbb{R}\}.$$

5.4.1 Stability of pulses and fronts

Recall the precise notion of orbital stability from Definition 5.1. An application of [144, 145] gives the following conditional result. For more information on semisimple eigenvalues in Banach spaces we refer to [114, Appendix A.2].

Proposition 2. *Let $\overline{u}$ have constant asymptotic states. Assume $\lambda = 0$ is a semisimple eigenvalue of $\mathcal{L}$ with eigenfunction $\overline{u}'$, i.e., $\ker \mathcal{L} = \mathrm{span}\{\overline{u}'\}$ and $X_0 = \ker \mathcal{L} \oplus \mathrm{im}\, \mathcal{L}$. Assume further that the remaining part of $\mathrm{spec}\, \mathcal{L}$ is strictly contained in $\{\mathrm{Re}\, \lambda < 0\}$. Then the travelling wave u_* is orbitally stable with asymptotic phase, and limit translates $u(\cdot + \tau_\infty)$ are approached exponentially.*

Proof. By translation invariance it suffices to consider S in a neighbourhood of $\tau = 0$. The framework of Theorem 5.1 is the one of [144, Theorem 2.1], provided that, in addition, A and F belong to C^1, which is guaranteed by the assumption on a and f. The setting of Theorem 5.6 is the one of [145, Example 3]. To apply [144, Theorem 2.1] and [145, Theorem 3.1] it remains to verify that zero is normally stable, in the sense of [144, 145]. We have that S is a one-dimensional C^1-manifold, with tangent space at $\tau = 0$ spanned by $\overline{u}'$. By assumption, the tangent space coincides with the kernel of $\mathcal{L}$ and zero is a semisimple eigenvalue. Hence normal stability follows. $\square$

For a quasilinear variant of the Huxley equation, the above conditions have been verified in [144, Section 5] by elementary arguments.

An abstract and more general variant of Proposition 2 and applications to semilinear problems can be found in [90, Chapter 4].

5.4.2 Instability of generalized pulses and fronts under localized perturbations

For localized perturbations, i.e., for $\mathcal{X} = H^2$ or $B_{2,p}^{2-2/p}$, a generalized pulse or front u_* is nonlinearly stable or unstable if the zero solution of (5.3.1) is stable or unstable, as a single equilibrium in the sense of Lyapunov. Nonlinear stability is a delicate issue (see the discussion in the introduction). In case of an unstable spectral value we have the following.

Proposition 3. *If $\overline{u}$ has a periodic asymptotic state and*

$$\operatorname{spec} \mathcal{L} \cap \{\operatorname{Re} \lambda > 0\} \neq \emptyset,$$

then the generalized front or pulse u_* is nonlinearly unstable with respect to localized perturbations from $\mathcal{X} = H^2$ or $\mathcal{X} = B_{2,p}^{2-2/p}$.

Proof. The Lemmas 5.2 and 5.3 together with Proposition 4 imply that the time-one solution map Φ_1 for (5.3.1) obtained in Theorems 5.4 and 5.5 from Theorem 5.1 is C^2 around zero, with $\Phi_1'(0) = e^{\mathcal{L}} \in \mathscr{L}(\mathcal{X})$. Considered on $\mathscr{L}(X_0)$, this operator has spectral radius larger than one by [114, Corollary 2.3.7]. Using $\mathcal{L} - \omega$ with sufficiently large $\omega > 0$ as a conjugate, this property carries over to $e^{\mathcal{L}}$ considered on $\mathscr{L}(X_1)$. Now it follows from interpolation that the realization of $e^{\mathcal{L}}$ on $\mathscr{L}(\mathcal{X})$ has spectral radius greater than one. Thus the zero solution of (5.3.1) is unstable by [78, Theorem 5.1.5]. $\qquad\square$

5.4.3 Orbital instability

Without assuming a spectral gap or the existence of an unstable eigenvalue we show that an unstable spectrum implies orbital instability.

Theorem 5.8. *The following assertions are true.*

- *Let $\overline{u}$ have constant asymptotic states. Assume*

$$\operatorname{spec} \mathcal{L} \cap \{\operatorname{Re} \lambda > 0\} \neq \emptyset.$$

  Then u_* is orbitally unstable with respect to localized and non-localized perturbations from $\mathcal{X} = H^2$, $B_{2,p}^{2-2/p}$ or $X = \mathrm{BUC}^2$.

- *Let $\overline{u}$ have a periodic asymptotic state. Assume*

$$\operatorname{spec} \mathcal{L} \cap \{\operatorname{Re} \lambda > 0\} \neq \emptyset.$$

  Then u_* is orbitally unstable with respect to non-localized perturbations from $\mathcal{X} = \mathrm{BUC}^2$.

This result is a direct consequence of the general orbital instability result Theorem 5.9 below for manifolds of equilibria: $\overline{u}' \in X_1$ in the settings under consideration and $\mathcal{L}\overline{u}' = 0$ by the exponential convergence of $\overline{u}'$ at infinity and translation invariance of the equation.

The following lemma and its proof are generalizations of [78, Theorem 5.1.5] and [168]. Similar to that result, the proof establishes that perturbations of suitable approximate unstable eigenfunctions deviate from the manifold of equilibria.

Lemma 5.1. *Let X be a real Banach space, let $\mathcal{V} \subseteq X$ be an open neighbourhood of zero and let $\mathcal{E} \subset \mathcal{V}$ be an m-dimensional C^2-manifold containing zero. Let $\mathcal{E}$ be parametrized by an injective map $\psi : U \subset \mathbb{R}^m \to \mathcal{E}$ with $\psi(0) = 0$, where $\psi'(0)$ has full rank m. Assume $T : \mathcal{V} \to X$ is continuous, that $T(u) = 0$ for $u \in \mathcal{E}$ and that there is $M \in \mathscr{L}(X)$ with spectral radius greater than one such that, for some $\sigma > 1$,*

$$\|T(u) - Mu\| = \mathcal{O}(\|u\|^\sigma) \qquad \text{as } u \to 0. \tag{5.4.1}$$

Suppose further that $\partial_1\psi(0), ..., \partial_m\psi(0) \in \ker(M - \mathrm{id})$. Then $u_* = 0$ is orbitally unstable with respect to $\mathcal{E}$ under iterations of T. More precisely, there is $\varepsilon_0 > 0$ such that for each $\delta > 0$ there are $u_\delta \in \mathcal{V}$ with $\|u_\delta\| \le \delta$ and $N \in \mathbb{N}$ such that $T^n(u_\delta) \in \mathcal{V}$ for $n = 1, ..., N$ and $\mathrm{dist}(T^N(u_\delta), \mathcal{E}) \ge \varepsilon_0$.

Proof. Step 1. Let $\alpha_0, \beta > 0$ such that $B_{5\alpha_0}(0) \subset \mathcal{V}$ and

$$\|T(u_0) - Mu_0\| \le \beta\|u_0\|^\sigma, \qquad \|u_0\| \le 5\alpha_0. \tag{5.4.2}$$

There is an approximate eigenvalue $\lambda = re^{i\theta}$ with $r > 1$ and $\theta \in \mathbb{R}$ in the spectrum of M. Furthermore, there are $\eta, K > 0$ with $r + \eta < r^\sigma$ and $\|M^n\| \le K(r+\eta)^n$ for all $n \ge 0$. In the sequel we choose $\alpha \in (0, \alpha_0)$ stepwise possibly smaller and smaller, only depending on K, r, η, β, ψ.

Step 2. Let $\delta \in (0, \alpha)$ be given. As in the proof of [78, Lemma 5.1.4] we find $N \in \mathbb{N}$ such that

$$\frac{\alpha}{r^N} \le \delta, \qquad |\sin(N\theta)| \le \alpha, \tag{5.4.3}$$

and $u, v \in X$ with $\|u\| = 1$ and $\|v\| \le 1$ such that

$$\|M^n(u + iv) - \lambda^n(u + iv)\| \le \alpha. \qquad n = 1, ..., N. \tag{5.4.4}$$

Here the norm is actually the complexified one, i.e., $\|w_1 + iw_2\| = \|w_1\| + \|w_2\|$ for $w_1, w_2 \in X$.

Define $u_\delta := \frac{\alpha}{r^N} u \in X$, such that $\|u_\delta\| = \frac{\alpha}{r^N} \le \delta$. Let $n = 1, ..., N$ be given. Assume inductively that $\|T^k(u_\delta)\| \le 5\alpha r^{k-N}$ for $k = 0, ..., n-1$. Then $T^n(u_\delta)$ is well-defined and as in the proof of [78, Theorem 5.1.5] we write

$$T^n(u_\delta) - \lambda^n u_\delta = \left(M^n u_\delta - \lambda^n u_\delta\right) + \sum_{k=0}^{n-1} M^{n-k-1}\left(T^{k+1}(u_\delta) - MT^k(u_\delta)\right).$$
(5.4.5)

Denote the right-hand side by $G_n + H_n$. We claim that

$$\|G_n\| \le \alpha^2 r^{-N} + 2\alpha|\sin(\theta n)|r^{n-N}, \qquad \|H_n\| \le C_M \alpha^\sigma r^{n-N}, \qquad (5.4.6)$$

where $C_M = \frac{5^\sigma K\beta}{r^\sigma - r - \eta}$ is independent of n. To see this, we use (5.4.4) to obtain

$$
\begin{aligned}
\|G_n\| &\le \frac{\alpha}{r^N}\left(\|M^n u - (\mathrm{Re}\,\lambda^n)u + (\mathrm{Im}\,\lambda^n)\,v\| + \|(\mathrm{Im}\,\lambda^n)\,v\| + \|(\mathrm{Im}\,\lambda^n)\,u\|\right) \\
&\le \frac{\alpha}{r^N}\left(\|\mathrm{Re}((M^n - \lambda^n)(u + \mathrm{i}v))\| + 2r^n|\sin(\theta n)|\right) \qquad\qquad (5.4.7) \\
&\le \alpha^2 r^{-N} + 2\alpha|\sin(\theta n)|r^{n-N}.
\end{aligned}
$$

For the sum H_n we use (5.4.2), that $\|T^k(u_\delta)\| \le 5\alpha r^{k-N} \le 5\alpha_0$ for $k \le n-1$ and that $r + \eta < r^\sigma$ to obtain

$$
\begin{aligned}
\|H_n\| &\le \sum_{k=0}^{n-1} K(r+\eta)^{n-k-1}\beta(5\alpha r^{k-N})^\sigma \\
&\le \alpha^\sigma 5^\sigma K\beta r^{\sigma(n-1-N)}\sum_{k=0}^{n-1}\left(\frac{r+\eta}{r^\sigma}\right)^{n-k-1} \le C_M \alpha^\sigma r^{n-N}.
\end{aligned}
$$

This shows the claim (5.4.6).

Now it follows from (5.4.5), (5.4.6) and $\sigma > 1$ that $\|T^n(u_\delta)\| \le 5\alpha r^{n-N}$, provided $\alpha \le 1$ is such that $C_M \alpha^{\sigma-1} \le 1$. By induction, for all $n = 0, ..., N$ we obtain that $T^n(u_\delta)$ is well-defined and the estimates $\|T^n(u_\delta)\| \le 5\alpha r^{n-N}$ and (5.4.6) hold true.

Step 3. As a consequence, for $\mathrm{dist}(T^N(u_\delta), \mathcal{E})$ we only have to consider $\zeta \in U$ such that $\|\psi(\zeta)\| \le 10\alpha$. Indeed, for $\|\psi(\zeta)\| > 10\alpha$ we have $\|T^N(u_\delta) - \psi(\zeta)\| > 5\alpha$, but $\|T^N(u_\delta) - \psi(0)\| = \|T^N(u_\delta))\| \le 5\alpha$. There is small $\tau_0 > 0$ such that

$$\psi(\zeta) = \psi'(0)\zeta + \rho(\zeta), \qquad |\zeta| \le \tau_0, \qquad (5.4.8)$$

where $\|\rho(\zeta)\| \leq C_\rho |\zeta|^2$ for a constant C_ρ independent of $\zeta \in B_{\tau_0}(0)$. Since $\psi'(0)$ has full rank m, we have $C_{\psi'} = \min_{|\xi|=1} \|\psi'(0)\xi\| > 0$ and we can choose τ_0 such that $C_\rho \tau_0 \leq C_{\psi'}/2$. Hence, with $\vartheta = 20/C_{\psi'}$ and small α, we obtain

$$\|\psi(\zeta)\| \geq \|\psi'(0)\zeta\| - C_\rho |\zeta|^2 > 10\alpha \qquad \text{for } \tau_0 \geq |\zeta| > \vartheta\alpha.$$

Then, with these choices,

$$\text{dist}(T^N(u_\delta), \mathcal{E}) = \inf_{|\zeta| \leq \vartheta\alpha} \|T^N(u_\delta) - \psi(\zeta)\|.$$

Step 4. Now let $|\zeta| \leq \vartheta\alpha$. Then (5.4.5), (5.4.8) and the estimates (5.4.6) and $|\sin(N\theta)| \leq \alpha$ yield

$$\begin{aligned}\|T^N(u_\delta) - \psi(\zeta)\| &\geq \|\lambda^N u_\delta - \psi'(0)\zeta\| - \|G_N\| - \|H_N\| - \|\rho(\zeta)\| \\ &\geq \|\alpha e^{iN\theta} u - \psi'(0)\zeta\| - 3\alpha^2 - C_M \alpha^\sigma - \vartheta^2 C_{\psi''}\alpha^2. \quad (5.4.9)\end{aligned}$$

The vectors u and $\psi'(0)\zeta$ are linearly independent if α is sufficiently small. In fact, otherwise our assumption $\psi'(0)\zeta \in \ker(M - \text{id})$ would imply that $Mu = u$. But as in (5.4.7), the estimate (5.4.4) then yields $|\lambda - 1| = \|\lambda u - Mu\| \leq \alpha^2 + 2\alpha$, which is impossible for small α.

We conclude that $\|e^{iN\theta}u - \frac{1}{\alpha}\psi'(0)\zeta\|$ is bounded away from zero, uniformly for $|\zeta| \leq \vartheta\alpha$. Hence, decreasing α once more if necessary, we obtain from (5.4.9) and $\sigma > 1$ that $\text{dist}(T^N(u_\delta), \mathcal{E}) \geq \varepsilon_0$, where $\varepsilon_0 > 0$ is a multiple of α independent of δ. $\qquad\square$

Let us now apply the lemma to abstract quasilinear problems

$$\partial_t u = A(u)u + F(u), \quad t > 0, \qquad u(0) = u_0. \qquad (5.4.10)$$

We denote by $\mathcal{L}(u_*) = A(u_*) + A'(u_*)[\cdot, u_*] + F'(u_*)$ the linearization of the right-hand side at u_*.

Theorem 5.9. *Assume the setting of either Theorem 5.1 or Theorem 5.6, and in addition that A and F are C^2. Let $\mathcal{E} \subset \mathcal{V} \cap X_1$ be an m-dimensional C^2-manifold of equilibria of (5.4.10), parametrized by $\psi : U \subset \mathbb{R}^m \to \mathcal{E}$, and let $u_* \in \mathcal{E}$ satisfy*

- $\text{spec}\,\mathcal{L}(u_*) \cap \{\text{Re}\,\lambda > 0\} \neq \emptyset$,
- $\partial_1\psi(\zeta_*), ..., \partial_m\psi(\zeta_*) \in \ker\mathcal{L}(u_*)$ *for* $u_* = \psi(\zeta_*)$.

Then u_* is orbitally unstable in $\mathcal{V} \subseteq \mathcal{X}$ with respect to $\mathcal{E}$.

Proof. Shrink $\mathcal{V}$ around u_* if necessary such that $t^+(u_0) \geq 1$ for each $u_0 \in \mathcal{V}$. Let $\Phi_1 : V \to \mathcal{X}$ be the time-one solution map for (5.4.10). Define $T(u_0) = \Phi_1(u_* + u_0) - (u_* + u_0)$ for u_0 close to u_*. Then T is continuous, $T(u) = 0$ for $u \in \mathcal{E} \cap \mathcal{V}$, and T satisfies (5.4.1) with $M = e^{\mathcal{L}(u_*)} \in \mathscr{L}(\mathcal{X})$, as a consequence of Proposition 4 for the setting of Theorem 5.1 and of [126, Proposition 6.2] for the setting of Theorem 5.6. Moreover, M has spectral radius larger than one by [114, Corollary 2.3.7] and interpolation, and $\partial_j \psi(\zeta_*) \in \ker(M - \mathrm{id})$ follows from the assumption. Thus Lemma 5.1 applies. $\qquad\square$

Of course, Lemma 5.1 applies in any well-posedness setting for nonlinear parabolic problems.

5.5 A generalized Gray-Scott-Klausmeier model

For illustration of the previous results, let us consider the model (5.1.2) for water-vegetation interaction in semi-arid landscapes

$$
\begin{aligned}
w_t &= (w^2)_{xx} + Cw_x + A(1 - w) - wv^2, \\
v_t &= Dv_{xx} - Bv + wv^2.
\end{aligned}
\tag{5.5.1}
$$

Here A is roughly a measure of the rainfall. On the one hand, (5.5.1) is (a rescaling of) the Klausmeier model for banded vegetation patterns on a sloped terrain from [97], when removing the porous medium term $(w^2)_{xx}$. On the other hand, upon replacing $(w^2)_{xx}$ by w_{xx} and setting $C = 0$, (5.5.1) is precisely the semilinear Gray-Scott model, which has been extensively studied in the past decades, see, e.g., [24, 49, 130] and the references therein. The relations between these different models in terms of periodic patterns have been studied in [199]. From an application point of view it is important to know in which patterned state these model systems may reside, and thus to establish well-posedness as well as existence, stability and instability of patterns.

In order to illustrate the straightforward applicability of the frameworks of the previous sections, we show well-posedness around travelling waves with first component bounded away from zero. We then consider homogeneous steady states and wavetrains, and derive the dispersion relations. These are illustrated by numerical computations of spectra when passing a Turing-Hopf bifurcation and a sideband instability.

5.5.1 Well-posedness for perturbations of travelling waves

To cast (5.5.1) into the form (5.1.1) we set $\mathbf{u} = (w, v)$ and define the smooth nonlinearities $a : \mathbb{R}^2 \to \mathbb{R}^{2 \times 2}$ and $f : \mathbb{R}^2 \to \mathbb{R}^2$ by

$$a(\mathbf{u}) = \begin{pmatrix} 2w & 0 \\ 0 & D \end{pmatrix}, \qquad f(\mathbf{u}, \mathbf{u}_x) = \begin{pmatrix} Cw_x + A(1 - w) - wv^2 \\ -Bv + wv^2 \end{pmatrix}.$$

Then (5.5.1) is equivalent to

$$\mathbf{u}_t = (a(\mathbf{u})\mathbf{u}_x)_x + f(\mathbf{u}, \mathbf{u}_x).$$

We see that $a(\mathbf{u})$ is positive definite only for $w > 0$, and thus (5.5.1) fails to be parabolic for $w \leq 0$. We therefore restrict to $w > 0$. From the quasi-positive structure of f for $A > 0$ and the smoothness of solutions given by the well-posedness, it readily follows that (5.5.1) preserves $w > 0$ on the maximal existence interval.

Assume that $\mathbf{u}_*(t, x) = \overline{\mathbf{u}}(x - ct)$ is a travelling wave solution of (5.5.1) with profile

$$\overline{\mathbf{u}} = (\overline{w}, \overline{v}) \in \mathrm{BC}^\infty(\mathbb{R}, \mathbb{R}^2)$$

satisfying $\overline{w} \geq \delta > 0$, and speed $c \in \mathbb{R}$. Note that this includes homogeneous steady states. Denote the co-moving frame $x - ct$ again by x. As for (5.3.1), the evolution of perturbations $\mathbf{u}$ of $\overline{\mathbf{u}}$ under (5.5.1) is governed by

$$\mathbf{u}_t = (a(\overline{\mathbf{u}} + \mathbf{u})\mathbf{u}_x)_x + (a(\overline{\mathbf{u}} + \mathbf{u})\overline{\mathbf{u}}_x)_x + c(\overline{\mathbf{u}}_x + \mathbf{u}_x) + f(\overline{\mathbf{u}} + \mathbf{u}, \overline{\mathbf{u}}_x + \mathbf{u}_x). \quad (5.5.2)$$

Choose $\mathcal{V}$ as any open subset of $\mathcal{X} = H^2$, $\mathcal{X} = B_{2,p}^{2-2/p}$ with $p > 2$ sufficiently large or $\mathcal{X} = \mathrm{BUC}$, such that $\overline{w} + w$ is positive and bounded away from zero for all $\mathbf{u} = (w, v) \in \mathcal{V}$. This is possible in view of the Sobolev embeddings $H^2 \subset \mathrm{BUC}$ and (5.2.7). The Theorems 5.4, 5.5 or 5.7 apply and yield local well-posedness of (5.5.2) in $\mathcal{V}$, respectively, in a sense as for the Theorems 5.1 and 5.7. Solutions are in fact smooth in space and time (see Remark 5.3).

The eigenvalue problem for the linearization of the right-hand side of (5.5.2) in $\mathbf{u} = 0$ is for $\lambda \in \mathbb{C}$ given by

$$\lambda w = 2\overline{w}w_{xx} + 4\overline{w}_x w_x + 2\overline{w}_{xx}w + (C + c)w_x - Aw - \overline{v}^2 w - 2\overline{w}\,\overline{v}v,$$
$$\lambda v = Dv_{xx} + cv_x - Bv + \overline{v}^2 w + 2\overline{w}\,\overline{v}v.$$
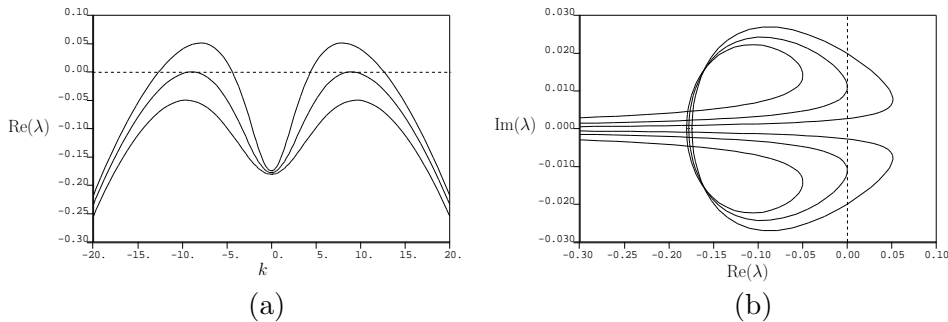$$(5.5.3)$$

Figure 5.1: Spectra of the homogeneous steady state (w^+, v^+) of (5.5.1) for $B = C = 0.2$, $D = 0.001$ before the Turing-Hopf instability, $A = 0.63$ (stable), near to it, $A = 0.53$, and after it, $A = 0.43$ (unstable). (a) Real part of spectrum vs. linear wavenumber, (b) Imaginary part of spectrum vs. real part.

By Proposition 1, the spectrum of the linearization is independent of the above functional analytical frameworks. A brief account for the computation of the spectrum is given in §5.3.3, and we refer to [157] for a survey. Nonlinear stability or instability of $\mathbf{u}_*$ can be deduced from the results in §5.4 in some situations, as pointed out below.

5.5.2 Homogeneous steady states

These are solutions $w(t, x) = w_*, v(t, x) = v_* \in \mathbb{R}$ to (5.5.1) that are time and space independent, and thus solve the algebraic equations arising from vanishing space and time derivatives. We readily compute that the possibilities are $(w_0, v_0) = (1, 0)$ and, in case $A \geq 4B^2$,

$$w_\pm = \frac{1}{2A} \left(A \mp \sqrt{A^2 - 4AB^2} \right), \qquad v_\pm = \frac{1}{2B} \left(A \pm \sqrt{A^2 - 4AB^2} \right).$$

The state (w_0, v_0), with zero vegetation, represents the desert (even though there is non-zero 'water'), while the equilibria (w_+, v_+) and (w_-, v_-) represent co-existing homogeneously vegetated states. At $A = A_{\mathrm{sn}} = 4B^2$, the latter two collapse in a saddle-node bifurcation. The spectrum of the linearization in (w_*, v_*) can be computed from the usual dispersion relation $d(\lambda, \kappa) = 0$, where

$$d(\lambda, \kappa) = \det \begin{pmatrix} -2w_*\kappa^2 + i\kappa(C + c) - A - v_*^2 - \lambda & -2w_*v_* \\ v_*^2 & -D\kappa^2 + i\kappa c - B + 2w_*v_* - \lambda \end{pmatrix}$$

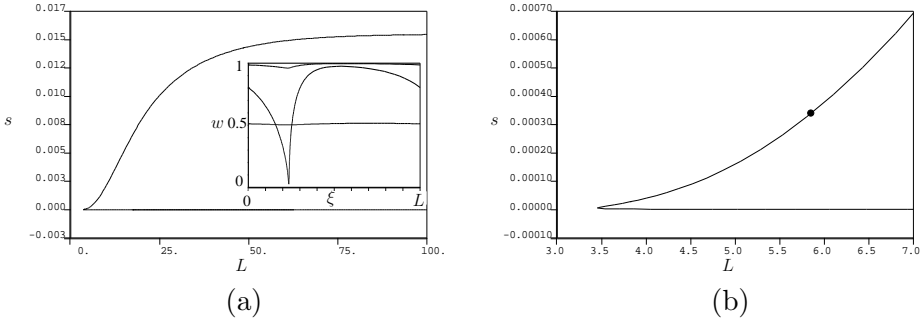is obtained from Fourier transform, see §5.3.3.

Figure 5.2: (a) Sample bifurcation diagram of wavetrains for $A = 0.02$, $B = C = 0.2$, $D = 0.001$. At $L \approx 3.45$ a fold occurs, and both branches appear to terminate in a homoclinic bifurcation as $L \to \infty$. The inset shows profiles of solutions at the fold ($w \approx 0.5$) and near $L = 80$ on upper and lower ($w \approx 1$) branch. (b) Magnification of the bifurcation diagram with bullet marking the location of the sideband instability at $L \approx 5.98$. Solutions on the branch for increasing period are spectrally stable.

An origin of patterns is a (supercritical) Turing-Hopf bifurcation of the steady state (w_+, v_+) that occurs as A decreases from larger values, as shown in [199]. It is in fact straightforward to study bifurcations of spatially periodic travelling waves as this only involves ODE analysis. As a side note on Turing-Hopf bifurcations, we mention that the dynamics of (5.5.1) near onset is formally approximated by a complex Ginzburg-Landau equation (see [199]), but the rigorous justification has not been established for quasilinear problems, to our knowledge.

In order to locate the Turing-Hopf bifurcation, we need to study the spectrum of the linearization in (w_+, v_+). For illustration, in Figure 5.1 we plot the spectrum obtained numerically (using AUTO [42]) from the dispersion relation as the parameter A passes through the aforementioned Turing-Hopf bifurcation. Since the spectrum is unstable after passing the Turing-Hopf instability (e.g. $A = 0.43$ in Figure 5.1), the steady state is expected to be unstable under the nonlinear evolution. Indeed, this is the case thanks to Theorem 5.8.

5.5.3 Wavetrains

The patterns emerging at the Turing-Hopf bifurcation are periodic wavetrains, which are solutions to (5.5.1) of the form

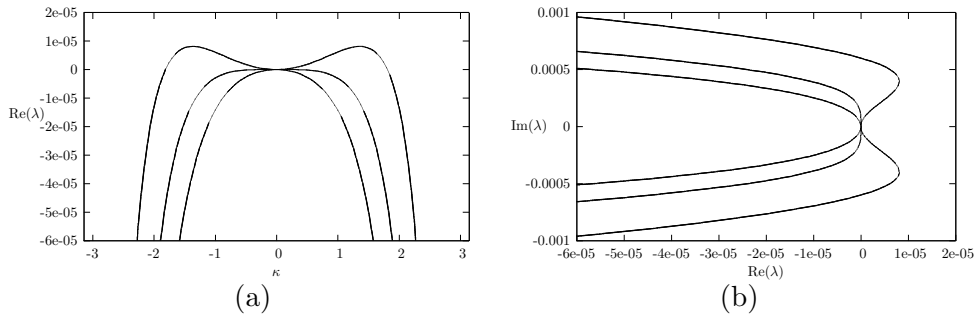$$(w_*, v_*)(t, x) = (\tilde{w}, \tilde{v})(kx - \omega t),$$

Figure 5.3: Spectra of the wavetrains for $B = C = 0.2$, $D = 0.001$, $A = 0.02$ before the sideband instability, $L = 5.9$ (stable), near to it, $L \approx 5.98$, and after it, $L = 6.1$ (unstable). (a) Real part vs. linear wavenumber, (b) Imaginary part vs. real part.

with a 2π-periodic profile $(\tilde{w}, \tilde{v})$. Here ω is called the frequency and k the wavenumber. As noted in [199], the existence region of wavetrains to (5.5.1) in parameter space extends far from the Turing-Hopf bifurcation and even beyond the saddle-node bifurcation $A = A_{\mathrm{sn}}$ of homogeneous equilibria with vegetation. In Figure 5.2 we plot a branch of wavetrain solutions for $A < A_{\mathrm{sn}}$ that appears to terminate in another type of travelling waves: pulses, which are spatially homoclinic orbits.

In order to link to the formulations for travelling waves, let us cast wavetrains as equilibria $(w_*, v_*)(t, x) = (\overline{w}, \overline{v})(x - ct)$ in the co-moving frame $x - ct$ with speed $c = \frac{\omega}{k}$. The eigenvalue problem of the linearization of (5.5.1) in a wavetrain is then given by (5.5.3), with coefficients of period $L = 2\pi/k$ stemming from $(\overline{w}, \overline{v})$.

The approach via Fourier transform is less useful, because the linearization is not diagonal in Fourier space due to the x-dependent coefficients. As a substitute, one uses the Floquet-Bloch transform, which replaces the eigenvalue problem on $\mathbb{R}$ by a family of eigenvalue problems on the wavelength interval $[0, L]$ (see §5.3.3). Specifically, this can be cast as the family of boundary value problems for $\kappa \in [0, 2\pi)$ given by (5.5.3) with ∂_x replaced by $\partial_x + i\kappa/L$ and L-periodic boundary conditions.

With a curve of spectrum of a wavetrain connected to the origin $\lambda = 0$ (due to translation symmetry), a change in its curvature is a typical destabilization upon parameter variation. This so-called *sideband instability* is illustrated in Figure 5.3, where we plot spectra of wavetrains in (5.5.1) passing through a sideband instability as the wavelength L changes. For these computations, we implemented the first order formulation of the dispersion

relation numerically in AUTO based on the algorithm from [147].

As for the homogeneous steady state, the wavetrains with unstable spectrum (e.g., $L = 6.1$ in Figure 5.3) are expected to be (orbitally) unstable under the nonlinear evolution of (5.5.1), see Proposition 3 and Theorem 5.8.

5.A Auxiliary results

5.A.1 Superposition operators

We give some details for the properties of the nonlinear maps employed in the well-posedness results.

Lemma 5.2. *Let $U_1, U_2 \subset \mathbb{R}^N$ be open neighbourhoods of zero, let*

$$a : \mathbb{R} \times U_1 \to \mathbb{R}^N \text{ be } C^{k+3} \text{ and let } f : \mathbb{R} \times U_1 \times U_2 \to \mathbb{R}^N \text{ be } C^{k+2},$$

with $f(\cdot, 0, 0) \in H^1$. Define the superposition operators

$$A(u)v = (a(\cdot, u)v_x)_x, \qquad F(u) = f(\cdot, u, u_x).$$

Then there is an open subset $\mathcal{V}$ of H^2 such that $A \in C^k(\mathcal{V}, \mathscr{L}(H^3, H^1))$ and $F \in C^k(\mathcal{V}, H^1)$, and both maps are Lipschitz on bounded subsets of $\mathcal{V}$. One can take $\mathcal{V} = H^2$ if $U_1 = U_2 = \mathbb{R}^N$. At $\overline{u} \in \mathcal{V}$, the derivatives are for $u \in H^2$ and $v \in H^3$ given by

$$A'(\overline{u})[u, v] = (\partial_2 a(\cdot, \overline{u})[u, v_x])_x, \quad F'(u_0)v = \partial_2 f(\cdot, \overline{u}, \overline{u}_x)v + \partial_3 f(\cdot, \overline{u}, \overline{u}_x)v_x.$$

Proof. Choose $\mathcal{V} \subseteq H^2$ such that for $u \in \mathcal{V}$ the closure of the images of $u, u_x \in H^1 \subset \mathrm{BC}$ are uniformly contained in U_1 and U_2, respectively. Let $u \in \mathcal{V}$. For $h \in H^2$ we use $\|uh\|_{L^2} \leq \|u\|_{\mathrm{BC}}\|h\|_{L^2}$ and $\|u\|_{\mathrm{BC}} \leq C\|u\|_{H^1}$ to estimate

$$\begin{aligned}
\|\partial_2 f(\cdot, u, u_x)h\|_{H^1} &\leq \|\partial_2 f(\cdot, u, u_x)\|_{\mathrm{BC}}(\|h\|_{L^2} + \|h_x\|_{L^2}) \\
&\quad + \|f''(\cdot, u, u_x)\|_{\mathrm{BC}}(\|h\|_{L^2} + \|u_x\|_{L^2}\|h\|_{\mathrm{BC}} + \|u_{xx}\|_{L^2}\|h\|_{\mathrm{BC}}) \\
&\leq C(\|f'(\cdot, u, u_x)\|_{\mathrm{BC}} + \|f''(\cdot, u, u_x)\|_{\mathrm{BC}}\|u\|_{H^2})\|h\|_{H^1}.
\end{aligned}$$

In the same way we obtain

$$\|\partial_3 f(\cdot, u, u_x)h_x\|_{H^1} \leq C(\|f'(\cdot, u, u_x)\|_{\mathrm{BC}} + \|f''(\cdot, u, u_x)\|_{\mathrm{BC}}\|u\|_{H^2})\|h\|_{H^2}.$$

Defining $F'(u)h = \partial_2 f(\cdot, u, u_x)h + \partial_3 f(\cdot, u, u_x)h_x$ we thus have $F'(u) \in \mathscr{L}(H^2, H^1)$, and that $u \mapsto F'(u)$ is bounded on bounded subsets of $\mathcal{V}$. If h is small, then the pointwise identity

$$F(u + h) - F(u) - F'(u)h = \int_0^1 \int_0^1 \big(\partial_{22} f(\cdot, u + \tau s h, u_x)[h, \tau h]$$
$$+ \partial_{33} f(\cdot, u, u_x + \tau s h_x)[h_x, \tau h_x]\big) \mathrm{d}\tau \mathrm{d}s$$

and the same types of estimates as above yield

$$\|F(u + h) - F(u) - F'(u)h\|_{H^1} \leq C(f, h)\|h\|_{H^2}^2,$$

where $C(f, h)$ is bounded as $h \to 0$. These arguments and $f(\cdot, 0, 0) \in H^1$ yield $F(u) \in H^1$ for $u \in \mathcal{V}$ and the differentiability of F in $\mathcal{V}$. The Lipschitz property follows from the boundedness of F'. Iteration for higher derivatives gives $F \in C^k$. The arguments apply to $u \mapsto a(u)$ on H^2 as well, which yields the assertion on A. $\qquad\square$

Note that if f is independent of u_x, then the arguments from the proof above show that $f : H^1 \to H^1$ is smooth.

Lemma 5.3. *In the situation of Theorem 5.5, assume in addition that a and f are C^{k+2} for some $k \geq 0$. Let A and F be defined by*

$$A(u)v = \partial_i(a_{ij}(\overline{u} + u)\partial_j v), \quad F(u) = \partial_i(a_{ij}(\overline{u} + u)\partial_j \overline{u}) + c_i\partial_i(\overline{u} + u) + f(\overline{u} + u).$$

Then for all sufficiently large $p > 2$ there is is an open neighbourhood

$$\mathcal{V} \subset B_{2,p}^{2 - 2/p}$$

of the zero function such that $F \in C^k(\mathcal{V}, L^2)$ and $A \in C^k(\mathcal{V}, \mathscr{L}(H^2, L^2))$, and both maps are Lipschitz on bounded sets. One can take $\mathcal{V} = B_{2,p}^{2-2/p}$ if $U = \mathbb{R}^N$.

Proof. Since $n \leq 3$, from Sobolev's embedding (5.2.7) we find $p > 2$ such that $B_{2,p}^{2-2/p} \subset H^{1,4} \cap \mathrm{BC}$. Then $\mathcal{V}$ can be chosen such that the image of $\overline{u} + u$ is strictly contained in U, uniformly in $u \in \mathcal{V}$. The regularity of A and F can be derived as in Lemma 5.2, using $F(0) = 0$. The need for $B_{2,p}^{2-2/p} \subset H^{1,4}$ and thus also $H^2 \subset H^{1,4}$ comes from the nonlinear gradient terms. Indeed,

assume for simplicity that $\overline{u} = 0$. Then for $u_1, u_2 \in B_{2,p}^{2-2/p}$ and $v \in H^2$ we can estimate

$$\|a'_{ij}(u_1)\partial_i u_1 \partial_j v - a'_{ij}(u_2)\partial_i u_2 \partial_j v\|_{L^2}$$
$$\leq \|a'_{ij}(u_1)\partial_i u_1 - a'_{ij}(u_2)\partial_i u_2\|_{L^4}\|\partial_j v\|_{L^4}$$
$$\leq \left(\|a'_{ij}(u_1)\|_{\mathrm{BC}}\|u_1 - u_2\|_{H^{1,4}} + \|u_2\|_{H^{1,4}}\|\|a'_{ij}(u_1) - a'_{ij}(u_2)\|_{\mathrm{BC}}\right)\|v\|_{H^{1,4}},$$

employing Hölder's inequality $L^4 \cdot L^4 \subset L^2$ in the first equation. $\qquad\square$

5.A.2 A commuting isomorphism for elliptic operators

The following auxiliary result for second order differential operators allows to transfer spectral properties from L^2 to H^1 by conjugation.

Lemma 5.4. *Let $\alpha, \beta, \gamma \in \mathrm{BC}^1(\mathbb{R}, \mathbb{R}^{N \times N})$, and assume that $\alpha(x)$ is positive definite, uniformly in x. Then there is a continuous isomorphism $T : H^1 \to L^2$, which also maps $T : H^3 \to H^2$ isomorphically, that commutes on H^3 with the operator $\varphi \mapsto \mathcal{L}\varphi := \alpha\varphi_{xx} + \beta\varphi_x + \gamma\varphi$.*

Proof. The isomorphism T will be the square root of a shift of $\mathcal{L}$. The main point is to show that its domain for the realization on H^2 is H^3.

Denote by $\mathcal{L}_{L^2}$ the realization of $\mathcal{L}$ on L^2, with domain H^2. The properties of α together with [7, Theorem 9.6] imply that there is $\omega > 0$ such that $B = \omega - \mathcal{L}_{L^2}$ is a (negative) sectorial operator and has a bounded holomorphic functional calculus of angle strictly smaller than $\frac{\pi}{2}$. In particular, $T := B^{1/2}$ is a well-defined continuous isomorphism $D(B^{1/2}) \to L^2$, see [188, Theorem 1.15.2]. The boundedness of the holomorphic calculus of B implies that it has the property of bounded imaginary powers. Therefore, combining [115, Lemma 4.1.11] with [188, Theorem 1.15.3] (or [115, Theorem 4.2.6]), we have $D(B^{1/2}) = [L^2, H^2]_{1/2}$, where $[\cdot, \cdot]_{1/2}$ denotes complex interpolation (see [18, 115, 188]). Since $[L^2, H^2]_{1/2} = H^1$ by [188, Remark 2.4.2/2], it follows that $T : H^1 \to L^2$ is an isomorphism.

Next, we show that $T : H^3 \to H^2$ is an isomorphism. Again by [188, Theorem 1.15.2], T also maps isomorphically $D(B^{3/2}) \to D(B) = H^2$. We show that $D(B^{3/2}) = H^3$ as Banach spaces. By [115, Lemma 4.1.16, Theorem 4.1.11] and the previous considerations we have

$$D(B^{3/2}) = \{u \in D(B) : Bu \in D(B^{1/2})\} = \{u \in H^2 : \mathcal{L}u \in H^1\}.$$

For $u \in H^3$ we clearly have $\mathcal{L}u \in H^1$, hence $H^3 \subseteq D(B^{3/2})$. Conversely, let $u \in H^2$ such that $\mathcal{L}u \in H^1$. Then $\alpha u_{xx} = \psi := -\beta u_x - \gamma u + \mathcal{L}u \in H^3$. By assumption, the coefficient α is pointwise invertible, with $\alpha^{-1} \in$ BC^1. Therefore $u_{xx} = \alpha^{-1}\psi \in H^1$, and so $u \in H^3$. We conclude that $D(B^{3/2}) = H^3$ as sets. Arguing as before, we get

$$\|u\|_{D(B^{3/2})} = \|u\|_{H^2} + \|\mathcal{L}u\|_{H^1} \leq C\|u\|_{H^3},$$

for a constant independent C of u. Since we already know that H^3 is complete with respect to $\|\cdot\|_{D(B^{3/2})}$ and $\|\cdot\|_{H^3}$, the converse estimate follows from the open mapping theorem.

Finally, it follows from [115, Theorem 4.1.6] that $\omega - \mathcal{L}_{L^2}$ and its square root T commute on H^3. This implies that also $\mathcal{L}_{L^2}$ commutes with T. $\qquad\square$

The assertion of the above lemma remains valid, with literally the same proof, if one replaces the L^2-setting by an L^q-setting, where $q \in (1,\infty)$.

5.A.3 The time-one solution map

We use the implicit function theorem to prove that in the neighbourhood of an equilibrium the solution semiflow obtained from Theorem 5.1 for (5.2.1) is as smooth as the right-hand side. See [78, Theorem 3.4.4] for the semilinear case, as well as [114, Theorem 8.3.4] and [6, Theorem 4.1] for quasilinear frameworks.

Proposition 4. *In the situation of Theorem 5.1, assume additionally that*

$$A \in C^k(\mathcal{V}, \mathcal{L}(X_1, X_0)), \quad F \in C^k(\mathcal{V}, X_0), \quad \text{for some } k \in \mathbb{N}.$$

Let $u_* \in \mathcal{V} \cap X_1$ be an equilibrium of (5.2.1), i.e., $A(u_*)u_* + F(u_*) = 0$. Then for any $\tau > 0$ there is a neighbourhood $\mathcal{U} \subseteq \mathcal{V}$ of u_* such that the time-τ map $u_0 \mapsto \Phi_\tau(u_0) = u(\tau; u_0)$ for the solution semiflow for (5.2.1) is well-defined and belongs to $C^k(\mathcal{U}, \mathcal{X})$. Moreover, let $\mathcal{L}_* = A(u_*) + A'(u_*)[\cdot, u_*] + F'(u_*)$. Then $\Phi_\tau'(u_*) = e^{\tau\mathcal{L}_*}$.

Proof. We assume $\mathcal{V} = \mathcal{X}$. Set $\mathbb{E}_1 = H^{1,p}(0, \tau; X_0) \cap L^p(0, \tau; X_1)$ and $\mathbb{E}_0 = L^p(0, \tau; X_0)$, and consider

$$\Psi : \mathbb{E}_1 \times \mathcal{X} \to \mathbb{E}_0 \times \mathcal{X}, \qquad \Psi(u, u_0) = (\partial_t u - A(u)u - F(u), u(0) - u_0).$$

Note that $u \in \mathbb{E}_1$ solves (5.2.1) on $(0, \tau)$ with initial value $u_0 \in \mathcal{X}$ if and only if $\Psi(u, u_0) = (0, 0)$. Consider u_* as an element of $\mathbb{E}_1$. Then $\Psi(u_*, u_*) = (0, 0)$. The assumptions on A and F imply $\Psi \in C^k(\mathbb{E}_1 \times \mathcal{X}, \mathbb{E}_0 \times \mathcal{X})$ and

$$D_1\Psi(u_*, u_*)v = (\partial_t v - \mathcal{L}_* v, v(0)), \qquad v \in \mathbb{E}_1.$$

From the proof of Theorem 5.1 we know that $-A(u_*)$ enjoys maximal L^p-regularity. The linear operator $A'(u_*)[\cdot, u_*] + F'(u_*)$ is continuous from $\mathcal{X} = (X_0, X_1)_{1-1/p, p}$ to X_0, i.e., it is of lower order. Thus $-\mathcal{L}_*$ has maximal L^p-regularity as well, see [55, Theorem 6.2]. In other words, $D_1\Psi(u_*, u_*) \in \mathcal{L}(\mathbb{E}_1, \mathbb{E}_0 \times \mathcal{X})$ is an isomorphism. This gives a neighbourhood $\mathcal{U}$ of u_* in $\mathcal{X}$ such that $u_0 \mapsto u(\cdot; u_0)$ belongs to $C^k(\mathcal{U}, \mathbb{E}_1)$, where $u(\cdot; u_0)$ is the solution of (5.2.1) on $(0, \tau)$. Moreover, for $v_0 \in \mathcal{X}$ we differentiate $\Psi(u(\cdot; u_0), u_0) = 0$ in u_* to get that

$$D_{u_0}u(\cdot; u_*)v_0 = -D_1\Psi(u_*, u_*)^{-1}D_2\Psi(u_*, u_*)v_0 = -D_1\Psi(u_*, u_*)^{-1}(0, -v_0)$$

is the unique solution $v \in \mathbb{E}_1$ of $\partial_t v - \mathcal{L}_* v = 0$ on $(0, \tau)$ with $v(0) = v_0$, i.e., $D_{u_0}u(\cdot; u_*) = e^{\cdot \mathcal{L}_*}$. Finally, the trace at time τ is linear and continuous as a map $\mathbb{E}_1 \to \mathcal{X}$, see [188, Theorem 1.14.5]. Applying this to $u(\cdot; u_0)$ gives the assertion for Φ_τ. $\qquad\square$

6 Outlook

We briefly outline future research topics, motivated by the results presented in this thesis.

Stability of 2D patterns

In Chapter 2 and 3, following [147,199] we have extended the stability analysis from spatially homogeneous vegetation to banded vegetation patterns. Banded patterns are periodic in one space dimension and constant in the other. For assessing the stability of these patterns against perturbations we have applied a Floquet-Bloch decomposition in the dimension of periodicity and Fourier analysis in the other.

Spotted patterns are periodic in two space dimensions. A next important step is to determine stability of spotted patterns, which requires the application of Floquet-Bloch decomposition in two space dimensions. The stability of these patterns is crucial for the understanding of the final steps in the desertification process.

Observability of dashed vegetation patterns

In Chapter 3 we have seen that under increasing environmental stress banded vegetation tends to break up in dashed vegetation: spots aligned in stripes. The power spectrum (or periodogram, obtained after Fourier transformation) of dashed vegetation shows similarity both to striped patterns and more hexagonal distributions of spots.

In existing observational studies dashed patterns could have both been identified as banded or spotted patterns [12,35,193]. An observational framework in which dashed patterns can be identified separately would help in the validation or falsification of the banded vegetation breakup process.

Gapped patterns in advective reaction-diffusion systems

In Chapter 3 we have shown that for a very general two-component reaction-advection-diffusion system, the spatially homogeneous state is first destabilized by perturbations in the direction of advection. Although this doesn't exclude the possibility of observable gapped patterns on slopes, their observation for a wide range of rainfall parameter values for all relevant slopes [12] is interesting. Analytical analysis near the onset of pattern formation for reaction-advection-diffusion systems in two space dimensions may shed light on the origins of gapped vegetation patterns.

Field data input for the modeling of grazing

In Chapter 4 a framework has been introduced to include nonlocal grazing in arid ecosystem modeling. Based on the extended Klausmeier model, several qualitatively distinct changes in vegetation pattern stability have been presented, depending on which modeling choices are made.

Because the framework allows for different implementation possibilities, extraction of foraging responses (distributional, numerical and functional) from field data is desired to make an informed decision about the modeling choice.

Bibliography

[1] J. Alexander, R. Gardner, and C.K.R.T. Jones. A topological invariant arising in the stability analysis of travelling waves. *J. Reine Angew. Math.*, 410:167–212, 1990.

[2] V.G. Allen, C. Batello, E.J. Berretta, J. Hodgson, M. Kothmann, X. Li, J. McIvor, J. Milne, C. Morris, A. Peeters, and M. Sanderson. A international terminology for grazing lands and grazing animals. *Grass and Forage Science*, 66:2–28, 2011.

[3] H. Amann. Nonhomogeneous linear and quasilinear elliptic and parabolic boundary value problems. In *Function spaces, differential operators and nonlinear analysis*. Vieweg+Teubner Verlag, 1993.

[4] H. Amann. *Linear and quasilinear parabolic problems. Volume I: Abstract linear theory*. Birkhäuser, 1995.

[5] H. Amann. Nonlocal quasilinear parabolic equations. *Russian Math. Surveys*, 60:1021–1035, 2005.

[6] H. Amann. Quasilinear parabolic problems via maximal regularity. *Advances Diff. Eqs.*, 10:1081–1110, 2005.

[7] H. Amann, M. Hieber, and G. Simonett. Bounded h_∞-calculus for elliptic operators. *Diff. Int. Eqs.*, 7:613–653, 1994.

[8] S.B. Angenent. Nonlinear analytic semiflows. *Proc. R. Soc. Edinb. A*, 115:91–107, 1990.

[9] R.A. Distel ans A.I. Kröpfl. Degradation and recovery of semi-arid rangelands in the transitional zone between the caldenal and monte regions of argentina. In *Proceedings of the IX International Rangeland Congress*, 2011.

[10] Millennium Ecosystem Assessment. *Ecosystems and Human Well-being; A Framework for Assessment*. Island Press, 2003.

[11] M. Baldwin and H.W. Hawker. Soil survey of the fort lauderdale area, florida. Technical report, US Department of Agriculture. Bureau of Soils, 1915.

[12] N. Barbier, P. Couteron, and V. Deblauwe. Case Study of Self-Organized Vegetation Patterning in Dryland Regions of Central Africa. In *Patterns of Land Degradation in Drylands: Understanding Self-Organised Ecogeomorphic Systems*. Springer, 2014.

[13] A.P. Barrett, T.H. Painter, and C.C. Landry. Desert dust enhancement of mountain snowmelt. *Intermountain West Climate Summary*, 4(2), 2008.

[14] J.T. Beale. Large-time regularity of viscous surface waves. *Arch. Rational Mech. Anal.*, 84:307–352, 1984.

[15] M. Beck, B. Sandstede, and K. Zumbrun. Nonlinear stability of time-periodic shock waves. *Arch. Rat. Mechanics and Anal.*, 196:1011–1076, 2010.

[16] G. Bel, A. Hagberg, and E. Meron. Gradual regime shifts in spatially extended ecosystems. *Theoretical Ecology*, 5:591–604, 2012.

[17] A. Ben-Artzi and I. Gohberg. Dichotomy of systems and invertibility of linear ordinary differential operators. *Operator Theory: Advances and Applications*, 56:90–119, 1992.

[18] J. Bergh and J. Löfström. *Interpolation Spaces: An Introduction*. Springer, 1976.

[19] F. Borgogno, P. D'Odorico, F. Laio, and L. Ridolfi. Mathematical models of vegetation pattern formation in ecohydrology. *Rev. Geophys.*, 47, 2009.

[20] B.M. Brown, M.S.P. Eastham, and K.M. Schmidt. *Periodic Differential Operators*. Springer

Basel, 2013.

[21] F. Busse. Non-linear properties of thermal convection. *Reports on Progress in Physics*, 41:1929–1967, 1978.

[22] J. Carballido-Landeira, P. Taboada, and A.P. Muñuzuri. Effect of electric field on turing patterns in a microemulsion. *Soft Matter*, 8, 2012.

[23] J.G. Charney. Dynamics of deserts and drought in the sahel. *Quarterly Journal of the Royal Meteorological Society*, 101(428):193–202, 1975.

[24] W. Chen and M.J. Ward. Oscillatory instabilities and dynamics of multi-spike patterns for the one-dimensional Gray-Scott model. *European J. Appl. Math.*, 20:187–214, 2009.

[25] W. Chen and M.J. Ward. The stability and dynamics of localized spot patterns in the two-dimensional Gray-Scott model. *SIAM J. Appl. Dyn. Sys.*, 10:582–666, 2011.

[26] C. Chicone and Y. Latushkin. *Evolution semigroups in dynamical systems and differential equations.* American Mathematical Society, 1999.

[27] J. Cholewa and T. Dlotko. *Global attractors in abstract parabolic problems.* Cambridge University Press, 2000.

[28] P. Clément and S. Li. Abstract parabolic quasilinear equations and applications to a ground-water flow problem. *Adv. Math. Sci. Appl.*, 3:17–32, 1994.

[29] P. Clément and G. Simonett. Maximal regularity in continuous interpolation spaces and quasilinear parabolic problems. *J. Evol. Eqs.*, 1:39–67, 2001.

[30] P. Couteron and O. Lejeune. Periodic spotted patterns in semi-arid vegetation explained by a propagation-inhibition model. *Journal of Ecology*, 89:616–628, 2001.

[31] B.D. Dalziel, J.M. Morales, and J.M. Fryxell. Fitting probability distributions to animal movement trajectories: Using artificial neural networks to link distance, resources, and memory. *The American Naturalist*, 172(2):248–258, 2008.

[32] H.J. de Boer, E.I. Lammertsma, F. Wagner-Cremer, D.L. Dilcher, M.J. Wassen, and S.C. Dekker. Climate forcing due to optimization of maximal leaf conductance in subtropical vegetation under rising CO_2. *Proceedings of the National Academy of Sciences*, 108(10):4041–4046, 2011.

[33] L. de Simon. Un'applicazione del la teoria degli integrali singolari al lo studio del le equazioni differenziali lineari astratte del primo ordine. *Rendiconti del Seminario Matematico della Universita di Padova*, 34:205–223, 1964.

[34] D.L. DeAngelis, W.M. Post, and C.C. Travis. *Positive Feedback in Natural Systems.* Springer-Verlag, 1980.

[35] V. Deblauwe, 2014. Personal communication.

[36] V. Deblauwe, N. Barbier, P. Couteron, O. Lejeune, and J. Bogaert. The global biogeography of semi-arid periodic vegetation patterns. *Global Ecology and Biogeography*, 17:715–723, 2008.

[37] V. Deblauwe, N. Barbier, P. Couteron, O. Lejeune, and J. Bogaert. The global biogeography of semi-arid periodic vegetation patterns. *Global Ecology and Biogeography*, 17:715–723, 2008.

[38] V. Deblauwe, P. Couteron, J. Bogaert, and N. Barbier. Determinants and dynamics of banded vegetation pattern migration in arid climates. *Ecological Monographs*, 82:3–21, 2012.

[39] V. Deblauwe, P. Couteron, O. Lejeune, J. Bogaert, and N. Barbier. Environmental modulation of self-organized periodic vegetation patterns in sudan. *Ecography*, 34:990–1001, 2011.

[40] S. Díaz, I. Noy-Meir, and M. Cabido. Can grazing response of herbaceous plants be predicted from simple vegetative traits? *Journal of Applied Ecology*, 38:497–508, 2001.

[41] E. Doedel. Auto: A program for the automatic bifurcation analysis of autonomous systems.

Congressus Numerantium, 30:265–284, 1981.

[42] E.J. Doedel. Auto-07p: Continuation and bifurcation software for ordinary differential equations. http://cmvl.cs.concordia.ca/auto.

[43] A. Doelman, W. Eckhaus, and T.J. Kaper. Slowly-modulated two-pulse solutions in the Gray–Scott model i: Asymptotic construction and stability. *SIAM J Appl. Math.*, 61:1080–1102, 2000.

[44] A. Doelman, W. Eckhaus, and T.J. Kaper. Slowly-modulated two-pulse solutions in the Gray–Scott model ii: Geometric theory, bifurcations, and splitting dynamics. *SIAM J Appl. Math.*, 61:2036–2062, 2001.

[45] A. Doelman, R.A. Gardner, and T.J. Kaper. Stability analysis of singular patterns in the 1-D Gray–Scott model: a matched asymptotics approach. *Physica D*, 122:1–36, 1998.

[46] A. Doelman, R.A. Gardner, and T.J. Kaper. Large stable pulse solutions in reaction-diffusion equations. *Indiana Univ. Math. J.*, 50:443–507, 2001.

[47] A. Doelman, R.A. Gardner, and T.J. Kaper. A stability index analysis of 1-d patterns of the Gray-Scott model. *Memoirs of the AMS*, 155(737), 2002.

[48] A. Doelman and T.J. Kaper. Semistrong pulse interactions in a class of coupled reaction-diffusion equations. *SIADS*, 2:53–96, 2003.

[49] A. Doelman, T.J. Kaper, and P. Zegeling. Pattern formation in the one-dimensional Gray-Scott model. *Nonlinearity*, 10(2):523–563, 1997.

[50] A. Doelman, T.J. Kaper, and P. Zegeling. Pattern formation in the one-dimensional gray-scott model. *Nonlinearity*, 10:523–563, 1997.

[51] A. Doelman, J.D.M. Rademacher, and S. van der Stelt. Hopf dances near the tips of busse balloons. *Discrete and Continuous Dynamical Systems*, 5:61–92, 2012.

[52] A. Doelman, B. Sandstede, A. Scheel, and G. Schneider. *The dynamics of modulated wave trains*. American Mathematical Society, 2009.

[53] A. Doelman and H. van der Ploeg. Homoclinic stripe patterns. *SIAM J. Appl. Dyn. Syst.*, 1(1):65–104, 2002.

[54] T. Dohnal, J.D.M. Rademacher, H. Uecker, and D. Wetzel. pde2path 2.0: multi-parameter continuation and periodic domains. In *ENOC 2014 - Proceedings of 8th European Nonlinear Dynamics Conference*, 2014.

[55] G. Dore. Maximal regularity for abstract cauchy problems. *Adv. Diff. Eqns.*, pages 293–322, 2000.

[56] G.P. Drazin and W.H. Reid. *Hydrodynamic stability*. Cambridge Univ. P., 1982.

[57] D. Dunkerley. Banded vegetation: development under uniform rainfall from a simple cellular automaton model. *Plant Ecology*, 129:103–111, 1997.

[58] D.L. Dunkerley. Vegetation Mosaics of Arid Western New South Wales, Australia: Considerations of their Origin and Persistence. In *Patterns of Land Degradation in Drylands: Understanding Self-Organised Ecogeomorphic Systems*. Springer, 2013.

[59] L. Edelstein-Keshet. *Mathematical models in biology*. McGraw-Hill, 1988.

[60] K.-J. Engel and R. Nagel. *One-Parameter Semigroups for Linear Evolution Equations*. Springer Verlag, 2000.

[61] M.B. Eppinga, P.C. de Ruiter, M.J. Wassen, and M. Rietkerk. Nutrients and hydrology indicate the driving mechanisms of peatland surface patterning. *The American naturalist*, 173:803–818, 2009.

[62] J. Escher, J. Prüss, and G. Simonett. A new approach to the regularity of solutions for parabolic equations. In *Evolution Equations*. Taylor & Francis Inc, 2003.

[63] J.W. Evans. Nerve axon equations. iv. the stable and the unstable impulse. *Indiana Univ. Math. J.*, 24:1169–1190, 1974/75.

Bibliography

[64] S. Focardi and P. Marcellini ans P. Montanaro. Do ungulates exhibit a food density threshold? a fieldstudy of optimal foraging and movement patterns. *Journal of Animal Ecology*, 65:606–620, 1996.

[65] S.D. Fretwell and H.L. Lucas Jr. On territorial behavior and other factors influencing habitat distribution in birds. *Acta Biotheoretica*, 19(1):16–36, 1969.

[66] J.M. Fryxell, M. Hazell, L. Brger, B.D. Dalziel, D.T. Haydon, J.M. Morales, T. McIntosh, and R.C. Rosatte. Multiple movement modes by large herbivores at multiple spatiotemporal scales. *PNAS*, 105(49):19114–19119, 2008.

[67] R.A. Gardner. On the structure of the spectra of periodic travelling waves. *J. Math. Pures Appl.*, 9:415–439, 1993.

[68] A. Gierer and H. Meinhardt. A theory of biological pattern formation. *Kybernetik*, 12:30–9, 1972.

[69] E. Gilad, M. Shachak, and E. Meron. Dynamics and spatial organization of plant communities in water-limited systems. *Theoretical Population Biology*, 72(2):214–230, 2007.

[70] E. Gilad, J. von Hardenberg, A. Provenzale, M. Shachak, and E. Meron. Ecosystem engineers: From pattern formation to habitat creation. *Physical Review Letters*, 93:1–4, 2004.

[71] M. Golubitsky, J.W. Swift, and E. Knobloch. Symmetries and pattern selection in Rayleigh-Benard convection. *Physica D*, 10:249–276, 1984.

[72] K. Gowda, H. Riecke, and M. Silber. Transitions between patterned states in vegetation models for semiarid ecosystems. *Physical Review E*, 89, 2014.

[73] A. Grainger, M. Stafford Smith, V.R. Squires, and E.P. Glenn. Disertification and climate change: the case for greater convergence. *Mitigation and Adaptation Strategies for Global Change*, 5(4):361–377, 2000.

[74] P. Gray and S.K. Scott. Autocatalytic reactions in the isothermal, continuous stirred tank reactor: oscillations and instabilities in the system a + 2b → 3b, b → c. *Chemical Engineering Science*, 39:1087–1097, 1984.

[75] J.A. Griepentrog and L. Recke. Local existence, uniqueness, and smooth dependence for nonsmooth quasilinear parabolic problems. *J. Evol. Equ.*, 10:341–375, 2012.

[76] L. Gunderson. Ecological resilience–in theory and application. *Annual Review of Ecology and Systematics*, 31, 2000.

[77] T. Häcker, H. Uecker, and G. Schneider. Self-similar decay to the marginally stable ground state in a model for film flow over inclined wave bottoms. *Electronic Journal of Differential Equations*, pages 1–51, 2012.

[78] D. Henry. *Geometric theory of semilinear parabolic equations*. Springer, 1981.

[79] R. HilleRisLambers, M. Rietkerk, F.V.D. Bosch, H.H.T. Prins, and H.D. Kroon. Vegetation pattern formation in semi-arid grazing systems. *Ecology*, 82:50–61, 2001.

[80] C.S. Holling. The components of predation as revealed by a study of small-mammal predation of the european pine sawfly. *The Canadian Entomologist*, 91(5):234–261, 1959.

[81] C.S. Holling. Resilience and stability of ecological systems annual review of ecology and systematics. *Annual Review of Ecology and Systematics*, 4:1–23, 1973.

[82] M. Holzer, A. Doelman, and T.J. Kaper. Existence and stability of traveling pulses in a reaction-diffusion-mechanics system. *J Nonlinear Sci*, 23:129–177, 2013.

[83] W. Horsthemke and R. Lefever. *Noise-Induced Transitions. Theory and Applications in Physics, Chemistry, and Biology*. Springer-Verlag, 2 edition, 2006.

[84] H.N. Le Houérou. Rain use-efficiency: a unifying concept in arid-land ecology. *Journal of Arid Environments*, 7:213–247, 1984.

[85] R. Hoyle. *Pattern Formation: An Introduction to Methods*. Cambridge University Press, Cambridge, UK, 2006.

[86] Working Group I. Climate change 2007: The physical science basis. Technical report, IPCC, 2007.

[87] Working Group I. Climate change 2013: The physical science basis. Technical report, IPCC, 2013.

[88] J.J.S. Jerome and J.-M. Chomaz. Extended Squire's transformation and its consequences for transient growth in a confined shear flow. *J. Fluid Mech.*, 744:430–456, 2014.

[89] F. Joos and R. Spahni. Rates of change in natural and anthropogenic radiative forcing over the past 20,000 years. *Proceedings of the National Academy of Sciences*, 105:1425–1430, 2008.

[90] T. Kapitula and K. Promislow. Spectral and dynamical stability of nonlinear waves. *Applied Mathematical Sciences*, 185, 2013.

[91] T. Kato. Quasi-linear equations of evolution, with applications to partial differential equations. *Springer-Verlag Lecture Notes in Mathematics*, 448:25–70, 1975.

[92] T. Kato. *Perturbation theory for linear operators. Corrected Printing of the Second Edition.* Springer, 1980.

[93] S. Kawashima. Systems of a hyperbolic-parabolic composite type with applications to the equations of magnetohydrodynamics. Master's thesis, Kyoto University, 1983.

[94] B.J. Kealy and D.J. Wollkind. A nonlinear stability analysis of vegetative turing pattern formation for an interaction-diffusion plant-surface water model system in an arid flat environment. *Bulletin of mathematical biology*, 74:803–833, 2012.

[95] S. Kefi, M. Rietkerk, and G.G. Katul. Vegetation pattern shift as a result of rising atmospheric co2 in arid ecosystems. *Theoretical population biology*, 74:332–344, 2008.

[96] S. Kinast, Y.R. Zelnik, G. Bel, and E. Meron. Interplay between turing mechanisms can increase pattern diversity. *Physical Review Letters*, 2014.

[97] C.A. Klausmeier. Regular and irregular patterns in semi-arid vegetation. *Science*, 284:1826–1828, 1999.

[98] A.Y. Kletter, J. von Hardenberg, E. Meron, and A. Provenzale. Patterned vegetation and rainfall intermittency. *Journal of Theoretical Biology*, 256:574–583, 2009.

[99] M. Köhne, J. Prüss, and M. Wilke. On quasilinear parabolic evolution equations in weighted l_p-spaces. *J. Evol. Equ.*, 10:443–463, 2010.

[100] T. Kolokolnikov, W. Sun, M.J. Ward, and J. Wei. The Stability of a Stripe for the Gierer-Meinhardt Model and the Effect of Saturation. *SIAM J. Appl. Dyn. Sys.*, 5(2):313–363, 2006.

[101] T. Kolokolnikov, M.J. Ward, and J. Wei. The existence and stability of spike equilibria in the one–dimensional Gray–Scott model: the pulse–splitting regime. *Physica D*, 202:258–293, 2005.

[102] T. Kolokolnikov, M.J. Ward, and J. Wei. The existence and stability of spike equilibria in the one-dimensional Gray–Scott model: the low feed rate regime. *Studies in Appl. Math.*, 115(1):21–71, 2005.

[103] T. Kolokolnikov, M.J. Ward, and J. Wei. Zigzag and Breakup Instabilities of Stripes and Rings in the Two-Dimensional Gray-Scott Model. *Studies in Appl. Math.*, 116(1):35–95, 2006.

[104] N. Kumar and W. Horsthemke. Turing bifurcation in a reaction-diffusion system with density-dependent dispersal. *Physica A*, 389:1812–1818, 2010.

[105] O. Ladyzhenskaya, V. Solonnikov, and N. Ural'ceva. *Linear and quasi-linear equations of parabolic type.* American Mathematical Society, 1968.

[106] Y. Latushkin, J. Prüss, and R. Schnaubelt. Stable and unstable manifolds for quasilinear parabolic systems with fully nonlinear boundary conditions. *J. Evol. Equ.*, 6:537–576, 2006.

[107] Y. Latushkin, J. Prüss, and R. Schnaubelt. Center manifolds and dynamics near equilibria

of quasilinear parabolic systems with fully nonlinear boundary conditions. *Discr. Cont. Dyn. Sys. Ser. B*, 9:595–633, 2008.

[108] R. Lefever and O. Lejeune. On the origin of tiger bush. *Bulletin of Mathematical Biology*, 59:263–294, 1997.

[109] O. Lejeune, P. Couteron, and R. Lefever. Short range co-operativity competing with long range inhibition explains vegetation patterns. *Acta Oecologica*, 20:171–183, 1999.

[110] O. Lejeune and M. Tlidi. A model for the explanation of vegetation stripes (tiger bush). *Journal of Vegetation Science*, 10:201–208, 1999.

[111] O. Lejeune, M. Tlidi, and P. Couteron. Localized vegetation patches: A self-organized response to resource scarcity. *Physical Review E*, 2002.

[112] J.L. Lions and E. Magenes. *Non-Homogeneous Boundary Value Problems and Applications II*. Springer, 1972.

[113] C.M. Luke and P.M. Cox. Soil carbon and climate change: from the Jenkinson effect to the compost-bomb instability. *European Journal of Soil Science*, 62:5–12, 2011.

[114] A. Lunardi. *Analytic semigroups and optimal regularity for parabolic problems*. Birkhäuser, 1995.

[115] A. Lunardi. *Interpolation theory*. Springer, 2009.

[116] W. Macfadyen. Vegetation patterns in the semi-desert plains of british somaliland. *Geographical Journal*, 116:199–211, 1950.

[117] P.K. Maini, M.R. Myerscough, J.D. Murray, and K.H. Winters. Bifurcating spatially heterogeneous solutions in a chemotaxis model for biological pattern formation. *Bul l. Math. Biol.*, 53:701–719, 1991.

[118] C. Malmström. *Degerö stormyr: en botanisk, hydrologisk och utvecklingshistorisk undersökning över ett nordsvenskt myrkomplex*. PhD thesis, Uppsala University, 1923.

[119] Y. Mau, L. Haim, and E. Meron. Reversing desertification as a spatial resonance problem. *Physical Review E*, 91, 2015.

[120] H. Meinhardt. *Models of biological pattern formation*. Academic Press, 1982.

[121] H. Meinhardt. *The algorithmic beauty of sea shells*. Springer-Verlag, 1995.

[122] J. Merkin, R. Satnoianu, and S. Scott. The development of spatial structure in an ionic chemical system induced by applied electric fields. *Dynamics and Stability of Systems: An International Journal*, 15(3):209–230, 2000.

[123] J.H. Merkin, R.A. Satnoianu, and S.K. Scott. Spatiotemporal chaos in a differential flow reactor. *J. Chem. Soc., Faraday Trans.*, 94:1211–1216, 1998.

[124] E. Meron. Pattern-formation approach to modelling spatially extended ecosystems. *Ecological Modelling*, 234:70–82, 2012.

[125] E. Meron, E. Gilad, J. von Hardenberg, M. Shachak, and Y. Zarmi. Vegetation patterns along a rainfall gradient. *Chaos, Solitons & Fractals*, 19:367–376, 2004.

[126] M. Meyries. Local well-posedness and instability of travelling waves in a chemotaxis model. *Adv. Diff. Equations*, 16:31–60, 2011.

[127] M. Meyries, J.D.M. Rademacher, and E. Siero. Quasilinear parabolic reaction-diffusion systems: user's guide to well-posedness, spectra and stability of travelling waves. *SIAM J. Appl. Dyn. Sys.*, 13:249–275, 2014.

[128] A. Mielke. Instability and stability of rolls in the swift–hohenberg equation. *Comm. Math. Phys.*, 189:829–853, 1997.

[129] A.S. Moretto and R.A. Distel. Effects of selective defoliation on the competitive interaction between palatable and unpalatable grasses. *Journal of Arid Environment*, 42:167–175, 1999.

[130] D.S. Morgan, A. Doelman, and T.J. Kaper. Stationary periodic patterns in the 1d gray-scott model. *Meth. Appl. Anal.*, 7:105–150, 2000.

[131] T. Nagaia and T. Ikeda. Traveling waves in a chemotactic model. *J. Math. Biol.*, pages 169–184, 1991.

[132] R. Nagel. Towards a "matrix theory" for unbounded opefrator matrices. *Math. Z.*, 201:57–68, 1989.

[133] W-M Ni. Diffusion, cross-diffusion, and their spike-layer steady states. *Notices of the AMS*, 45(1), 1998.

[134] I. Noy-Meir. Stability of grazing systems: An application of predator-prey graphs. *Journal of Ecology*, 63(2):459–481, 1975.

[135] T. Okayasu and Y. Aizawa. Systematic analysis of periodic vegetation patterns. *Progress of Theoretical Physics*, 106(4):705–720, 2001.

[136] T. Okayasu, T. Okuro, U. Jamsran, and K. Takeuchi. Degraded rangeland dominated by unpalatable forbs exhibits large-scale spatial heterogeneity. *Plant Ecology*, 213(4):625–635, 2012.

[137] K.J. Palmer. Exponential dichotomies and transversal homoclinic points. *J. Diff. Eqns.*, 55:225–256, 1984.

[138] K.J. Palmer. Exponential dichotomies and fredholm operators. *Proceedings of the American Mathematical Society*, 104:149–156, 1988.

[139] J.E. Pearson. Complex patterns in a simple system. *Science*, 261:189–192, 1993.

[140] B. Peña, C. Pérez-García, A. Sanz-Anchelergues, D.G. Míguez, and A.P. Muñuzuri. Transverse instabilities in chemical Turing patterns of stripes. *Phys. Rev. E*, 68, 2003.

[141] A.J. Perumpanani, J.A. Sherratt, and P.K. Maini. Phase differences in reaction-diffusion-advection systems and applications to morphogenesis. *IMA Journal of Applied Mathematics*, 55:19–33, 1995.

[142] S.D. Prince, E. Brown de Colstoun, and L.L. Kravitz. Evidence from rain-use efficiencies does not indicate extensive sahelian desertification. *Global Change Biology*, 4:359–374, 1998.

[143] J. Prüss. Maximal regularity for evolution equations in l_p-spaces. *Conferenze del Seminario di Matematica dell'Università di Bari*, 285:1–39, 2003.

[144] J. Prüss, G. Simonett, and R. Zacher. On convergence of solutions to equilibria for quasilinear parabolic problems. *J. Diff. Eq.*, 246:3902–3931, 2009.

[145] J. Prüss, G. Simonett, and R. Zacher. On normal stability for nonlinear parabolic problems. *Discrete Contin. Dyn. Syst. Supplement*, pages 612–621, 2009.

[146] F. Räbiger and R. Schnaubelt. The spectral mapping theorem for evolution semigroups on spaces of vector-valued functions. *Semigroup Forum*, 52:225–239, 1996.

[147] J.D.M. Rademacher, B. Sandstede, and A. Scheel. Computing absolute and essential spectra using continuation. *Physica D*, 229:166–183, 2007.

[148] M. Rietkerk, M.C. Boerlijst, F. van Langevelde, R. Hillerislambers, J. van de Koppel, L. Kumar, H.H.T. Prins, and A.M. de Roos. Self-Organization of Vegetation in Arid Ecosystems. *The American naturalist*, 160:524–530, 2002.

[149] M. Rietkerk, S.C. Dekker, P.C. de Ruiter, and J. van de Koppel. Self-organized patchiness and catastrophic shifts in ecosystems. *Science*, 305:1926–1929, 2004.

[150] M. Rietkerk, P. Ketner, J. Burger, B. Hoorens, and H. Olff. Multiscale soil and vegetation patchiness along a gradient of herbivore impact in a semi-arid grazing system in west africa. *Plant Ecology*, 148:207–224, 2000.

[151] M. Rietkerk and J. van de Koppel. Regular pattern formation in real ecosystems. *Trends in ecology & evolution*, 23:169–75, 2008.

[152] C.J. Roussel and M.R. Roussel. Reaction–diffusion models of development with state-dependent chemical diffusion coefficients. *Progress in Biophysics & Molecular Biology*, 86:113–160, 2004.

Bibliography

[153] M.R. Roussel and J. Wang. Transition from self-replicating behavior to stationary patterns induced by concentration-dependent diffusivities. *PRL*, 87:188–302, 2001.

[154] A.B. Rovinsky and M. Menzinger. Chemical instability induced by a differential flow. *Phys. Rev. Lett.*, 69, 1992.

[155] A.B. Rovinsky and M. Menzinger. Self-organization induced by the differential-flow of activator and inhibitor. *Phys. Rev. Lett.*, 70:778–781, 1993.

[156] P.M. Saco, G.R. Willgoose, and G.R. Hancock. Eco-geomorphology of banded vegetation patterns in arid and semi-arid regions. *Hydrol. Earth Syst. Sci.*, 11:1717–1730, 2007.

[157] B. Sandstede. Stability of travelling waves. In *Handbook of Dynamical Systems, II*, pages 983–1055. Elsevier, 2002.

[158] B. Sandstede and A Scheel. On the structure of spectra of modulated travelling waves. *Math. Nachr.*, 232:39–93, 2001.

[159] B. Sandstede and A. Scheel. Defects in oscillatory media: toward a classification. *SIAM J. Appl. Dyn. Syst.*, 3:1–68, 2004.

[160] B. Sandstede and A. Scheel. Relative morse indices, fredholm indices, and group velocities. *Discrete and Continuous Dynamical Systems A*, 20:139–158, 2008.

[161] R.A. Satnoianu, J.H. Merkin, and S.K. Scott. Spatio-temporal structures in a differential flow reactor with cubic autocatalator kinetics. *Physica D*, 124:345–367, 1998.

[162] M. Scheffer. *Critical Transitions in Nature and Society*. Princeton University Press, 2009.

[163] M. Scheffer, J. Bascompte, W.A. Brock, V. Brovkin, S.R. Carpenter, V. Dakos, H. Held, E.H. van Nes, M. Rietkerk, and G. Sugihara. Early-warning signals for critical transitions. *Nature*, 461:53–59, 2009.

[164] M. Scheffer, S. Carpenter, J. Foley, C. Folke, and B. Walker. Catastrophic shifts in ecosystems. *Nature*, 413:591–596, 2001.

[165] M. Scheffer, E.H. Nes, M. Holmgren, and T. Hughes. Pulse-driven loss of top-down control: The critical-rate hypothesis. *Ecosystems*, 11:226–237, 2008.

[166] G. Schneider. Nonlinear diffusive stability of spatially periodic solutions– abstract theorem and higher space dimensions. In *Proceedings of the International Conference on Asymptotics in Nonlinear Diffusive Systems (Sendai, 1997)*, pages 159–167, 1998.

[167] L. Sewalt and A. Doelman. Spatially periodic multi-pulse patterns in a generalized Klausmeier–Gray–Scott model. In preparation.

[168] J. Shatah and W. Strauss. Spectral condition for instability. *Contemp. Math.*, 255:189–198, 2000.

[169] E. Sheffer, H. Yizhaq, M. Shachak, and E. Meron. Mechanisms of vegetation-ring formation in water-limited systems. *Journal of Theoretical Biology*, 273:138–146, 2011.

[170] J.A. Sherratt. An Analysis of Vegetation Stripe Formation in Semi-Arid Landscapes. *J. Math. Biol.*, 51:183–197, 2005.

[171] J.A. Sherratt. Numerical continuation of boundaries in parameter space between stable and unstable periodic travelling wave (wavetrain) solutions of partial differential equations. *Advances in Computational Mathematics*, 2012.

[172] J.A. Sherratt. History-dependent patterns of whole ecosystems. *Ecological Complexity*, 14:8–20, 2013.

[173] J.A. Sherratt. Pattern solutions of the klausmeier model for banded vegetation in semi-arid environments V: the transition from patterns to desert. *SIAM J. Appl. Math.*, 73:1347–1367, 2013.

[174] J.A. Sherratt and G.J. Lord. Nonlinear dynamics and pattern bifurcations in a model for vegetation stripes in semi-arid environments. *Theoretical population biology*, 71:1–11, 2007.

[175] N.M. Shnerb, P. Sarah, H. Lavee, and S. Solomon. Reactive glass and vegetation patterns.

Physical Review Letters, 90(3), 2003.

[176] E. Siero, A. Doelman, M.B. Eppinga, J.D.M. Rademacher, M. Rietkerk, and K. Siteur. Striped pattern selection by advective reaction-diffusion systems: Resilience of banded vegetation on slopes. *Chaos*, 25, 2015.

[177] G. Simonett. Center manifolds for quasilinear reaction-diffusion systems. *Differential Integral Equations*, 8:753–796, 1995.

[178] K. Siteur, M.B. Eppinga, A. Doelman, E. Siero, and M.G. Rietkerk. Ecosystems off track: Rate-induced critical transitions in ecological models. Preprint.

[179] K. Siteur, M.B. Eppinga, D. Karssenberg, M. Baudena, M.F.P. Bierkens, and M. Rietkerk. How will increases in rainfall intensity affect semiarid ecosystems? *Water Resources Research*, 50(7):5980–6001, 2014.

[180] K. Siteur, E. Siero, M.B. Eppinga, J.D.M. Rademacher, A. Doelman, and M.G. Rietkerk. Beyond Turing: the response of patterned ecosystems to environmental change. *Ecological Complexity*, 20:81–96, 2014.

[181] M.E. Solomon. The natural control of animal populations. *Journal of Animal Ecology*, 18(1):1–35, 1949.

[182] D.E. Spalinger and N.T. Hobbs. Mechanisms of foraging in mammalian herbivores: New models of functional response. *The American Naturalist*, 140(2):325–348, 1992.

[183] H.B. Squire. On the stability of 3D disturbances of viscous flow between parallel walls. *Proc. R. Soc. Lond. A*, 142:621–628, 1933.

[184] W. Sun, M.J. Ward, and R. Russell. The slow dynamics of two-spike solutions for the Gray–Scott and Gierer–Meinhardt systems: Competition and oscillatory instabilities. *SIADS*, 4:904–953, 2005.

[185] S. Thompson, G. Katul, and S.M. McMahon. Role of biomass spread in vegetation pattern formation within arid ecosystems. *Water Resources Research*, 44, 2008.

[186] S.E. Thompson, C.J. Harman, P. Heine, and G.G. Katul. Vegetation-infiltration relationships across climatic and soil type gradients. *Journal of Geophysical Research*, 2010.

[187] A. Toth, D. Horvath, and W. van Saarloos. Lateral instabilities of cubic autocatalytic reaction fronts in constant electric field. *J. Chem. Phys.*, 111:10964–10968, 1999.

[188] H. Triebel. *Interpolation theory, function spaces, differential operators*. North-Holland, 1978.

[189] H. Triebel. *Theory of function spaces II*. Birkhäuser, 1983.

[190] A. Turing. The chemical basis of morphogenesis. *Philosophical Transactions of the Royal Society of London. Series B, Biological Sciences*, 237:37–72, 1952.

[191] H. Uecker. Self-similar decay of spatially localized perturbations of the nusselt solution for the inclined film problem. *Arch. Rational Mech. Anal.*, 184:401–447, 2007.

[192] H. Uecker, D. Wetzel, and J.D.M. Rademacher. pde2path - A Matlab package for continuation and bifurcation in 2D elliptic systems. *Num. Math.: Th. Meth. Appl.*, 7:58–106, 2014.

[193] C. Valentin, J.M. d'Herbès, and J. Poesen. Soil and water components of banded vegetation patterns. *CATENA*, 37:1–24, 1999.

[194] J. van de Koppel and M. Rietkerk. Herbivore regulation and irreversible vegetation change in semi-arid grazing systems. *OIKOS*, 90:253–260, 2000.

[195] J. van de Koppel, M. Rietkerk, N. Dankers, and P.M.J. Herman. Scale-dependent feedback and regular spatial patterns in young mussel beds. *The American naturalist*, 165(3):E66–77, 2005.

[196] J. van de Koppel, M. Rietkerk, F. van Langevelde, L. Kumar, C.A. Klausmeier, J.M. Fryxell, J.W. Hearne, J. van Andel, N. de Ridder, A. Skidmore, L. Stroosnijder, and H.H.T. Prins. Spatial heterogeneity and irreversible vegetation change in semiarid grazing systems. *The*

Bibliography

American Naturalist, 159(2):209–218, 2002.

[197] H. van der Ploeg and A. Doelman. Stability of spatially periodic pulse patterns in a class of singularly perturbed reaction-diffusion equations. *Indiana Univ. Math. J.*, 54:1219–1302, 2005.

[198] S. van der Stelt. *Rise and Fall of Periodic Patterns in a Generalized Klausmeier-Gray-Scott Model*. PhD thesis, Universiteit Leiden, 2012.

[199] S. van der Stelt, A. Doelman, G. Hek, and J.D.M. Rademacher. Rise and fall of periodic patterns for a Generalized Klausmeier-Gray-Scott model. *J. Nonl. Sc.*, 23:39–95, 2013.

[200] J.L. Vàzquez. *The Porous Medium Equation*. Oxford University Press, 2007.

[201] B.Z. Virany, A. Szommer, A. Toth, and D. Horvath. Lateral instability controlled by constant electric field in an acid-catalyzed reaction. *Phys. Chem. Chem. Phys.*, 6:3396–3401, 2004.

[202] J. von Hardenberg, E. Meron, M. Shachak, and Y. Zarmi. Diversity of Vegetation Patterns and Desertification. *Physical Review Letters*, 87:3–6, 2001.

[203] R.-H. Wang, Q.-X. Liu, G.-Q. Sun, Z. Jin, and J. van de Koppel. Nonlinear dynamic and pattern bifurcations in a model for spatial patterns in young mussel beds. *J. R. Soc. Interface*, 6:705–718, 2009.

[204] M. Westoby, B. Walker, and I. Noy-Meir. Opportunistic management for rangelands not at equilibrium. *Journal of Range Management*, 42:266–274, 1989.

[205] X. Zhao Y. Wu. The existence and stability of travelling waves with transition layers for some singular cross-diffusion systems. *Physica D*, 200:325–358, 2005.

[206] A. Yagi. *Abstract Parabolic Evolution Equations and their Applications*. Springer, 2010.

[207] H. Yizhaq, E. Gilad, and E. Meron. Banded vegetation: biological productivity and resilience. *Physica A: Statistical Mechanics and its Applications*, 356:139–144, 2005.

[208] Y.R. Zelnik, S. Kinast, H. Yizhaq, G. Bel, and E. Meron. Regime shifts in models of dryland vegetation. *Philosophical Transactions of the Royal Society A*, 371, 2013.

[209] S. Zhao, J. Ovadia, X. Liu, Y.-T. Zhang, and Q. Nie. Operator splitting implicit integration factor methods for stiff reaction-diffusion-advection systems. *J Comput Phys.*, 230(15):5996–6009, 2011.

[210] K. Zumbrun. Center stable manifolds for quasilinear parabolic pde and conditional stability of nonclassical viscous shock waves. Preprint, available as arXiv:0811.2788.

[211] K. Zumbrun. Planar stability criteria for viscous shock waves of systems with real viscosity. In *Hyperbolic systems of balance laws*. Springer, 2007.

[212] K. Zumbrun and P. Howard. Pointwise semigroup methods and stability of viscous shock waves. *Indiana Univ. Math. J.*, 47:741–872, 1998.

Nederlandse samenvatting

Een woestijn als toetje

Ecosystemen in droge gebieden staan onder toenemende druk door klimaatverandering en een groeiende bevolking. Het is mogelijk dat de druk toeneemt tot voorbij een kritiek punt, waarna in een snelle transitie alle vegetatie verdwijnt. Het is belangrijk om dit verwoestijningsproces te begrijpen om het vervolgens tegen te kunnen gaan.

In dit proefschrift bestuderen we een fenomenologisch model - het *extended Klausmeier model* - waarin de opname van het zeldzame water door de vegetatie een cruciale rol speelt. In dit model gaat ruimtelijk homogene vegetatie onder toenemende druk over in ruimtelijk periodieke vegetatiepatronen. Deze patronen ontstaan door competitie voor water op de lange lengteschaal maar (in aanwezigheid van vegetatie) een betere bodeminfiltratie op de korte lengteschaal. Hierdoor heeft vegetatie nabij een positieve invloed op de plantengroei (facilitatie) terwijl vegetatie verder weg juist een negatief effect heeft.

We bekijken de verschillende scenario's van opeenvolgende vegetatiepatronen onder afnemende regenval, met als eindresultaat een kale woestijn - als toetje.

Op hellingen spelen vegetatiebanden of -strepen langs hoogtecontouren een centrale rol. Onder afnemende regenval komen deze patronen tevoorschijn uit een ruimtelijk homogeen begroeide toestand. Onder verder afnemende regenval neemt de golflengte van het patroon stapsgewijs toe. De grote van deze sprongen in golflengte hangt af van de snelheid waarmee de regenval afneemt en de mate waarin het proces door ruis verstoord wordt. Dit wordt beschreven in Hoofdstuk 2.

In Hoofdstuk 3 nemen we mee dat op een gegeven moment vegetatiebanden opbreken in *spots*. Hoe steiler de helling hoe langer dit moment op zich laat wachten. Hiermee vormen de *spots* een volgende stap in het verwoestijningsproces. Daarnaast laten we op basis van een lineaire analyse zien dat

op het moment van patroonvorming de homogene toestand overgaat in een streeppatroon, voor een ruime klasse van stelsels van partiële differentiaalvergelijkingen die het extended Klausmeier model omvat.

Nieuwe expliciete termen voor het modelleren van begrazing worden geïntroduceerd in Hoofdstuk 4. Begrazing op één locatie hangt af van het bestaan van alternatieve voedselbronnen elders, waardoor de nieuwe termen een niet-lokaal karakter hebben. Afhankelijk van hoe we de begrazing modelleren, kan het woestijnvormingsproces op verschillende manieren kwalitatief veranderen.

In het laatste hoofdstuk presenteren we voor zogenaamde quasi-lineaire stelsel van partiële differentiaalvergelijkingen, functieruimten waarbinnen oplossingen bestaan. Modellen voor vegetatie in droge ecosystemen kunnen quasi-lineair zijn, bijvoorbeeld als de stroming van water wordt beschreven door een *shallow water equation*. De bestudering van een model binnen een functieruimte waarin geen oplossingen bestaan moet vermeden worden. Door vergelijkingen op te stellen voor de verstoringen en daarvoor te laten zien dat oplossingen bestaan (binnen een geschikte functieruimte), kunnen we op een zinvolle manier stabiliteit bestuderen.

Curriculum Vitae

In 2009, Eric Siero obtained two bachelor diplomas: one in mathematics and one in physics, both from Leiden University. He continued his education with a master in mathematics (2011, *cum laude*), his master research was done as a trainee at CWI Amsterdam. During his studies he was active as tutor at the Leiden Institute of Physics and later as teaching assistant of the Mathematical Institute.

He subsequently started working towards his PhD within a NWO Complexity programme funded project, again in Leiden, leading up to this thesis. He has been an active member of the NWO Complexity programme and the Dutch mathematics cluster NDNS+, organizing meetings for both. He also organized and joined seminars at the Mathematical Institute in Leiden. At the SIAM DS13 conference in Snowbird (USA) he won the 'Red Sock' poster award. In 2014 he spent a semester at Universität Bremen for research.

Next to his studies Eric has been treasurer of study association De Leidsche Flesch, chairman of the committee organizing the physics olympiad PION for students (as a member of the winning team the previous year) and secretary of the ultimate frisbee association PANIC.